Dissertation

Agent-based modelling of the spatio-temporal interaction between immune cells and human-pathogenic fungi

Zur Erlangung des akademischen Grades
- Doctor rerum naturalium (Dr. rer. nat) -

Vorgelegt dem Rat der
Fakultät für Biowissenschaften
der Friedrich-Schiller-Universität Jena

von M. Sc. Sandra Timme
geboren am 28. April 1990 in Gera

Gutachter:

1. Prof. Dr. Marc Thilo Figge (Hans-Knöll-Institut Jena)
2. Prof. Dr. Oliver Kurzai (Hans-Knöll-Institut Jena, Julius-Maximilians-Universität Würzburg)
3. Prof. Dr. Lars Kaderali (Universität Greifswald)

Die Disputation der Doktorarbeit erfolgte am 18.12.2018 in Jena.

Table of Contents

Summary

Human-pathogenic fungi constitute a serious problem in medical health care due to the increasing number of immunocompromised patients and are associated with high mortality rates. The immune system – a highly complex system – provides an arsenal of effector mechanisms that protect the healthy status of the host. However, various causes may intimidate the protective function of the immune system, which allows invading microbes to cause severe infections. The research on host-pathogen interactions between human-pathogenic fungi and the immune system is essential for the development of new diagnostic and therapeutic approaches. In this thesis, these host-pathogen interactions have been investigated according to the concept of systems biology. Based on an experimental data basis, virtual infection modelling has been applied, in order to decipher the driving forces during the innate immune response against the fungal pathogens *Candida albicans*, *Candida glabrata* and *Aspergillus fumigatus*.

The opportunistic pathogens *C. albicans* and *C. glabrata* are commensals in the microbiota of large fractions of the world population. Typically, they colonize skin and mucosal surfaces and do not cause infections in healthy individuals. However, under immunocompromised conditions they can become pathogenic and can cause superficial as well as systemic infections due to pathogen translocation into the bloodstream. In a previous study, a whole-blood infection assay with *C. albicans* has been established in order to investigate the innate immune response against this fungus. Based on the measured data, a *state-based model* (SBM) was developed that quantifies innate immune reaction rates. In this thesis, a bottom-up modelling approach, which incorporates an extended version of the previously developed SBM and its spatial counterpart – an *agent-based model* (ABM) was developed. The ABM enabled prediction of immune cell migration parameters, which are not directly accessible in experiment. In order to keep computational costs within limits, the ABM takes advantage of estimated immune reaction rates from the SBM. This bottom-up modelling approach was used to address various research questions regarding the host-pathogen interaction in whole-blood infection assays with *C. albicans* and *C. glabrata*. In another study, the SBM was used for hypothesis testing of an immune evasion mechanism that could not be elucidated until now and was observerd in whole-blood infection assays. Furthermore, we simulated neutropenia and immune dysregulation and found that the infection outcome during impaired neutrophil migration resembles the infection outcome during neutropenia. Thus, we hypothesize that an improved neutrophil activity might recover the infection outcome in neutropenic patients to that of non-neutropenic individuals. We addressed this hypothesis using the bottom-up modelling approach, where we first determined immune reaction rates and migration parameters under healthy immune conditions. Subsequently, we simulated virtual neutropenic patients and investigated the infection outcome with *C. albicans* and *C. glabrata*. Eventually, we simulated an *in silico* cytokine treatment that enhanced phagocytic activity and migration of the remaining neutrophils, which indeed could successfully clear the fungal infections in the neutropenic patients and was more efficient for *C. glabrata*.

Contrary, to *Candida* spp., *A. fumigatus* naturally does not colonize humans, but occurs in soil. Its conidia are distributed via the air and every human individual inhales several hundreds up to thousands of them every day. Their small size allows the conidia to reach the alveoli in the lower respiratory tract, where they immediately face host immune responses, which efficiently clear the lung from the conidia in healthy hosts. However, if the immune system is compromised conidia are not eliminated before onset of the germination, leading to severe pulmonary infections. In this thesis, two publications focus on the host-pathogen interaction between the innate immune response and *A. fumigatus*. In a first publication, evolutionary game theory on graphs was applied that simulated different stages of this immune response in response to the fungus. To this end, a sequence of interaction situations, called *games*, was simulated, including the complement system, alveolar macrophages and neutrophils. This approach enabled to investigate the key parameters of the biological system and revealed the different roles of alveolar macrophages under various infection doses. In a second publication, we adapted a previously developed realistic to-scale hybrid ABM of a human alveolus to the murine system. This model included migration of alveolar macrophages as well as chemokine secretion and diffusion. Using the human and murine virtual alveoli, a comparative analysis of the early infection process during experimental *A. fumigatus* infection in mice and physiological *A. fumigatus* infection in humans was performed with regard to differences in their lung morphology and infection doses.

In this thesis, virtual infection modelling was applied to investigate host-pathogen interactions between the innate immune response and the human-pathogenic fungi *C. albicans*, *C. glabrata* and *A. fumigatus*. Different individual-based modelling techniques have been applied to investigate the driving forces in the immune response against the aforementioned pathogens and to generate relevant hypotheses. These hypotheses need to be addressed in future experimental studies starting the cycle of systems biology anew.

Zusammenfassung

Human-pathogene Pilze stellen aufgrund der zunehmenden Anzahl von immungeschwächten Patienten ein zunehmendes Problem im Gesundheitswesen dar und sind mit hohen Sterblichkeitsraten assoziiert. Das menschliche Immunsystem – ein hochkomplexes System – stellt ein Arsenal an Effektormechanismen bereit, die den gesunden Zustand des Wirts schützen. Vielfältige Ursachen können jedoch diese schützende Funktion des Immunsystems beeinträchtigen, was es eindringenden Mikroben erlaubt, schwere Infektionen zu verursachen. Die Forschung an Wirt-Pathogen-Interaktionen zwischen humanpathogenen Pilzen und dem Immunsystem ist essentiell für die Entwicklung neuer diagnostischer und therapeutischer Verfahren. In dieser Arbeit wurden diese Wirt-Pathogen-Interaktionen entsprechend des Konzepts der Systembiologie, untersucht. Basierend auf experimentellen Daten wurden virtuelle Infektionsmodelle entwickelt, um die treibenden Kräfte der angeborenen Immunantwort gegen die pilzlichen Erreger *C. albicans*, *C. glabrata* und *A. fumigatus* zu entschlüsseln.

Die opportunistischen Pilze *C. albicans* und *C. glabrata* kommen in der Mikrobiota großer Teile der Weltbevölkerung als Kommensal vor. Typischerweise kolonisieren sie Haut und Schleimhäute, verursachen aber bei gesunden Menschen keine Infektionen. In immungeschwächten Patienten können sie jedoch krankheitserregend werden und oberflächliche sowie systemische Infektionen, durch das Eindringen in die Blutbahn, verursachen. In einer vorangegangenen Studie wurde ein Vollblut-Infektionsassay mit *C. albicans* etabliert, um die angeborene Immunantwort gegen diesen Pilz zu untersuchen. Basierend auf den gemessenen Daten wurde ein zustandsbasiertes Modell (SBM) entwickelt, das Immunreaktionsraten des angeborenen Immunsystems quantifiziert. In dieser Arbeit wurde ein Bottom-up-Modellierungsansatz entwickelt, welcher eine erweiterte Version des zuvor entwickelten SBM sowie dessen räumliches Pendant – ein agentenbasiertes Modell (ABM) – beinhaltet. Das ABM erlaubt die Vorhersage von Migrationsparametern von Immunzellen, welche nicht direkt experimentell zugänglich sind. Um die Rechenkosten in Grenzen zu halten, nutzt das ABM die geschätzten Immunreaktionsraten aus dem SBM. Dieser Bottom-up-Modellierungsansatz wurde verwendet, um verschiedene Forschungsfragen bezüglich der Wirt-Pathogen-Interaktion in Vollblut-Infektionsassays mit *C. albicans* und *C. glabrata* zu behandeln. In einer weiteren Studie wurde der SBM zur Hypothesenprüfung eines Immunevasionsmechanismus verwendet, der in Vollblut-Infektionsassays beobachtet wurde und bis heute nicht aufgeklärt werden konnte. Darüber hinaus haben wir Neutropenie und die Dysregulation des Immunsystems simuliert und festgestellt, dass der Infektionsausgang während der gestörten Neutrophilenmigration dem Infektionsausgang unter Neutropenie ähnelt. Daher vermuten wir, dass eine verbesserte Neutrophilen-Aktivität den Infektionsausgang bei neutropenischen Patienten auf das von nicht-neutropenischen Individuen zurückführen könnte. Wir haben diese Hypothese mithilfe des Bottom-up-Modellierungsansatzes untersucht, bei dem wir zunächst die Immunreaktionsraten und Migrationsparameter unter gesunden Immunbedingungen bestimmt haben. Anschließend simulierten wir virtuelle neutropenische Patienten und untersuchten den Infektionsausgang mit *C. albicans* und *C. glabrata*. Schließlich

simulierten wir eine *in silico* Zytokin-Behandlung, die die phagozytische Aktivität und Migration der verbleibenden Neutrophilen verbesserte, was tatsächlich die Pilzinfektionen in neutropenischen Patienten beseitigen konnte und für *C. glabrata* effizienter war.

Im Gegensatz zu *Candida* Spezies werden Menschen nicht von *A. fumigatus* Konidien kolonisiert, welche vorwiegend im Erdreich vorkommen. Die über die Luft verbreiteten Konidien werden von jedem Menschen jeden Tag hundert- bis tausendfach eingeatmet. Ihre kleine Größe erlaubt ein Vordringen bis in die Lungenbläschen in den unteren Atemwegen, wo sie sofort mit der Immunantwort des Wirts konforntiert werden, welche in gesunden Menschen die Konidien in der Lunge effizient eliminiert. Wenn das Immunsystem geschwächt ist, werden die Konidien jedoch nicht rechtzeitig beseitigt und können auskeimen, was zu schweren Infektionen der Lunge führen kann. Teil dieser Dissertation sind zwei Veröffentlichungen, die die Wirt-Pathogen-Interaktion zwischen dem angeborenen Immunsystem und *A. fumigatus* untersuchen. In der ersten Veröffentlichung wurde evolutionäre Spieltheorie genutzt, um mehrere Stadien dieser Immunantwort zu simulieren. Dazu wurde eine Sequenz aus mehreren Spielen, d.h. Interaktionen zwischen Komponenten des Immunsystems, wie dem Komplementsystem, alveolaren Makrophagen und Neutrophilen, simuliert. Dies erlaubte die Untersuchung der Schlüsselparameter des biologischen Systems und klärte die unterschiedlichen Rollen alveolarer Makrophagen unter verschiedenen Infektionsdosen auf. In einer zweiten Publikation haben wir ein zuvor entwickeltes, realistisches, skalengerechtes, hybrides ABM eines menschlichen Lungenbläschens für das Maussystem angepasst. Dieses Modell umfasst die Migration alveolarer Makrophagen sowie die Sekretion und Diffusion von Chemokinen. Unter Nutzung der virtuellen Lungenbläschen für Mensch und Maus haben wir eine vergleichende Analyse des frühen Infektionsprozesses während experimenteller *A. fumigatus* Infektion in Mäusen und physiologischer *A. fumigatus* Infektion in Menschen durchgeführt. Dabei haben wir insbesondere die verschiedenen Lungenmorphologien sowie Infektionsdosen betrachtet.

In dieser Dissertation wurden virtuelle Infektionsmodelle erstellt, um Wirt-Pathogen-Interaktionen zwischen dem angeborenem Immunsystem und den humanen Pilzerregern *C. albicans*, *C. glabrata* und *A. fumigatus* zu erforschen. Verschiedene individuenbasierte Modellierungstechniken wurden angewandt, um die treibenden Kräfte in der Immunantwort gegen die zuvor genannten Erreger zu ermitteln und relevante Hypothesen zu generieren. Zukünftige experimentelle Untersuchungen dieser Hypothesen werden den Kreislauf der Systembiologie von Neuem starten.

Abbreviations

Biological

ABPA allergic bronchopulmonary aspergillosis

AEC alveolar epithelial cells

CNPA chronic necrotizing pulmonary aspergillosis

CPA chronic pulmonary aspergillosis

CR3 complement receptor 3

DNA deoxyribonucleic acid

FACS fluorescence-activated cell sorting

FHL-1 factor-H-like protein 1

G-CSF granulocyte colony-stimulating factor

GM-CSF granulocyte-macrophage colony-stimulating factor

HIV human immunodeficiency virus

IFNγ interferon γ

IL-8 interleukin 8

NETs neutrophil extracellular traps

NK cells natural killer cells

PAMPs pathogen associated molecular patterns

PIDs primary immune disorders

Pra1 pH-regulated antigen 1

PRRs pattern recognition receptors

RNA ribonucleic acid

ROS reactive oxygen species

Saps secreted aspartyl proteases

SCID severe combined immunodeficiency

SCN severe congenital neutropenia

XLA X-linked agammaglobulinemia

Computational

ABM agent-based model

CA cellular automata

CGT classical game theory

CPM cellular Potts model

EGT evolutionary game theory

GT game theory

hABM hybrid agent-based model

IBM individual-based model

LSE least squares error

ODE ordinary differential equation

PDE partial differential equation

RSS residual sum of squares

SBM state-based model

SDE stochastic differential equation

VNP virtual neutropenic patients

Part I.

Introduction

Humankind tried to classify living organisms into kingdoms ever since. From Aristotle to the mid of the 20th century living organisms on earth were grouped into plants and animals. However, with increasing knowledge about biology this concept turned out to be not sufficient to describe the huge variety of living organisms. In the past, several proposals for the classification of organisms into groups have been made on the basis of different criteria. For example, in 1866 Ernst Haeckel proposed a three-kingdom system that incorporated not only plants and animals but also the kingdom of *protista* that contained microscopic organisms. Further research revealed a much more complex picture of the phylogeny of life on earth. New technologies and further research on the molecular level, especially DNA-Sequencing allowed for an increasingly better classification of the kingdoms of live. Nowadays, a five- or six-kingdom system is widely accepted. The five kingdom system includes *animalia*, *plantae*, *fungi*, *protista* and *monera*, while the six kingdom system further separates *monera* into *archea* and *eubacteria*. This emphasizes the importance of fungi for life on earth, as they constitute a separate kingdom of life. Fungi are eukaryotic organisms that occupy all habitats on earth in air, soil and water in all climate zones, as they are highly adaptable and can cope with extreme environmental conditions [1]. Currently, over 21,000 different fungal species are described in *"The Dictionary of the fungi"* by Ainsworth and Bisby [2]. However, there exist several estimates on the total number of fungal species that range between 712,000 [3] up to 5.1 million [4]. Furthermore, some species have mutualistic, commensalistic or parasitic relationships with other organisms like plants, insects and vertebrates.

The research on fungi is, among other issues, driven by economical, ecological, pharmaceutical and medical interests. Some fungal species constitute a major problem in agriculture where they are responsible for vast harvest losses [5]. However, other species like white-rot fungi are used as bioremediators as they are able to degrade for example heavy metals, dyes, pesticides, herbicides, plastic and thereby help in counteracting environmental pollution [6]. Furthermore, some fungal species like *A. fumigatus*, *C. albicans*, *C. glabrata*, *Pseudomonas aeruginosa* and many others are opportunistic or pathogenic to human individuals. Due to the increasing number of immunocompromised patients, fungal infections, ranging from superficial up to systemic infections, are an increasing problem in medical health care [7, 8]. Besides these problems caused by some species, fungi yield also an enormous potential in their secondary metabolites to find new natural products that might be useful in different fields of applications, such as antibiotics, immunosuppressants, angiogenesis inhibitors, anti-osteoporosis agents and anti-migraine [9].

The subject of research of the present thesis is the host-pathogen interaction of the human innate immune system with the fungal pathogens *C. albicans*, *C. glabrata* and *A. fumigatus*, which was investigated using a *systems biology* approach. The concept of systems biology describes an iterative cycle between wet-lab studies, *i.e.* experiments performed in laboratories, and computational data analysis, modelling and simulation.

The work on which this thesis is build upon was conducted within a transregional Collaborative Research Center (CRC/Transregio 124) funded by the *Deutsche Forschungsgemeinschaft* (DFG), called *FungiNet*. This transregional project is a collaborative work of experts on fungal pathogens in the two cities Jena and Würzburg. It aims at understanding the cause and process of fungal infections of the two major fugal human pathogens *A. fumigatus* and *C. albicans*. Special focus is placed on virulence factors of the fungal pathogens, the immune response as well as host-pathogen interactions. Of

particular note is the complementary work of experimental and theoretical groups that collaborate according to the cycle of systems biology. These investigations drive the development of new diagnostic and therapeutic methods with regard to fungal infections.

In the first chapter of the introduction human-pathogenic fungi will be introduced, with special emphasis on the species *C. albicans*, *C. glabrata* and *A. fumigatus*. The second chapter focuses on the human immune system with regard to the innate immune response against these human-pathogenic fungi. Eventually, the third chapter introduces the concept of systems biology and gives an overview about computational modelling and parameter estimation methods, that are of relevance for this thesis.

1. Human-pathogenic fungi

– an underestimated threat –

Besides bacteria and viruses, fungi constitute a major threat to the health of the human body [10]. It is estimated that there are around 600 human-pathogenic fungi that infect mucosa, skin, hair, nails and cause allergies [11]. Most people face benign superficial fungal infections during their life-time that are usually easy to treat [7].

On the contrary, millions of people worldwide per year acquire invasive fungal infections, which are often diagnosed too late, treated not appropriately and come along with high mortality rates up to 50 % [7]. The number of invasive fungal infections increased during the last years due to the increased use of immunosuppressive and invasive medical interventions worldwide [12]. These possibly lethal infections occur mainly in patients with a compromised or suppressed immune system. For example, HIV patients, neutropenic patients, patients that underwent anti-cancer chemotherapy or patients that receive immunosuppressive therapy due to an organ transplantation are at high risk for invasive fungal infections [12].

The most prevalent invasive fungal infections are *aspergillosis*, mainly caused by *A. fumigatus*, *candidiasis*, mainly caused by *C. albicans* and *cryptococcosis*, mainly caused by *Cryptococcus neoformans*. However, there are many other fungal species that cause invasive fungal infections as well [7]. The focus of this thesis mainly laid on *Candida* blood stream infection and *Aspergillus* lung infection. Therefore, this chapter introduces morphology, life cycle and the occurrence in the human body of the human-pathogenic fungi *C. albicans*, *C. glabrata* and *A. fumigatus*. Furthermore, associated diseases and the course of infection of these pathogens will be part of this chapter.

1.1. The human commensals *Candida albicans* and *Candida glabrata*

The cell number of the human body is estimated on $3.72 \cdot 10^{13}$ cells [13]. About the same number of microbial cells colonise skin and mucosal surfaces forming the 'normal flora' – the so called *microbiota* [14]. The human microbiota contains an enormous diversity of microbial species, with fungal species among them [15].

A common fungal commensal that colonizes over 75 % of all humans is *C. albicans* [16]. However, the genus *Candida* comprises approximately 150 different species [16], of which more than 17 are opportunistic pathogens to humans and colonize skin and mucosal surfaces of a large fraction of the world population [17, 18]. Over the last 15 years cases of non-albicans candidiasis increased 2 to 10-fold [19, 20], where in European countries, the USA and Australia, *C. glabrata* was the second most prevalent isolate. However, *C. albicans* is still the main cause of invasive candida blood stream infections [17, 21]. Therefore, the main focus with regard to candidiasis in this thesis is on the two species *C. albicans* and *C. glabrata*.

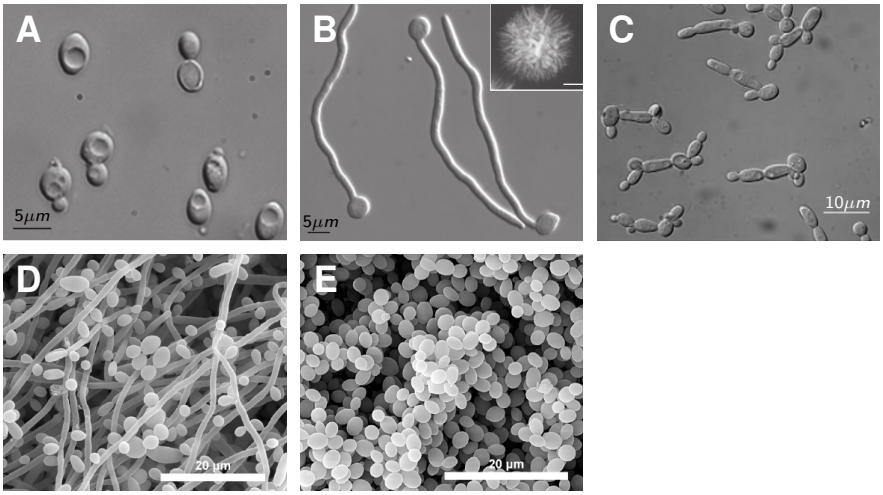

Figure 1.: Morphology of *C. albicans* and *C. glabrata*. Upper panel shows different morphological stages of *C. albicans*, which can be in the yeast form (A), in the hyphal form (B) [22] or form pseudo-hyphae (C) [23]. The lower panel shows electron microscopy images of *C. albicans* (A) and *C. glabrata* biofilms [24]. Images were taken from Sudbery (2011), Sudbery *et al.* (2004) and Vila and Rozental (2012).

1.1.1. Morphology and occurrence in the human body

As *Candida* spp. are part of the human microbiota, they are present on skin and mucosal surfaces, like the oral cavity, the gastrointestinal or the urogenital tract. Despite the fact that *C. albicans* and *C. glabrata* belong to the same genus, they feature some fundamental differences. For instance, *C. albicans* is a polymorphic fungus, while *C. glabrata* is exclusively present in the typical yeast form also called blastoconidia [25, 26]. The different morphologies that *C. albicans* can exhibit, feature different functionalities and occur under different conditions. Furthermore, the morphological changes of *C. albicans* contribute also to the virulence of this species.

Under healthy immune conditions *C. albicans* stays in its benign commensal form, where it is present in its typical round-to-oval yeast form (see Figure 1 (A)) [16]. If the immune system is weakened, *C. albicans* is able to germinate and form elongated cells with parallel cell walls, which are called *true hyphae* (see Figure 1 (B)). Usually in infections yeast and true hyphae are found [16, 27, 28]. While hyphae are invasive, yeast cells are usually involved in the dissemination during invasive bloodstream infections [28]. The morphology of *C. albicans* cells depends on various factors, such as the pH, temperature, CO_2 level and the contact to serum or specific medium. Besides yeast and hyphal forms, this fungus can also exhibit other morphologies, such as *pseudohyphae*, which are elongated ellipsoid cells with constrictions at the septa (see Figure 1 (C)).

Although *C. glabrata* exhibits the yeast form and is not polymorphic, it nevertheless can also undergo the switch from the commensal to the pathogenic state. To date the exact mechanisms of *C. glabrata* invasion is not fully understood. However, *C. glabrata* is also able to invade the human body by the production of tissue-damaging enzymes, such as proteases, phospholipases, and hemolysins, and thereby causes bloodstream infections [18, 25, 29].

Furthermore, *Candida* spp. have the ability to form biofilms on epithelial cells as well

as on various materials (see Figure 1 (D,E)) [30, 31]. Biofilm formation of *C. albicans* is a major problem in health care, since it comes along with resistance against antifungals and host-immune responses and is responsible for a major fraction of nosocomial fungal infections [9, 32–34]. Particularly, biofilm formation on catheters as used in hospitals pose a major risk factor for bloodstream infections, since they allow *Candida* spp. to enter the blood stream.

Taken together, *C. albicans* and *C. glabrata* feature a large variety of virulence factors, which make them successful pathogens. These virulence factors include for example the yeast-to-hyphae transition, the adhesion to host epithelia, biofilm formation, the adaptation to different nutrient sources, the production of hydrolytic enzymes and immune evasion mechanisms [34].

1.1.2. Course of infection and associated diseases

Superficial infections with both pathogens arise on mucosal surfaces that are colonized by these fungi. First, the fungal cells attach to epithelial cells. In the case of *C. albicans*, germination and hyphae formation is initiated, which allows penetration of the tissue and invasion. *C. glabrata* is also able to invade the tissue, though without morphological changes. Superficial *Canidia* infections can be acute, recurrent or chronic. The most common diseases are pseudomembranous candidiasis, also known as *thrush* and vulvovaginal candidiasis. Oral thrush often occurs in patients with acute leukaemia undergoing chemotherapy as well as HIV patients [35]. Moreover, vulvovaginal candidiasis can be acute or recurrent and affects up to 75% of all women in child-bearing age [36].

Invasive candidiasis is the fourth most common cause of bloodstream infections in intensive care units with 250 000 cases per year and mortality rates of 40% [37]. Risk factors are extremes of age, central vascular catheters, recent abdominal surgeries and broad-spectrum antibiotic therapy [37]. Fungal cells can enter the blood stream through catheters or due to a disturbed integrity of the intestinal epithelial barrier [37–39]. Surgeries or medical treatments may cause leakages or a higher permeability in the intestinal epithelium allowing fungal cells to invade the blood stream. Furthermore, patients suffering from sepsis in immunoparalysis are predisposed for candidemia [37, 39] but also patients suffering from candidemia may develop sepsis. Furthermore, *Candida* blood stream infections may lead to deep-seated infections in organs and other sites, such as bones, muscles, joints, the central nervous system, liver and kidney [37]. Typical drugs applied in invasive candidiasis are fluconacole, caspofungin and variconacole [18, 37].

1.2. The airborne fungus *Aspergillus fumigatus*

The genus *Aspergillus* comprises approximately 200 different species, of which about 20 species are pathogenic for humans [40, 41]. Among these 20 species *A. fumigatus* is the most prevalent isolate causing invasive fungal infections [41, 42]. *A. fumigatus* is an airborne saprophytic mould that naturally occurs in soil, where it recycles carbon and nitrogen sources by decaying organic material [40, 41, 43].

1.2.1. Morphology, life cycle and course of infection

Naturally, *A. fumigatus* does not colonize human individuals. However, since its spores, also called *conidia*, are distributed over the air, every human individual inhales several

thousand of these spores every day [43]. Due to their small size of about $2-3\,\mu$m they are able to overcome several filter mechanism of the respiratory tract and enter the lung alveoli in the lower respiratory tract. Typically, this poses no problem in healthy people as the immune system can efficiently clear the conidia from the lung. However, in immunocompromised patients this clearance may not work properly and *A. fumigatus* can become infectious. During its life cycle *A. fumigatus* undergoes morphological changes that are associated with different properties in their virulence, like cell wall composition as well as metabolic and reproductive activity [42].

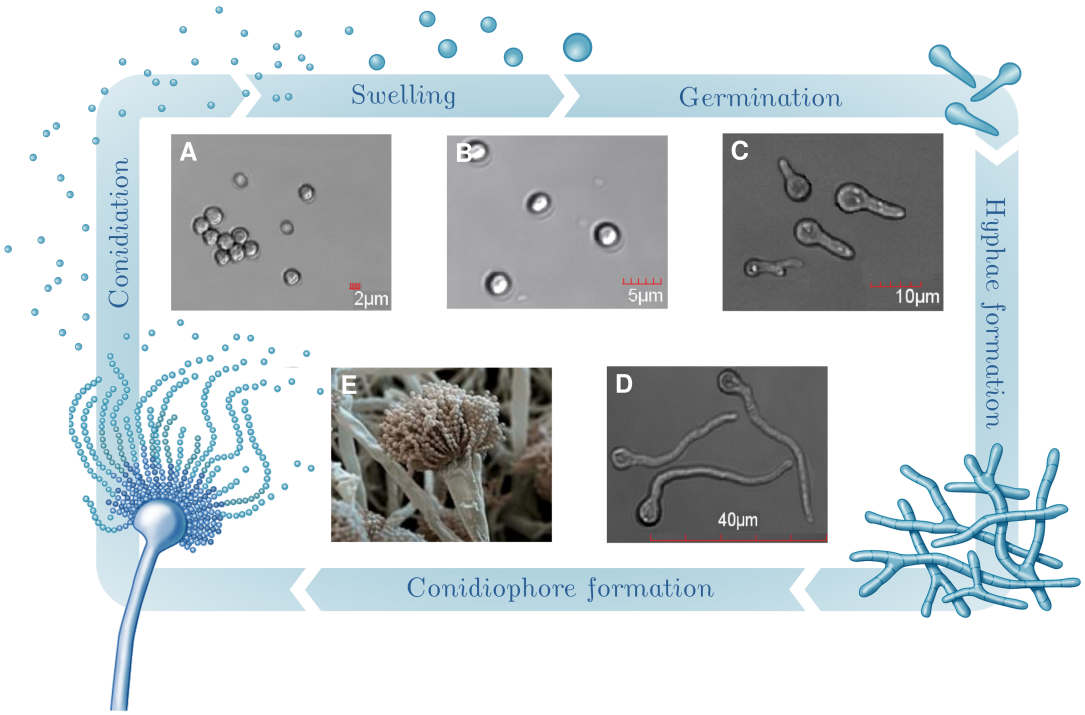

Figure 2.: Life cycle of *A. fumigatus*: (A) Conidia with a size of about $2-3\,\mu m$ in diameter. In contact to water and nutrients conidia begin to swell (B) and germinate (C), which leads to hyphae formation (D). In contact to air, *A. fumigatus* forms conidiophores (E) that in turn produce asexual conidia, which has the potential to spread the fungus. This figure is adapted from Dagenais and Keller (2009), Margalit and Kavanagh (2015) and Shapiro *et al.* (2011).

The spherical conidia of *A. fumigatus* (see Fig. 2 (A)) are ubiquitous and are, due to their hydrophobic surface, predestined to be distributed via the air. This hydrophobic surface is composed of a *rodlet* layer on the outer layer of the fungal cell wall, which shields the underlying polysaccharides and thereby makes the conidia immunologically inert [46]. The metabolic activity of conidia is very low, *i. e.* they are in a *resting* state, where they require only little nutrients and water, but also are not able to grow or replicate. When the conidia are exposed to water and nutrients they begin to swell and germinate (see Fig. 2 (B,C)) [45, 47]. A physiological temperature of 37°C provides optimal growth conditions and therefore attributes to the virulence of *A. fumigatus*. Swelling and germination involve an increase in size causing the burst of the rodlet layer, which leads to the uncovering of the underlying polysaccharides, that can be bound by

receptors of innate immune cells. Furthermore, swelling and germination is followed by hyphae formation (see Fig. 2 (D)). Hyphae are elongated cells that constitute an important virulence factor of *A. fumigatus*, since hyphae are able to break epithelial barriers. This further leads to invasion and dissemination in the body. Furthermore, *A. fumigatus* is able to form biofilms, where hyphae are embedded in an extracellular matrix [43, 48]. Changes in the cell wall composition of the different morphologies trigger distinct immune reactions [46, 49].

1.2.2. Associated diseases

Pulmonary aspergillosis can occur in various clinical cases and can be distinguished in three different groups, which are chronic, asthmatic and invasive aspergillosis [43, 44]. The most lethal examples for chronic aspergilloses are *chronic pulmonary aspergillosis* (CPA) or *chronic necrotizing pulmonary aspergillosis* (CNPA). Here, fungal growth occurs within damaged tissue or cavities in the lung that are for example caused by tuberculosis or sarcoidosis [42]. This often leads to the formation of aspergilloma, also known as "fungal balls", in the lung [43]. The most common allergic aspergillosis is *allergic bronchopulmonary aspergillosis* (ABPA), where fungal allergens provoke an inflammatory response but no fungal growth takes place [42, 43]. ABPA often occurs in asthmatic and cystic fibrosis patients. Immunocompromised patients that retrieve immuno-suppressive drugs like in hematopoetic stem cell or solid organ transplantation, as well as chemotherapy or AIDS patients are at high risk for invasive aspergillosis. This disease develops very fast and is associated with mycelial growth and invasion in the lung leading to high mortality rates.

2. Host-pathogen interactions

– an arms race –

When infectious microbes enter the human body they are immediately combated by the immune system. However, pathogens try to evade or counteract host immune mechanisms. This chapter introduces general aspects of the human immune system and host-pathogen interactions of the innate immune system and the human-pathogenic fungi *C. albicans*, *C. glabrata* and *A. fumigatus*.

2.1. The human immune system

During evolution a sophisticated and highly efficient system – the immune system – has developed, in order to combat possible threats by invading microbes and thus secure the health of our body. The immune system comprises various mechanisms on humoral and cellular scales that are strongly regulated and interwoven. In general, one can distinguish two major parts of the immune system, that complement and regulate each other: the *innate* and the *adaptive immune system* [50].

The innate immune system

The innate or in-born immune system provides an immediate active defence upon encounter of cues that intimidate the healthy status of an individual. Its defence mechanisms range from physical barriers, like the skin and mucosa, via the humoral response of cytokines and the *complement system* up to the cellular response of *phagocytes* and *antigen-presenting cells* [51].

The complement system is the fist line of defence of the immune system against foreign cells as well as altered host cells and is activated within seconds [52, 53]. It comprises three different pathways – the classical pathway, the lectin pathway and the alternative pathway – that work as a cascade and converge in a common terminal pathway [52–57]. The complement system comprises approximately 30 to 40 soluble and surface-expressed molecules [58, 59], where most of them are inactive precursors that become enzymatically active upon cleavage and can work in a self-amplified fashion [53, 54]. These molecules opsonize pathogens and create an inflammatory milieu that guides cellular components of the immune system. The central component along the cascade of the complement system is C3, an inactive precursor. The activation of all three pathways ultimately leads to cleavage of C3 into C3a, an inflammatory mediator, and C3b, an opsonin that covalently binds to cell membranes and tags cells for phagocytosis. Moreover, the complement system can also actively destroy microbial invaders by formation of the *membrane attack complex* that causes perforation of the cell membrane leading to death of the pathogen [52, 55]. In order to prevent opsonization of host cells regulatory proteins, such as factor H, provide *self* from *non-self* discrimination mechanisms [57].

PHAGOCYTES comprise three major cell types that contribute to the innate immune system: monocytes, granulocytes and dendritic cells [52]. Granulocytes consist of three different cell types – neutrophils, eosinophils and basophils – where neutrophils make up over 70 % of all blood leukocytes [60]. While the main task of monocytes and neutrophils in humans is their phagocytic activity, dendritic cells are antigen-presenting cells, *i. e.* they phagocytose and digest detected pathogens or altered host cells and present the cell fragments on their surface in order to activate adaptive immune responses. Monocytes are phagocytes that are present in the blood circulation. They can enter various tissues and differentiate into tissue specific macrophages and stay their as resident immune cells that are often the first immune cells to encounter invading pathogens. Upon inflammatory signals, produced by the complement system and resident macrophages, neutrophils are recruited from the blood stream to the site of infection [52]. They provide an arsenal of defence mechanisms against pathogens, such as phagocytosis and the formation of a cytotoxic milieu due to the secretion of antimicrobial peptides and the production of *reactive oxygen species* (ROS). Furthermore, as a final act of defence neutrophils can commit an altruistic suicide, where they release their *deoxyribonucleic acid* (DNA) content and form *neutrophil extracellular traps* (NETs), in order to trap the fungus [61, 62]. The recognition of pathogens by phagocytes is realized by so called *pattern recognition receptors* (PRRs), which bind to *pathogen associated molecular patterns* (PAMPs), specific molecules that are present on microbial surfaces [63, 64]. PRRs can activate signalling cascades that orchestrate the immune response through transcriptional responses, like the production of pro-inflammatory cytokines, and the increase of phagocytic activities. The binding of pathogens by receptors of professional phagocytes leads to engulfment of the pathogen into the phagosome. Eventually, lysosomes fuse with the phagosome, forming the phagolysosome, which leads to acidification and thereby killing of the pathogen [52].

The adaptive immune system

Often innate immune reactions initiate adaptive immune responses by building up an inflammatory milieu. Since the adaptive immune response is not subject of this thesis this section will only give a brief overview of the most important components of the adaptive immune system. Similar to the innate immune system the adaptive immune system comprises cellular and humoral components. While the innate immune system acts within seconds, minutes and hours, the onset of the adaptive immune system may take several days or weeks [52]. Additionally, it provides highly pathogen-specific immunologic effector mechanisms and includes an immunologic memory [65]. Lymphocytes constitute the most important cellular components of the adaptive immune system. They include T and B lymphocytes [65], which intensely interact with dendritic cells in the lymph nodes, where they maturate and develop highly specialised receptors against detected pathogens. After maturation B cells can develop into plasma cells that produce antibodies [65]. These antibodies, also called immunoglobulins, are Y-shaped proteins that bind specific to antigens – characteristic pathogenic molecules [66]. The opsonization of pathogens with antibodies tags them for recognition by phagocytes, is able to directly neutralize them and, thus, prevents invasion and activates the complement system [52, 66]. Furthermore, memory B cells allow for a faster production of antibodies upon repeated pathogen encounter. Thereby, B cells mediate the humoral adaptive immune response [65].

Disorders and Dysregulation of the Immune System

The immune system involves highly complex and interwoven mechanisms that in most cases successfully protect the human body against external and internal threats. However, this protective property might be impaired due to various disorders that can affect different components of the immune system. Such disorders can be classified into primary and secondary immune deficiencies. While, *primary immune disorders* (PIDs) are in-born and therefore have a genetic origin, secondary disorders are acquired during life [67, 68]. Examples for PIDs are *severe combined immunodeficiency* (SCID), where T cells and in some forms also B cells are completely missing, and *X-linked agammaglobulinemia* (XLA), the most common form of antibody deficiency, where the process of B cell maturation is disturbed and no functional antibodies are produced [67, 69]. Secondary immune deficiencies are much more common than PIDs and can have various causes, such as extremes of age, malnutrition, infectious agents, drugs, metabolic diseases and environmental conditions [68]. Drug-related immune deficiencies can be caused by corticosteroids and immunosuppressive drugs that are for example used in hematopoetic stem cell transplantations, solid organ transplantations and anti-cancer chemotherapy. Furthermore, the *human immunodeficiency virus* (HIV) is the most prominent example for secondary immune diseases caused by infectious agents [68]

Furthermore, severe infections with bacterial, viral and fungal pathogens can lead to dysregulation of the host immune response, which can result in life-threatening organ dysfunction, referred to as sepsis [70, 71].

The condition of neutropenia, *i.e.* a reduced absolute neutrophil count, constitutes a major risk factor for candidiasis and aspergillosis and can arise due to congenital impairments, such as *severe congenital neutropenia* (SCN) [72]. However, most cases of neutropenia are acquired and constituted by diverse causes, such as autoimmune disorders, where antibodies attack neutrophils in blood, anti-cancer chemotherapy [73], leukemia, alcoholism as well as nutrition deficiencies. Infections like hepatitis A, B, C as well as HIV/AIDS, but also sepsis can cause high neutrophil consumption. In combination with exhausted bone marrow reservoirs this might lead to neutropenia [60, 74, 75].

2.2. Innate immune response to *Candida* in blood and immune evasion

Candida spp. such as *C. albicans* and *C. glabrata* can enter the bloodstream through catheters as well as through a disturbed intestinal barrier. In the bloodstream the yeast cells face several innate humoral and cellular defence mechanisms as depicted in Figure 3 [76]. Upon entering the bloodstream the complement system is immediately activated and the central components C3 and C5 are cleaved. Thus, yeast cells are opsonized by C3b and the anaphylatoxins C3a and C5a contribute to an inflammatory milieu [77]. Thereby, the complement system triggers the activation of cellular immune responses, where the most important cell types are monocytes, *natural killer cells* (NK cells) and neutrophils [76].

Neutrophils are the most abundant leukocytes in blood and constitute the primary effector cells against *Candida* spp. during bloodstream infection. They accomplish highly effective killing by phagocytosis and the formation of a cytotoxic environment as described in section 2.1 [76]. Thus, neutropenia constitutes a major risk factor for candidiasis and is associated with increased mortality rates. Neutrophils are efficiently

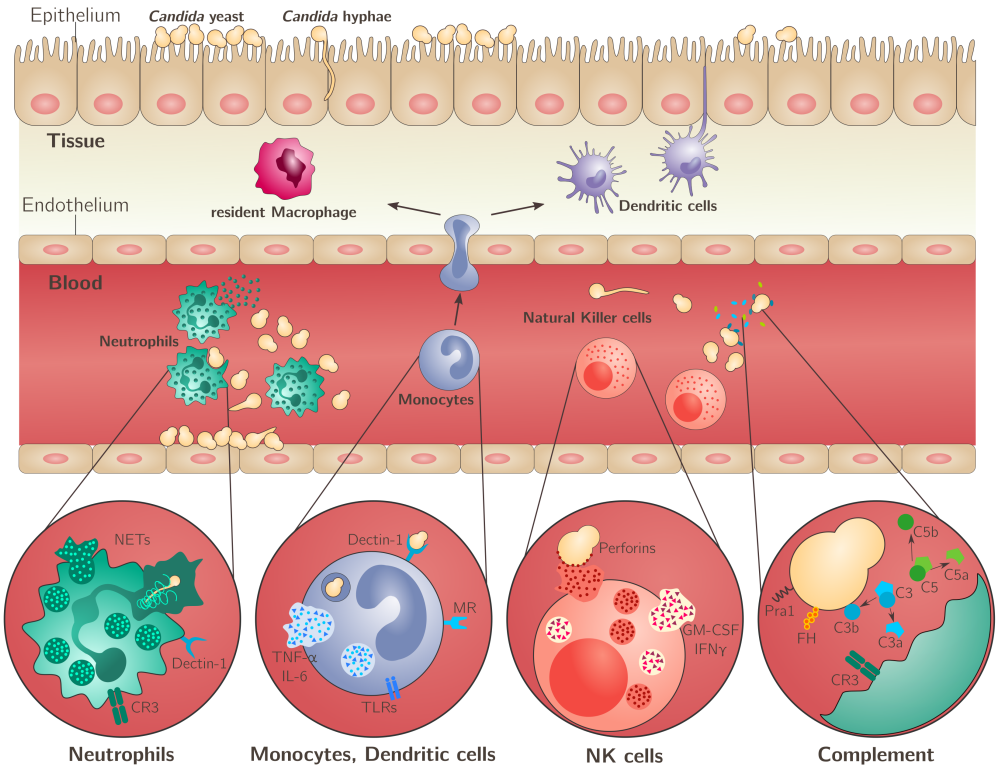

Figure 3.: Early immune response against *C. albicans* in human blood. Upon entering the bloodstream complement is activated and the central complement proteins C3 and C5 are cleaved. *C. albicans* cells are opsonized by C3b and C3a as well as C5a consitute a pro-inflammatory milieu. Monocytes bind *C. albicans* via the PRR Dectin-1, can phagocytose the fungal cells and secrete cytokines like TNFα and IL-6 leading to recruitment of neutrophils. Neutrophils can phagocytose the *C. albicans* cells and build up a cytotoxic milieu by secretion of anti-microbial peptides and ROS. As a final act of defence they can form NETs, which has fungistatic activity. The figure was created based on figures by Duggan *et al.* [76] and Netea *et al.* [78].

recruited by different cytokines, released by the complement and monocytes, to the site of infection. Upon activation they release for example *interleukin 8* (IL-8) leading to further recruitment of neutrophils. A central surface molecule of neutrophils is the *complement receptor 3* (CR3) that can recognise both, *C. albicans* yeast and hyphae. CR3 can bind the complement molecule C3b as well as the *C. albicans* membrane protein β-glucan and the *C. albicans* surface molecule Pra1. Monocytes are the second most abundant leukocytes in blood and are also involved in the immune response against *Candida* spp., although their killing ability is less effective in blood. Monocytes recognise *Candida* spp. via the Dectin-1 receptor. Upon activation they release cytokines, such as TNFα and IL-6, which contribute to the inflammatory milieu and mediate activation and recruitment of other immune cells, such as neutrophils. Monocytes seem to play a more important role in locations of dissemination, such as the kidney [76]. NK cells are cells of the innate immune system that secrete perforins forming a cytotoxic environment that can act against *C. albicans* germ tubes. Furthermore, NK cells can phagocytose yeast cells and are able to trigger antifungal effector mechanisms of neutrophils, dendritic cells and T cells by secretion of cytokines like *interferon* γ (IFNγ), TNFα and *granulocyte-macrophage*

colony-stimulating factor (GM-CSF) [79].

Despite this orchestrated cellular and humoral immune response, *Candida* spp. are not at the mercy of these immune defence mechanisms, but have developed themselves a repertoire of immune evasion mechanism. This repertoire includes mechanisms to evade the complement system, to prevent recognition and phagocytosis by immune cells as well as phagosome maturation [77]. *Candida* spp. are able to bind several complement regulators, such as Factor H, plasminogen or *factor-H-like protein 1* (FHL-1) form the human plasma to circumvent the attack by the complement system. Moreover, *Candida* spp. are also able to release *secreted aspartyl proteases* (Saps) and *pH-regulated antigen 1* (Pra1). Saps degrade and inactivate the complement molecules C3b, C4b and C5. Pra1 is able to bind C3 and thereby blocks all downstream effects of the complement system [77, 80, 81]. During hyphal growth *C. albicans* shields β-glucan of the fungal cell wall with a mannan layer that prevents binding of PRRs of phagocytes and thus phagocytosis. The dimorphism of *C. albicans* constitutes an escape mechanism, *i.e.* if hyphal growth exceeds a certain limit, macrophages are not able to phagocytose these cells [81]. However, phagocytosis can often not be prevented by the fungal pathogens. Therefore, several mechanisms developed to subvert phagocytosis. In case of *C. albicans* hyphal growth is initiated upon intracellular CO_2 production, which leads to disruption of the immune cell membrane and thus killing of these cells [81]. In contrast, *C. glabrata* is a non-dimorphic fungus but is still able to escape macrophages, since it can proliferate within macrophages and is able to prevent phagolysosome formation and acidification. The proliferation also leads to lysis of the immune cells [81, 82]. Furthermore, biofilm formation of *C. albicans* and *C. glabrata* increases resistance against host defence mechanisms and allows the fungi to grow and proliferate. Thus, the defence of the host and the evasion strategies of *C. albicans* and *C. glabrata* constitutes an immunological cross talk or arms race.

2.3. Innate immune response to *Aspergillus fumigatus* in the lung and immune evasion

When the conidia of *A. fumigatus* are inhaled they reach the alveoli in the lower respiratory tract (see Figure 4). Each alveolus is composed of *alveolar epithelial cells* (AEC) that are in close proximity to blood capillaries where the gas exchange takes place. The inner surface of these alveoli is lined with a thin layer of pulmonary surfactant that reduces the surface tension between alveolar epithelial cells and the air and therefore contributes to the stability of the lung [83]. Once conidia of *A. fumigatus* enter an alveolus, they are embedded within the surfactant, where the complement system is immediately activated [40]. The complement regulators C3 and C5 are cleaved and C3b opsonizes the conidium, while the anaphylatoxins C3a and C5a build up an inflammatory milieu (see Figure 4 right side) [40, 84].

The resident phagocytes in the lung are *alveolar macrophages* (AM), which are the first immune cells that get into contact with the conidia and therefore constitute the first cellular line of defence. The *complement receptor 3* (CR3) on the surface of the AM enables recognition of opsonized conidia [84] and several PRRs are involved in the immune response against *A. fumigatus* that can bind cell wall components, such as $\beta - 1,3-$glucan, and thus enhance the phagocytic activity of AM [85]. TLR2 and TLR4 mediate cytokine production, such as TNF-α, IL-1α, IL-1β, IL-6, MIP-1, MIP-2, G-CSF and GM-CSF. Thus, they constitute an inflammatory milieu that supports

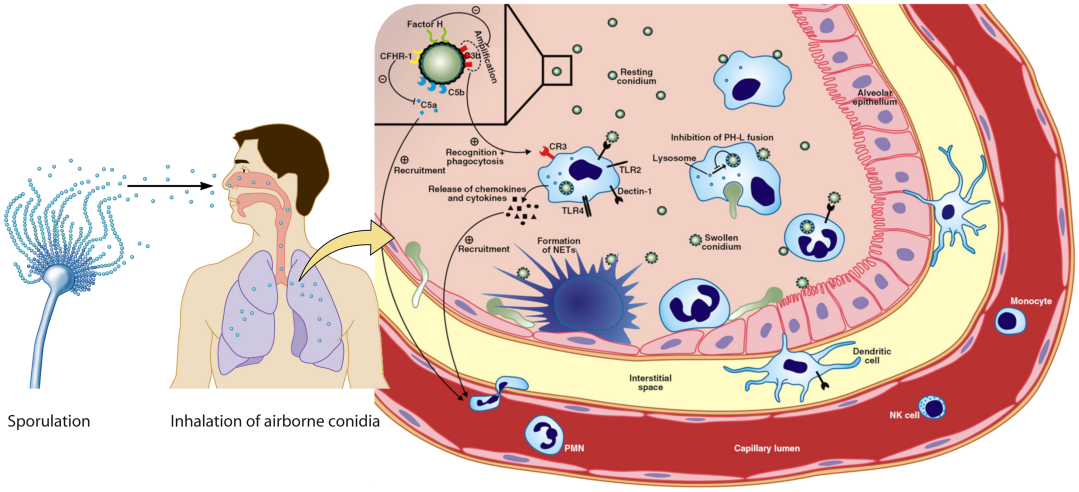

Figure 4.: Route of infection and early immune response against *A. fumigatus* in the human lung. *A. fumigatus* is an airborne fungus and human individuals inhale several thousand of its conidia every day. Due to their small size they can enter the lung alveoli, where they are immediately faced with immune responses of the complement system and the resident phagocytes, which are *alveolar macrophages* (AM). Complement and AM constitute an inflammatory milieu leading to recruitment of neutrophils. The figure is based on figures by Dagenais and Keller (2009) and Brakhage *et al.* (2010).

recruitment of neutrophils from the blood stream [84, 85]. However, in resting conidia these PAMPs are covered by a rodlet layer, that makes resting conidia immunologically inert. Swelling and growth of the conidia leads to breakage of the surface layer and uncovers the underlying carbohydrates [85]. NK cells are recruited early during the immune response and contribute mainly to the immune response by secretion of the pro-inflammatory cytokine IFNγ, which increases the fungicidal activity of phagocytes. The inflammatory milieu, established by the complement as well as AM and NK cells, leads to recruitment of neutrophils from the bloodstream. Particularly, the susceptibility of neutropenic patients to severe aspergillosis highlights their function during the immune response [85]. The recognition of *A. fumigatus* in neutrophils is also mediated through the aforementioned receptors. Upon recognition neutrophils are able to phagocytose conidia and germ tubes of a certain size. The secretion of anti-microbial peptides allows the attack of large hyphae. Furthermore, the formation of NETs enables trapping hyphae and preventing further hyphal growth [85].

However, *A. fumigatus* also developed mechanism to evade this immune responses. First, the rodlet layer of conidia, enables evasion of recognition by immune cells. Secondly, *A. fumigatus* produces melanin, a conidial pigment that prevents phagolysosome acidification and ROS production [43, 81]. Furthermore, hyphae secrete proteases that degrade the complement molecules C3, C4b and C5 and thereby inhibit complement activation. *A. fumigatus* can also form biofilms, which increase resistance of fungal cells against phagocytes, anti-microbial peptides and ROS [43, 81].

3. Virtual infection modelling

– complementing experimental studies –

The vast knowledge increase over the past decades in biology was mainly driven by new techniques in molecular biology and biochemistry that allowed for investigation of DNA, *ribonucleic acid* (RNA), proteins and other molecules as well as signalling pathways [86–88]. These technologies constitute still valuable tools in biological research. However, often considering only single aspects of a biological system is not enough but that "*the whole is more than the sum of its parts*".

Thus, *systems biology* has emerged as a concept that considers a more holistic view on biology [86, 88]. It developed from two different roots that are on the one hand biochemistry and molecular biology and on the other hand physics and mathematical biology [88]. Therefore, systems biology aims to investigate complex biological phenomena by the complementary work of wet-lab experiments and dry-lab studies (see Figure 5) [89–91]. The development of systems biology is driven by (i) new molecular and imaging technologies and (ii) by modern mathematical, physical and engineering concepts as well as novel modelling strategies [87]. A *system* is a collection of entities within an enclosed

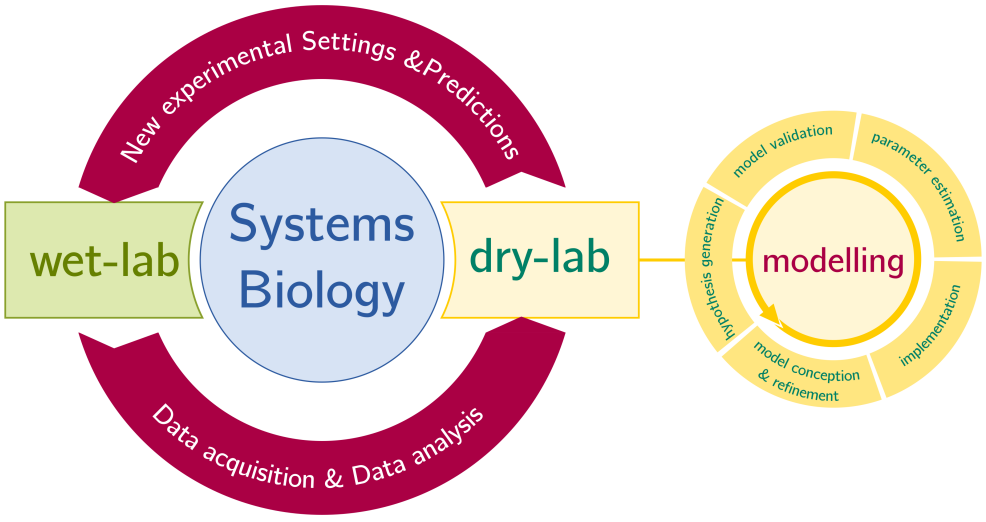

Figure 5.: Cycle of systems biology. Complex biological phenomena can be investigated using complementary techniques of wet- and dry-lab. Experiments performed in wet-lab can be analysed by automated data analysis and may serve as a data basis for modelling of the biological system. Modelling itself constitutes a cycle within the cycle of systems biology. After model conception and implementation parameters need to be determined by calibration of the model to the experimental data basis. Model validation and refinement can improve the model. From the generated model and the estimated parameters new hypotheses and predictions can be generated, which can be tested in experiment, starting the cycle of systems biology anew.

domain that are interconnected or interacting. Biological systems can be considered as complex systems that feature various characteristics, such as non-lineartity, nested complexity and modularity, many interacting constituents, redundancy and robustness as well as emergent behaviour [90, 92].

The cycle of systems biology constitutes a powerful tool to investigate complex biological systems by combining wet-lab and dry-lab investigations that mutually support and complement each other (see Figure 5) [89–91]. The theoretical side of this cycle comprises experimental data analyses as well as modelling of the biological system under consideration. The data analysis involves all kind of data that is produced in experiments. Especially, when large amounts of data are generated automated data analysis becomes essential. For example, recent advances in microscopy technologies lead to increasing amounts of microscopy data that can not be analysed by hand. Often, the results from such data analyses form the basis for modelling and simulation of the biological system.

Systems biology has been successfully applied in a broad range of scientific fields, such as systems based medicine, biotechnology and drug discovery [88]. For example, in the field of immunology and infection research systems biology has been used to investigate viral [93], bacterial and fungal infections [94]. Furthermore, it considers knowledge transfer from bench to bed and *vice versa* as well as the interaction along various organisational scales, such as genes, proteins and enzymes, cells, tissues, organs and whole organisms [95, 96]. Furthermore, the research of unknown physiological processes in health and disease, such as interspecies interactions in the human microbiome is driven by the systems biology approach.

In this thesis, systems biology has been applied in order to investigate host-pathogen interactions *in silico*. Systems biology of infection often faces several problems: (i) biological processes may not be directly accessible in experiments, (ii) *in vivo* studies often rely on animal models, but the transferability and comparability of results from these experiments to the human system is unclear and (iii) even in animal experiments infection dynamics cannot be captured in all sites of infection, such as the lung.

Virtual infection modelling provides the possibility to overcome the aforementioned limitations by integration of all available experimental data and thereby drives the research in systems biology of infection.

The Cycle of Modelling

A MODEL is a simplified mathematical description of a system and allows simulation of temporal and/ or spatial dynamics. Models consists of entities that act or interact and thus change over time. Modelling should follow the idea of "*as much as necessary, as little as possible*", *i.e.* the model should on the one hand map all necessary components and processes in order to resemble certain biological phenomena and on the other hand reduce complexity and enhance understandability. The process of modelling comprises some essential steps that build up another cycle within the cycle of systems biology (see Figure 5).

CONCEPTION First, the model needs to be designed. This process involves several steps: (i) the problem description, (ii) the systems analysis and (iii) the set-up of a conceptual model [92]. During this process the close work of experimentalists and theoreticians is essential in order to create a meaningful model that maps the biological processes in an appropriate manner. In addition, careful literature research needs to be done in order

to determine the most important entities of the system as well as their behaviour and relationships. Using this prior knowledge a mathematical description can be found that includes all entities and describes their action and interaction processes that are defined by parameters.

Implementation The model implementation is the transformation of the conceptual model into an executable model, which is used for numerical simulations [92]. Thereby, an appropriate modelling technique has to be chosen and the software package or programming language that should be used to realise the implementation. Several modelling techniques exists, such as differential equations, state-based and individual-based modelling. Some of these modelling approaches will be explained in greater detail in section *3.1*. For the implementation existing software packages or self-written frameworks can be used. Software packages and frameworks exist for several modelling techniques that allow for a fast implementation of the model but are also often restricted in their functionalities. Sometimes a more tailor-made solution is needed. In this case, programming languages, such as `Java` and `C++`, or scripting languages as `Python`, `R`, and `Mathlab` allow for more flexibility. Which programming language should be used depends on various factors, such as the complexity of the model, the expected computational costs and the time that needs to be invested into programming. While scripting languages are usually easier and faster to implement they often require higher simulation run times compared to programming languages that are based on program compilation.

Parameter estimation All action and interaction processes of model entities are defined by parameters that influence the simulation outcome. These parameters need to be defined in order to perform simulations. Appropriate parameter values can either be determined by literature research or have to be identified by a calibration of the model to experimental data. During the calibration process parameters are estimated such that the simulation result can reproduce experimental results as good as possible. Hence, the process of parameter estimation is an optimization process, where a functional, such as the *residual sum of squares* (RSS) that measures the differences of experimental and *in silico* data, should be minimized. Different techniques for parameter estimation are described in more detail in section *3.3 Model parameter estimation*.

Model validation In order to validate the model and its parameters, uncertainty and sensitivity analyses as well as parameter identifiability can be of help. Thereby, the impact of uncertainty of experimental data and of the model on the simulation outcome is evaluated. Parameter identifiability describes whether model parameters are identifiable given the experimental data. Furthermore, sensitivity analysis investigates robustness and importance of model parameters. In order to determine parameter robustness, local sensitivity analysis can be performed. Thereby, parameters are changed in a certain range and if the model outcome is not significantly affected the parameter is considered to be robust [97, 98]. Furthermore, global sensitivity analysis allows to determine the parameters that mainly influence the model and parameters that have no or low impact on the model. Therefore, parameter identifiability and sensitivity analysis allow for model simplification [97, 98].

HYPOTHESIS GENERATION If a model is designed, implemented and validated properly it can be used in various ways that pose a unique feature of modelling: (i) the system behaviour can be predicted under any perturbation and (ii) redesign or perturbation of the model can result in completely new emergent systems properties [90]. Thus, modelling allows to generate relevant predictions and new hypotheses that can be tested in wet-lab experiments starting the cycle of systems biology anew. These experiments might lead to new findings that can result in new models or adjustment of existing models.

MODEL REFINEMENT Model validation or new experimental insights might reveal the need for model adjustment. New findings have to be included in the model implementation and the calibration has to be repeated, starting the cycle of modelling anew.

3.1. MECHANISTIC MODELLING OF SYSTEM DYNAMICS

Virtual infection modelling can be applied to a broad spectrum of scientific questions in immunology and infection biology, considering various pathogens, immunological aspects and scales. These scales range from molecules like DNA, RNA and proteins up to cells, tissues, whole organs or even organisms. According to the properties of the biological system as well as the hypotheses and the available resources appropriate modelling approaches have to be chosen. There exist several modelling approaches that can be classified in many different ways. In the following a brief overview about the most common modelling techniques used in infection modelling will be given.

First, modelling techniques can be classified into population-based and individual-based approaches. Population-based approaches comprise for example *ordinary differential equation*s (ODEs), *partial differential equation*s (PDEs), *stochastic differential equation*s (SDEs), Markov Models, the Master Equation and SBMs. Here, cells, molecules or other types of individuals are viewed as average concentrations that can be simulated in time (and space). Therefore, these approaches assume high concentrations of the modelled entities. While ODEs assume well-mixed systems, spatial inhomogeneities can be modelled using PDEs. On the contrary, individual-based approaches resolve entities as discrete objects and do not assume high concentrations of them. These approaches involve various techniques, such as *cellular automata* (CA), *cellular Potts model*s (CPMs) and ABMs.

Furthermore, modelling techniques can be distinguished whether they are deterministic or stochastic. Deterministic modelling approaches neglect random processes and assume that a certain process arises due to a defined cause. However, random processes are an essential part of nature. Nevertheless, if entities occur in high concentrations the system can be considered to be deterministic as random processes average each other out. If this assumption can not be met stochastic modelling approaches, which include random processes, should be chosen. Modelling of stochastic processes requires the generation of random numbers during the simulation process as well as repeated simulations for the same parameter set in order to yield statistically robust results. Thus, in comparison to their deterministic relatives stochastic approaches in general require higher computational costs. Deterministic models are for example ODEs and PDEs, while SDEs, SBMs and *individual-based model*s (IBMs) are stochastic modelling approaches.

In general, the choice for a certain modelling approach is often driven by the trade-off between computational costs and the realism of the model. A higher degree of detail in

terms of the resolution of space, entities and internal degrees of freedom increase realism at the prize of higher computational costs. Since in this thesis the mechanistic modelling techniques state-based and agent-based modelling have been primarily used, they will be described in greater detail in the following.

3.1.1. State-based modelling

State-based modelling is a stochastic population-based modelling approach where the dynamic behaviour of discrete entities is simulated in discrete time steps and space is neglected. Typically, they are applied for biological systems where discrete events take place with low frequency and space is not important or no information on spatial properties is available. In order to simulate discrete events in biological systems with SBMs, populations of entities are modelled as states and processes in the system are modelled by transitions between states. All entities occupy a certain state and actions and interactions of these entities are simulated by state transitions, which occur with certain rates that denote the frequency of an event per time step. Thus, similar event-based modelling techniques are Markov models [99], interacting-state machines [100] and probabilistic finite state machines based on Turing machines [101]. By fitting SBM simulations to experimental data, transition rate values can be determined, which allows for quantification of immune and infection processes in virtual infection modelling.

3.1.2. Agent-based modelling

Contrary to SBMs, ABMs resolve model entities as single autonomous decision-making individuals, also termed *agents* [102]. In virtual infection modelling agents can represent for example cells or molecules. These discrete agents migrate, act and interact within a two- or three-dimensional discrete or continuous environment, where the latter one requires sophisticated collision handling of agents in order to keep run time within limits, since pairwise collision checks would lead to quadratic runtime. An approach for agent monitoring and neighbourhood handling in continuous space is the subdivision of the environment, where a lattice is placed within the continuous environment and each agent is associated to its nearest grid point [103]. Using this lattice-based agent monitoring approach close to linear runtime can be reached, if the grid constant corresponds to the diameter of the largest agent within the model [103]. Hence, the number of collision checks is minimized and it is sufficient to examine all agents located in the agent's Moore neighbourhood.

Furthermore, boundary handling needs to be implemented that manages agent handling across the boundaries of the environment. Such boundary conditions can be for example *fixed*, where agents are not allowed to move across the boundaries, *periodic*, where agents leave the system and enter the system at the opposite site or *random periodic*, where agents leave the system and enter the system at a randomly chosen point.

Individuals in biology often feature versatile morphologies, that can be implemented in the ABM, increasing the degree of detail of the model. Furthermore, agents consist of a set of behavioural rules that determine their migration, action and interaction. These rules are characterized by rates and can be influenced by environmental factors. Examples for such rules in virtual infection modelling are phagocytosis, cell death, cell division and the secretion and/or sensing of anti-microbial peptides, cytokines and chemokines. Due to the consideration of space in ABM direct interaction processes, such as phagocytosis

events, depend on the physical contact of cells. In general, it can be stated, that a greater detail in terms of environmental structures, agent morphologies and behavioural rules enhance model realism, but also increase computational costs and increase the number of parameters that need be determined.

Several ABM frameworks have been developed in the area of immunology and disease modelling [104]. These frameworks involve the true immune simulators IMMSIM [105, 106], SIMMUNE [107, 108], SIS [109] and ENISI [110] as well as several general disease simulators, such as CyCell [111, 112] and PathSim [113, 114]. Furthermore, general agent-based frameworks such as NetLogo [115] have been widely applied to immune and infection modelling[116, 117] and several frameworks that concentrate on specific immune processes or diseases have been developed [104].

3.2. Decision optimization to model system dynamics

In virtual infection modelling the aforementioned mechanistic modelling approaches are commonly used. However, these approaches often require lot of *a priori* knowledge on underlying processes and rely on many parameters. If the majority of these parameters cannot be fixed with values from literature dimensions of the parameter space rapidly increase rendering parameter estimation infeasible.

Game theory (GT) is a mathematical concept that provides a set of analytical tools and solution concepts in order to recast and analyse (social) dilemmas. In particular, it allows to elegantly condense different effector mechanisms and therefore reduces the dimensions of the parameter space by still allowing for identification of key parameters of the biological system. Neumann and Morgenstern [118] developed in 1944 the concept of GT to resolve strategies in economy. Since then, GT has spread to various fields, such as psychology, sociology, ethics, political science and military strategy, computer science and biology [119] and allows also modelling of host-pathogen interactions during infection and inflammation. Despite, the severity of the context the term *game* refers to the complex situation, where conflicting entities, such as the host immune system and invading pathogens, interact with each other. GT models comprise three major components, which are:

Players: Individual agents with their own aims, goals, preferences and possibly conflicting interests try to maximize their utility in an interactive decision situation [119].

Strategies: Each player consists of a set of possible strategies that can be applied in the context of the decision situation [119].

Payoffs: The strategy combination of the player and its opponent is associated with a payoff that denotes the utility (satisfaction) of the player in the game and is usually defined in the payoff matrix [119].

Nash developed in (1950) a concept to resolve such interactive decision situations [120]. This concept describes the static equilibrium in non-cooperative games, *i.e.* the strategy profile of all players, where no player has the incentive to deviate from its strategy [119].

The original concept of GT is also termed *classical game theory* (CGT) or *rational game theory*, since all players are considered to be perfectly rational, *i.e.* they have

complete knowledge about possible strategies of themselves and their opponents and are able to deduce the best strategy [119]. This concept is highly debated in the field of GT and attempts have been made to soften this strong assumption. Particularly, in the field of biology perfect rationality often cannot be justified, since living entities like cells or organisms do not consciously optimize over strategic alternatives, but rather inherit a fixed phenotype and replication depends on the fitness (payoff) of the individual [121]. Thus, the concept of *bounded rationality* has been inferred in the framework of *evolutionary game theory* (EGT) [119].

EGT aims to remedy the main weaknesses of CGT, which are (i) perfect rationality, (ii) the lack of dynamics and (iii) the equilibrium selection in case of multiple Nash equilibria. Thus, EGT is the theory of dynamic adaptation in repeated games played by bounded rational agents [119]. Originally, EGT developed as a population-based method at macroscopic level that can be applied to large populations. For biological systems, where lower numbers of individuals are involved an individual-based approach is more appropriate [119]. The behaviour of each individual is implemented by microscopic strategy update rules, that depend for example on the local environment, the aims and history of an individual and can be for example genetically coded Darwinian selection. These microscopic update rules can be very diverse and depends on the modelled system. They can be deterministic or stochastic representing random mutations. The strategy update of all individuals in the model can be synchronized or performed in a randomly sequential fashion.

Spatial inhomogeneities of a biological system can be represented by graphs, where nodes refer to single individuals and edges between them pairwise interactions of individuals that are for example in close proximity or genetically related [122, 123]. Microscopic strategy update rules in individual EGT on graphs might lead to changes of the interaction graph during evolution of the system [119].

Evolution in EGT refers to the evolution of strategy patterns of the simulated entities and therefore does to resmeble temporal dynamics. However, as realized by Pollmächer *et al.* [124] pseudo-temporal resolution of a EGT model can be achieved by coupling several games to each other, such that games located later in the time line depend on outcomes of prior games.

3.3. Model parameter estimation

After appropriate model design and implementation the model needs to be calibrated to the experimental data basis in order to (i) quantify model parameters and/or (ii) use the calibrated model for simulation of perturbations of the biological system. During calibration rates that describe processes in the model are estimated such that the *in silico* results match the experimental data as good as possible. In order to quantify the agreement between experimental and *in silico* data a functional, such as the *least squares error* (LSE), also termed RSS, is minimized for experimental data μ^{exp} and simulated data μ^{sim} over all data points $i = 1, \ldots, n$ by

$$LSE = \sum_{i=0}^{n} (\mu_i^{\text{exp}} - \mu_i^{\text{sim}})^2. \tag{3.1}$$

Thus, the process of parameter estimation resembles an optimization problem. This basic LSE is often used in an extended way, where data subsets are weighted in a certain

manner or the standard deviation is considered [99].

Various techniques exist that can be used for the parameter estimation task, where the model parameter space is searched in a certain way in order to find a set of parameters that minimizes the aforementioned functional. Generally, these techniques can be classified according to their search strategy and the solution property, which can be both global or local [125]. In case of a global search strategy the whole search space is taken into consideration. This also allows to find the global optimum, while local search strategies typically search for optimal parameter values within a local area of the search space and therefore only allow detection of local optima [125].

LOCAL SEARCH STRATEGIES involve *direct methods* as well as *gradient-based methods*. *Gradient-based methods* are based on the calculation of derivatives and, thus, the gradient of model solutions. Based on the calculated gradients the search strategy converges to a local optimum. Examples are Newton's method, the steepest descent algorithm, the Gauss-Newton algorithm and the Levenberg-Marquardt algorithm [99, 126]. These methods are well suitable for equation-based modelling techniques, such as ODE or PDE, where derivatives can be calculated relatively easy. In case of rule-based models, such as ABM these derivatives can not be analytically derived, but can only be approximated by performing simulations within a certain step size. However, this proceeding would require large amounts of simulations, which, especially in case of ABM, would render the computational load infeasible.

For non-equation-based models direct search strategies that do not rely on derivatives are more appropriate. A simple approach is the *discrete grid approach*, where a local region within the search space is scanned along a regular grid [127]. This method can be extended by multiple iterations, where regions with low LSEs are scanned in a more fine-grained manner in a subsequent step. Other direct methods are for example the Hooke-Jeeves method [128] and the Nelder-Mead simplex algorithm [129].

GLOBAL SEARCH STRATEGIES consider the whole search space and therefore allow to find the global optimum. These global methods involve heuristic strategies, such as *simulated annealing* and *evolutionary algorithms*, and *model-based approaches* [125].

Simulated annealing is a stochastic global heuristic search strategy [130]. This approach resembles the physical process of slowly cooling down melted material, where molecules arrange in a crystalline structure with minimum energy that corresponds in the parameter estimation process to minimizing a functional, such as the LSE [126]. The current temperature determines the probability at which solutions with a worse LSE are accepted. The further progressed the cooling process is, the lower the probability to accept worse solutions. This method allows to leave local optima at the beginning of the optimization, but prevents leaving the global optimum towards the end of the optimization. Thereby the rate that determines the cooling process is of particular importance, since it determines, if the algorithm gets stuck in a local minimum. In order to find the global minimum, the algorithm is repeatedly executed.

Evolutionary algorithms, such as *Differential Evolution* [131] are population-based, *i.e.* they simulate a population of points in the parameter space, which corresponds to a certain parameter vector [126]. Concepts from evolutionary biology, such as fitness, mutation, selection and crossover are applied to the population to vary the current points and to generate a next generation. The fitness of each individual (parameter

configuration) corresponds to its LSE.

Furthermore, there exist *model-based approaches* featuring a global search strategy, which can be applied if little is known about the search space. Examples for model-based optimisation strategies are *nested partitioning* and *swarm intelligence*. In *nested partitioning* a model of the search space is build that subdivides the search space in an inner interval, where the optimum is suspected and the search is performed in a fine-grained manner, and an outer interval, in order to consider the whole search space [132]. *Swarm intelligence* tries to find the global optimum by resembling biological swarms, where lot of entities are simulated, that can communicate in a certain way. Each individual of the swarm performs a local optimisation, while considering the quality of neighbouring solutions and thus changing its position within the search space [133].

The choice for a certain parameter estimation approach depends on various factors, such as the computational costs of the underlying model, the required number of simulations of a certain search strategy and the *a priori* knowledge about the search space. Often it is advantageous to use *hybrid methods*, that combine global and local search strategies, where the global one is applied to find the region where the global optimum is located and, subsequently, the local strategy for a targeted search [99, 134].

In virtual infection modelling parameter values can often be restricted due to biologically relevant ranges. Furthermore, the choice of the search strategy depends also on the type of model. For example, ABMs are very demanding in terms of computational costs, therefore, a search strategy that requires only low number of simulations should be chosen.

Part II.

Objectives of this Thesis

The research on host-pathogen interactions is essential for the development of new diagnostics and therapeutics. Since the incidence of fungal infections is increasing in the last years and these infections are associated with high mortality rates [7], host-pathogen interactions of the immune system and human pathogenic fungi are of major interest.

The innate immune system is the first line of defence against fungal invaders and is studied in many wet-lab experiments. However, wet-lab experiments alone can not always elucidate the complex mechanisms of such interactions. For example, while some sites of infections cannot be investigated under physiological conditions, others can not be investigated due to technical limitations.

The goal of this thesis is to implement virtual infection models that allow to overcome such limitations and are able to generate new hypotheses that can be tested in experiment and further allow for uncovering of obscure processes. The studies that are part of this thesis aim to understand host-pathogen interactions of the innate immune response during:

(i) *Candida* blood stream infections and

(ii) *A. fumigatus* lung infections.

We generated various individual-based virtual infection models that allowed to overcome experimental limitations and to investigate spatio-temporal aspects of these biological systems.

Invasive *Candida* blood stream infections are intensively investigated in wet-lab experiments, such as whole-blood infection assays. To date, microscopy of whole-blood assays to investigate spatial dynamics of the infection process with *Candida* spp. is not applicable, since the number of erythrocytes exceeds the number of immune cells by one order of magnitude [135]. Individual-based modelling allows a glimpse on spatial aspects of the host-pathogen interactions based on non-spatial data from whole-blood infection assays, which are usually conducted with blood from healthy donors.

However, especially immunocompromised individuals, such as neutropenic patients, are at high risk for invasive candidiasis [39, 78, 136, 137]. Using blood samples from neutropenic patients for whole-blood infection assays is not straightforward due to availability of these blood samples as well as ethical concerns. Thus, we applied the virtual infection model to simulate virtual neutropenic patients that were subsequently simulated an *in silico* cytokine treatment. In this topic of the thesis the following questions will be addressed:

1. What are the migration parameters of monocytes and neutrophils during whole-blood infection assays with *C. albicans* and *C. glabrata*?

2. How do possible immune-evasion mechanisms impact on the infection outcome during *C. albicans* and *C. glabrata* whole-blood infection and how can they be investigated in future experiments?

3. How does the condition of neutropenia affect the infection outcome with various *C. albicans* and *C. glabrata* in virtual patients?

4. Can the infection outcome with *Candida* spp. in neutropenic patients be recovered to that of non-neutropenic patients using a cytokine treatment?

Experimental investigation of *A. fumigatus* lung infections *in vivo* under physiological conditions is difficult, since appropriate technologies are not available to date. *In vitro* studies are also limited, since alveolar epithelial cells (AEC) of type I are difficult to isolate and experiments have only been conducted for AEC of type II. However, 95% of the alveolar surface is composed of AEC type I [138]. Nevertheless, much is known about the lung morphology as well as cell numbers and sizes. This enabled Pollmächer *et al.* to overcome the aforementioned limitations by development of an agent-based virtual infection model that simulates the early immune response of alveolar macrophages against *A. fumigatus* in a single to-scale alveolus [139, 140]. Based on these studies, we used evolutionary games on graphs to simulate the early immune response to *A. fumigatus* in a broader context, *i.e.* considering a whole alveolar sac and, besides alveolar macrophages, included the complement system and neutrophils. Furthermore, we used the previously established agent-based model for a comparative study between natural lung infections with *A. fumigatus* in humans and experimental *A. fumigatus* infections in mice. Both systems have fundamental differences in their lung morphology, the number of immune cells as well as the infection dose. Therefore, it is not trivial to conclude how knowledge can be transferred from mouse experiments to the human system. In the scope of *A. fumigatus* lung infections, we wanted to shed light on the following questions:

1. What are the key parameters of the innate immune response during *A. fumigatus* infection clearance?

2. Which morphological states of *A. fumigatus* are favoured under different infection doses and host immune states?

3. What is the role of alveolar macrophages during the innate immune response against *A. fumigatus*?

4. How do differences in the lung morphology and in the infection dose affect the infection outcome in human and mice?

Part III.

Overview of Manuscripts

REVIEW ARTICLE

Cytometry
PART A
Journal of the International Society for Advancement of Cytometry

Image-based Systems Biology of Infection

Anna Medyukhina,[1] Sandra Timme,[1,2] Zeinab Mokhtari,[1,2] Marc Thilo Figge[1,2]*

Status: Published in *Cytometry A* 87(6), 462-470

Summary: In this publication we review the current work flow and techniques applied in the field of *Image-based Systems Biology of Infection*. Approaches on image acquisition and analysis as well as the quantification of infection processes and further modelling based on these images are discussed.

Authors' contributions: AM and MTF coordinated the review. All authors wrote parts of the manuscript and revised it critically.

frontiers in Microbiology

ORIGINAL RESEARCH
published: 19 June 2015
doi: 10.3389/fmicb.2015.00608

Bottom-up modeling approach for the quantitative estimation of parameters in pathogen-host interactions

Teresa Lehnert[1,2†], *Sandra Timme*[1,2†], *Johannes Pollmächer*[1,2], *Kerstin Hünniger*[3], *Oliver Kurzai*[2,3] *and Marc Thilo Figge*[1,2*]

[1] *Applied Systems Biology, Leibniz Institute for Natural Product Research and Infection Biology - Hans-Knöll-Institute, Jena, Germany,* [2] *Faculty of Biology and Pharmacy, Friedrich Schiller University Jena, Jena, Germany,* [3] *Fungal Septomics, Septomics Research Center, Friedrich Schiller University and Leibniz Institute for Natural Product Research and Infection Biology Hans-Knöll-Institute, Jena, Germany*

Status: Published in *Frontiers in Microbiology* 6(608)

Summary: In this study a bottom-up modelling approach was developed to investigate the host-pathogen interaction of the human pathogenic fungus *Candida albicans* and human innate immune cells, such as neutrophils and macrophages in human whole blood. Based on experimental time-resolved data a previously developed state-based virtual infection model (PI-SBM) was extended in order to account for immune cell quantities. This PI-SBM was used to estimate transition rates and to quantify the main route of immune response against this fungus. Building on the PI-SBM we further developed an agent-based virtual infection model in order to account for spacial aspects, such as migration parameters of neutrophils and macrophages.

Authors' contributions: TL, ST and MTF conceived and designed the investigation and work. MTF contributed materials and computational resources. TL, ST, JP and MTF processed the data, implementation and applied the computational algorithm. TL, ST, JP, KH, OK and MTF evaluated and analysed the results, wrote the manuscript and revising it critically.

www.nature.com/scientificreports

SCIENTIFIC REPORTS

OPEN

Received: 16 March 2016
Accepted: 20 May 2016
Published: 13 June 2016

Deciphering the Counterplay of *Aspergillus fumigatus* Infection and Host Inflammation by Evolutionary Games on Graphs

Johannes Pollmächer[1,2], Sandra Timme[1,2], Stefan Schuster[3], Axel A. Brakhage[2,4], Peter F. Zipfel[2,5] & Marc Thilo Figge[1,2]

Status: Published in *Nature Scientific Reports* 6, 27807

Summary: In this study, the counterplay of pathogen-driven infection and host-driven inflammation was examined using the example of *Aspergillus fumigatus* infection in the human lung. For this purpose evolutionary game theory on graphs was applied in order to investigate general aspects and different parameter regimes of this counterplay. The graph-based approach provided spatial resolution, while temporal resolution was achieved by sequential combination of different games that resemble various aspects of the innate immune response against this fungus. We investigated the infection process under normal inhalation doses and high inhalation doses as well at weak and strong immune conditions. Thereby, we were able to reconcile the contradictory view on the role of alveolar macrophages (AM) during the early immune response against *A. fumigatus*. During daily inhalation in most cases AM were able to clear the infection, while at higher infection doses their function shifts towards chemokine secretion for neutrophil recruitment.

Authors' contributions: JP, PFZ. and MTF. conceived and designed the study. MTF. contributed materials and computational resources. JP processed the data, implemented and applied the computational algorithm. JP, ST, SS, AAB, PFZ and MTF evaluated and analysed the results. JP, ST, SS, AAB, PFZ and MTF. wrote the manuscript and revised it critically.

frontiers in Immunology

ORIGINAL RESEARCH
published: 21 March 2018
doi: 10.3389/fimmu.2018.00560

Predictive Virtual Infection Modeling of Fungal Immune Evasion in Human Whole Blood

*Maria T. E. Praße[1,2], Teresa Lehnert[1,3], Sandra Timme[1,2], Kerstin Hünniger[4,5], Ines Leonhardt[3,4], Oliver Kurzai[3,4,5] and Marc Thilo Figge[1,2,3]**

[1] Applied Systems Biology, Leibniz Institute for Natural Product Research and Infection Biology, Hans Knöll Institute (HKI), Jena, Germany, [2] Faculty of Biological Sciences, Friedrich Schiller University Jena, Jena, Germany, [3] Center for Sepsis Control and Care (CSCC), Jena University Hospital, Jena, Germany, [4] Fungal Septomics, Leibniz Institute for Natural Product Research and Infection Biology, Hans Knöll Institute (HKI), Jena, Germany, [5] Institute of Hygiene and Microbiology, University of Würzburg, Würzburg, Germany

Status: Published in *Frontiers in Immunology* 9, 560

Summary: This publication is based on the observation by Hünniger *et al.* [141]. They found that in human whole-blood infection assays with *C. albicans* a subpopulation of cells develops that is able to evade killing and phagocytosis by monocytes and neutrophils. To date, the mechanism of immune evasion could not be elucidated. In this study we used a previously established state-based virtual infection model to test several hypothesis and to generate predictions that can be tested in further experiments. Therefore, we compared a *sponatneous* and a *neutrophil-mediated* immune evasion mechanism.

Authors' contributions: Conceived and designed this study: TL and MF. Provision of computational resources: MF. Provision of materials: OK. Data processing, implementation, and application of the computational algorithm: MP, TL, and MF. Performed experiments: KH and IL. Evaluation and analysis of the results: MP, TL, ST, KH, IL, OK, and MF. Draft and revision of the manuscript: MP, TL, ST, KH, IL, OK, and MF.

frontiers in Immunology

ORIGINAL RESEARCH
published: 04 April 2018
doi: 10.3389/fimmu.2018.00667

Quantitative Simulations Predict Treatment Strategies Against Fungal Infections in Virtual Neutropenic Patients

*Sandra Timme[1,2], Teresa Lehnert[1,3], Maria T. E. Praußе[1,2], Kerstin Hünniger[4,5], Ines Leonhardt[3,4], Oliver Kurzai[3,4,5] and Marc Thilo Figge[1,2,3]**

[1]Research Group Applied Systems Biology, Leibniz Institute for Natural Product Research and Infection Biology—Hans Knöll Institute, Jena, Germany, [2]Faculty of Biological Sciences, Friedrich Schiller University Jena, Jena, Germany, [3]Center for Sepsis Control and Care (CSCC), Jena University Hospital, Jena, Germany, [4]Fungal Septomics, Septomics Research Center, Leibniz Institute for Natural Product Research and Infection Biology—Hans Knöll Institute, Friedrich Schiller University, Jena, Germany, [5]Institute for Hygiene and Microbiology, University of Würzburg, Würzburg, Germany*

Status: Published in *Frontiers in Immunology* 9, 560

Summary: In this publication we applied the bottom-up modelling approach [142] in order to investigate infection processes in human whole blood with *C. albicans* and *C. glabrata* in virtual neutropenic patients. Additionally, we performed an *in silico* cytokine treatment of these virtual patients, where we improved neutrophil activity in terms of phagocytosis and migration. We found, that this treatment of the remaining neutrophils can indeed recover the infection outcome of the neutropenic patients and that this was more efficient for *C. glabrata*.

Authors' contributions: ST and MTF conceived and designed this study. MTF and OK provided computational resources and materials, respectively. Data processing, implementation and application of the computational algorithm was done by ST, TL, MP and MTF. Experiments were performed by KH and IL. ST, TL, MP, KH, IL, OK, MTF evaluated and analyzed the results of this study. ST, TL, MP, KH, IL, OK and MTF drafted the manuscript and revised it critically for important intellectual content and final approval of the version to be published. Agreement to be accountable for all aspects of the work in ensuring that questions related to the accuracy or integrity of any part of the work are appropriately investigated and resolved: ST, TL, MP, KH, IL, OK, MTF.

frontiers in Immunology

ORIGINAL RESEARCH
published: 05 February 2019
doi: 10.3389/fimmu.2019.00142

Comparative Assessment of Aspergillosis by Virtual Infection Modeling in Murine and Human Lung

Marco Blickensdorf[1,2], *Sandra Timme*[1,2] *and Marc Thilo Figge*[1,2*]

[1] Research Group Applied Systems Biology, Leibniz Institute for Natural Product Research and Infection Biology-Hans Knöll Institute, Jena, Germany, [2] Faculty of Biological Sciences, Friedrich Schiller University of Jena, Jena, Germany

Status: Published in *Frontiers in Immunology* 10, 142

Summary: In this manuscript, we performed a comparative analysis of the immune response and infection outcome during *A. fumigatus* lung infection in human and mice. Hereby, we considered their different lung physiology as well as differences in the infection dose resulting from natural daily inhalation and experimentally administered doses that can differ by several orders of magnitude. Therefore, we adapted an existing hybrid agent-based framework and simulated the immune response by alveolar macrophages as well as chemokine secretion and diffusion, which we screened for physiological relevant parameter ranges. We found that the infection can be more efficiently cleared in mice in most cases of natural and experimental doses.

Authors' contributions: MB, ST and MTF conceived and designed this study. MTF provided computational resources. Data processing, implementation and application of the computational algorithm was done by MB, ST and MTF. MB, ST and MTF evaluated and analyzed the results of this study. MB, ST and MTF drafted the manuscript and revised it critically for important intellectual content and final approval of the version to be published. Agreement to be accountable for all aspects of the work in ensuring that questions related to the accuracy or integrity of any part of the work are appropriately investigated and resolved: MB, ST, MTF.

Paper	Status	Journal	Authors	Contribution
1	published	*Cytometry A*	Medyukhina A	45%
			Timme S	**30%**
			Mokhtari Asl Z	20%
			Figge MT	5%
2	published	*Frontiers in Microbiology*	Lehnert T	35%
			Timme S	**35%**
			Pollmächer J	15%
			Hünniger K	5%
			Kurzai O	5%
			Figge MT	5%
3	published	*Scientific Reports*	Pollmächer J	45%
			Timme S	**35%**
			Schuster S	5%
			Brakhage A	5%
			Zipfel P	5%
			Figge MT	5%
4	published	*Frontiers in Immunology*	Prauße M	55%
			Lehnert T	15%
			Timme S	**10%**
			Leonhardt I	5%
			Hünniger K	5%
			Kurzai O	5%
			Figge MT	5%
5	published	*Frontiers in Immunology*	**Timme S**	**60%**
			Lehnert T	10%
			Prauße M	10%
			Leonhardt I	5%
			Hünniger K	5%
			Kurzai O	5%
			Figge MT	5%
6	published	*Frontiers in Immunology*	Blickensdorf M	65%
			Timme S	**30%**
			Figge MT	5%

Part IV.

Manuscripts

4. Image-based systems biology of infection

REVIEW ARTICLE

Cytometry
PART A
Journal of the International Society for Advancement of Cytometry

Image-based Systems Biology of Infection

Anna Medyukhina,[1] Sandra Timme,[1,2] Zeinab Mokhtari,[1,2] Marc Thilo Figge[1,2]*

REVIEW ARTICLE

Cytometry PART A Journal of the International Society for Advancement of Cytometry

Image-based Systems Biology of Infection

Anna Medyukhina,[1] Sandra Timme,[1,2] Zeinab Mokhtari,[1,2] Marc Thilo Figge[1,2]*

[1]Applied Systems Biology, HKI-Center for Systems Biology of Infection, Leibniz-Institute for Natural Product Research and Infection Biology, Hans–Knöll–Institute (HKI), Jena, Germany

[2]Applied Systems Biology, Friedrich Schiller University, Jena, Germany

Received 17 June 2014; Revised 5 January 2015; Accepted 7 January 2015

Grant sponsor: Deutsche Forschungsgemeinschaft (DFG), Grant number: CRC124 (project B4 to MTF)

Grant sponsor: Joint Intravital Microscopy and Imaging, Grant number: Ni1167/3-1

*Correspondence to: Marc Thilo Figge, Applied Systems Biology, HKI-Center for Systems Biology of Infection, Leibniz-Institute for Natural Product Research and Infection Biology, Hans-Knöll-Institute (HKI), Jena, Germany. E-mail: thilo.figge@hki-jena.de

Published online 29 January 2015 in Wiley Online Library (wileyonlinelibrary.com)

DOI: 10.1002/cyto.a.22638

• **Abstract**

The successful treatment of infectious diseases requires interdisciplinary studies of all aspects of infection processes. The overarching combination of experimental research and theoretical analysis in a systems biology approach can unravel mechanisms of complex interactions between pathogens and the human immune system. Taking into account spatial information is especially important in the context of infection, since the migratory behavior and spatial interactions of cells are often decisive for the outcome of the immune response. Spatial information is provided by image and video data that are acquired in microscopy experiments and that are at the heart of an image-based systems biology approach. This review demonstrates how image-based systems biology improves our understanding of infection processes. We discuss the three main steps of this approach—imaging, quantitative characterization, and modeling—and consider the application of these steps in the context of studying infection processes. After summarizing the most relevant microscopy and image analysis approaches, we discuss ways to quantify infection processes, and address a number of modeling techniques that exploit image-derived data to simulate host-pathogen interactions *in silico*. © 2015 International Society for Advancement of Cytometry

• **Key terms**

systems biology; image analysis; mathematical modeling; live-cell imaging; infection; host–pathogen interactions

INFECTIOUS diseases still remain one of the main causes of death, especially in developing countries (1). To effectively treat infections, it is indispensable to understand how the pathogenic microorganisms interact with the host immune system. The mechanisms of these interactions can be extremely complex and also difficult to observe in experiment under physiological conditions. For example, if contacts between immune cells last longer than can be recorded in a typical microscopy study, this hinders a direct measurement of their duration and complicates interpretations (2). Computer simulations of immune processes can decrease the costs of systems biology studies by reducing the need for time-consuming experiments, expensive chemicals and animal testing. For instance, simulations by Beltman et al. (2,3) estimated the duration of contacts between T cells and dendritic cells, which are not accessible in laboratory experiments. Furthermore, the knowledge provided by data-derived computer models can direct further experimental studies. For example, the virtual infection model of a human whole blood assay by Hünniger et al. (4) predicted the importance of extracellular killing of the pathogenic fungus *Candida albicans* by antimicrobial factors released from neutrophils during the first hour of infection, suggesting to study this mechanism in this particular time-frame. This iterative "experiment—modeling—experiment" cycle represents the central component of systems biology and aims to reveal the mechanisms of a biological process by quantifying the experimental data, building predictive computer models based on these data, and suggesting new experimental settings (5).

Most applications of systems biology to immunology rely upon "omics" data, which profile the activity of genes, RNA or proteins in a sample and by that unravel

mechanisms of immune response regulation (6,7). However, "omics" analyses do not capture the spatial and temporal distribution of infection-related cells and molecules necessary to characterize dynamical, functional and morphological aspects of infection. The required spatial and temporal features can be accessed by combining systems biology with microscopic studies, known as image-based systems biology (IbSB) (8,9). The IbSB approach includes three essential steps (Fig. 1): (i) acquisition and analysis of image data, (ii) quantitative characterization of biological processes, and (iii) computer simulations of image-derived models. The IbSB approach has been successfully employed in a variety of biological applications (10–13). In this review, we discuss advantages of the IbSB approach in the context of infection studies, with special emphasis on the construction of predictive image-derived models.

Glossary

Image-based systems biology (IbSB)—modeling of biological systems based on the analysis of image data with the aim to optimize and direct further experimental studies
Omics data—the data obtained from, e.g., genome, transcriptome or proteome analyses
Host–pathogen interactions—interactions between host cells (e.g. immune cells) and pathogenic microorganisms.
Live-cell imaging—microscopy imaging of living cells, tissues, or organisms.
Image segmentation—separation of an image into background and regions of interest (ROI).
Region of interest (ROI)—the part of the image containing an object that needs to be analyzed (e.g., an immune cell or a pathogen).
Tracking—finding the correspondence between identical objects in different time frames.
Mathematical model—a set of mathematical expressions that describes a certain aspect of the system's behavior in a simplified manner.
Spatiotemporal model—a mathematical model that describes the dynamics of the system in space and time.
Deterministic behavior—a model behavior that obeys defined rules, excludes randomness, and always leads to the same outcome given the same starting conditions.
Stochastic/probabilistic behavior—a model behavior that includes randomness and can result in different outcomes even for the same starting conditions.
Ordinary differential equations (ODE)—equations containing functions of only one variable (usually time coordinates) and the derivatives of these functions.
Partial differential equations (PDE)—equations containing functions of multiple variables (usually time and spatial coordinates) and partial derivatives of these functions.
State-based model (SBM)—a model that represents each individual entity, its state properties, and transitions between the states according to specified rules, but assumes that the entities are homogeneously distributed in space.
Individual-based model (IBM)—an extension of SBM that includes spatial aspects such as migration and interactions of each individual entity.
Cellular automata (CA)—an IBM where each entity is represented by one lattice site (computational cell).
Cellular Potts Models (CPM)—an IBM where each entity is represented by several adjacent lattice sites.
Agent-based models (ABM)—an IBM where the shapes and positions of entities are not restricted by a lattice but can be defined flexibly with regard to the space representation and the agent properties.

Acquisition and Analysis of Image Data

Imaging is a key technique in biological research to acquire spatiotemporal information on the morphology and dynamics of infection processes; such information is also indispensable to construct spatiotemporal mathematical models (11–13). The imaging phase comprises image acquisition and automated image analysis; both steps are essential to characterize spatial and/or temporal aspects of infection in a high-throughput manner.

Available image acquisition tools range from conventional wide-field and confocal microscopy to super-resolution PALM and STED techniques (12,14). For instance, contemporary fluorescence microscopy can display the spatial distribution of almost any target protein by applying adequate labeling strategies (15–17). One of the most valuable tools in infection research is live-cell imaging (9) including, e.g., multi-photon microscopy (MPM) and fluorescence resonance energy transfer (FRET) microscopy (Fig. 2). MPM is a type of fluorescence microscopy where two or more excitation photons are simultaneously absorbed and a fluorescence photon of higher energy is subsequently emitted (18). This enables the use of near-infrared light, which penetrates deeper into tissue and causes less damage (19). FRET microscopy can detect two co-localized fluorescent proteins (20) where energy is transferred from a donor protein to an acceptor protein, producing the FRET signal, which has a spectrum different from the spectra of the donor and the acceptor proteins. Because this does only occur if any two proteins are closer than about 10 nm, this technique allows detecting real interactions at the molecular level—in contrast to the plain overlay of images for two fluorescent proteins. Further advantages of live-cell microscopy and its applications in infection research are discussed in the comprehensive reviews by Coombes and Robey (21) and Konjufka and Miller (22).

To quantify an infection process in an objective and high-throughput manner, automated analysis of the images is essential, comprising the steps of preprocessing, segmentation, classification, and tracking in the case of time-lapse data. The preprocessing step enhances the overall quality of an image by, e.g., correcting the background illumination and reducing noise and/or artifacts in the images. Segmentation—generally the most challenging step—aims to separate the regions of interest (ROI) from the background based on their intensity, texture and other features. Extracted ROI are then classified as different immune cells, pathogen cells and/or virus particles based on the object's size, shape, dye color and other properties. If time-lapse data are available, object tracking can be performed, which refers to finding the correspondence between objects in different time frames.

A large variation of image analysis techniques and specialized software tools exist for different types of microscopy

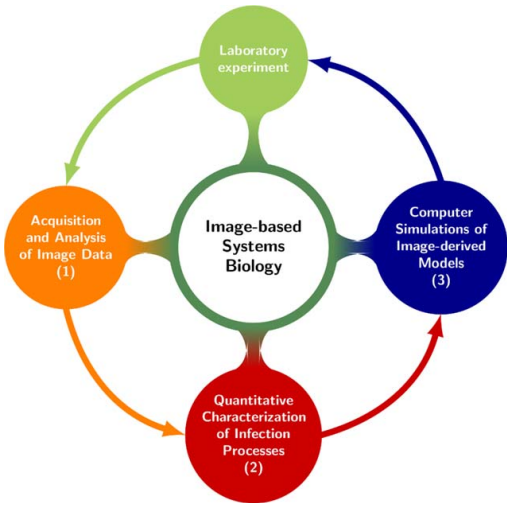

Figure 1. Diagram of the image-based systems biology (IbSB) approach.

data (23–25). The choice of the most appropriate image analysis workflow is not the subject of this review; a summary of available techniques can be found elsewhere both for static image analysis and for object tracking in time-lapse data (24–27). Furthermore, an objective comparison of methods for tracking virus-like particles and cells was presented by Chenouard et al. (28) and Maška et al. (29), respectively.

Here, we briefly refer to an example of image analysis carried out in the context of the IbSB approach (30). In this study, the invasion dynamics of *Candida albicans* into epithelial cells is quantitatively analyzed. *Candida albicans* is an opportunistic fungal pathogen that can cause severe sepsis in immunocompromised patients by switching from the commensal yeast form into the pathogenic filamentous form. Figure 3A illustrates the automated image analysis workflow implemented in the Definiens Developer XD software. The procedure detects *C. albicans* cells and individual filaments (hyphae), and classifies the hyphae as having invaded epithelial cells or as being non-invasive, which yields such quantities as the number of hyphae, the number of invasions per *C. albicans* cell, the total length of hyphae, and the relative lengths of noninvasive and invasive fragments. These quantities serve as the basis for constructing a mathematical model of the invasion kinetics (Figs. 3B and 3C).

Quantitative Characterization of Infection Processes

Automated image analysis is closely connected with the quantitative characterization of the biological process under consideration. The set of quantitative measures that can be extracted for each object during image analysis (e.g., size or speed of an individual cell) is statistically evaluated to serve either as the final readout of the image analysis or as input parameters of virtual infection models that can be simulated on the computer. A quantitative description of the infection process allows for a comprehensive and detailed understanding of pathogenicity mechanisms. For example, computing the phagocytosis ratio from image data reveals, which pathogen strains are phagocytized more effectively (31,32) and which drugs inhibit this process (33). Furthermore, image-derived quantities can aid in disease diagnostics, for instance with regard to detecting malaria parasites in blood smears (34–36).

However, the quantitative characterization alone may fail to reveal the complex infection mechanisms on the desired level of detail, because not all quantities are accessible from image data. From the viewpoint of a systems biology approach, extracted quantitative parameters are intermediate results serving as a basis for mathematical models. Thus,

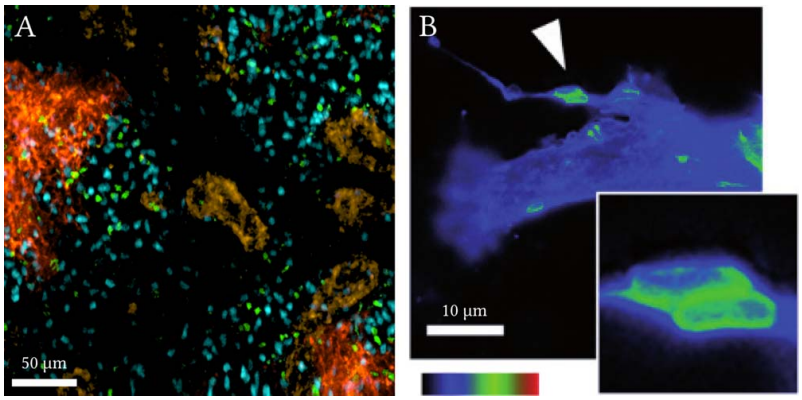

Figure 2. Live-cell imaging. (**A**) A peripheral lymph node visualized with two-photon microscopy to investigate the motility of B cells during infection with lymphocytic choriomeningitis virus (LCMV) (74). Red: CD35; brown: high endothelial venules (HEV); blue: B cells transferred 24 h before imaging; green: B cells transferred 2.5 h before imaging. Reproduced from Coelho et al. (74). (**B**) FRET microscopy image of *Yersinia pseudotuberculosis* binding to a non-phagocytic host cell. Color coding represents the level of GTPase Rac1 promoting the phagocytosis event. Reproduced from Hayward et al. (75) © 2010 BioMed Central.

computational models are used to interpret the experimental outcome, to analyze different scenarios in a comparative fashion, and to make quantitative predictions for parameters that are unavailable in experiment. For example, the probability of virus binding to a cell cannot be directly measured, but can be estimated from a computer model that relies on the observable virus concentration and distribution of cells in the culture (37). Similarly, the migration and activation of alveolar macrophages in response to infection with the human-pathogenic fungus *Aspergillus fumigatus* cannot be directly observed under physiological conditions in the human lung, but it can be predicted from a virtual infection model that is based on the information derived from images of histological sections (38).

Although many parameters can be estimated during model simulation and optimization, this process is computationally extremely intensive. Therefore, the more parameters can be extracted from experimental data the more computational resources and computing times can be saved. For example, quantifying the migration of cells or viruses is especially relevant for spatiotemporal modeling: it can yield speed values, turning angles and motility coefficients of cells (39), or more complex staggered track measures (40) that can be essential for modeling the migratory behavior of cells. Thus—in the context of the IbSB approach—experiment, parameter quantification and modeling are tightly interconnected: quantification provides essential parameters for theoretical modeling, while the predictive power of model simulations can narrow down the space of relevant parameters and point to new conclusive experiments.

Computer Simulations of Image-derived Models

Mathematical modeling is a common approach in various fields of science describing real processes through mathematical expressions. It simplifies complex processes and focuses on their most important aspects in order to make relevant predictions and initiate new experiments. A typical modeling procedure consists of several stages: selection of a modeling approach and its particular mathematical representation, optimization of model parameters, and computer simulation of the model.

A number of techniques exist that enable spatiotemporal modeling. The choice of the approach depends on the level of complexity of the biological process, as well as on the type and amount of available image data (10). We categorize existing modeling techniques based on two criteria—space resolution and resolution of individual objects—and use additional criteria to discriminate between model sub-types (see Table 1). In the following, we discuss three common types of modeling approaches and their applications to infection study: differential equations, state-based models, and individual-based models.

Differential Equation Models

The simplest way to describe the dynamics of a biological system is offered by differential equations that can be either of ordinary or partial type. Differential equations describe the change of so-called state variables, e.g., molecular concentration, motion speed, chemical gradients, etc.

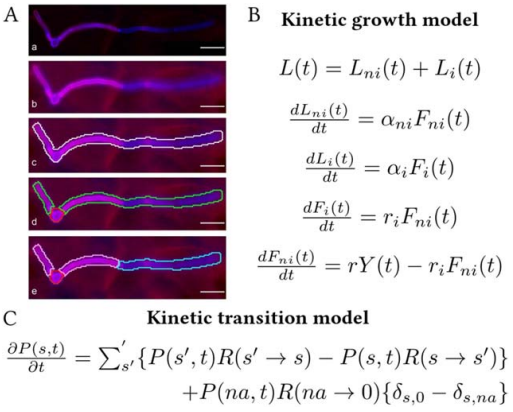

Figure 3. Image-based systems biology approach applied to study the epithelial invasion of C*andida albicans* (30). (**A**) Automated analysis of *C. albicans* invasion of epithelial cells in fluorescence microscopy images: (a) Original image (z-slice). (b) Maximum intensity transformation of the original z-stack. (c) *C. albicans* cell separated from the background. (d) *C. albicans* cell separated into its yeast region (red outline) and its two hyphae (green outlines). (e) Hyphae separated into invaded (blue) and non-invaded (pink) segments. Scale bar 10 μm. Reproduced, with permission, from (30) © 2013 International Society for Advancement of Cytometry. (**B**) Kinetic growth model based on ordinary differential equations (ODE) describing the growth of fungal hyphae. $L(t)$, $L_i(t)$, and $L_{ni}(t)$ refer to the total hyphal length, the length of invasive and of non-invasive hyphae as a function of time t, respectively; $F_i(t)$ and $F_{ni}(t)$ refer to the number of invasive and non-invasive filamentous cells, respectively; α_i and α_{ni} denote the growth rate constants in units of length over time for invasive and non-invasive filamentous cells, respectively; r_i denotes the rate constant in units of inverse time for the transition from non-invasive to invasive growth; r denotes the rate constant in units of inverse time for the transition from yeast cell to non-invasive filamentous cell; $Y(t)$ denotes the number of yeast cells. (**C**) Kinetic transition model based on the master equation (76) describing the transitions between states with different number of invasive or non-invasive hyphae. $P(s,t)$ denotes the probability to find a *C. albicans* cell in the state s at time t; $R(s' \to s)$ is the rate of transition from state $s' \neq s$ into state s; $\delta_{i,j}$ is the Kronecker delta (returning 1 if $i = j$ and 0 otherwise); s = na and $s = 0$ correspond to non-adapted and adapted cells, respectively, taking into account the usual adaptation phase of yeast cells in the medium. A *C. albicans* cell in state $s > 0$ ($s < 0$) is non-invasive (invasive) with a total number of $|s|$ hyphae.

Ordinary differential equations (ODE) describe the temporal evolution of state variables completely neglecting their variation in space by assuming that the model entities—e.g., cells or molecules—are homogeneously distributed in space. For instance, ODE served as a basis for the kinetic growth and kinetic transition models for invasion of *Candida albicans* into epithelial cells, which were constructed with the help of image-derived quantities (30). The kinetic growth model (see Fig. 3B for detail) quantified the change of total length of invasive and non-invasive hyphae and predicted the proportion of invasive and non-invasive hyphal lengths in the

Table 1. Comparison of modeling approaches

MODELING APPROACH		SPACE RESOLUTION	RESOLUTION OF INDIVIDUAL OBJECTS	CONTINUOUS OR DISCRETE SPACE	CHARACTERIZATION OF OBJECT SHAPE
Ordinary differential equations (ODE)		No	No	–	No
Partial differential equations (PDE)		Yes	No	Continuous	No
State-based models (SBM)		No	Yes	–	No
Individual-based models (IBM)	Cellular automata (CA)	Yes	Yes	Discrete	No
	Cellular Potts models (CPM)			Discrete	Yes
	Agent-based models (ABM)			Discrete or continuous	Yes

subsequent invasion process. The kinetic transition model (see Fig. 3C for detail) quantified transitions from yeast to filamentous cells, from non-invasive to invasive growth, and between the states with different number of hyphae. The combination of these models revealed that the switch from the commensal to the pathogenic form of *C. albicans* is associated with immediate invasion after formation of the first hypha, rather than forming further hyphae before invasion. This result emphasizes the importance of suppressing the yeast-to-hypha transition in order to prevent epithelial invasion and illustrates the benefits of ODE models to study the time-evolution of infection.

Not only temporal but also spatial changes of variables (e.g., molecular gradients) play an important role in infection processes. It can be characterized either by arranging an ODE model as a so-called compartment model, or by the use of partial differential equations (PDE). In a compartmentalized ODE model, each compartment refers to a delimited area with its own set of ODE that are coupled across the compartments to effectively model the spatial change of state-variables. For example, a two-compartment ODE model characterized the immune response to *Mycobacterium tuberculosis* based on bright-field microscopy and flow cytometry data (41). The two compartments represented the lung and the draining lymph nodes, and the ODE described the time evolution of the concentrations of different immune cells, bacteria and cytokines. The model revealed that dendritic cells are crucial to establish immunity in tuberculosis infection, which suggested a possible way of treatment by activation of these immune cells.

A different way to introduce spatial gradients into a model is to use partial differential equations (PDE), which describe the change of variables depending on both time and spatial coordinates. PDE are often used to characterize chemokine gradients, which are crucial in the process of guiding immune cells to the site of infection (42). For instance, different variations of the diffusion equation can describe the production of chemokines by immune cells and the complex landscape due to their spreading in the tissue (Fig. 4A). PDE can also characterize various growth processes. For instance, a PDE model based on electron microscopy images described the growth of fungal hyphae: it predicted the existence of a vesicle supply center, which was not known before, but could be experimentally validated afterwards (43–45). Another PDE model based on confocal fluorescence microscopy data characterized the mechanism of phagocytosis by describing the growth of a so-called phagocytic cup around IgG-coated particles (46). This model revealed the existence of a mechanical bottleneck—the cup stops to grow if it does not deform sufficiently strong—explaining the high variability in the size of phagocytic cups observed in microscopy experiments.

Though differential equations are easy to implement, they inherently assume that the nature of the modeled process is continuous in the variables. This approach works well in cases where similar objects occur in large amounts (e.g., chemokine molecules). However, biological entities like cells are discrete, often occur in small amounts, and, hence, cannot be represented by continuous variables such as concentrations. Moreover, these discrete entities interact on an individual basis, which again cannot be adequately modeled by differential equations. Such cases require modeling on a more advanced level. Depending on whether the spatial aspects are relevant, either state-based models or individual-based models can be applied (Table 1). In both cases single entities are treated as individuals by introducing rules that mimic their interaction behavior.

State-based Models

In contrast to differential equations, state-based models (SBM) characterize the state of each biological object individually. The states of objects evolve according to defined rules: either deterministic or stochastic. For example, Hünniger et al. (4) introduced a SBM for human whole blood infection by *Candida albicans*, which simulated the states of *C. albicans* (e.g., alive or killed) and different immune cells (e.g., phagocytizing monocytes and neutrophils) and quantified the transition rates between these states. The distribution of *C. albicans* among immune cells, predicted by the model, agreed with the microscopic study of Giemsa-stained blood smears. The model predicted that neutrophils play the crucial role in eliminating *C. albicans*—not only directly by phagocytosis, but also indirectly by promoting extracellular killing, which was subsequently confirmed in experiment (4).

Another example of a SBM is the modeling of cytoplasmic transport of human adenovirus based on virus trajectories extracted from time-lapse confocal fluorescence microscopy images (47). Stochastic simulation of binding and unbinding

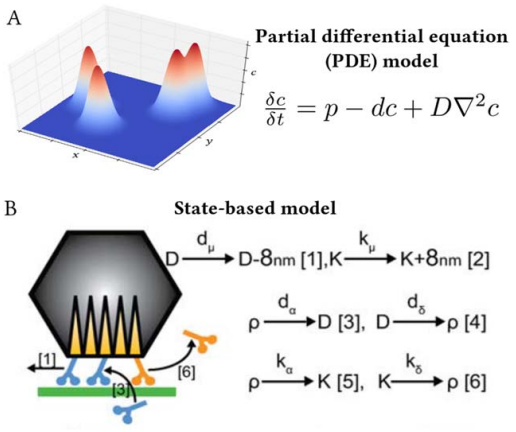

Figure 4. (**A**) Partial differential equation (PDE) model for chemokine diffusion (42) and an exemplary profile of the chemokine concentration *c(t)* in two-dimensional space at a fixed time point. The reaction-diffusion equation contains the following parameters characterizing the chemokine: D—diffusion coefficient, *p*—production term, *d*—degradation term. (**B**) Stochastic state-based model (SBM) describing the transport of human adenovirus along a microtubule (green) by dynein (D, blue) and kinesin (K, orange) motors (47). [1]/[2]—dynein/kinesin motor stepping with stepping rates d_μ/k_μ; [3]/[5]—dynein/kinesin binding to the virus capsid and decrease of the number of available motor binding sites ρ with binding rates d_α/k_α; [4]/[6]—dynein/kinesin unbinding from the virus capsid and increase of the number of available motor binding sites ρ with unbinding rates d_δ/k_δ. Reproduced from (47).

of microtubule motors (see Fig. 4B) predicted the number of motors taking part in the virus transport and the number of binding sites on the virus surface.

These examples demonstrate that SBM can contribute to the study of the infection processes where characterizing the states of the individual objects is crucial, while the spatial distribution of objects can be neglected. In most cases SBM do not require image data for their adjustment and, hence, they are rare in image-based systems biology. In contrast, individual-based modeling is the prevailing approach for simulating microscopy-visualized processes, because it combines individual characterization of objects with simulation of their migration and interaction in the spatial environment.

Individual-based Models

Individual-based models (IBM) can be viewed as the spatial extension of SBM. They represent biological objects as discrete entities that can migrate and interact in space and time according to defined rules of deterministic or stochastic type. Depending on the level of model complexity and on specific aspects of implementation, one can distinguish cellular automata (CA), cellular Potts models (CPM), and agent-based models (ABM), though the boundaries between these three classes are not very strict.

Cellular automata (CA), first introduced by John von Neumann (48), are the simplest type of IBM. The environment is represented by a discrete lattice consisting of computational cells (i.e., the unit cells of the lattice) that may be empty or occupied by a single entity (e.g., a biological cell) that can adopt different states (see e.g., Fig. 5A). The state of each entity depends on its own previous states and on the states of individuals in neighboring computational cells. Movements and interactions of entities between computational cells are simulated by corresponding state changes according to defined rules.

Bankhead et al. (37) implemented CA with probabilistic rules, where each computational cell of the automaton was empty or occupied by an epithelial cell, and the cell state indicated the stage of a viral infection. This model simulated the spread of viral infection in epithelial cells and enabled estimating such measure as, e.g., viral release and probability of virus binding to the cell, which were inaccessible in experiment. A similar approach based on live-cell fluorescence microscopy simulated the spread of human adenovirus in a cell culture and revealed the predominant role of the cell-free transmission in this process (49).

Bru and Cardona (50) introduced a model of granuloma formation in tuberculosis, where they combined CA to simulate immune cells and bacilli (Fig. 5A) with PDE to describe chemokine gradients. Segovia-Juarez et al. (51) exploited a similar approach, but represented the concentration of bacilli as a continuous variable. Both studies contributed to the understanding of mechanisms of granuloma formation; among other results, they demonstrated that the concentration of chemokines plays a crucial role in infection control by attracting immune cells to the site of infection.

In contrast to CA, cellular Potts models (CPM) can represent the shape of objects. CPM are based on a lattice where a biological cell is represented by numerous adjacent lattice sites (see e.g., Fig. 5B), allowing for a realistic shape representation of cells. To conserve the integrity of a cell under its shape deformations, a specific surface- and volume-energy measure must be minimized at each iteration step.

Ariotti et al. (52) exploited the advantage of CPM to represent cellular shape and simulated the migration of skin-resident memory T cells based on two-photon microscopy data. They revealed that memory T cells have to form dendrites in order to persistently move in one direction and to effectively scan the tissue for antigens.

In another study, Vroomans et al. (42) combined CPM for cells (Fig. 5B) with PDE for chemokine gradients (Fig. 4A) to model the interactions between T cells and dendritic cells in a lymph node. This study demonstrated that the most efficient way for dendritic cells to stimulate antigen recognition is to chemo-attract T cells and desensitize them after contact: cells still appear to perform random walk migration—as observed in two-photon microscopy experiments—but the impact of chemotaxis makes the recognition of rare antigens much more efficient.

Agent-based models (ABM) are the most complex type of IBM. Each agent (e.g., a cell or a molecule) possesses a set of properties (e.g., size, shape, and spatial coordinate) and obeys certain behavioral rules (Fig. 5C). In contrast to CA and

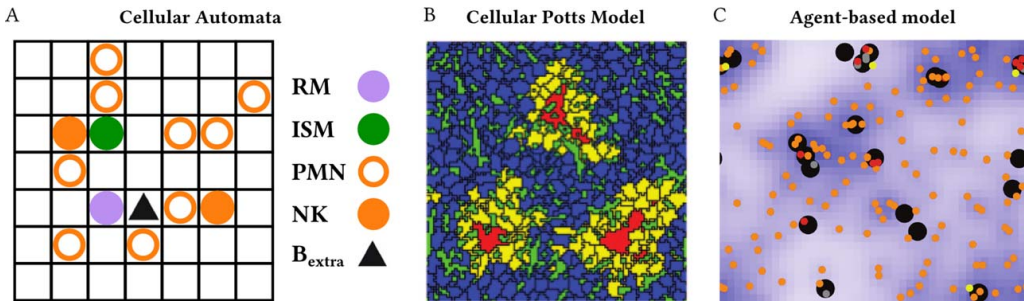

Figure 5. Examples of individual-based models (IBM) of infection processes. (**A**) Cellular automata (CA) model for granuloma formation in tuberculosis infection (50). RM—resting macrophage, ISM—infected sentenced macrophage, PMN—neutrophil, NK—natural killer cell, B_{extra}—extracellular bacilli. Grid size 20 × 20 μm^2. Adapted from (50). (**B**) Cross-section of a 3D Cellular Potts model (CPM) for interactions between T cells and dendritic cells in a lymph node (42). Blue—sensitive T cells, yellow—insensitive T cells, red—dendritic cells, green—reticular network. Reproduce from (42). (**C**) Agent-based model (ABM) for phagocytosis of *Aspergillus fumigatus* by neutrophils (53): neutrophils (black) search for extracellular spores (orange), which they can drag (yellow) or phagocytize (red) and kill (gray); the levels of blue represent the concentration of chemokines produced by the spores. Reproduced from (53).

CPM, the properties and behavior of agents are not attributed to the lattice, but specified for each agent individually. The positions of agents are also not bound to certain lattice sites; hence, the environment can be either discrete or continuous. The behavioral rules regulate, for example, cell migration, morphology changes, release or uptake of molecules, occurrence of cell division and cell death. Interaction rules may be specific for agents of the same type or of different types. The framework provided by ABM can represent individual objects in a highly realistic manner and capture the highest level of details.

Tokarski et al. (53) combined ABM with PDE to simulate the phagocytosis of *Aspergillus fumigatus* by neutrophils based on fluorescence microscopy data (Fig. 5C). Neutrophils and fungal spores were represented as discrete agents and the chemokine gradients as continuous variables in this hybrid ABM. This study revealed that the chemo-attraction of neutrophils toward the fungal spores significantly improves the phagocytosis efficiency in comparison to random walk migration of neutrophils, while the communication between these immune cells by chemokines accelerates under certain conditions the elimination of fungal spores even more.

In another study, an ABM was used to model the interaction of the pathogenic bacterium *Pseudomonas aeruginosa* with the gut epithelium after surgery (54). The simulation demonstrated the crucial role of this bacterium in hindering the healing process, predicted potential sites for bacterial binding, and suggested possible mechanisms of killing the epithelial cells.

These studies exemplify how image-derived ABMs can improve our understanding of infection mechanisms. ABMs enable modeling of a biological system in a highly realistic fashion, but at the price of greater computational costs compared to other modeling approaches. On the other hand, models based on differential equations are easy to implement and computationally cheap, but rely on many assumptions that strongly simplify the processes under consideration. The choice of the appropriate modeling approach is a crucial step in systems biology and may involve combining several approaches to adequately represent the complexity of the infection process under consideration.

Model Implementation

The art of modeling complex biological systems relies on solving the dilemma of describing these systems at a level where they become computationally feasible but still have the predictive power to motivate new testable hypotheses. Besides selecting the adequate modeling approach, particular equations, behavioral rules and/or agents, two other important aspects of model implementation should be mentioned: parameter optimization and modeling software.

Each model requires adjusting model parameters, e.g. diffusion rates or cell sizes. Many of these parameters can be obtained from experimental data, as discussed above. However, some parameters may not be directly accessible from experiment, e.g. growth rates or the probability of a pathogen to be phagocytized after contact with an immune cell. Such parameters have to be adjusted during model simulation by minimizing a specific functional that measures the dissimilarity between the simulation outcome and the outcome of the real experiment. In the optimization procedure, the parameters of the model are varied until the dissimilarity functional is minimized and the modeling output fits the experimental readout. Dissimilarity measures and search strategies can differ depending on the particular application and modeling approach and can aim at finding of either a local or the global minimum in the landscape of the dissimilarity functional. Local search strategies resemble hill down-climbing: at each iteration step only those changes of parameters are accepted that decrease the dissimilarity functional. On the other hand, global search strategies as, e.g., simulated annealing (55), occasionally admit the parameter sets that increase the dissimilarity: this can prevent solutions to be trapped in a local minimum. More dissimilar solutions are accepted with a certain probability that is controlled to decrease over time simulating

cooling of the system. A detailed overview and comparison of various optimization strategies can be found in (56).

Finally, it should be mentioned that many specific software tools exist that can aid to implement and simulate different modeling approaches. For instance, CompuCell3D (57) enables developing CPMs on a 3D lattice; CellSys (58) provides tools to simulate ABM and differential equation models in 2D and 3D; Chaste (59) presents a C++ library for differential equation modeling and all types of IBM; CellOrganizer (60) allows constructing models of subcellular organization learned from 2D and 3D images. The detailed description and comparison of available software tools for ABM and other IBM can be found elsewhere (61). Simpler models can be implemented using special mathematical tools (Mathematica, MATLAB, Scilab), or even general-purpose programming languages (C++, Java, Python). Available modeling libraries can considerably simplify the implementation process and—at the same time—make it more flexible.

Discussion and Future Perspectives

Image-based systems biology (IbSB) is a relatively new scientific approach that comprises imaging, quantitative characterization and modeling (10,11). IbSB contributed to exploring viral, bacterial, fungal and protozoan infections. For instance, in viral infection, image-based models describe how viral particles move through the cell cytoplasm (47) and how they spread in cell culture (37,49,62). Among bacterial infections, IbSB was intensively applied in the study of tuberculosis (41,50,51), including aspects as, e.g., granuloma formation (51). In host-fungal interactions, both the phagocytosis of fungal spores (53) and the growth of fungal hyphae (30,44,45) have been described by image-derived models. Furthermore, IbSB helped to clarify some aspects of parasitic infections, e.g. *Toxoplasma gondii* invasion and formation of cysts (63,64). Finally, IbSB greatly advanced our understanding of many aspects of migration and interaction behavior of immune cells, which has been comprehensively reviewed in (10,65,66).

Although IbSB has contributed to the study of many host-pathogen interactions, a lot of aspects of infection still remain unclear. Recent advances in live-cell imaging provided a unique opportunity to study the infection process in the natural environment of living organisms (9,21,22). Computer models can be constructed, virtually, for any host–pathogen interaction that can be visualized by live-cell microscopy: from initial encounter of pathogens in peripheral tissues to complex immune responses in lymph nodes (21,22).

Further progress in systems biology of infection should relate to multiscale modeling (6,67,68), since any biological system encompasses multiple levels of complexity. Integrating different modeling approaches into a hybrid model accounts for different levels of complexity that exist in real biological systems. For instance, combining ABM at the cellular level with PDEs at the molecular level clarified mechanisms of antibody affinity maturation in germinal centers in response to bacterial infections (69). This revealed the central role of Toll-like receptors on follicular dendritic cells (70) and high-affinity antibodies in regulating this process (71), as well as the evidence that B cell migration in germinal centers combines chemotactic signaling and random walks (72).

Multi-scale modeling can also refer to combining image-derived data with genomic, proteomic, or other "omics" data. While image and video data unravel the morphology, dynamics and function of a biological system, "omics" data provide information on gene/protein activity and gene regulatory networks. The combination of these approaches can aid to connect the activity patterns of genes and proteins to their real function in the context of infection processes (73). Complementary use of in vivo, in vitro and *in silico* studies—i.e., live-cell microscopy, "omics" analyses, and modeling—should advance our understanding of infectious diseases and aid in the design of novel treatment methodologies.

Acknowledgments

The authors thank the anonymous reviewers for their valuable suggestions that helped to improve the quality of this review. They are also thankful to Jens Stein for providing the two-photon microscopy image on B cell motility in the peripheral lymph node.

Literature Cited

1. WHO. World Health Statistics 2014. Available at: http://www.who.int/gho/publications/world_health_statistics/2014/en/.
2. Beltman JB, Marée AF, De Boer RJ. Spatial modelling of brief and long interactions between T cells and dendritic cells. Immunol Cell Biol 2007;85:306–314.
3. Beltman JB, Henrickson SE, von Andrian UH, de Boer RJ, Marée AFM. Towards estimating the true duration of dendritic cell interactions with T cells. J Immunol Methods 2009;347:54–69.
4. Hünniger K, Lehnert T, Bieber K, Martin R, Figge MT, Kurzai O. A virtual infection model quantifies innate effector mechanisms and *Candida albicans* immune escape in human blood. PLoS Comput Biol 2014;10:e1003479.
5. Lodhi H. Advances in computational systems biology. Elem Comput Syst Biol 2009; 8:1–17.
6. Forst CV. Host–pathogen systems biology. Drug Discov Today 2006;11:220–227.
7. Germain RN, Meier-Schellersheim M, Nita-Lazar A, Fraser IDC. Systems biology in immunology: A computational modeling perspective. Annu Rev Immunol 2011;29: 527–585.
8. Megason SG, Fraser SE. Imaging in systems biology. Cell 2007;130:784–795.
9. Witt C, Raychaudhuri S, Chakraborty AK. Movies, measurement, and modeling: The three ms of mechanistic immunology. J Exp Med 2005;201:501–504.
10. Figge MT, Meyer-Hermann M. Modelling intravital two-photon data of lymphocyte migration and interaction. New York: Springer. Math Models Immune Cell Biol 2011, p 121–139.
11. Sbalzarini IF. Modeling and simulation of biological systems from image data. BioEssays 2013;35:482–490.
12. Verveer PJ, Bastiaens PIH. Quantitative microscopy and systems biology: Seeing the whole picture. Histochem Cell Biol 2008;130:833–843.
13. Zhao T, Murphy RF. Automated learning of generative models for subcellular location: Building blocks for systems biology. Cytometry A 2007;71A:978–990.
14. Kherlopian AR, Song T, Duan Q, Neimark MA, Po MJ, Gohagan JK, Laine AF. A review of imaging techniques for systems biology. BMC Syst Biol 2008;2:74.
15. Marks KM, Nolan GP. Chemical labeling strategies for cell biology. Nat Methods 2006;3:591–596.
16. Pepperkok R, Ellenberg J. High-throughput fluorescence microscopy for systems biology. Nat Rev Mol Cell Biol 2006;7:690–696.
17. Wouters FS, Verveer PJ, Bastiaens PIH. Imaging biochemistry inside cells. Trends Cell Biol 2001;11:203–211.
18. Diaspro A, Robello M. Two-photon excitation of fluorescence for three-dimensional optical imaging of biological structures. J Photochem Photobiol B 2000;55:1–8.
19. Hoppe AD, Seveau S, Swanson JA. Live cell fluorescence microscopy to study microbial pathogenesis. Cell Microbiol 2009;11:540–550.
20. Hoppe AD, Shorte SL, Swanson JA, Heintzmann R. Three-dimensional FRET reconstruction microscopy for analysis of dynamic molecular interactions in live cells. Biophys J 2008;95:400–418.
21. Coombes JL, Robey EA. Dynamic imaging of host–pathogen interactions in vivo. Nat Rev Immunol 2010;10:353–364.
22. Konjufca V, Miller MJ. Two-photon microscopy of host–pathogen interactions: Acquiring a dynamic picture of infection in vivo. Cell Microbiol 2009;11:551–559.

REVIEW ARTICLE

23. Eliceiri KW, Berthold MR, Goldberg IG, Ibáñez L, Manjunath BS, Martone ME, Murphy RF, Peng H, Plant AL, Roysam B, Stuurman N, Swedlow JR, Tomancak P, Carpenter AE. Biological imaging software tools. Nat Methods 2012;9:697–710.
24. Rittscher J. Characterization of biological processes through automated image analysis. Annu Rev Biomed Eng 2010;12:315–344.
25. Shariff A, Kangas J, Coelho LP, Quinn S, Murphy RF. Automated image analysis for high-content screening and Analysis. J Biomol Screen 2010;15:726–734.
26. Yilmaz A, Javed O, Shah M. Object tracking: A Survey. ACM Comput Surv 2006;38: 13.
27. Brandes S, Mokhtari Z, Essig F, Hünniger K, Kurzai O, Figge MT. Automated segmentation and tracking of non-rigid objects in time-lapse microscopy videos of polymorphonuclear neutrophils. Med Image Anal 2015;20:34–51.
28. Chenouard N, Smal I, de Chaumont F, Maška M, Sbalzarini IF, Gong Y, Cardinale J, Carthel C, Coraluppi S, Winter M, Cohen AR, Godinez WJ, Rohr K, Kalaidzidis Y, Liang L, Duncan J, Shen H, Xu Y, Magnusson KEG, Jaldén J, Blau HM, Paul-Gilloteaux P, Roudot P, Kervrann C, Waharte F, Tinevez J-Y, Shorte SL, Willemse J, Celler K, van Wezel GP, Dan H-W, Tsai Y-S, de Solórzano CO, Olivo-Marin J-C, Meijering E. Objective comparison of particle tracking methods. Nat. Methods 2014; 11:281–289.
29. Maška M, Ulman V, Svoboda D, Matula P, Matula P, Ederra C, Urbiola A, España T, Venkatesan S, Balak DMW, Karas P, Bolcková T, Štreitová M, Carthel C, Coraluppi S, Harder N, Rohr K, Magnusson KEG, Jaldén J, Blau HM, Dzyubachyk O, Křížek P, Hagen GM, Pastor-Escuredo D, Jimenez-Carretero D, Ledesma-Carbayo MJ, Muñoz-Barrutia A, Meijering E, Kozubek M, Ortiz-de-Solorzano C. A benchmark for comparison of cell tracking algorithms. Bioinformatics 2014;30:1609–1617.
30. Mech F, Wilson D, Lehnert T, Hube B, Thilo Figge M. Epithelial invasion outcompetes hypha development during *Candida albicans* infection as revealed by an image-based systems biology approach. Cytometry A 2014;85A:126–139.
31. Kraibooj K, Park H-R, Dahse H-M, Skerka C, Voigt K, Figge MT. Virulent strain of *Lichtheimia corymbifera* shows increased phagocytosis by macrophages as revealed by automated microscopy image analysis. Mycoses 2014;57:56–66.
32. Mech F, Thywißen A, Guthke R, Brakhage AA, Figge MT. Automated image analysis of the host–pathogen interaction between phagocytes and *Aspergillus fumigatus*. PLoS One 2011;6:e19591.
33. Yeo JC, Wall AA, Stow JL, Hamilton NA. High-throughput quantification of early stages of phagocytosis. BioTechniques 2013;55:115–124.
34. Moon S, Lee S, Kim H, Freitas-Junior LH, Kang M, Ayong L, Hansen MAE. An image analysis algorithm for malaria parasite stage classification and viability quantification. PLoS One 2013;8:e61812.
35. Ross NE, Pritchard CJ, Rubin DM, Dusé AG. Automated image processing method for the diagnosis and classification of malaria on thin blood smears. Med Biol Eng Comput 2006;44:427–436.
36. Di Ruberto C, Dempster A, Khan S, Jarra B. Analysis of infected blood cell images using morphological operators. Image Comput 2002;20:133–146.
37. Bankhead A, Mancini E, Sims AC, Baric RS, McWeeney S, Sloot PMA. A simulation framework to investigate in vitro viral infection dynamics. J Comput Sci 2013;4:127–134.
38. Pollmächer J, Figge MT. Agent-based model of human alveoli predicts chemotactic signaling by epithelial cells during early *Aspergillus fumigatus* infection. PLoS One 2014;9:e111630.
39. Arhel N, Genovesio A, Kim K-A, Miko S, Perret E, Olivo-Marin J-C, Shorte S, Charneau P. Quantitative four-dimensional tracking of cytoplasmic and nuclear HIV-1 complexes. Nat Methods 2006;3:817–824.
40. Mokhtari Z, Mech F, Zitzmann C, Hasenberg M, Gunzer M, Figge MT. Automated characterization and parameter-free classification of cell tracks based on local migration behavior. PLoS One 2013;8:e80808.
41. Marino S, Pawar S, Fuller CL, Reinhart TA, Flynn JL, Kirschner DE. Dendritic cell trafficking and antigen presentation in the human immune response to mycobacterium tuberculosis. J Immunol 2004;173:494–506.
42. Vroomans RMA, Marée AFM, de Boer RJ, Beltman JB. Chemotactic migration of T cells toward dendritic cells promotes the detection of rare antigens (Haugh JM, editor). PLoS Comput Biol 2012;8:e1002763.
43. Bartnicki-Garcia S, Hergert F, Gierz G. Computer simulation of fungal morphogenesis and the mathematical basis for hyphal (tip) growth. Protoplasma 1989;153:46–57.
44. Bartnicki-Garcia S, Bartnicki DD, Gierz G, López-Franco R, Bracker CE. Evidence that spitzenkörper behavior determines the shape of a fungal hypha: A test of the hyphoid model. Exp Mycol 1995;19:153–159.
45. Reynaga-Peña CG, Gierz G, Bartnicki-Garcia S. Analysis of the role of the spitzenkörper in fungal morphogenesis by computer simulation of apical branching in *Aspergillus niger*. Proc Natl Acad Sci USA 1997;94:9096–9101.
46. Van Zon JS, Tzircotis G, Caron E, Howard M. A mechanical bottleneck explains the variation in cup growth during FcγR phagocytosis. Mol Syst Biol 2009;5:298.
47. Gazzola M, Burckhardt CJ, Bayati B, Engelke M, Greber UF, Koumoutsakos P. A stochastic model for microtubule motors describes the in vivo cytoplasmic transport of human adenovirus (Sauro HM, editor). PLoS Comput Biol 2009;5:e1000623.
48. Von Neumann J. The general and logical theory of automata. Proceedings: Cereb Mech Behav 1951;1–41.
49. Yakimovich A, Gumpert H, Burckhardt CJ, Lutschg VA, Jurgeit A, Sbalzarini IF, Greber UF. Cell-free transmission of human adenovirus by passive mass transfer in cell culture simulated in a computer model. J Virol 2012;86:10123–10137.
50. Bru A, Cardona P-J. Mathematical modeling of tuberculosis bacillary counts and cellular populations in the organs of infected mice (Pai M, editor). PLoS One 2010;5: e12985.
51. Segovia-Juarez JL, Ganguli S, Kirschner D. Identifying control mechanisms of granuloma formation during *M. tuberculosis* infection using an agent-based model. J Theor Biol 2004;231:357–376.
52. Ariotti S, Beltman JB, Chodaczek G, Hoekstra ME, van Beek AE, Gomez-Eerl R, Ritsma L, van Rheenen J, Maree AFM, Zal T, de Boer RJ, Haanen JBAG, Schumacher TN. Tissue-resident memory CD8+ T cells continuously patrol skin epithelia to quickly recognize local antigen. Proc Natl Acad Sci USA 2012;109:19739–19744.
53. Tokarski C, Hummert S, Mech F, Figge MT, Germerodt S, Schroeter A, Schuster S. Agent-based modeling approach of immune defense against spores of opportunistic human pathogenic fungi. Front Microbiol 2012;3:129.
54. Stern JR, Olivas AD, Valuckaite V, Zaborina O, Alverdy JC, An G. Agent-based model of epithelial host–pathogen interactions in anastomotic leak. J Surg Res 2013;184:730–738.
55. Kirkpatrick S. Optimization by simulated annealing: quantitative studies. J Stat Phys 1984;34:975–986.
56. Fu MC. Optimization via simulation: A review. Ann Oper Res 1994;53:199–247.
57. Swat MH, Thomas GL, Belmonte JM, Shirinifard A, Hmeljak D, Glazier JA. Multi-scale modeling of tissues using CompuCell3D. Methods Cell Biol 2012;110:325–366.
58. Hoehme S, Drasdo D. A cell-based simulation software for multi-cellular systems. Bioinformatics 2010;26:2641–2642.
59. Mirams GR, Arthurs CJ, Bernabeu MO, Bordas R, Cooper J, Corrias A, Davit Y, Dunn S-J, Fletcher AG, Harvey DG, Marsh ME, Osborne JM, Pathmanathan P, Pitt-Francis J, Southern J, Zemzemi N, Gavaghan DJ. Chaste: An open source C++ library for computational physiology and biology. PLoS Comput Biol 2013;9:e1002970.
60. Murphy RF. CellOrganizer: image-derived models of subcellular organization and protein distribution. Methods Cell Biol 2012;110:179–193.
61. Railsback SF, Lytinen SL, Jackson SK. Agent-based simulation platforms: Review and development recommendations. Simulation 2006;82:609–623.
62. Snijder B, Sacher R, Rämö P, Damm E-M, Liberali P, Pelkmans L. Population context determines cell-to-cell variability in endocytosis and virus infection. Nature 2009; 461:520–523.
63. Kafsack BFC, Carruthers VB, Pineda FJ. Kinetic modeling of toxoplasma gondii invasion. J Theor Biol 2007;249:817–825.
64. Sullivan AM, Zhao X, Suzuki Y, Ochiai E, Crutcher S, Gilchrist MA, von mering C, editor. Evidence for finely regulated asynchronous growth of toxoplasma gondii cysts based on data-driven model selection. PLoS Comput Biol 2013;9:e1003283.
65. Mirsky HP, Miller MJ, Linderman JJ, Kirschner DE. Systems biology approaches for understanding cellular mechanisms of immunity in lymph nodes during infection. J Theor Biol 2011;287:160–170.
66. Mrass P, Petravic J, Davenport MP, Weninger W. Cell-autonomous and environmental contributions to the interstitial migration of T cells. Semin Immunopathol 2010; 32:257–274.
67. Ludewig B, Stein JV, Sharpe J, Cervantes-Barragan L, Thiel V, Bocharov G. A global "imaging" view on systems approaches in immunology: Highlights. Eur J Immunol 2012;42:3116–3125.
68. Figge MT. Stochastic discrete event simulation of germinal center reactions. Phys Rev E 2005;71:051907.
69. Meyer-Hermann M, Figge MT, Toellner K-M. Germinal centres seen through the mathematical eye: B-cell models on the catwalk. Trends Immunol 2009;30:157–164.
70. Garin A, Meyer-Hermann M, Contie M, Figge MT, Buatois V, Gunzer M, Toellner K-M, Elson G, Kosco-Vilbois MH. Toll-like receptor 4 signaling by follicular dendritic cells is pivotal for germinal center onset and affinity maturation. Immunity 2010; 33:84–95.
71. Zhang Y, Meyer-Hermann M, George LA, Figge MT, Khan M, Goodall M, Young SP, Reynolds A, Falciani F, Waisman A, Notley CA, Ehrenstein MR, Kosco-Vilbois M, Toellner K-M. Germinal center B cells govern their own fate via antibody feedback. J Exp Med 2013;210:457–464.
72. Figge MT, Garin A, Gunzer M, Kosco-Vilbois M, Toellner K-M, Meyer-Hermann M. Deriving a germinal center lymphocyte migration model from two-photon data. J Exp Med 2008;205:3019–3029.
73. Horn F, Heinekamp T, Kniemeyer O, Pollmächer J, Valiante V, Brakhage AA. Systems biology of fungal infection. Front Microbiol 2012;3:p 108.
74. Coelho FM, Natale D, Soriano SF, Hons M, Swoger J, Mayer J, Danuser R, Scandella E, Pieczyk M, Zerwes H-G, Junt T, Sailer AW, Ludewig B, Sharpe J, Figge MT, Stein JV. Naïve B cell trafficking is shaped by local chemokine availability and LFA-1-independent stromal interactions. Blood 2013;121:4101–4109.
75. Hayward RD, Goguen JD, Leong JM. No better time to FRET: Shedding light on host pathogen interactions. J Biol 2010;9:12.
76. Kampen NGV. Stochastic Processes in Physics and Chemistry. Amsterdam, the Netherlands: Elsevier; 1992. 482 p.

5. Bottom-up modeling approach for the quantitative estimation of parameters in pathogen-host interactions

frontiers in Microbiology

ORIGINAL RESEARCH
published: 19 June 2015
doi: 10.3389/fmicb.2015.00608

Bottom-up modeling approach for the quantitative estimation of parameters in pathogen-host interactions

Teresa Lehnert[1,2†], Sandra Timme[1,2†], Johannes Pollmächer[1,2], Kerstin Hünniger[3], Oliver Kurzai[2,3] and Marc Thilo Figge[1,2]*

[1] Applied Systems Biology, Leibniz Institute for Natural Product Research and Infection Biology - Hans-Knöll-Institute, Jena, Germany, [2] Faculty of Biology and Pharmacy, Friedrich Schiller University Jena, Jena, Germany, [3] Fungal Septomics, Septomics Research Center, Friedrich Schiller University and Leibniz Institute for Natural Product Research and Infection Biology Hans-Knöll-Institute, Jena, Germany

OPEN ACCESS

frontiers in Microbiology

ORIGINAL RESEARCH
published: 19 June 2015
doi: 10.3389/fmicb.2015.00608

Bottom-up modeling approach for the quantitative estimation of parameters in pathogen-host interactions

Teresa Lehnert[1,2†], *Sandra Timme*[1,2†], *Johannes Pollmächer*[1,2], *Kerstin Hünniger*[3], *Oliver Kurzai*[2,3] *and Marc Thilo Figge*[1,2*]

[1] *Applied Systems Biology, Leibniz Institute for Natural Product Research and Infection Biology - Hans-Knöll-Institute, Jena, Germany,* [2] *Faculty of Biology and Pharmacy, Friedrich Schiller University Jena, Jena, Germany,* [3] *Fungal Septomics, Septomics Research Center, Friedrich Schiller University and Leibniz Institute for Natural Product Research and Infection Biology Hans-Knöll-Institute, Jena, Germany*

OPEN ACCESS

Edited by:
Saliha Durmus, Gebze Technical University, Turkey

Reviewed by:
Reiko Tanaka, Imperial College London, UK
Muhammed Erkan Karabekmez, Bogazici University, Turkey

***Correspondence:**
Marc Thilo Figge, Applied Systems Biology, Leibniz Institute for Natural Product Research and Infection Biology - Hans Knöll Institute, Adolf-Reichwein-Straße 23, Beutenberg Str 11a, 07745 Jena Germany
thilo.figge@hki-jena.de

[†] *These authors have contributed equally to this work.*

Specialty section:
This article was submitted to Infectious Diseases, a section of the journal Frontiers in Microbiology

Received: *15 April 2015*
Accepted: *02 June 2015*
Published: *19 June 2015*

Citation:
Lehnert T, Timme S, Pollmächer J, Hünniger K, Kurzai O and Figge MT (2015) Bottom-up modeling approach for the quantitative estimation of parameters in pathogen-host interactions. Front. Microbiol. 6:608. doi: 10.3389/fmicb.2015.00608

Opportunistic fungal pathogens can cause bloodstream infection and severe sepsis upon entering the blood stream of the host. The early immune response in human blood comprises the elimination of pathogens by antimicrobial peptides and innate immune cells, such as neutrophils or monocytes. Mathematical modeling is a predictive method to examine these complex processes and to quantify the dynamics of pathogen-host interactions. Since model parameters are often not directly accessible from experiment, their estimation is required by calibrating model predictions with experimental data. Depending on the complexity of the mathematical model, parameter estimation can be associated with excessively high computational costs in terms of run time and memory. We apply a strategy for reliable parameter estimation where different modeling approaches with increasing complexity are used that build on one another. This bottom-up modeling approach is applied to an experimental human whole-blood infection assay for *Candida albicans*. Aiming for the quantification of the relative impact of different routes of the immune response against this human-pathogenic fungus, we start from a non-spatial state-based model (SBM), because this level of model complexity allows estimating *a priori* unknown transition rates between various system states by the global optimization method *simulated annealing*. Building on the non-spatial SBM, an agent-based model (ABM) is implemented that incorporates the migration of interacting cells in three-dimensional space. The ABM takes advantage of estimated parameters from the non-spatial SBM, leading to a decreased dimensionality of the parameter space. This space can be scanned using a local optimization approach, i.e., *least-squares error estimation* based on an *adaptive regular grid search*, to predict cell migration parameters that are not accessible in experiment. In the future, spatio-temporal simulations of whole-blood samples may enable timely stratification of sepsis patients by distinguishing hyper-inflammatory from paralytic phases in immune dysregulation.

Keywords: state-based model, agent-based model, pathogen-host interaction, parameter estimation, whole-blood infection assay, *Candida albicans*

1. Introduction

The human fungal pathogen *Candida albicans* is part of the normal microbial flora in more than half of the global population. In immunocompromised patients it can become invasive and may enter the blood stream via medical devices, e.g., catheters, or translocation in the gut and can cause severe systemic infections. The immune response against *C. albicans* in human blood comprises the interplay of various complex biological processes involving different immune mechanisms (Duggan et al., 2015b). Most importantly, the whole-blood infection assay allows multiple immune effector mechanisms to occur at the same time and thus modulate the overall outcome (Luo et al., 2013; Cunha et al., 2014; Hünniger et al., 2015). Applying a systems biology approach, we quantified individual processes and in this way revealed the main route of the immune response against *C. albicans* in human blood (Hünniger et al., 2014). This was achieved by an iterative systems biology cycle involving experiment, mathematical modeling, hypothesis generation and further experimental investigation.

The choice of an appropriate mathematical modeling approach strongly depends on the questions to be answered and the hypothesis, as well as the characteristics of the underlying experimental data with regard to temporal and spatial information. A wide range of modeling approaches exists that differ by their computational complexity and can be classified depending on the degree of spatial representation as well as the internal degrees of freedom attributed to the model entities. The computationally cheapest modeling approach for dynamic systems is represented by ordinary differential equations (ODE), where biological entities are assumed to be present in high numbers and spatial information is not required such that they can be collectively represented by a homogeneously distributed concentration variable. State-based models (SBM) resolve the biological entities as individuals that occupy states and are able to perform transitions between states representing dynamic processes. In contrast to ODE, this approach allows modeling discrete events for any entity number in a biological system. However, SBM are in turn limited in that they do not represent spatial aspects. Individual-based models (IBM) such as cellular automata (CA) and agent-based models (ABM) do simulate discrete entities in space and time (Medyukhina et al., 2015). In a CA simulation, these entities can undergo state changes associated with their internal degrees of freedom as well as positional changes on a pre-defined spatial grid of computational cells (Von Neumann, 1951; Bittig and Uhrmacher, 2010). The discrete number of individual entities as well as the spatial representation of the environment result in increasing computational costs in terms of run-time and memory. Even more computationally expensive but biologically more realistic simulations can be performed by the ABM approach. Here, biological objects are represented as individual entities, so-called agents, that are able to move in space and can act as well as interact with other agents according to individual properties. Examples of ABM for the pathogen-host interaction between the human-pathogenic fungus *Aspergillus fumigatus* and phagocytes were presented by Tokarski et al. (2012) and Pollmächer and Figge (2014). In particular, the ABM developed by Pollmächer and Figge (2014) simulates the detection of *A. fumigatus* conidia by macrophages in a to-scale representation of human alveoli and predicts the requirement of a chemotactic signal guiding the phagocytes to the spatial positions of conidia.

In general, parameters of bio-mathematical models characterize the components by their morphology and their dynamic behavior. For example, cells may be defined by parameters for size and shape as well as by parameters for interactions in the spatial environment that are associated with the typical frequency of interaction processes. Model parameters associated with dynamical, functional and morphological aspects of biological processes may be extracted from microscopic images by applying an image-based systems biology approach (Horn et al., 2012; Mech et al., 2014; Medyukhina et al., 2015). However, in many cases microscopy experiments cannot be performed for technical reasons, as is also the case for whole-blood infection assays where the majority of cells are erythrocytes blocking the view on leukocytes, let alone fungal pathogens that are present in even lower numbers. In situations like these, numerical estimation of *a priori* unknown parameter values by comparison with experimental time-series data becomes a highly relevant issue. Parameter estimation algorithms are applied to find the optimal match between the experimental data and simulated model data. These optimization algorithms can be characterized by their search technique within the parameter space, i.e., as global or local approaches, and their mathematical procedures, i.e., as stochastic or deterministic approaches (Moles et al., 2003; Ashyraliyev et al., 2009). Local optimization techniques search for better parameter values within a locally restricted parameter space, where the direct search method and gradient based methods are widely used (Ashyraliyev et al., 2009). They show fast convergence to the optimal parameter values, but since local optimization algorithms will get stuck in a nearby local optimum, an educated guess of the initial parameter values is absolutely required. In contrast, global optimization strategies search a wide range of the parameter space with possibly various local optima and the subclass of deterministic optimization strategies can find the global optimum with pre-defined accuracy (Ashyraliyev et al., 2009). High-dimensional parameter spaces may be searched by stochastic optimization algorithms that make use of probabilistic elements to avoid getting trapped in local optima in order to find the global optimum. Common stochastic search algorithms of this type are Metropolis Monte Carlo (MMC) (Metropolis et al., 1953), adaptive random search and evolutionary computation techniques such as differential evolution (DE) (Storn and Price, 1997). Additionally, heuristics can be applied in support of a fast convergence rate of global or local optimization strategies, e.g., simulated annealing (SA) (Kirkpatrick et al., 1983; Gonzalez et al., 2007), great deluge (Dueck, 1993), or performing multiple searches from random start parameters. The selection of the most suitable optimization algorithm depends on specific model properties, such as the dimension of the parameter space and the computational costs for the model simulations that have to be repeatedly performed. For computationally cheap ODE models, the computationally expensive stochastic global optimization algorithms may be used,

such as DE applied by Hernandez-Vargas et al. (2014) and SA based on MMC applied by Hünniger et al. (2014) and Mech et al. (2014).

The non-spatial virtual infection model of the immune response against *C. albicans* in human blood was formulated as a SBM and its parameters were fitted to the experimentally determined time-evolution of concentrations for *C. albicans* cells that are alive or killed and that can either reside in extracellular space or inside immune cells of different types, i.e., monocytes or granulocytes (polymorphonuclear neutrophils, PMN) (Hünniger et al., 2014). Furthermore, we observed a cell population of *C. albicans* that remained alive or killed in extracellular space, i.e., these fungal cells are resistant against phagocytosis and/or killing. The different *C. albicans* cell populations were assigned states and individual cells could perform transitions between states, such as phagocytosis by immune cells, subsequent intracellular killing, extracellular killing by antimicrobial peptides or acquiring resistance against phagocytosis and/or killing. Resistant *C. albicans* cells are a population of cells that were found to be protected against phagocytosis and/or killing and that remained in the extracellular space of the whole-blood infection assay (Hünniger et al., 2014). Since the model is restricted to the dynamics of states occupied by pathogenic cells we refer to the model by Hünniger et al. (2014) as P-SBM. In the present study, motivated by newly measured experimental data regarding the immune cell number of monocytes and PMN in the whole-blood assays, we take the next step and modify the P-SBM to drop its implicit assumption that the number of immune cells for samples from different individuals would be the same. Since in the modified SBM states are assigned to the pathogenic cells as well as to the two types of immune cells, which have been found to actively participate in *C. albicans* elimination, we will refer to this model as PI-SBM. Taking individual immune cells explicitly into account obviously makes the simulations of the whole-blood infection assay more realistic, albeit at the expense of higher computational costs for global parameter optimization that will be performed using SA based on the MMC scheme as was the case for the P-SBM.

A timely stratification of sepsis patients in different phases of immune dysregulation requires spatio-temporal simulations of whole-blood samples. To achieve this goal, an ABM of the whole-blood infection assay was established that builds on the PI-SBM and incorporates spatial properties of the blood sample in a three-dimensional continuous representation. In particular, in the ABM *C. albicans* cells as well as monocytes and PMN are agents that can migrate in the environment and interact with each other. Apart from the model parameters associated with the migration of cells, the ABM was based on the transition rates of the PI-SBM after appropriate conversion. This procedure strongly reduces the number of *a priori* unknown parameters of agents to the subset of migration parameters. The latter can be estimated using the computationally cheap grid search algorithm and enables the prediction of the migration behavior for the different immune cell types that are otherwise not directly accessible in experiment. The interrelations between the different modeling approaches are schematically shown in **Figure 1** demonstrating that results are re-used across different modeling approaches to simultaneously facilitate an increase in model complexity and a decrease in computational expense for parameter estimation. Our step-wise computational biology approach avoids typical limitations of realistic models by focusing parameter estimation on those parameters that arise at the next level of model complexity.

2. Materials and Methods

2.1. Non-spatial State-based Model

The initial version of the non-spatial SBM describes the dynamics of state transitions for the human-pathogenic fungus *C. albicans* in whole-blood samples of healthy donors (Hünniger et al., 2014). In agreement with experimental data, the time-evolution of different *C. albicans* cells that are alive or killed and in extracellular space or phagocytosed by either monocytes or PMN can be simulated in this way. Since this SBM assumes the number of immune cells to be constant across blood samples of different donors and does only simulate the dynamics of the pathogenic (P) cells, it is hereafter referred to as P-SBM. However, it is known that the number of immune cells may strongly vary across human individuals and in particular for patients. Therefore, we increase the model complexity by advancing the P-SBM to a model that does explicitly account for the number of immune cells being present in a hemogram. Data including immune cell counts can easily be obtained both in an experimental as well as in a clinical setting. This model is hereafter referred to as PI-SBM to indicate that state transitions are computed for pathogenic (P) as well as immune (I) cells.

For comparison between the model predictions and the experimentally determined kinetics in the whole-blood infection assay, we introduce specific combinations of states, referred to as *combined units*, that are measurable and useable for the parameter estimation. These comprise all extracellular *C. albicans* cells C_E,

$$C_E \equiv C_{AE} + C_{KE} + C_{AR} + C_{KR}\,, \tag{1}$$

that are either alive (C_{AE}) or killed (C_{KE}) cells in extracellular space as well as cells resistant against killing and/or phagocytosis that are either alive (C_{AR}) or killed (C_{KR}). Next, the combined units C_M and C_G refer to *C. albicans* cells that are phagocytosed, respectively, by monocytes

$$C_M \equiv \sum_{i\geq 0}\sum_{j\geq 0} M_{i,j}\,(i+j)\,, \tag{2}$$

or by granulocytes

$$C_G \equiv \sum_{i\geq 0}\sum_{j\geq 0} G_{i,j}\,(i+j)\,. \tag{3}$$

Here, $M_{i,j}$ and $G_{i,j}$ refer to the number of monocytes and granulocytes (PMN), respectively, with i alive and j killed phagocytosed *C. albicans* cells. We limit the maximal number of *C. albicans* cells that can be phagocytosed by an immune

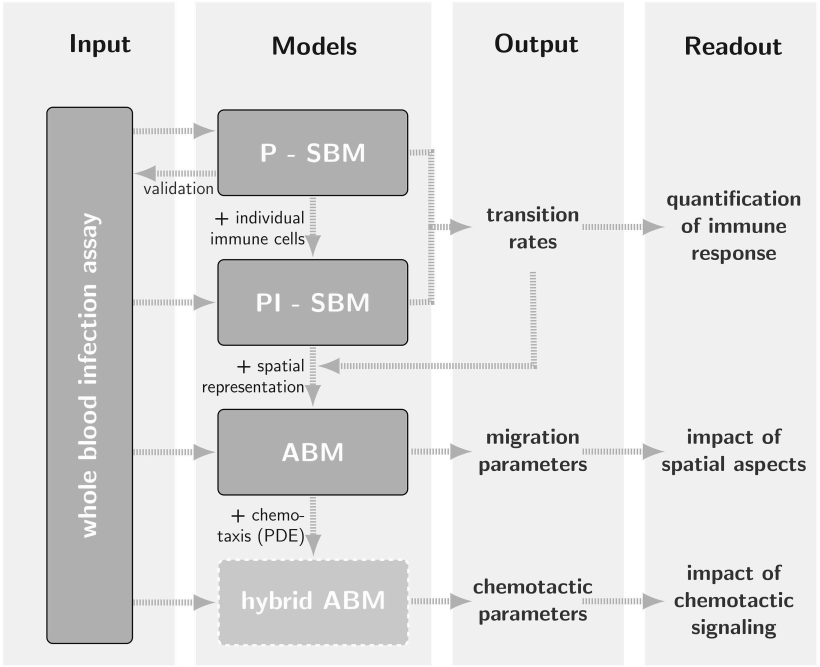

FIGURE 1 | Schematic representation of the bottom-up modeling approach as a strategy for parameter estimation where different mathematical models with increasing levels of complexity build on one another. Using model outputs at one level for calibration of models at a higher level is by way of example demonstrated for *Candida albicans* infection in a human whole-blood assay (Hünniger et al., 2014). The state-based model P-SBM, which focuses on the viewpoint of pathogens, was modified into the state-based model PI-SBM by accounting for actions of individual immune cells. After calibration of transition rates in the non-spatial state-based model, these were used to simulate the infection process in an agent-based model (ABM) that accounts for the spatial representation of the whole-blood infection assay. In the future, the calibration of migration parameters may for example serve as input for a hybrid ABM that captures the time-evolution of chemotactic signaling by solving reaction-diffusion equations.

cell to 18, i.e., $i, j < 10$, being much larger than observed in experiment (Hünniger et al., 2014). Furthermore, all killed *C. albicans* cells are given by the combined unit

$$C_K \equiv C_{KE} + C_{KR} + \sum_{i\geq 0}\sum_{j\geq 1}(M_{i,j} + G_{i,j})\, j\,, \tag{4}$$

and all alive *C. albicans* cells by the combined unit

$$C_A \equiv C_{AE} + C_{AR} + \sum_{i\geq 1}\sum_{j\geq 0}(M_{i,j} + G_{i,j})\, i\,. \tag{5}$$

It should be noted that only three of the five combined units are independent of each other, due to the conservation relations $C = C_E + C_G + C_M$ and $C = C_K + C_A$ for the total number of *C. albicans* cells C.

The simulation algorithm for the time-evolution of the PI-SBM is implemented in C++ that is available upon request. In **Figure 2A**, the simulation algorithm is schematically depicted and can be compared to the simulation algorithm of the P-SBM in Supplementary Figure 1. We simulate a blood sample of 1 ml containing 5×10^5 monocytes, 5×10^6 PMN and 1×10^6 *C. albicans* cells that are initially extracellular and alive. In each time-step, which we set to $\Delta t_{PI-SBM} = 1$ min, the algorithm tests for each individual cell in the system whether or not it does undergo a state transition. To this end, a cell is first randomly selected by sampling its relative frequency of occurrence among all cell types in the system. Next, the state of this cell is updated using a random selection procedure for the one transition in this time-step that the cell can possibly make among all currently enabled transitions. Once the type of transition between states s and s' with rate $r_{s\to s'}$ is selected, it will be executed with probability $P_{s\to s'} = r_{s\to s'}\,\Delta t_{PI-SBM}$ and the system is updated accordingly. **Table 1** provides an overview of the transition rates for all possible state transitions of the model. After testing all individuals in the system for performing a state transition, the simulation time is advanced by one time-step and the whole procedure is repeated until the total simulation time is reached. Note that, since the ratio of the number of immune cells over the number of pathogenic cells is larger than five, the simulation run time of the PI-SBM is significantly increased compared with the P-SBM.

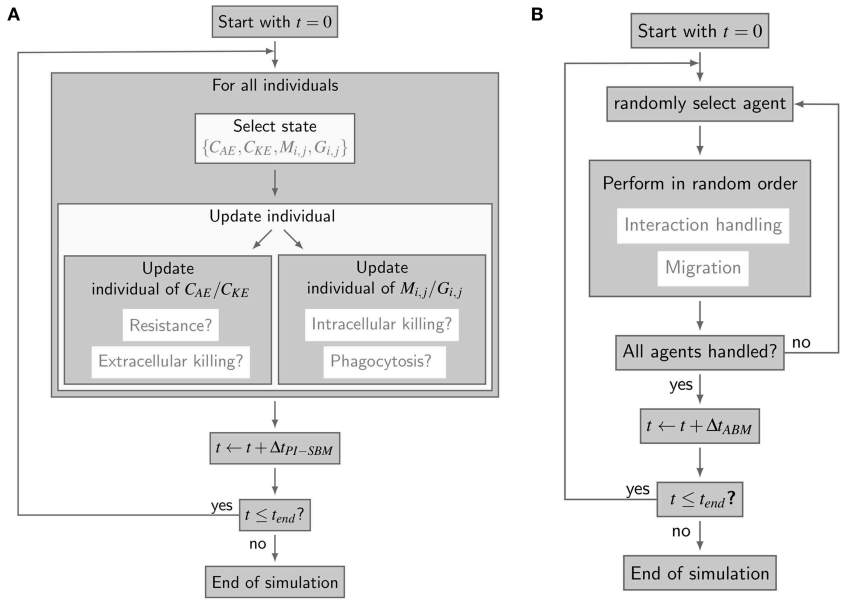

FIGURE 2 | Simulation algorithms of virtual infection models for whole-blood assays. (A) Flow-chart of the non-spatial PI-SBM simulation algorithm. In each time-step Δt_{PI-SBM}, all individuals are tested for possible state transitions. Individuals of extracellular alive and killed *C. albicans* states, i.e., C_{AE} and C_{KE}, respectively, are tested for becoming resistant and for extracellular killing. Individuals of immune cell states ($M_{i,j}$ or $G_{i,j}$) are tested for phagocytosis of *C. albicans* and for intracellular killing. **(B)** Flow chart of the spatial ABM simulation algorithm. In each time-step Δt_{ABM}, the migration and interaction handling is performed in random order for every randomly chosen agent.

2.2. Spatial Agent-based Model

The spatial virtual infection model for *C. albicans* in human blood is realized using an ABM approach. This model is implemented in C++ based on a previously established framework of Pollmächer and Figge (2014) and is the spatial counterpart of the non-spatial PI-SBM introduced in Section 2.1. The C++ source code of the ABM simulation algorithm is available upon request. In the ABM, the two types of immune cells—monocytes and PMN—as well as the pathogenic *C. albicans* cells are incorporated as virtual objects. These virtual objects are agents that are characterized by a spherical morphology with the physiological diameters of $d_M = 16\,\mu$m for monocytes, $d_G = 13.5\,\mu$m for PMN (Mak and Saunders, 2011) and $d_C = 7\,\mu$m for *C. albicans* (Mendling, 2006) (see **Figure 3A**) and that can migrate and interact with each other on encounter in the three-dimensional spatial environment (see **Figure 3B**). We impose a cuboid environment with an edge length of $1000\,\mu$m representing $1\,\mu$l blood and use *random periodic* boundary conditions for the cuboid, i.e., an agent which leaves the environment at some boundary point is deleted from the system and a new agent with identical properties re-enters the environment at some other randomly chosen boundary point. The cuboid environment is represented as a continuous space, i.e., allowing agents to move in a manner that is more realistic than could be captured by a lattice-based approach. This advantage is accompanied by the drawback that well-defined neighborhood relations as naturally existing between neighboring sites on a lattice are not present in continuous space representations. However, in order to efficiently determine cell–cell encounters, we use a neighborhood list method, which reduces the computational complexity to a close-to linear dependency on the number of agents in the system (Rapaport, 1996). At time point $t = 0$, agents are initialized with all *C. albicans* cells being in the state alive-and-extracellular. The time-evolution of the system is simulated by the random selection method (Skvoretz, 2002; Figge, 2005) that handles the migration and interaction of agents per time-step Δt in a random fashion (see **Figure 2B**).

We use ratios in cell numbers that are equivalent to those in the PI-SBM, where $1\,\mu$l of blood contains 5×10^3 PMN, 5×10^2 monocytes and 1×10^3 *C. albicans* cells, i.e., in total 6.5×10^3 cells. Viewing cells as interacting point particles, an average volume of $v \approx \frac{1}{6.5}\times10^6\,\mu\text{m}^3$ can be attributed to each cell, implying an average distance of $l \approx v^{1/3} \approx 55\,\mu$m between immune cells and *C. albicans* cells. Even though this distance is clearly larger than the diameters of these cells, $l \gg d_M, d_G, d_C$, we assume that the migration behavior of immune cells and *C. albicans* cells in blood resembles a random walk of agents without directional persistence. This assumption is based on the fact that the total number of erythrocytes in human blood ranges from $4\times10^6-6\times10^6$ cells/μl (McClatchey, 2003). Estimating the total number of cells in $1\,\mu$l of blood to be about six millions, an average volume

TABLE 1 | Rates of state transitions in the non-spatial PI-SBM.

Transition rate	Description	State transition
ϕ_M	Phagocytosis by monocytes	$M_{i,j} + C_{AE} \to M_{i+1,j}$ $M_{i,j} + C_{KE} \to M_{i,j+1}$
κ_M	Intracellular killing by monocytes	$M_{i,j} \to M_{i-1,j+1}$
ϕ_G	Phagocytosis by PMN for first-time phagocytosis event	$G_{0,0} + C_{AE} \to G_{1,0}$ $G_{0,0} + C_{KE} \to G_{0,1}$
$\phi_{G^\star}$	Phagocytosis by PMN for repeated phagocytosis events	$G_{i,j} + C_{AE} \to G_{i+1,j}$ $G_{i,j} + C_{KE} \to G_{i,j+1}$
κ_G	Intracellular killing by PMN	$G_{i,j} \to G_{i-1,j+1}$
$\kappa_{EK}(t)$	Extracellular killing by antimicrobial peptides released by first-time PMN phagocytosis with decreasing activity Rate depends on the activity of antimicrobial peptides ($\bar{\kappa}_{EK}$) and the decay of their antimicrobial activity (γ) as defined in Hünniger et al. (2014)	$C_{AE} \to C_{KE}$
ρ	Resistance against phagocytosis and/or killing	$C_{AE} \to C_{AR}$, $C_{KE} \to C_{KR}$

For details see (Hünniger et al., 2014).

of $v_c \approx \frac{1}{6}\times 10^3\,\mu\mathrm{m}^3$ can be attributed to each cell, implying a mean free path of $l_{fp} \approx v_c^{1/3} \approx 5\,\mu$m between point particles. This distance is not only clearly smaller than the distance between immune cells and *C. albicans* cells, $l_{fp} \ll l$, but also smaller than the diameters of erythrocytes, *C. albicans* cells as well as of the immune cells under consideration. It can be concluded that cells are not migrating with directional persistence in blood, because frequent collisions with the overwhelming number of erythrocytes will induce diffusive migration of cells with diffusion coefficients in whole-blood that can be very different for the different cell types. This is a consequence of the fact that monocytes and PMN perform active migration, whereas *C. albicans* cells are immotile due to the complete lack of cellular organelles for motility (Margulies and Schwartz, 1998) and its movement in whole blood is only passive.

Even though blood is a non-Newtonian fluid, i.e., showing pseudoplastic properties with variable viscosity depending on the exerted shear stress in capillaries of different sizes (Fahraus and Lindqvist, 1931), the experimental setup of the whole-blood infection assay is such that the viscosity as well as the temperature in the mildly stirred test tube remain constant (Hünniger et al., 2014). Therefore, the Stokes-Einstein equation (Einstein, 1905) can be applied to infer the diffusion coefficient D_C for the passive movement of *C. albicans* cells. Based on a whole-blood viscosity of about $\eta \approx 4\,mPa\,s$ (Rosenson et al., 1996), Boltzmann constant k_B and temperature $T = 37^\circ$C (Hünniger et al., 2014), this yields the relatively small diffusion coefficient $D_C = k_B T/(3\pi\eta d_C) \approx 1\,\mu\mathrm{m}^2/\mathrm{min}$. In contrast, the active migration of monocytes and PMN requires to estimate their diffusion coefficients numerically.

The time-step Δt_{ABM} for simulations in the ABM has to be chosen such that a smooth migration of cells is sampled in time. In order to ensure this, we require that during one time-step Δt_{ABM} cells do not migrate further than a certain distance, which we set to equal the mean free path $l_{fp} = 5\,\mu$m:

$$\Delta t_{ABM} = \frac{l_{fp}^2}{6\,D_{max}}\,. \tag{6}$$

Here, $D_{max} \equiv \max\{D_C, D_M, D_G\}$ denotes the largest out of the three diffusion coefficients for *C. albicans* cells (D_C), monocytes (D_M), and PMN (D_G). Since it can be expected that the active migration of immune cells is associated with diffusion coefficients D_M and D_G with $D_M, D_G \gg 1\,\mu\mathrm{m}^2/\mathrm{min}$ in the whole-blood infection assay, it follows from Equation (6) that the time-step in the ABM will be much smaller than in the state-based model PI-SBM: $\Delta t_{ABM} \ll \Delta t_{PI-SBM} = 1$ min. Moreover, stochasticity in the ABM requires that each simulation has to be repeated multiple times, resulting into relatively high computational costs compared with the PI-SBM, in particular, if we would have envisaged to estimate each model parameter instead of following the strategy of a bottom-up modeling approach.

Computational costs associated with parameter estimation in the ABM can be significantly reduced by making use of the previously estimated rates of state transitions in the state-based model PI-SBM (see Section 2.1 and **Table 1**). In the course of a simulation, migrating cells in the ABM may either spontaneously undergo state transitions or interact with each other upon spatial contact. In **Figure 3C**, we present a schematic overview of processes that occur according to defined rules associated with certain probabilities. It is important to note that, due to the spatial aspects that are captured by the ABM but not the PI-SBM, we have to distinguish between processes that are *contact-dependent* and *contact-independent*.

For *contact-independent* processes—such as intracellular and extracellular killing as well as the occurrence of *C. albicans* resistance against phagocytosis and/or killing—the conversion of rates from the PI-SBM to the ABM is straightforward. Since these processes are not determined by any spatial requirements, a simple re-scaling is performed. For example, *C. albicans* cells become resistant in the PI-SBM with probability $P_{PI-SBM}(\rho) = \rho\,\Delta t_{PI-SBM}$. In the ABM, where the resolution of time is set by the time-step $\Delta t_{ABM} \ll \Delta t_{PI-SBM}$, we check in each time-step with probability

$$P_{ABM}(\rho) = P_{PI-SBM}(\rho)\frac{\Delta t_{ABM}}{\Delta t_{PI-SBM}} \tag{7}$$

whether this process occurs.

In contrast, *contact-dependent* processes in the ABM are characterized by the requirement that two cells have to get into spatial contact first, before such a process—for example, a phagocytosis event of a *C. albicans* cell by a monocyte with transition rate ϕ_M—can take place. In the PI-SBM, spatial contact is not explicitly modeled; rather, the interaction partner for each monocyte is randomly chosen once per time-step Δt_{PI-SBM}. The associated probability is determined by the time-dependent ratio of non-resistant fungal cells over the sum of extracellular fungal cells and immune cells. Once an interaction partner was chosen, the phagocytosis event itself occurs with probability

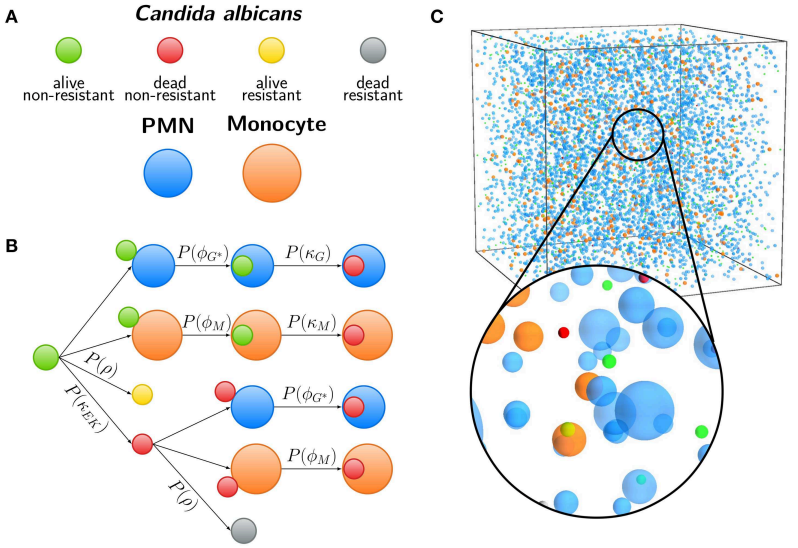

FIGURE 3 | Agent-based model (ABM) of the human whole-blood infection assay. (A) Agents used in the ABM are *Candida albicans* cells in the four states (i) alive and non-resistant (green), (ii) dead and non-resistant (red), (iii) alive and resistant (yellow), and (iv) dead and resistant (gray). Furthermore, granulocytes (polymorphonuclear neutrophils, PMN) and monocytes are shown in blue and orange, respectively. **(B)** Schematic overview of examples for interactions in the ABM. Each arrow indicates the execution of an interaction event, either depending on spatial contact between different cells or by a contact-independent process. *C. albicans* cells that are in extracellular space and alive (C_{AE}) or killed (C_{KE}) can become resistant with probability $P(\rho)$. After spatial contact, alive or killed *C. albicans* cells can be phagocytosed by PMN or monocytes with probabilities $P(\phi_G|\phi_{G^*})$ or $P(\phi_M)$, respectively. Intracellular alive *C. albicans* cells are killed with probabilities $P(\kappa_G)$ or $P(\kappa_M)$ depending on the type of phagocyte. **(C)** Visualization of the three-dimensional cuboid environment of the ABM that corresponds to 1 μl of the whole-blood infection assay, containing 5000 PMN, 500 monocytes, and 1000 *C. albicans* cells. The time-evolution of the simulated infection scenario can be viewed in Supplementary Video 1.

$P_{PI-SBM}(\phi_M) = \phi_M \, \Delta t_{PI-SBM}$ in the PI-SBM. Correspondingly, in the ABM, we request that this process takes place with the same probability,

$$P_{ABM}(\phi_M) = P_{PI-SBM}(\phi_M)\,, \tag{8}$$

on every encounter between a monocyte and a *C. albicans* cell. This correspondence of event probabilities for the two modeling approaches imposes a condition on the spatial dynamics of cells, i.e., on the values of the diffusion coefficients in the ABM and by that on the time-step Δt_{ABM} (see Equation 6). For optimal migration parameters, i.e., parameters that result in good agreement with the experimental data, it is expected that measurement of the associated phagocytosis rate in the ABM coincides with the corresponding rate from the PI-SBM.

2.3. Parameter Estimation

2.3.1. Simulated Annealing

The *a priori* unknown transition rates of the PI-SBM are determined by the method of Simulated Annealing based on the Metropolis Monte Carlo scheme (SA-MMC) that is depicted in **Figure 4A**. This optimization method randomly explores the parameter space of transition rates to find the global minimum of the fitting error, i.e., the most suitable parameter set that produces the best fit of the simulation to the experimental data obtained from the whole-blood infection assay.

The parameter estimation algorithm starts with a randomly chosen set of parameter values within the interval of $[0, 1]$ per minute, represented by the vector $\vec{p}$, and calculates the resulting time-evolution of state occupations from the simulation algorithm of the PI-SBM (see Section 2.1). To score the simulation result for a particular set of parameters, we combined different kinetics of the PI-SBM, referred to as *combined units*, which are identical with the experimental kinetics measured in the whole-blood infection assay (see Section 2.1). In this way, the experimental kinetics can be directly compared with the combined units c obtained from the model simulation, which is then scored by calculating the least-squares error (LSE) at experimental data points k as the weighted sum over c:

$$E[\vec{p}] = \sum_c \epsilon_c \, \frac{1}{2} \sum_k (x^{dat}_{k,c} - x^{sim}_{k,c}[\vec{p}])^2 \,. \tag{9}$$

Here, ϵ_c is adjusted as to fit each combined unit comparably well to the experimental data. The same values for ϵ_c were used in the PI-SBM and the ABM and are given in Supplementary Table 1. Next, the parameter set $\vec{p}$ is randomly varied within a pre-defined neighborhood of 10% variation, leading to a new

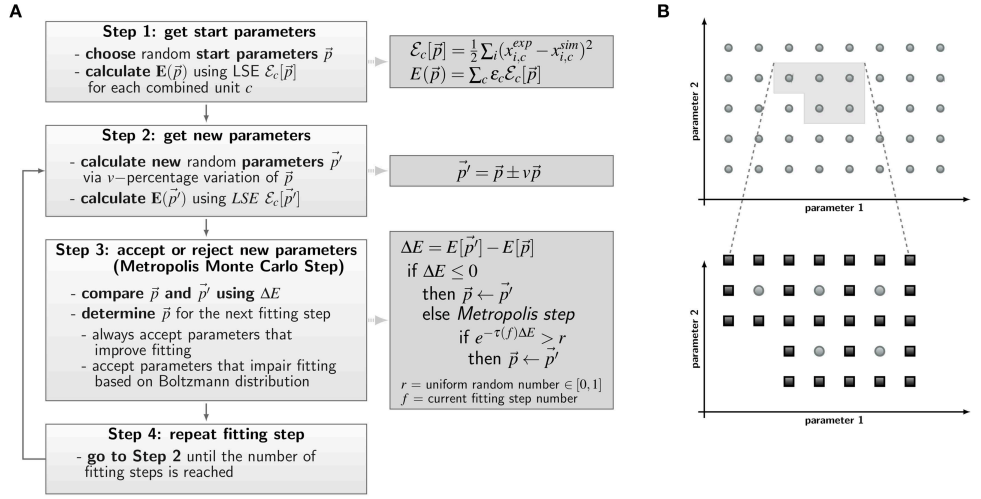

FIGURE 4 | Concepts of parameter estimation algorithms for non-spatial state-based models (SBM) and spatial agent-based models (ABM). (A) Flow chart of parameter estimation by the global optimization method Simulated Annealing based on the Metropolis Monte Carlo (SA-MMC). Light gray boxes describe Steps 1–4 of the algorithm; equations and pseudo code applied in these steps are provided in the dark gray boxes. **(B)** Schematic overview of the local optimization method *adaptive grid search algorithm* used for estimation of ABM migration parameters. Simulations are performed for sets of parameters on a regular grid in a predefined area of the search space and are evaluated by the *least squares error* (LSE). The initial grid (upper panel) contains sets of parameters with smallest LSE (light gray area) and this area is refined for a more accurate identification of the optimal parameter set (lower panel). Here, light gray dots represent parameter configurations from the first refinement level and dark gray squares represent parameter configurations of the subsequent refinement level.

set of parameter values, $\vec{p}\,'$, as indicated in **Figure 4A**, Step 2. Subsequently, the simulation of the PI-SBM is performed again for parameter values $\vec{p}\,'$ and the corresponding score $E[\vec{p}\,']$ is calculated. Whether the new simulated data will be accepted or rejected is decided by applying the MMC scheme that is depicted in **Figure 4A**, Step 3. The probability to accept worse parameter values is influenced by $\tau(f)$, representing the "inverse system temperature" in a SA process. The simulation of the annealing process involves a gradual decrease of the system temperature with progressed fitting, i.e., $\tau(f)$ is increased with the number of performed fitting steps f (see Supplementary Information 2.1).

After performing a total number of fitting steps, the fitting algorithm is repeated starting from a newly chosen random parameter set. This is done for a certain number of runs and the set of parameters with the minimal fitting error ($\vec{p}_{min}$) is saved from each fitting process. The mean values of the parameter values and their standard deviations are computed over all runs to determine the robustness of the estimated parameters.

We repeatedly perform the parameter estimation procedure for different system sizes in terms of the total number of individual cells. In doing so, the system size is stepwise increased by factors of ten, which is associated with increasing computing time for the model simulation but is partly compensated by a decrease in the number of fitting steps to avoid computational overload (see Supplementary Table 2). We start the estimation algorithm with a low number of individuals and a large number of fitting steps. The resulting parameter values are subsequently used as start parameter values for the system with next-higher number of individuals, i.e., for a 10-fold larger system. This procedure is repeated until a system size is reached where the number of individuals correspond to the measured numbers of PMN (about 5×10^6) and monocytes (about 5×10^5).

2.3.2. Adaptive Regular Grid Search

As described in Section 2.2, probabilities for state transitions in the ABM of the whole-blood infection assay can be derived from the interaction rates of the PI-SBM. This reduces the space of parameters that has to be searched in the process of parameter estimation, leaving only two migration parameters—i.e., the diffusion coefficients D_M and D_G, respectively, for monocytes and PMN—to be calibrated. However, even for a reduced parameter search space, there still is need for a calibration strategy that keeps the number of ABM simulations within limits, because simulating stochastic processes requires sufficient numbers of repetitions in order to obtain numerical results that are statistically sound.

We apply the *adaptive regular grid search algorithm* (Powell, 1998) to search iteratively for a local optimum in the parameter space (see **Figure 4B**). Motivated by biological constraints this is done for a pre-defined region of the parameter space. This region is represented on a regular grid and for each grid point the ABM is simulated with the corresponding set of parameter

values. Afterwards, simulations are evaluated with the least-squares error (LSE), scoring deviations between the simulation results and the experimental data for all combined units $c = \{C_K, C_A, C_E, C_M, C_G\}$ (see Section 2.1 and Equation 9). The values for the LSE are used to determine the adaptive refinement of the grid before the next iteration step, where intermediate grid points are calculated by bisection of the grid constant for the sets of parameters with lowest LSE. This imposes a grid refinement that ensures a more detailed scanning of the parameter space in relevant regions and defines the refinement level. The initial grid constant and the number of refinement steps determine how fine-grained the parameter space is represented by grid points and their values have to be chosen depending on the LSE landscape.

We further decrease computational costs associated with parameter estimation in the ABM by system scaling. Thus, similar to the procedure applied for the state-based model PI-SBM, we first scan the parameter space with a small system of 1/5 μl blood and subsequently re-scan the relevant parameter region with the system of 1 μl blood as defined in Section 2.2.

3. Results

3.1. Quantification of the Immune Response by the State-based Model

We quantified innate immune mechanisms in human whole-blood assays of infection with the pathogenic fungus *C. albicans* using a SBM. To this end, we modified a previously introduced SBM, referred to as P-SBM. This model was derived with the focus on state transitions of the pathogen (P) that may be induced by immune cells. However, immune cells in the P-SBM were only effectively modeled and not explicitly account for as individual cells (Hünniger et al., 2014). In the present work, we modified the P-SBM to model the interaction with individual immune cells—monocytes and granulocytes (PMN)—in detail. Since the focus of this model is on state transitions of both pathogen (P) and immune cells (I), we term this model PI-SBM. For reasons of comparison with the P-SBM, we used the same experimental data as in Hünniger et al. (2014) to quantify innate immune mechanisms by estimating the transition rates that yield the best fit to the data. Specific combinations of *C. albicans* states, referred to as *combined units*, were introduced that are directly related to different *C. albicans* populations measured over 4 h post-infection in experiment. As explained in detail in the Materials and Methods Section, the combined units include all extracellular *C. albicans* cells (C_E), *C. albicans* cells that are phagocytosed, respectively, by monocytes (C_M) or by granulocytes (C_G). Furthermore, all killed and alive *C. albicans* cells are given by the combined units C_K and C_A, respectively. The manually adjusted scores ϵ_c of combined units c are given in Supplementary Table 1. We simulate a blood sample of 1 ml containing 5×10^5 monocytes, 5×10^6 PMN and 1×10^6 *C. albicans* cells that are initially extracellular and alive.

To estimate the values of transition rates in the PI-SBM that yield the best fit to experimental data, i.e., the fit with the smallest least squares error (LSE), we applied the method of SA-MMC scheme (for details see Section 2.3.1). In **Figure 5**, the resulting transition rates of the PI-SBM are compared with those previously obtained within the P-SBM (for a quantitative comparison see also Supplementary Tables 3, 4). The direct comparison between the P-SBM and PI-SBM revealed that most transition rates are quantitatively similar in the two models.

The largest deviations in the values of transition rates between the two models were observed for the phagocytosis rate of monocytes (ϕ_M) and the killing rate of monocytes (κ_M). This was further investigated by performing the parameter estimation for the PI-SBM again, where only ϕ_M and κ_M were randomly varied while all other rates were kept fixed. We performed 50 runs and obtained very different standard deviations for these transition rates: while the standard deviation of ϕ_M was only 4%, this was 16% in the case of κ_M. We conclude that the PI-SBM is generally robust in all transition rates, except for κ_M that is also not directly determined by the data, because alive and killed *C. albicans* cells in phagocytes were not distinguished in these experiments. Similar observations were made for the P-SBM, where it was shown that variations in κ_M did not lead to significant differences in the fitting error (Hünniger et al., 2014).

To determine the impact of variations in the transition rates on the kinetics of the combined units in the PI-SBM, we performed 50 simulations with transition rates that were randomly sampled within their respective standard deviations. The kinetics of individual sub-populations are plotted in Supplementary Figure 2 while the results for the combined units are given in **Figure 6**. It can be seen that the simulated combined units agree well with the corresponding experimental data. In

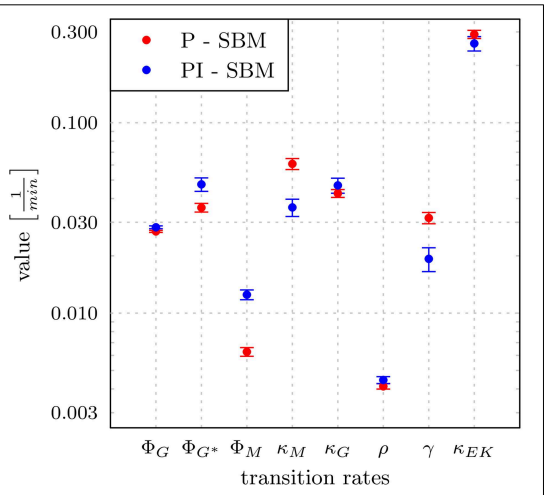

FIGURE 5 | Transition rates obtained from the model calibration to experimental data of the whole-blood infection assay. The results for the modified state-based model PI-SBM are compared to the P-SBM (Hünniger et al., 2014). The values are compared for the rate of phagocytosis by monocytes (ϕ_M), and by PMN on initial and subsequent events (ϕ_G,ϕ_{G^*}), rate of killing by monocytes (κ_M) and PMN (κ_G), rate of acquiring resistance against phagocytsis and/or killing (ρ) as well as the values of parameters for extracellular killing (γ, $\tilde{\kappa}_{EK}$). Error bars correspond to standard deviations.

particular, the resulting kinetics of the PI-SBM revealed that 4 h post-infection 82% *C. albicans* cells were phagocytosed by PMN, whereas only 4% *C. albicans* cells were phagocytosed by monocytes. Furthermore, PMN play a major role in the immune response, because these phagocytes are associated with 97% of all killed *C. albicans* cells (see Supplementary Figure 2A). This is achieved either directly, via phagocytosis and intracellular killing (66.5%) of the pathogen, or indirectly by the release of antimicrobial peptides on a pathogen's first event of phagocytosis (30.5%) (see Supplementary Figure 2H). Four hours post-infection, most *C. albicans* cells were killed (89%) while a minority of 11% cells were extracellular and became resistant against killing and phagocytosis. These results are in quantitative agreement with those obtained previously for the P-SBM (Hünniger et al., 2014).

3.2. Predictions on Monocytopenia and Neutropenia from PI-SBM

The state-based model PI-SBM opens the possibility to study the dependence of the immune response against *C. albicans* on the number of PMN and monocytes in blood. Simulating the virtual infection scenario with the previously estimated parameters (see Supplementary Table 3), we considered various cases of immune cell deficiencies. The model predictions at 4 h post-infection and for gradual decreases in the immune cell numbers are presented in **Figure 7** for the cases of monocytopenia and neutropenia separately.

We found, as expected from the above quantification of the immune response, that monocytopenia is not a critical condition with regard to *C. albicans* infections: deficiency of monocytes and even their complete absence was fully compensated by PMN-mediated killing. In fact, patients with monocytopenia have not been reported to develop systemic candidiasis to date (Lionakis, 2014). The situation is extremely different in the case of neutropenia. In the absence of PMN, the number of killed *C. albicans* cells is predicted to decrease from about 89% under physiological conditions down to 45%, i.e., $C_K = 89\%$ for 5×10^6 PMN and $C_K = 45\%$ for $\leq 5 \times 10^3$ PMN (see **Figure 7B**). Monocytes compensated PMN deficiency by phagocytosis of *C. albicans* cells only partly, where the fraction increased from 3% under physiological conditions up to 48%. However, 42% of the *C. albicans* cells acquired resistance against killing and/or phagocytosis, resulting from the combined effect of absent PMN phagocytosis and extracellular killing that is normally mediated by PMN release of antimicrobial peptides.

For a decrease in PMN number by one order of magnitude from physiological conditions, we found that monocytes can sustain the immune response fairly well. In this case, the fraction of killed *C. albicans* cells was still 79% and the phagocytosis by monocytes and PMN reached, respectively, 20% and 55% of *C. albicans* cells. A significant deterioration of the immune response was observed for PMN concentrations below 5×10^5 cells/ml (see **Figure 7**). Interestingly, this concentration was reported to mark the transition from moderate to severe neutropenia (Munshi and Montgomery, 2000), which is a

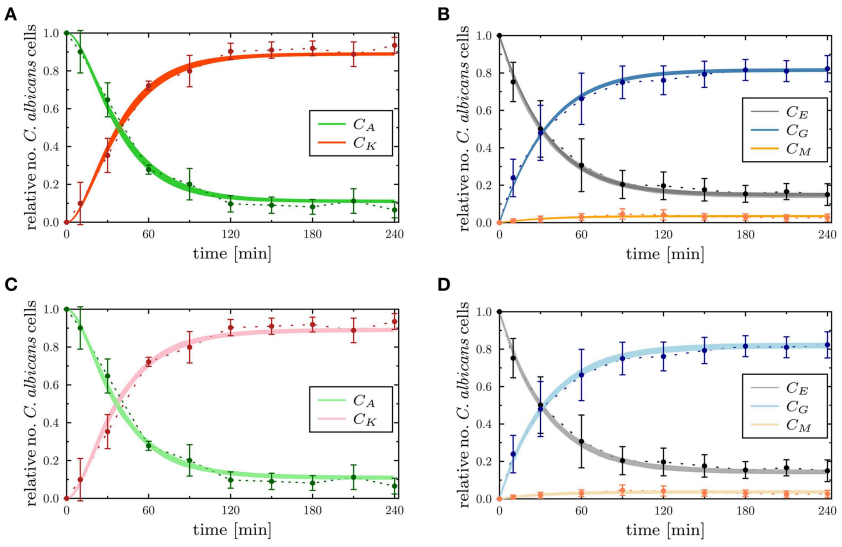

FIGURE 6 | Comparison of the time-evolution for the combined units from the experimental whole-blood infection assay (dotted lines as a guide for the eye) with the PI-SBM in (A,B), and the ABM in (C,D). In **(A,B)**, the thickness of the solid lines represents the standard deviation of the PI-SBM simulation results as obtained from 50 simulations for normally distributed transition rates as given in Supplementary Table 3. The thickness of the solid lines in **(C,D)** represents the standard deviation obtained by 30 simulations of the stochastic ABM. Time-evolution of killed (C_K) and alive (C_A) *C. albicans* cells are depicted in **(A,C)**, and the dynamics of *C. albicans* cells that are in extracellular space (C_E), phagocytosed by monocytes (C_M) and PMN (C_G) are shown in **(B,D)**.

condition that is known to be associated with high risks for candidemia in cancer patients (Lunel et al., 1999; Alangaden, 2011).

3.3. Agent-based Model Captures Immune Response in Time and Space

State-based models (SBM) do not account for any spatial aspects. For example, cells in the PI-SBM do not actually migrate during the immune response and, therefore, do not have to get into contact before a phagocytosis event can take place. In contrast, agent-based models (ABM) do capture spatial aspects in a defined environment. Applying a bottom-up modeling approach, we implemented an ABM that is—apart from its spatial aspects—the exact analog of the non-spatial PI-SBM. As depicted in **Figure 1**, all transition rates that were previously estimated for the PI-SBM were fed into the ABM (see Section 2.2 for details). The only parameters left to estimate were those related to cell migration, which in the dense cell system of the whole-blood assay resembles a random walk. In particular, while the diffusion coefficient associated with the passive movement of *C. albicans* cells could be inferred from the Stokes-Einstein equation to be $D_C \approx 1\,\mu\text{m}^2/\text{min}$, the active migration behavior of immune cells requires a rigorous parameter estimation of the diffusion coefficients D_M and D_G for monocytes and PMN, respectively.

It should be noted that, even in the case of low-dimensional parameter spaces, the estimation of parameters for ABM generally turn out to be computationally intensive. This is a consequence of the fact that ABM simulate the interactions between thousands of agents in continuous space as stochastic processes. To simultaneously facilitate an increase in model complexity and a decrease in computational expense for parameter estimation, we applied the local optimization algorithm *adaptive regular grid search*. This algorithm compares ABM simulations by evaluating the least squares error (LSE) regarding the experimental data of the whole-blood infection assay. Stochastic effects of the ABM were investigated by comparing simulation results for a fixed set of parameter values with varying number of *in silico* replicates. Using 100 *in silico* replicates as a reference for the mean value of the LSE, we generally observed for relevant parameter sets, i.e., parameter sets that yield reasonable agreement with the experimental data, that relative variations in the mean LSE were already well below 10% for 30 *in silico* replicates. Therefore, we set the number of *in silico* replicates to 30 throughout the whole parameter space.

The *adaptive regular grid search* algorithm searches the space of D_M and D_G on a pre-defined grid of diffusion coefficients, $0 < D_M, D_G < 800\,\mu\text{m}^2/\text{min}$. This range for the diffusion coefficients implies that the time step Δt_{ABM} varies between $5.2 \times 10^{-3}\,\text{min} \leq \Delta t_{\text{ABM}} \leq 4.2\,\text{min}$ (see Equation 6). As described in Section 2.3.2, we started with a relatively coarse grid of step size $100\,\mu\text{m}^2/\text{min}$ and computed at each grid point the LSE by comparing the experimental data with a small ABM system, i.e., representing $1/5\,\mu\text{l}$ of blood (see Supplementary Figure 3). These results were used to determine the regime of parameters in which the parameter estimation was continued for the large ABM system simulating $1\,\mu\text{l}$ of blood. The parameter regime was determined by the rectangle that contains all pairs of diffusion coefficients (D_G, D_M) for which the LSE values were found to be minimal from separately varying each parameter. The corner points of this rectangle were $(D_G, D_M) = (100, 0)\,\mu\text{m}^2/\text{min}$ and $(D_G, D_M) = (600, 800)\,\mu\text{m}^2/\text{min}$ (see gray region in Supplementary Figure 3). Subsequently, the grid was refined based on simulations of the large ABM by determining the path of minimal LSE values and adding grid points around this path by adaptive bisection. After simulation of the ABM for parameter sets corresponding to the added grid points, the procedure of grid refinement was repeated. This can be seen in **Figure 8**, where we plot a map of the LSE landscape together with the paths of minimal LSE values for each level of refinement. It was observed that the course of these paths covers a relatively broad range of diffusion coefficients for monocytes, D_M, whereas this is a fairly narrow range of D_G-values for PMN.

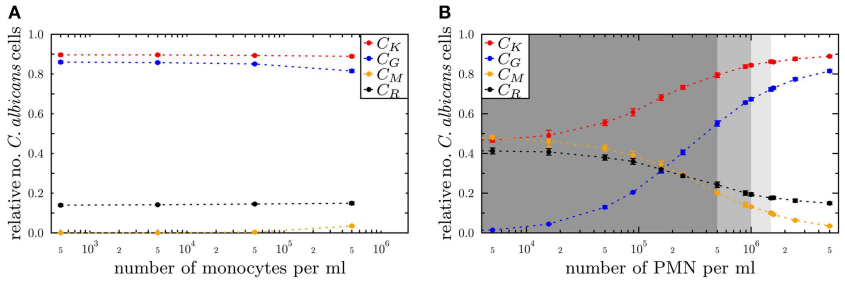

FIGURE 7 | Simulation results of the PI-SBM with different immune cell numbers at 4 h post-infection for the conditions (A) monocytopenia and (B) neutropenia. The relative numbers of *C. albicans* cells of killed cells (C_K), phagocytosed cells in monocytes (C_M) and in PMN (C_G) as well as cells that became resistant (C_R) against killing and/or phagocytosis are depicted for different numbers of monocytes and PMN. The number of **(A)** monocytes and **(B)** PMN in the simulations are reduced separately, starting from physiological concentrations of $5{\times}10^5$ /*ml* monocytes and $5{\times}10^6$ /ml PMN down to vanishing concentrations. In **(B)**, the light gray region represents the range of light neutropenia ($< 1.5 \times 10^6$ PMN per ml), medium gray region represents the range of moderate neutropenia ($< 1 \times 10^6$ PMN per ml) and dark gray region represents the range of severe neutropenia ($< 5 \times 10^5$ PMN per ml).

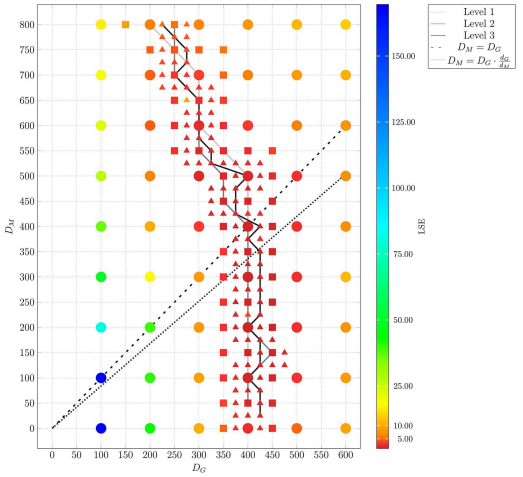

FIGURE 8 | Result of ABM parameter estimation by *adaptive regular grid search*. The diffusion coefficients for monocytes, D_M, and PMN, D_G, were scanned within the regime that was determined by parameter scanning for the small ABM (1/5 μl blood). At each grid point, 30 ABM simulations were performed for the large system (1 μl blood) and the mean least squares error (LSE) is depicted. By determining the path of minimal LSE values and adding grid points around this path by adaptive bisection, three refinement levels are considered. Dots represent grid points of the first refinement level, squares represent grid points of the second refinement level, and triangles represent grid points of the third refinement level. The paths of minimal LSE values for the first, second and third refinement level are traced by light gray, medium gray, and dark gray lines, respectively.

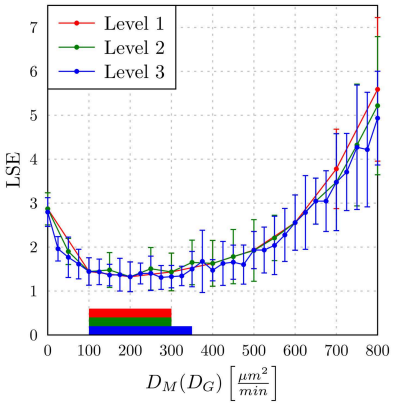

FIGURE 9 | The least squares error (LSE) of the paths of grid points along the diffusion coefficients for monocytes (D_M) as a function of the minimal diffusion coefficient for PMN (D_G): $D_M(D_G)$. Mean values and standard deviations were obtained from averaging over 30 ABM simulations. The paths of the first, second, and third refinement level are shown, respectively, as red, green, and blue lines (guide for the eyes). The horizontal bars indicate regions of diffusion coefficients with values comparable to the absolute LSE minimum of each refinement level. All values outside these regions are significantly different from the absolute LSE minimum (Wilcoxon rank sum test with $p < 0.05$).

In **Figure 9**, we present the LSE values as a function of $D_M(D_G)$ along the paths of minimal LSE values for the three levels of refinement. From the third level of refinement we inferred the point of absolute LSE minimum to be located at $(D_G^{min}, D_M^{min}) = (425, 275)\,\mu\text{m}^2/\text{min}$. However, since the landscape of $D_M(D_G)$ resembled an extended valley across neighboring data points, we performed a statistical analysis by applying the Wilcoxon rank sum test between the absolute LSE minimum and its neighboring points to check for significant differences between them. Imposing a p-value of $p < 0.05$ for significant difference, we obtained points with similar values of the LSE ranging in the interval $D_M = 100\,\mu\text{m}^2/\text{min}$ to $D_M = 350\,\mu\text{m}^2/\text{min}$ for monocytes and $D_G = 400\,\mu\text{m}^2/\text{min}$ to $D_G = 425\,\mu\text{m}^2/\text{min}$ for PMN (see **Figure 8**). These findings imply that the immune response in the whole-blood infection assay was much more sensitive to variations in the diffusion coefficients of PMN than of monocytes, emphasizing the dominant role of PMN over monocytes from the viewpoint of cell migration.

Our results are consistent with the absolute LSE minima of refinement level one and two, which were both at $(D_G^{min}, D_M^{min}) = (400, 200)\,\mu\text{m}^2/\text{min}$ and that also belong to this interval (see **Figure 9**). Interestingly, while we expected that monocytes are less migratory active than PMN, i.e., restricting the relevant parameter regime in **Figure 8** to the region below the dashed line, we also found that the interval around the absolute LSE minimum contains the parameter set $(D_G, D_M) = (425, 350)\,\mu\text{m}^2/\text{min}$. The ratio of these diffusion coefficients, $D_M/D_G \approx 0.82$, resembles the value expected from the Stokes-Einstein equation (Einstein, 1905) implying $D_M/D_G = d_G/d_M$ (dotted line in **Figure 8**). Taken together, we consider the diffusion coefficients $(D_G^{min}, D_M^{min}) = (425, 275)\,\mu\text{m}^2/\text{min}$ to represent the immune cell dynamics reasonably well and use these values in our further analyses below.

Next, we compared the ABM simulation results for the absolute LSE minimum with those of the PI-SBM. These are plotted together with the experimental data of the whole-blood infection assay in **Figure 6** and in Supplementary Figure 4 for the time evolution of *C. albicans* sub-populations. Thus, we found that both modeling approaches, the non-spatial SBM and the spatial ABM, yielded excellent agreement with the experimental data. Furthermore, we found that our simulation results obtained from the stochastic ABM were robust, which can be seen from the line thicknesses in **Figures 6C,D** representing the standard deviations obtained from 30 ABM simulations.

3.4. Predictions on Hyper- and Hypo-inflammation from ABM

To investigate the impact of hyper- and hypo-inflammation associated with the dynamics of immune cells, we varied the diffusion coefficients of monocytes and PMN separately around the absolute LSE minimum $(D_G^{min}, D_M^{min}) = (425, 275)\,\mu\text{m}^2/\text{min}$. Keeping the diffusion coefficient D_G fixed and varying the D_M for monocytes between $100\,\mu\text{m}^2/\text{min}$ and $600\,\mu\text{m}^2/\text{min}$, we

observed at 4 h post-infection no substantial changes in the populations of killed, resistant and phagocytosed *C. albicans* cells (see **Figure 10A**). At extreme values $D_M > D_G$, a slight increase (decrease) in the number of killed (resistant) *C. albicans* cells was observed accompanied by a slight increase in the phagocytosis by both monocytes and PMN. This may be attributed to a stronger mixing of the cell system for high diffusion coefficients D_M. In general, however, the immune response does not appear to be sensitive to this parameter, which is in agreement with the finding for monocytopenia that did not have a substantial impact on infection clearance (see **Figure 7A**).

In the opposite case, where D_M was fixed and D_G was varied between 100 $\mu m^2/min$ and 600 μm^2/min, it was again observed that for increased values $D_G > 425\,\mu$m^2/min the impact on the immune response against *C. albicans* is only weak. In contrast, for decreased values $D_G < 400\,\mu$m^2/min the immune response was strongly affected by the reduced migratory activity of PMN. This could be observed by a substantial increase (decrease) in the number of resistant (killed) *C. albicans* cells (see **Figure 10B**). In particular, for $D_G = 100\,\mu$m^2/min the phagocytosis of *C. albicans* cells by PMN was reduced by more than 20% and the relative number of resistant *C. albicans* cells reached the value of 28%. Comparing this scenario with the condition of PMN deficiency (see **Figure 7B**), we found that this PMN paralysis resembles moderate to severe neutropenia associated with a relative number of about 20% and 30% of resistant *C. albicans* cells, respectively.

4. Discussion

In this study, we applied a bottom-up modeling approach to simulate an experimental infection assay for *C. albicans* in human blood. As illustrated in **Figure 1**, this approach combines different mathematical models with increasing complexity that build on one another. We started from a previously developed state based model (SBM), here referred to as P-SBM (Hünniger et al., 2014), that neglects all spatial aspects and describes the time-evolution of pathogens in different states—e.g., alive, phagocytosed and killed—during the early response of the innate immune system. To include the immune response mediated by monocytes and granulocytes (PMN), in this work we modified the P-SBM into a SBM that does as well-explicitly account for the immune cell states and is therefore referred to as PI-SBM. The rates of state transitions in the PI-SBM were estimated by comparison with experimental data (Hünniger et al., 2014) using the global optimization method *simulated annealing* based on the Metropolis Monte Carlo scheme (SA-MMC).

The resulting model kinetics of both SBM were found to be in quantitative agreement with experimental data and confirmed that PMN play the major role in the immune defense against *C. albicans* in human blood. This is indicative for the general validity of both models, despite the structural difference of the simulation algorithms regarding the level of detail at which immune cells are modeled. Furthermore, the PI-SBM allows making predictions on infection scenarios in patients with immune cell deficiencies, i.e., neutropenia and monocytopenia. Performing *in silico* experiments with varying numbers of either monocytes or PMN, revealed that loss of monocytes was mainly compensated by PMN. In contrast, decreasing PMN number lead to a strongly reduced immune response against *C. albicans* for PMN numbers below 5×10^5 /ml (see **Figure 7**). Our quantitative prediction is substantiated by published data that account this PMN concentration as severe neutropenia (Munshi and Montgomery, 2000). It is also reported that neutropenia impairs the outcome of candidemia and is a risk factor, in particular, for cancer patients developing candidemia (Guiot et al., 1994; Bow et al., 1995; Lunel et al., 1999). From the quantitative agreement between predictions of the PI-SBM and reported findings for *C. albicans* infection, we attribute a high predictive potential to this virtual infection model that may be exploited in future studies, e.g., focusing on conditions of immune dysregulation and/or comparing the impact of different pathogens. The possibility to quantify functional alteration of immune cells rather than pure numerical aberrations is of particular interest in this regard.

In order to account for spatial aspects of the immune response, we extended the SBM to an agent-based model (ABM), where cells are simulated as agents that can migrate in continuous

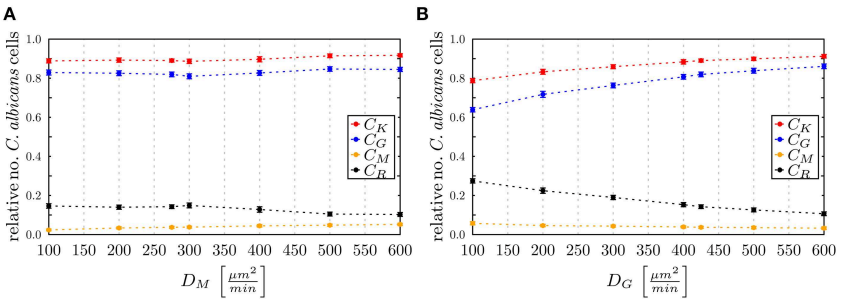

FIGURE 10 | Simulation results of the ABM at 4 h post-infection for varied diffusion coefficients around the absolute least squares error (LSE) minimum with (D_G^{min}, D_M^{min}) = (425, 275) μm^2/min for (A) monocytes keeping D_G fixed and (B) PMN keeping D_M fixed. The relative numbers of *C. ablicans* cells of killed cells (C_K), phagocytosed cells in monocytes (C_M) and in PMN (C_G) as well as cells that became resistant (C_R) against killing and/or phagocytosis are depicted.

three-dimensional space and can interact with each other on encounter in space. Applying the bottom-up modeling approach, we made use of the rates that were determined by fitting the PI-SBM to the experimental data and estimated the diffusion coefficients of immune cells in blood (see **Figure 1**). Due to high computational costs of ABM simulations, applying the global optimization method SA-MMC was no realistic option and we chose the computationally affordable local optimization method *adaptive regular grid search*. This method searches for the optimum within a pre-defined parameter space, which in the present case was a two-dimensional space spanned by the diffusion coefficients for monocytes and PMN. In contrast, applying SA-MMC was beneficial in the case of PI-SBM for three reasons: (i) the parameter space was eight-dimensional, (ii) limitations of the parameter space would have been difficult to motivate biologically, and (iii) computational costs for repeated simulations were still acceptable due to the neglect of spatial aspects.

As live cell imaging in whole-blood assays cannot yet be performed today, computer simulations are the only tool to predict diffusion coefficients of immune cells. Parameter estimation of the ABM predicted intervals for the diffusion coefficients that yielded quantitatively comparable results. For monocytes this interval, $D_M = 100\,\mu\text{m}^2/\text{min}$ to $D_M = 350\,\mu\text{m}^2/\text{min}$, was substantially broader than for PMN with $D_G = 400\,\mu\text{m}^2/\text{min}$ to $D_G = 425\,\mu\text{m}^2/\text{min}$, indicating the importance of fine-tuned PMN motility.

Furthermore, by varying the diffusion coefficients of the immune cells, we demonstrated the impact of hyper- and hypo-inflammation in immune dysregulation. In general, reducing (increasing) immune cell motilities around optimal values reduced (increased) the number of interaction events between cells and by that the phagocytosis of *C. albicans* cells. In the case of PMN, reduction of cell motility and phagocytosis events was additionally associated with a decrease in the release of antimicrobial peptides contributing to the decrease in killing of *C. albicans* cells. This in turn lead to an increase in the number of resistant *C. albicans* cells reaching levels that were well-beyond those observed for paralytic monocytes (see **Figure 10**). Comparing the hypo-inflammatory condition with PMN deficiency, we found that diffusion coefficients around $D_G = 100\,\mu\text{m}^2/\text{min}$ resembled the outcome of moderate to severe neutropenia.

The bottom-up modeling approach presented here may be extended in various ways. For example, the implementation of a hybrid ABM could be envisaged where molecular interactions, e.g., as mediated by antimicrobial peptides, are not simulated in a rule-based fashion but in an explicit way by a molecular diffusion solver. Other directions of future research include (i) focusing on conditions of immune dysregulation, (ii) comparing the impact of different pathogens, and (iii) including other types of innate immune cells. Furthermore, it is conceivable to combine modeling approaches with microscopy experiments of infection scenarios *in vitro* in an image-based systems biology approach (Mech et al., 2014; Figge and Murphy, 2015; Medyukhina et al., 2015). First steps into this direction have recently been made, e.g., by establishing algorithms for the automated image analysis of phagocytosis assays (Mech et al., 2011; Kraibooj et al., 2014) and for the automated tracking and classification of PMN from time-lapse microscopy (Mokhtari et al., 2013; Brandes et al., 2015) that was applied in the context of comparing *C. albicans* and *C. glabrata* infection (Duggan et al., 2015a). In the future, we expect that a systems medicine approach exploiting the predictive power of virtual infection models will play an important role in the context of infectious disease diagnosis.

Author Contributions

TL, ST, MTF: Conception and design of the investigation and work. MTF: Contribution of materials and computational resources. TL, ST, JP, MTF: Data processing, implementation and application of the computational algorithm. TL, ST, JP, KH, OK, MTF: Evaluation and analysis of the results. TL, ST, JP, KH, OK, MTF: Drafting the manuscript and revising it critically for important intellectual content and final approval of the version to be published. TL, ST, JP, KH, OK, MTF: Agreement to be accountable for all aspects of the work in ensuring that questions related to the accuracy or integrity of any part of the work are appropriately investigated and resolved.

Funding

This work was financially supported by the Deutsche Forschungsgemeinschaft (DFG) through the excellence graduate school Jena School for Microbial Communication (JSMC) and the CRC/TR124 FungiNet (project B4 to MTF and project C3 to OK).

Acknowledgment

We thank C. M. Svensson for valuable discussions on the statistical analysis of the agent-based model simulations.

Supplementary Material

The Supplementary Material for this article can be found online at: http://journal.frontiersin.org/article/10.3389/fmicb.2015.00608/abstract

References

Alangaden, G. J. (2011). Nosocomial fungal infections: epidemiology, infection control, and prevention. *Infect. Dis. Clin. North Am.* 25, 201–225. doi: 10.1016/j.idc.2010.11.003

Ashyraliyev, M., Fomekong-Nanfack, Y., Kaandorp, J. A., and Blom, J. G. (2009). Systems biology: parameter estimation for biochemical models. *FEBS J.* 276, 886–902. doi: 10.1111/j.1742-4658.2008.06844.x

Bittig, A. T., and Uhrmacher, A. M. (2010). "Spatial modeling in cell biology at multiple levels," in *Simulation Conference (WSC),*

Proceedings of the 2010 Winter, Number 2005 (Baltimore, MD: IEEE), 608–619.

Bow, E. J., Loewen, R., Cheang, M. S., and Schacter, B. (1995). Invasive fungal disease in adults undergoing remission-induction therapy for acute myeloid leukemia: the pathogenetic role of the antileukemic regimen. *Clin. Infect. Dis.* 21, 361–369.

Brandes, S., Mokhtari, Z., Essig, F., Hünniger, K., Kurzai, O., and Figge, M. T. (2015). Automated segmentation and tracking of non-rigid objects in time-lapse microscopy videos of polymorphonuclear neutrophils. *Med. Image Anal.* 20, 34–51. doi: 10.1016/j.media.2014.10.002

Cunha, C., Kurzai, O., Löffler, J., Aversa, F., Romani, L., and Carvalho, A. (2014). Neutrophil responses to aspergillosis: new roles for old players. *Mycopathologia* 178, 387–393. doi: 10.1007/s11046-014-9796-7

Dueck, G. (1993). New optimization heuristics. *J. Comput. Phys.* 104, 86–92.

Duggan, S., Essig, F., Hünniger, K., Mokhtari, Z., Bauer, L., Lehnert, T., et al. (2015a). Neutrophil activation by *Candida glabrata* but not *Candida albicans* promotes fungal uptake by monocytes. *Cell. Microbiol.* doi: 10.1111/cmi.12443. [Epub ahead of print].

Duggan, S., Leonhardt, I., Hünniger, K., and Kurzai, O. (2015b). Host response to *Candida albicans* bloodstream infection and sepsis. *Virulence*. doi: 10.4161/21505594.2014.988096. [Epub ahead of print].

Einstein, A. (1905). Über die von der molekularkinetischen theorie der Wärme geforderte Bewegung von in ruhenden Flüssigkeiten suspendierten Teilchen. *Ann. Phys.* 322, 549–560.

Fahraus, R., and Lindqvist, T. (1931). The viscosity of the blood in narrow capillary tubes. *Am. J. Physiol.* 96, 562–568.

Figge, M. T., and Murphy, R. (eds.). (2015). Image-based systems biology. *Cytometry A*. 87, 459–461. doi: 10.1002/cyto.a.22638

Figge, M. T. (2005). Stochastic discrete event simulation of germinal center reactions. *Phys. Rev. E* 71:051907. doi: 10.1103/PhysRevE.71.051907

Gonzalez, O. R., Kueper, C., Jung, K., Naval, P. C., and Mendoza, E. (2007). Parameter estimation using simulated annealing for S-system models of biochemical networks. *Bioinformatics* 23, 480–486. doi: 10.1093/bioinformatics/btl522

Guiot, H., Fibbe, W., and Van't Wout, J. (1994). Risk factors for fungal infection in patients with malignant hematologic disorders: implications for empirical therapy and prophylaxis. *Clin. Infect. Dis.* 18, 525–532.

Hünniger, K., Lehnert, T., Bieber, K., Martin, R., Figge, M. T., and Kurzai, O. (2014). A virtual infection model quantifies innate effector mechanisms and *Candida albicans* immune escape in human blood. *PLoS Comput. Biol.* 10:e1003479. doi: 10.1371/journal.pcbi.1003479

Hünniger, K., Bieber, K., Martin, R., Lehnert, T., Figge, M. T., Löffler, J., et al. (2015). A second stimulus required for enhanced antifungal activity of human neutrophils in blood is provided by Anaphylatoxin C5a. *J. Immunol.* 194, 1199–1210. doi: 10.4049/jimmunol.1401845

Hernandez-Vargas, E. A., Wilk, E., Canini, L., Toapanta, F. R., Binder, S. C., Uvarovskii, A., et al. (2014). The effects of aging on influenza virus infection dynamics. *J. Virol.* 88, 4123–4131. doi: 10.1128/JVI.03644-13

Horn, F., Heinekamp, T., Kniemeyer, O., Pollmächer, J., Valiante, V., and Brakhage, A. A. (2012). Systems biology of fungal infection. *Front. Microbiol.* 3:108. doi: 10.3389/fmicb.2012.00108

Kirkpatrick, S., Gelatt, C. D., and Vecchi, M. P. (1983). Optimization by simulated annealing. *Science* 220, 671–680.

Kraibooj, K., Park, H.-R., Dahse, H.-M., Skerka, C., Voigt, K., and Figge, M. T. (2014). Virulent strain of lichtheimia corymbifera shows increased phagocytosis by macrophages as revealed by automated microscopy image analysis. *Mycoses* 57, 56–66. doi: 10.1111/myc.12237

Lionakis, M. S. (2014). New insights into innate immune control of systemic candidiasis. *Med. Mycol.* 52, 555–564. doi: 10.1093/mmy/myu029

Lunel, F. M. V., Meis, J. F., and Voss, A. (1999). Nosocomial fungal infections: candidemia. *Diagn. Microbiol. Infect. Dis.* 34, 213–220.

Luo, S., Skerka, C., Kurzai, O., and Zipfel, P. F. (2013). Complement and innate immune evasion strategies of the human pathogenic fungus *Candida albicans*. *Mol. Immunol.* 56, 161–169. doi: 10.1016/j.molimm.2013.05.218

Mak, T. W., and Saunders, M. E. (2011). *Primer to the Immune Response: Academic Cell Update Edition*. Burlington; San Diego; London: Academic Press.

Margulies, L., and Schwartz, K. V. (1998). *Five Kingdoms - An Illustrated Guide to the Phyla of Life on Earth, 3rd Edn.* New York, NY: W. H. Freeman and Company.

McClatchey, K. D. (2003). Clinical laboratory medicine. *Clin. Chem.* 49, 344–345. doi: 10.1373/49.2.344

Mech, F., Thywißen, A., Guthke, R., Brakhage, A. A., and Figge, M. T. (2011). Automated image analysis of the host-pathogen interaction between phagocytes and *Aspergillus fumigatus*. *PLoS ONE* 6:e19591. doi: 10.1371/journal.pone.0019591

Mech, F., Wilson, D., Lehnert, T., Hube, B., and Thilo Figge, M. (2014). Epithelial invasion outcompetes hypha development during *Candida albicans* infection as revealed by an image-based systems biology approach. *Cytometry A* 85, 126–139. doi: 10.1002/cyto.a.22418

Medyukhina, A., Timme, S., Mokhtari, Z., and Figge, M. T. (2015). Image-based systems biology of infection. *Cytometry A* 87, 462–470. doi: 10.1002/cyto.a.22638

Mendling, W. (2006). *Vaginose, Vaginitis und Zervizitis*. Heidelberg: Springer Science & Business Media.

Metropolis, N., Rosenbluth, A. W., Rosenbluth, M. N., Teller, A. H., and Teller, E. (1953). Equation of state calculations by fast computing machines. *J. Chem. Phys.* 21, 1087.

Mokhtari, Z., Mech, F., Zitzmann, C., Hasenberg, M., Gunzer, M., and Figge, M. T. (2013). Automated characterization and parameter-free classification of cell tracks based on local migration behavior. *PLoS ONE* 8:e80808. doi: 10.1371/journal.pone.0080808

Moles, C. G., Mendes, P., and Banga, J. R. (2003). Parameter estimation in biochemical pathways: a comparison of global optimization methods. *Genome Res.* 13, 2467–2474. doi: 10.1101/gr.1262503

Munshi, H. G., and Montgomery, R. B. (2000). Evidence-based case review: severe neutropenia: a diagnostic approach. *West. J. Med.* 172, 248–252. doi: 10.1136/ewjm.172.4.248

Pollmächer, J., and Figge, M. T. (2014). Agent-based model of human alveoli predicts chemotactic signaling by epithelial cells during early *Aspergillus fumigatus* infection. *PLoS ONE* 9:e111630. doi: 10.1371/journal.pone.0111630

Powell, M. (1998). Direct search algorithms for optimization calculations. *Acta Numerica* 7, 287–336.

Rapaport, D. C. (1996). *The Art of Molecular Dynamics Simulation*. New York, NY: Cambridge University Press.

Rosenson, R., McCormick, A., and Uretz, E. (1996). Distribution of blood viscosity values and biochemical correlates in healthy adults. *Clin. Chem.* 42, 1189–1195.

Skvoretz, J. (2002). Complexity theory and models for social networks. *Complexity* 8, 47–55. doi: 10.1002/cplx.10062

Storn, R., and Price, K. (1997). Differential evolution – a simple and efficient heuristic for global optimization over continuous spaces. *J. Glob. Opt.* 11, 341–359.

Tokarski, C., Hummert, S., Mech, F., Figge, M. T., Germerodt, S., Schroeter, A., et al. (2012). Agent-based modeling approach of immune defense against spores of opportunistic human pathogenic fungi. *Front. Microbiol.* 3:129. doi: 10.3389/fmicb.2012.00129

Von Neumann, J. (1951). The general and logical theory of automata. *Cereb. Mech. Behav.* 1, 41.

Conflict of Interest Statement: The authors declare that the research was conducted in the absence of any commercial or financial relationships that could be construed as a potential conflict of interest.

Frontiers

Supplementary Material
9 June 2015

Supplementary Material: Bottom-up modeling approach for the quantitative estimation of parameters in pathogen-host interactions

Teresa Lehnert [1,2,+], **Sandra Timme** [1,2+], **Johannes Pollmächer** [1,2], **Kerstin Hünniger** [3], **Oliver Kurzai** [3,2] **and Marc Thilo Figge** [1,2*]

[1] *Applied Systems Biology, Leibniz Institute for Natural Product Research and Infection Biology Hans-Knöll-Institute (HKI), Jena, Germany*
[2] *Faculty of Biology and Pharmacy, Friedrich Schiller University Jena, Jena, Germany*
[3] *Fungal Septomics, Septomics Research Center, Friedrich Schiller University and Leibniz Institute for Natural Product Research and Infection Biology Hans-Knöll-Institute (HKI), Jena, Germany*
[+] *Authors contributed equally*

Correspondence*:
Marc Thilo Figge
Applied Systems Biology, Leibniz Institute for Natural Product Research and Infection Biology - Hans Knöll Institute (HKI), Adolf-Reichwein-Straße 23, Jena, 07745, Germany, thilo.figge@hki-jena.de

1 SUPPLEMENTARY DATA

Supplementary Video 1. Typical time evolution of the virtual infection scenario in the spatial ABM. The three-dimensional environment corresponds to $1\,\mu l$ of blood containing 500 monocytes, 5000 PMN and 1000 *C. albicans* cells. The cells are represented as spherical agents that migrate depending on their respective diffusion coefficients and interact depending on rules as depicted in Figure 3 (B). *C. albicans* cells occur in the four states (i) alive and non-resistant (green), (ii) dead and non-resistant (red), (iii) alive and resistant (yellow) and (iv) dead and resistant (gray). Furthermore, granulocytes (polymorphonuclear neutrophils, PMN) and monocytes are shown in blue and orange, respectively. The video comprises the immune response during four hours post infection. In the beginning of the video, most *C. albicans* cells are non-phagocytosed and are frequently found to be alive and non-resistant (green). Towards the end of the video, non-phagocytosed *C. albicans* cells are mostly resistant (*i.e.*, yellow and gray) while most of *C. albicans* cells have been phagocytosed.

2 SUPPLEMENTARY INFORMATION

2.1 ANNEALING FUNCTION τ

The function $\tau(f)$ determines the acceptance of worse parameters during the applied fitting procedure Metropolis Monte Carlo based on Simulated Annealing. This function of fitting steps f is defined in form of the Hill equation, *i.e.*

$$\tau(f) = \tau_0 + \frac{f^n}{(P^n + f^n)} (\tau_\infty - \tau_0) , \tag{1}$$

that ranges between τ_0 and τ_∞ (see Supplementary Table 1 for applied values) and is characterized by the coefficient $n = 3$ describing the slope of the function as well as the point of inflection $P = 0.5\, f_{total}$ (with f_{total} the total number of fitting steps). We determined the value for n and P by manual adjustment.

3 SUPPLEMENTARY TABLES AND FIGURES

Supplementary Table 1. Score values ϵ_c for combined units c.

combined unit c	score value ϵ_c
C_A	45
C_K	20
C_E	70
C_M	200
C_G	30

Manually adjusted score values ϵ_c of the combined units c that are used for comparison with experimental data from whole-blood infection assay. All states of the PI-SBM that represent alive (killed) *C. albicans* cells are summarized to the combined unit C_A (C_K). States of *C. albicans* cells in extracellular space, in monocytes or in PMN are represented by the combined units C_E, C_M or C_G, respectively.

Supplementary Table 2. Individual start conditions of the fitting algorithm.

$C_{AE}(0)$	$M_{0,0}(0)$	$G_{0,0}(0)$	number of runs	number of fitting steps	τ
100	50	500	100	3 000	[0.05,5.0]
1 000	500	5 000	50	1 000	[5.0;30.0]
10 000	5 000	50 000	20	250	[5.0;80.0]
100 000	50 000	500 000	10	50	[50.0;80.0]

Start conditions for the parameter fitting algorithm. The number of individuals of alive *C. albicans* cells in extracellular space ($C_{AE}(0)$), monocytes ($M_{0,0}(0)$) and PMN ($G_{0,0}(0)$) at time $t = 0$ min was stepwise increased by keeping their ratio constant. For each step, the number of runs with corresponding number of fitting steps per run and the range of τ was adjusted.

Supplementary Table 3. Transition rates for PI-SBM.

	rate $[min^{-1}]$	standard deviation $[min^{-1}]$	standard deviation $[\%]$
ϕ_G	$2.83 \cdot 10^{-2}$	$0.49 \cdot 10^{-3}$	1.7
ϕ_{G*}	$4.75 \cdot 10^{-2}$	$3.86 \cdot 10^{-3}$	8.13
ϕ_M	$1.25 \cdot 10^{-2}$	$0.74 \cdot 10^{-3}$	5.9
κ_M	$3.59 \cdot 10^{-2}$	$3.74 \cdot 10^{-3}$	10.4
κ_G	$4.69 \cdot 10^{-2}$	$4.25 \cdot 10^{-3}$	9.1
ρ	$0.45 \cdot 10^{-2}$	$0.19 \cdot 10^{-3}$	4.2
γ	$1.93 \cdot 10^{-2}$	$2.76 \cdot 10^{-3}$	14.3
$\bar{\kappa}_{EK}$	$26.07 \cdot 10^{-2}$	$22.65 \cdot 10^{-3}$	8.7

The transition rates of the P-SBM are given by the phagocytosis rate ϕ_G of PMN that phagocytose for their first time, the phagocytosis rate $\phi_{G^\star}$ of PMN that phagocytose for at least the second time, the phagocytosis rate ϕ_M of monocytes, the intracellular killing rate κ_M of monocytes, the intracellular killing rate κ_G of PMN, the resistance rate ρ and the rates that determine the extracellular killing κ_{EK} and γ.

Supplementary Table 4. Transition rates for P-SBM.

	rate $[min^{-1}]$	standard deviation $[min^{-1}]$	standard deviation $[\%]$
ϕ_G	$2.69 \cdot 10^{-2}$	$0.33 \cdot 10^{-3}$	1.24
$\phi_{G^\star}$	$3.58 \cdot 10^{-2}$	$1.88 \cdot 10^{-3}$	5.24
ϕ_M	$0.63 \cdot 10^{-2}$	$0.33 \cdot 10^{-3}$	5.25
κ_M	$6.08 \cdot 10^{-2}$	$4.04 \cdot 10^{-3}$	6.64
κ_G	$4.26 \cdot 10^{-2}$	$2.03 \cdot 10^{-3}$	4.76
ρ	$0.41 \cdot 10^{-2}$	$0.13 \cdot 10^{-3}$	3.25
γ	$3.16 \cdot 10^{-2}$	$2.15 \cdot 10^{-3}$	6.8
$\bar{\kappa_{EK}}$	$29.13 \cdot 10^{-2}$	$14.35 \cdot 10^{-3}$	4.93

The transition rates of the PI-SBM are given by the phagocytosis rate ϕ_G of PMN that phagocytose for their first time, the phagocytosis rate $\phi_{G^\star}$ of PMN that phagocytose for at least the second time, the phagocytosis rate ϕ_M of monocytes, the intracellular killing rate κ_M of monocytes, the intracellular killing rate κ_G of PMN, the resistance rate ρ and the rates that determine the extracellular killing κ_{EK} and γ.

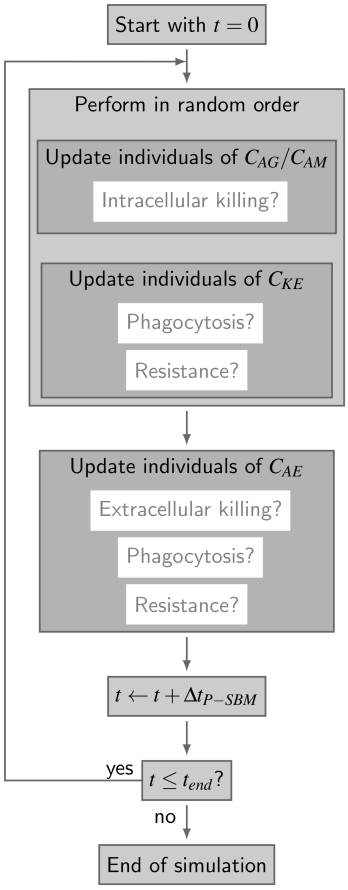

Supplementary Figure 1. Flow-chart of the non-spatial P-SBM simulation algorithm. In each time-step Δt_{P-SBM}, all individuals of *C. albicans* cell states are tested for possible state transitions. Individuals of alive *C. albicans* cells in monocytes (C_{AM}) or PMN (C_{AG}) are tested for intracellular killing. Individuals of the state killed-and-extracellular *C. albicans* cells (C_{KE}) are tested for phagocytosis and for becoming resistant. The individuals of the state alive-and-extracellular *C. albicans* cells (C_{AE}) are tested for phagocytosis, for extracellular killing and for becoming resistant.

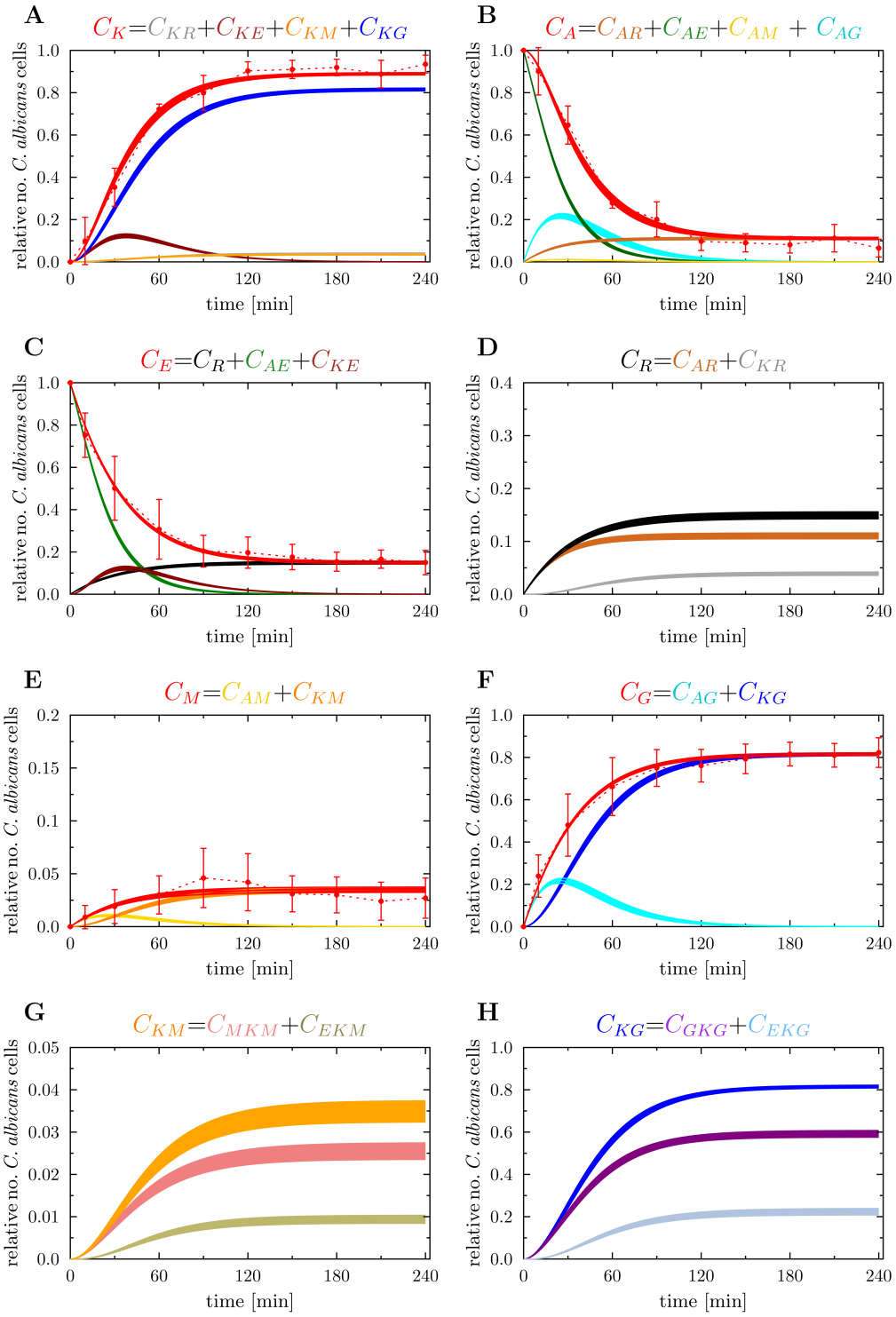
A
C_K=C_{KR}+C_{KE}+C_{KM}+C_{KG}
B
C_A=C_{AR}+C_{AE}+C_{AM} + C_{AG}
C
C_E=C_R+C_{AE}+C_{KE}
D
C_R=C_{AR}+C_{KR}
E
C_M=C_{AM}+C_{KM}
F
C_G=C_{AG}+C_{KG}
G
C_{KM}=C_{MKM}+C_{EKM}
H
C_{KG}=C_{GKG}+C_{EKG}
relative no. *C. albicans* cells
time [min]

Supplementary Figure 2. Kinetics of PI-SBM simulations (red solid lines) for the minimal least squares error (LSE) relative to the experimental data from whole-blood infection assays (red dotted lines as guide for the eye). The error bars correspond to the standard deviations of five independent experiments. The thickness of the solid lines represents the standard deviation of the simulation results as obtained from 50 simulations for normally distributed transition rates as given in Supplementary Table 2. Colored symbols refer to different *C. albicans* states, where their time courses are indicated by continuous lines with the same color. (A) Time-dependent relative number of killed *C. albicans* cells (C_K) that were experimentally measured by survival plates. The experimental results were compared with the combination of simulated data representing all killed *C. albicans* of the model, *i.e.* extracellularly killed *C. albicans* (C_{KE}), killed resistant *C. albicans* (C_{KR}), killed *C. albicans* that are in monocytes (C_{KM}) or PMN (C_{KG}). (B) Alive *C. albicans* (C_A) that were measured by survival plates and simulated by the combination of alive *C. albicans* that are in extracellular space (C_{AE}), in monocytes (C_{AM}), in PMN (C_{AG}) or became resistant against phagocytosis (C_{AR}). (C) Time course of *C. albicans* cells that are in extracellular space of blood (C_E). Experimental data was obtained by FACS analysis and simulated data is represented by the combination of *C. albicans* cells that are extracellular alive (C_{AE}), extracellularly killed (C_{KE}) and resistant against phagocytosis (C_R). (D) The simulated resistant *C. albicans* (C_R) are the sum of alive and dead resistant *C. albicans* cells at each time point of the simulation time. (E) Time course of *C. albicans* cells that were phagocytosed by monocytes (C_M). This is defined as sum of alive and killed *C. albicans* cells in monocytes, *i.e.* C_{AM} and C_{KM}, respectively. The corresponding experimental data was obtained by FACS analysis. (F) Relative number of *C. albicans* cells in PMN (C_G) during the whole-blood infection, where internalized *C. albicans* cells can be alive (C_{AG}) or dead (C_{KG}). (G) Simulation result of killed *C. albicans* cells within monocytes (C_{KM}), that is defined as the sum of internalized *C. albicans* that were intracellularly killed(C_{MKM}) and those who were extracellularly killed (C_{EKM}). (H) Simulated time course of killed *C. albicans* cells in PMN (C_{KG}), that is composed of intracellularly killed *C. albicans* cells (C_{GKG}) and extracellularly killed *C. albicans* cells (C_{EKG}) in PMN.

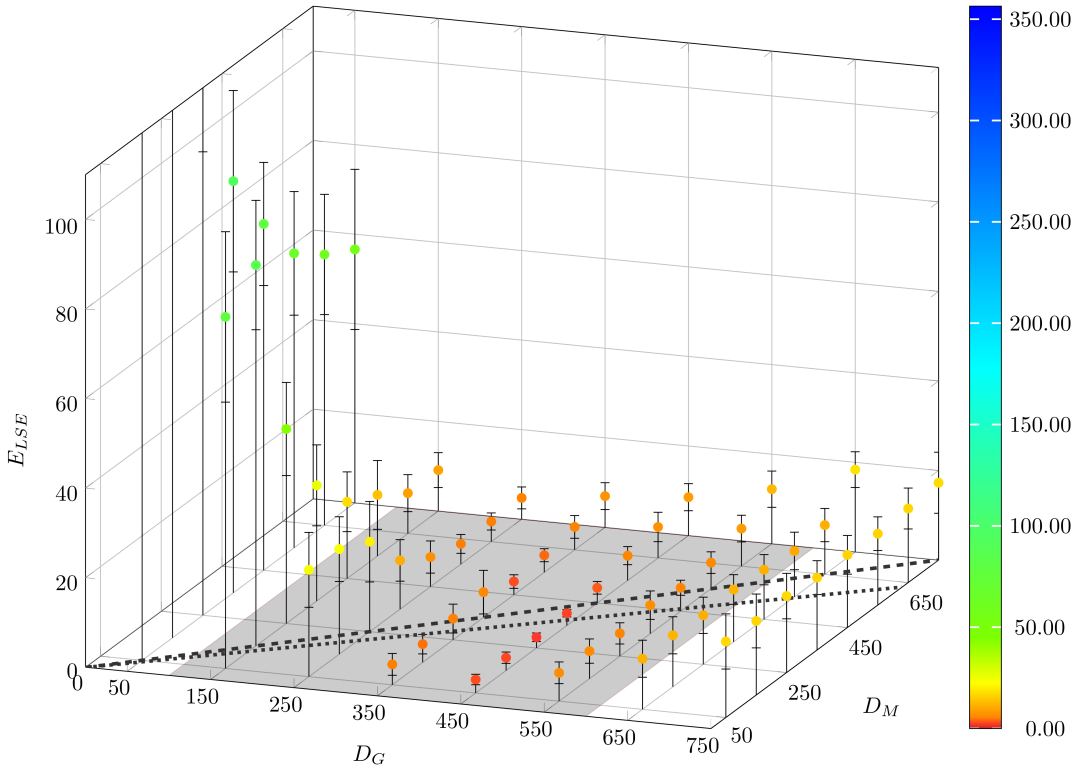

Supplementary Figure 3. Result of ABM parameter estimation by *adaptive regular grid search* applied to the small ABM representing $1/5\,\mu l$ blood. The space of diffusion coefficients of monocytes (D_M) and PMN (D_G) was scanned at the grid points in the pre-defined area. At each grid point the mean value of the least squares error (LSE) and the standard deviation over 30 simulations are shown. The gray region represents the rectangle that contains all pairs of diffusion coefficients for which the LSE values were found to be minimal from separately varying each diffusion coefficient. The dashed line corresponds to $D_M = D_G$ and the dotted line corresponds to diffusion coefficients that follow the Stokes-Einstein equation for monocytes and PMN, *i.e.* $D_G/D_M = d_M/d_G$ with monocyte diameter $d_M = 16\,\mu m$ and PMN diameter $d_G = 13.5\,\mu m$.

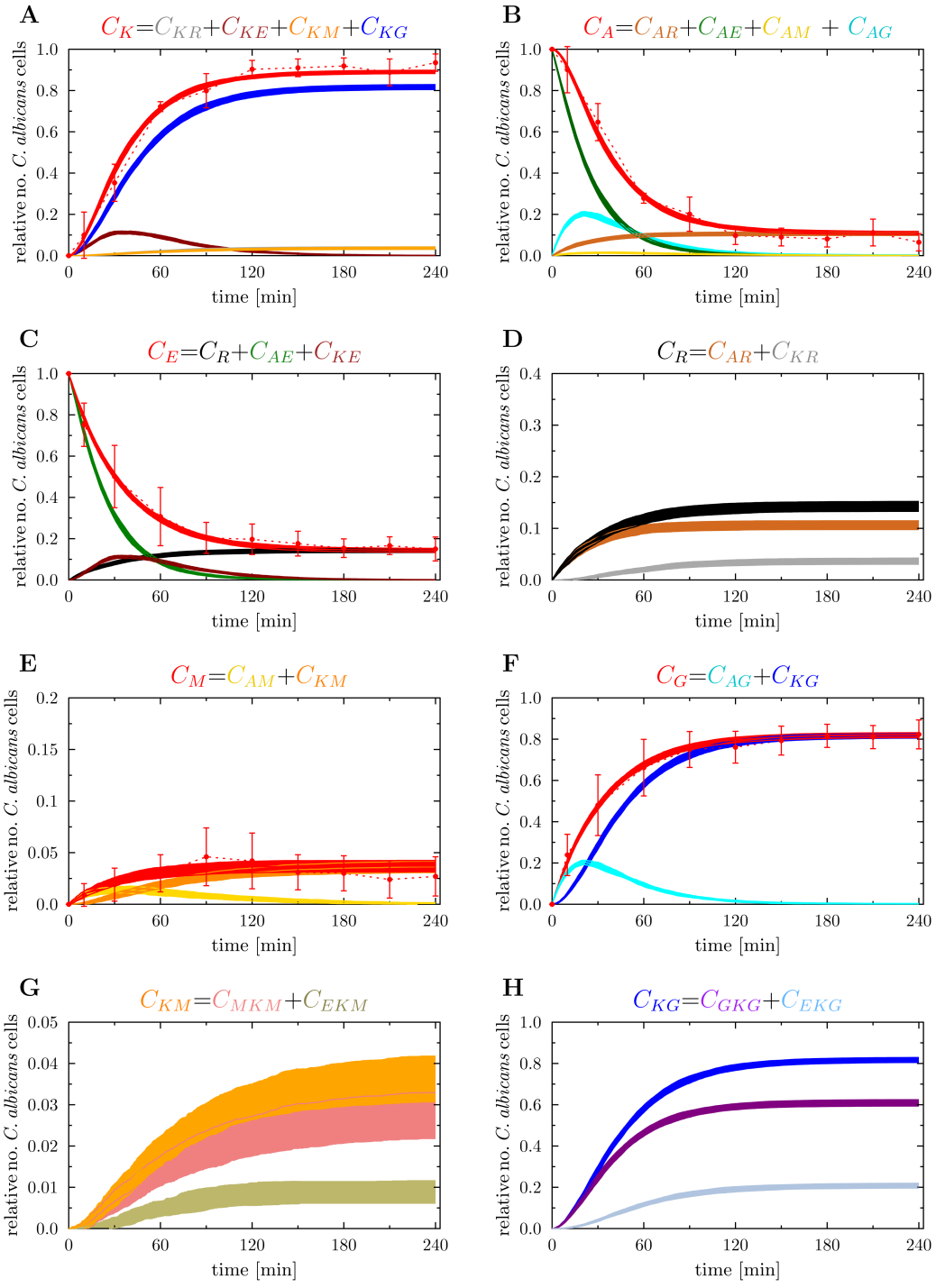
A
C_K=C_{KR}+C_{KE}+C_{KM}+C_{KG}
B
C_A=C_{AR}+C_{AE}+C_{AM} + C_{AG}
C
C_E=C_R+C_{AE}+C_{KE}
D
C_R=C_{AR}+C_{KR}
E
C_M=C_{AM}+C_{KM}
F
C_G=C_{AG}+C_{KG}
G
C_{KM}=C_{MKM}+C_{EKM}
H
C_{KG}=C_{GKG}+C_{EKG}
relative no. *C. albicans* cells
time [min]

Supplementary Figure 4. Kinetics of ABM simulations with $(D_G^{min}, D_M^{min}) = (425, 275)\,\mu m^2/min$ (red solid lines) for the minimal least squares error (LSE) relative to the experimental data from whole-blood infection assays (red dotted lines as guide for the eye). The error bars correspond to the standard deviations of five independent experiments. The thickness of the solid lines represents the standard deviation of the simulation results as obtained from 30 simulations. Colored symbols refer to different *C. albicans* states, where their time courses are indicated by continuous lines with the same color. (A) Time-dependent relative number of killed *C. albicans* cells (C_K) that were experimentally measured by survival plates. The experimental results were compared with the combination of simulated data representing all killed *C. albicans* of the model, *i.e.* extracellularly killed *C. albicans* (C_{KE}), killed resistant *C. albicans* (C_{KR}), killed *C. albicans* that are in monocytes (C_{KM}) or PMN (C_{KG}). (B) Alive *C. albicans* (C_A) that were measured by survival plates and simulated by the combination of alive *C. albicans* that are in extracellular space (C_{AE}), in monocytes (C_{AM}), in PMN (C_{AG}) or became resistant against phagocytosis (C_{AR}). (C) Time course of *C. albicans* cells that are in extracellular space of blood (C_E). Experimental data was obtained by FACS analysis and simulated data is represented by the combination of *C. albicans* cells that are extracellular alive (C_{AE}), extracellularly killed (C_{KE}) and resistant against phagocytosis (C_R). (D) The simulated resistant *C. albicans* (C_R) are the sum of alive and dead resistant *C. albicans* cells at each time point of the simulation time. (E) Time course of *C. albicans* cells that were phagocytosed by monocytes (C_M). This is defined as sum of alive and killed *C. albicans* cells in monocytes, *i.e.* C_{AM} and C_{KM}, respectively. The corresponding experimental data was obtained by FACS analysis. (F) Relative number of *C. albicans* cells in PMN (C_G) during the whole-blood infection, where internalized *C. albicans* cells can be alive (C_{AG}) or dead (C_{KG}). (G) Simulation result of killed *C. albicans* cells within monocytes (C_{KM}), that is defined as the sum of internalized *C. albicans* that were intracellularly killed(C_{MKM}) and those who were extracellularly killed (C_{EKM}). (H) Simulated time course of killed *C. albicans* cells in PMN (C_{KG}), that is composed of intracellularly killed *C. albicans* cells (C_{GKG}) and extracellularly killed *C. albicans* cells (C_{EKG}) in PMN.

6. Deciphering the Counterplay of *Aspergillus fumigatus* Infection and Host Inflammation by Evolutionary Games on Graphs

www.nature.com/scientificreports

SCIENTIFIC REPORTS

OPEN

Deciphering the Counterplay of *Aspergillus fumigatus* Infection and Host Inflammation by Evolutionary Games on Graphs

Received: 16 March 2016
Accepted: 20 May 2016
Published: 13 June 2016

Johannes Pollmächer[1,2], Sandra Timme[1,2], Stefan Schuster[3], Axel A. Brakhage[2,4], Peter F. Zipfel[2,5] & Marc Thilo Figge[1,2]

www.nature.com/scientificreports

SCIENTIFIC REPORTS

OPEN

Deciphering the Counterplay of *Aspergillus fumigatus* Infection and Host Inflammation by Evolutionary Games on Graphs

Received: 16 March 2016
Accepted: 20 May 2016
Published: 13 June 2016

Johannes Pollmächer[1,2], Sandra Timme[1,2], Stefan Schuster[3], Axel A. Brakhage[2,4], Peter F. Zipfel[2,5] & Marc Thilo Figge[1,2]

Microbial invaders are ubiquitously present and pose the constant risk of infections that are opposed by various defence mechanisms of the human immune system. A tight regulation of the immune response ensures clearance of microbial invaders and concomitantly limits host damage that is crucial for host viability. To investigate the counterplay of infection and inflammation, we simulated the invasion of the human-pathogenic fungus *Aspergillus fumigatus* in lung alveoli by *evolutionary games on graphs*. The layered structure of the innate immune system is represented by a sequence of games in the virtual model. We show that the inflammatory cascade of the immune response is essential for microbial clearance and that the inflammation level correlates with the infection-dose. At low infection-doses, corresponding to daily inhalation of conidia, the resident alveolar macrophages may be sufficient to clear infections, however, at higher infection-doses their primary task shifts towards recruitment of neutrophils to infection sites.

The great efficiency of the human immune system with regard to the recognition and elimination of infectious microbes is due to its layered and redundant structure and its well-orchestrated response across elevating levels. For example, the complex immune system is divided into the two main interacting levels of innate and adaptive immunity. Many infectious microbes are cleared already by the innate immune response that is immediately active but only grossly specific[1]. However, if the infectious microbe cannot be cleared in this way, inflammatory signals elevate the response from the level of innate immunity to the level of adaptive immunity. Activation of an adaptive response, *e.g.* involving affinity maturation of antibodies by B-cells in germinal centres, takes days to weeks, however, at the benefit of being highly specific for the invader[2].

The layered structure of the immune system is also recognised within the levels of innate and adaptive immunity itself. For example, adaptive immunity does not necessarily require to mount the tedious process of antibody affinity maturation, if the infectious microbe was encountered before and can be defeated by the activation of previously generated memory cells that directly go into production of the highly specific antibodies[2]. Similarly, innate immunity comprises the immediate response of humoral immunity, like the complement system, that may eliminate the infectious microbes by opsonisation associated with inflammatory signalling to recruit and activate phagocytic cells within a few hours and/or the formation of membrane attack complexes[3]. Furthermore, one can distinguish phagocytic cells that are resident in organs from those that are recruited in support from the blood-stream to the site of infection within tens of hours[1].

Apart from the fact that the layered structure of the immune system is beneficial for the strength and efficiency of the response, it is obvious that an elevating regulation between infection and inflammation is beneficial in being protective for the host itself. The danger for the human host due to dysregulation of the immune response

[1]Research Group Applied Systems Biology, Leibniz Institute for Natural Product Research and Infection Biology – Hans Knöll Institute, Jena, Germany. [2]Faculty of Biology and Pharmacy, Friedrich Schiller University Jena, Germany. [3]Department of Bioinformatics, Faculty of Biology and Pharmacy, Friedrich Schiller University Jena, Germany. [4]Department of Molecular and Applied Microbiology, Leibniz Institute for Natural Product Research and Infection Biology – Hans Knöll Institute, Jena, Germany. [5]Department of Infection Biology, Leibniz Institute for Natural Product Research and Infection Biology – Hans Knöll Institute, Jena, Germany. Correspondence and requests for materials should be addressed to M.T.F. (email: thilo.figge@leibniz-hki.de)

becomes impressively evident in the case of sepsis, *i.e.* a whole-body inflammatory response to an infection that may induce multi organ failure[4]. Thus, as important as it is that the human host responds with inflammation against infection, it is mandatory for the protection of the host against its own immune system to avoid unnecessary overshoots and to ensure a proper shut down of the response after infection clearance[5]. In what follows, we refer to the pathogen-induced infection and the host-driven inflammation, which are opposing actions from positions of defence, as *counterplay*.

Virtual infection-inflammation models can be constructed by different modelling techniques like for example by *ordinary differential equation models* (ODE), *state-based models* (SBM), *agent-based models* (ABM) and game theory. The purpose of a theoretical study and the complexity of a biological system determine how suitable a certain approach is.

ODE allow for straightforward modelling and have previously been applied in the context of bacterial infections[6–9] as well as for *A. fumigatus* infection[10]. However, ODE assume spatially homogeneous environments, where the constituents occur in high concentrations, making them inappropriate for a realistic simulation of the infection-inflammation scenarios of *A. fumigatus* conidia in the lung. SBM and ABM allow for the stochastic simulation of biological systems at the level of single events[11,12]. While SBM neglect spatial resolution, ABM simulate single individuals within a real spatial structure that may be represented on a grid or in continuous space. For example, a virtual infection-inflammation model of the human-pathogenic fungus *Candida albicans* in human blood was recently formulated in terms of a bottom-up modelling approach using SBM and ABM for quantitative parameter estimation[13,14]. Another ABM was developed for investigation of spatio-temporal dynamics of *A. fumigatus* infection of *in vitro* experiments[15] and in a virtual human alveolus with regard to inflammation-induced chemotaxis of AM[16]. The latter model was extended to a hybrid ABM that enabled investigation of molecular diffusion using *partial differential equations* to decipher quantitative properties of candidate chemokines[17].

The aforementioned modelling techniques simulate the time course of an underlying biological system by means of mechanistic processes. As a consequence, the dimensions of the parameter space are rapidly increasing and, since many of these parameters are unknown to date, a rigorous parameter estimation may render these approaches infeasible[14]. Therefore, to investigate the innate immune response against *A. fumigatus* in the human lung at the humoral and cellular level, we here pursue a game-theoretical approach that resolves the counterplay of infection and inflammation at the different levels.

Game theory is a mathematical concept of optimisation and the main advantage of this approach is that different effector mechanisms can be elegantly condensed into a reduced number of combined parameters. This renders computational simulations tractable and still allows for the identification of the key parameters that deserve particular attention in future experimental investigations. *Classical game theory* (CGT) was originally developed as decision support[18] in interactive situation in which the aims, goals and preferences of individual actors, *i.e.* the players of a game, are in conflict with each other[19]. The decisions available to the players correspond to strategies from which they can choose. Based on its own strategy and the strategies of the other players with which interactions are carried out players receive a benefit – also termed *payoff*[20]. However, each player in CGT was assumed to act perfectly rationally, to have the complete set of information about all possible outcomes of the game and their related payoffs as well as the cognitive capabilities to deduce from this information the optimal strategy[19]. To represent phenomena observed in interactions between living organisms, the paradigm of CGT turned out to be too restrictive.

The restrictions were softened by the concept of *evolutionary game theory* (EGT)[21]. This concept allowed for more flexibility and – inspired by evolution theory – implemented irrational behaviour, *e.g.* in terms of mutation. Thus, players do not simply optimise their payoff with regard to their strategic alternatives; rather, they replicate, survive or die based on the fitness associated with their respective strategy[22]. As a consequence, the dynamics of strategies involves a series of iterative evolutionary steps, a feature completely missing in CGT[19]. Moreover, the field of *evolutionary games on graphs* emerged, where not all players interact with each other, but the number of interactions is reduced to the ones that can be reasoned for by neighbourship relations between individuals, *e.g.* based on spatial proximity, social connections or genetic relationships[19]. There have been several contributions to the field of fungal infections using game-theoretic approaches in the recent past[23]: Hummert *et al.* investigated the cooperative behaviour between *Candida albicans* cells that were phagocytosed by macrophages[24]. In another study on *C. albicans* infection, the dynamics of the yeast-to-hyphal transition in response to various actions of the host was investigated by EGT[25]. It was found that the host requires a differentiated response to the distinct morphological states of *C. albicans* in order to keep the fungus in the least pathogenic state. Other examples, going beyond the context of fungal infections, have been reviewed by Hummert *et al.* regarding cellular interactions[20] and by Bohl *et al.* regarding molecular interactions[26].

In this study, we theoretically investigate the counterplay of infection and inflammation during the innate immune response against invading microbes by applying EGT. The main advantages of this stochastic modelling approach are that (i) systems with a small number of constituents are adequately captured, (ii) model parameters are reduced by a relative representation of processes, and (iii) spatial system resolution can be realized on a graph. While such a modelling approach is generally applicable to infection-inflammation scenarios caused by any kind of infectious microbe, for illustrative purposes we here focus on the concrete example of the saprophytic human-pathogenic fungus *Aspergillus fumigatus*[27]. This fungus represents a prime example, because humans inhale several thousands of its ubiquitously present airborne conidia every day[28]. Thus, while this fungus constitutes a common challenge to the human host, its potential threat can obviously be permanently managed under physiological immune conditions. This implies that an innate immune response against this infectious agent is generally sufficient, involving moderate inflammatory conditions that are usually mounted unnoticed in immunocompetent individuals. However, the situation is different for immunocompromised individuals and/or when high fungal doses are inhaled, in which case the pathogen can become a major cause of life-threatening

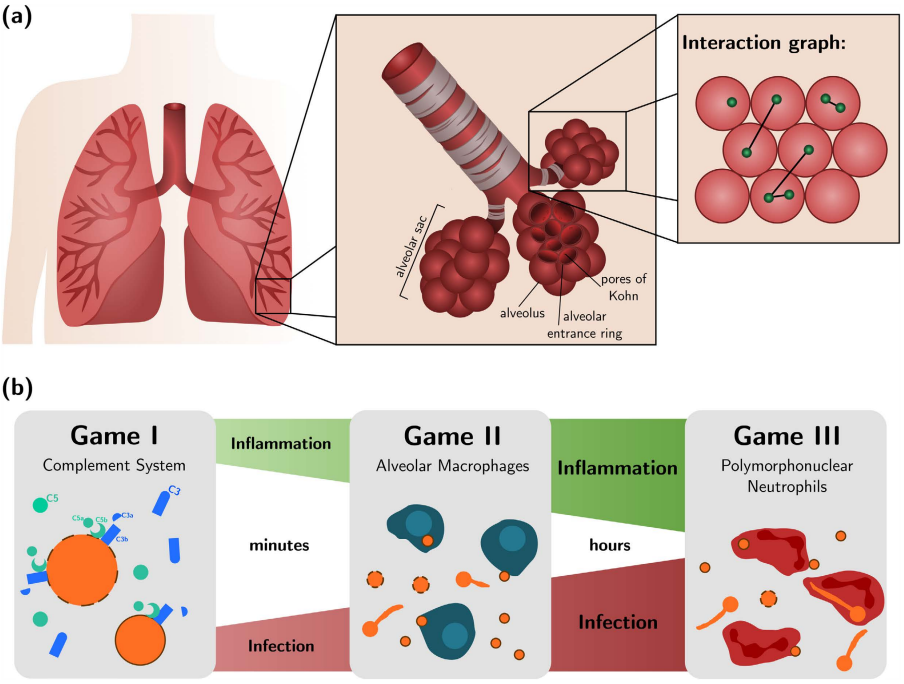

Figure 1. Lung architecture and design of evolutionary games. (**a**) Organisation of densely packed alveoli in alveolar sacs in the lower respiratory tract of the lung. An example distribution of eight fungal cells (shown in *green*) over a cross-sectioned alveolar sac and their proximity-based interactions (*black* connections). (**b**) Model design of the consecutive sequence of evolutionary games on graphs for the innate immune response against *A. fumigatus* infection in the lung.

infections[29]. The immune system of immunocompromised individuals may not be able to clear the lung from *A. fumigatus* conidia in due time, before the onset of conidial germination that may be followed by invasive growth[30]. Inhaled conidia typically are in a resting state, covered by a rodlet layer that renders them immunologically inert[31]. However, taking advantage of nutrient-rich conditions in the lung alveoli, resting conidia may swell and germinate, ultimately leading to the formation of hyphae and the ability of the fungus to penetrate tissue and eventually enter the bloodstream, disseminating through the whole body. As a consequence, invasive pulmonary aspergillosis is associated with high mortality rates ranging from 30–90%[32].

On invading the human organism, fungal cells are partly intercepted by mucosal epithelial cells, however, due to their small size of about 2–3 μm, significant amounts of the conidia can enter the lower respiratory tract of the lung (see Fig. 1(a)). They end up in so-called *alveolar sacs* (AS)[33] that consist of alveoli, which are the smallest units of the human lung[27]. Alveoli exist in various polyhedral shapes with a surface to volume ratio that optimises the gas exchange through their thin epithelial layers[34]. Once conidia enter the alveoli, they are embedded within the nutrient-rich and highly viscous alveolar lining layer, also called pulmonary surfactant, where they are faced with several defence mechanisms of the host[27,35]. During the innate immune response different sequential phases can be involved. Depending on how successful the pathogen can be cleared from the human host in one phase, the next phase, which is associated with a higher level of inflammation, may be initiated. As depicted in Fig. 1(b), the innate immune response against *A. fumigatus* conidia comprises humoral factors, like the complement system that is subject of Game I, and phagocytic cells, such as *alveolar macrophages* (AM) and *polymorphonuclear neutrophils* (PMN) being subjects of Game II and III, respectively.

As soon as conidia get into contact with the surfactant, complement is activated and proteins start to opsonise their surfaces, with amounts of bound complement proteins being proportional to the surface area of the fungal cell[36]. Opsonisation by complement proteins induces inflammation at the site of infection and the release of chemoattractants, *e.g.* C3a and C5a[3]. In addition to that, opsonisation of the fungal surface increases phagocytosis and the production of reactive oxygen intermediates (ROI) by AM and PMN enhancing phagocyte activation on direct physical contact with the pathogen[30]. Taken together, while the complement system drives the innate immune response against *A. fumigatus* by inflammatory signals, the formation of terminal membrane attack complexes are expected to be prohibited by the thickness of the cell wall[37].

Upon contact of *A. fumigatus* conidia with type II *alveolar epithelial cells* (AEC), these cells secrete inflammatory molecules, such as IL-6 and TNF-α as well as the chemoattractant IL-8[38]. AM are resident phagocytes in lung alveoli and are the first immune cells that get into contact with inhaled pathogens like *A. fumigatus* conidia[34,39].

They are able to phagocytose both resting and swollen conidia, but only swollen conidia are effectively killed intracellularly[39]. AM lack the ability to phagocytose the hyphal morphotype of *A. fumigatus*, but are critical for hyphal recognition because this leads to the chemotactic recruitment of circulating phagocytes, like PMN, from the bloodstream to the site of infection[29,40].

PMN phagocytose and kill conidia but also hyphal structures. If hyphal structures are too large for being phagocytosed, PMN may release the content of their granules into extracellular space[30]. These extracellular factors are involved in killing hyphae, but also cause damage to the surrounding host tissue[27]. Furthermore, PMN may commit an altruistic suicide as a final act of defence against hyphae, thereby releasing DNA fibers into the environment that may trap the fungus[41]. These so-called *neutrophilic extracellular traps* (NETs) were shown to have fungistatic rather than fungicidal effects[41]. AM and PMN are thought to be key players in the defence against *A. fumigatus* and an impairment of either phagocyte type is commonly associated with a relatively high susceptibility for severe infections by this fungus[42].

As is clear from the example of the human-pathogenic fungus *A. fumigatus*, investigating the counterplay of infection and inflammation is highly important in order to gain insights into the complex host-pathogen interactions that may ultimately reveal possibilities for therapeutic interventions. However, since it is virtually impossible to investigate these processes in alveoli of the human lung *in vivo* and under physiological conditions[16], we here pursue a systems biology approach starting with theoretical modelling. We apply EGT on graphs to investigate the counterplay of pathogen-induced infection and increasing levels of host inflammation during *A. fumigatus* infection in AS of the human lung according to the time course depicted in Fig. 1(b). The model is constructed on the firm basis of experimental data available today (see Methods section) and is applied to generate new hypothesis that can direct future experimental investigations (see Discussion section).

The present study, using infections by the human-pathogenic fungus *A. fumigatus* as an example, reveals the importance of the immune response to be tightly regulated and that this regulation is realised by the layered structure of the immune system. In particular, our simulations reconcile the contradictory view on the role of AM in the immune response[43,44]: We observe that AM have a key role in the regulation of the first steps of the immune response and that this regulation depends on the strength of the infection-dose. While the phagocytic activity of AM is sufficient to limit low infection-doses – corresponding to values of daily inhalation – inflammatory signalling by AM for recruitment of PMN becomes their primary task at higher infection-doses.

Results

In this section, we first analyse the degree of proximity between conidia of *A. fumigatus* in AS of the human lung. Based on the derived interaction graphs between fungal cells, we then consider the results of three evolutionary games representing distinct stages of the innate immune response against this human-pathogenic fungus (see Fig. 1(b)). These stages comprise the humoral response by the complement system (Game I), the cellular immune response by AM (Game II) and PMN (Game III). Finally, by linking these three individual games in a time-ordered fashion, we present the results of infection-inflammation scenarios in the human host. To quantify the infection-inflammation scenarios, we defined the infection score (see Eq. 6) and normalised inflammations that mediate between Game I and II (see Eq. (7)) and Game II and III (see Eq. (8)).

Virtual infection-inflammation model reveals degree of fungal interactions in alveolar sacs. We performed *in silico* experiments to simulate the counterplay of *A. fumigatus* infection and host inflammatory response by evolutionary games on graphs. A graph defines the proximity-based interactions between fungal cells in AS of the human lung (see Fig. 1(a)). Each game of the infection-inflammation scenario represented a consecutive sequence of three stages of innate immunity (see Fig. 1(b)). Within each AS, consisting on average of 21 densely packed alveoli, the drawn number of conidia n_{fc} were uniformly distributed over its alveoli. As shown in Fig. 2(a), we found that irrespective of the fungal dose, most likely there will be no conidium at all in a randomly chosen AS. However, of all the AS that contained fungal cells, their number clearly depended on the fungal dose and was associated with quite different upper limits of conidia that could be expected in the AS. For a fungal dose that corresponds to daily inhalation ($6.3 \cdot 10^3$ conidia), two conidia per AS are conceivable, whereas for extremely high doses (10^7 conidia) up to eight conidia may be encountered in a single AS.

Fungal individuals in the same AS may become engaged in a game among each other under the influence of the immune response at a certain stage. As described in the Methods section, the graph-based approach defines interactions between fungal cells, where the number of interactions per fungal cell depends on their number in the corresponding AS. As shown in Fig. 2(b), this analysis revealed that two fungal cells in an AS most likely stay solitary, whereas three to eight individuals in an AS typically lead to one expected interaction per conidium.

Complement activity drives emergence of fungal morphotypes. In Game I, different morphotypes emerge from the interaction of fungal cells with the complement system that are shown in Fig. 3 for different parameter combinations and for low ($n_{fc} = 2$) and high ($n_{fc} = 8$) infection-doses. As could be expected, with rising nutrient availability E_S for swollen conidia or diminishing complement effects c_S against swollen conidia, their fraction increases over that of resting conidia, $f_S > f_R$. Regions with comparable fractions of resting and swollen conidia, $f_R \approx f_S$, were found for both infection-doses, however, these regions were more extended for the lower infection-dose. At high infection-doses, where conidia had on average more interaction partners per alveolus, it was frequently observed that one of the two populations dominated over the other one with a fraction above 80 %. This effect could be attributed to the dose-dependent impact of adaptation and mutation events in each simulation time-step. For low relative to high infection-doses, mutations occur more often than adaptation events due to a lack of interaction neighbours among the widely separated fungal cells.

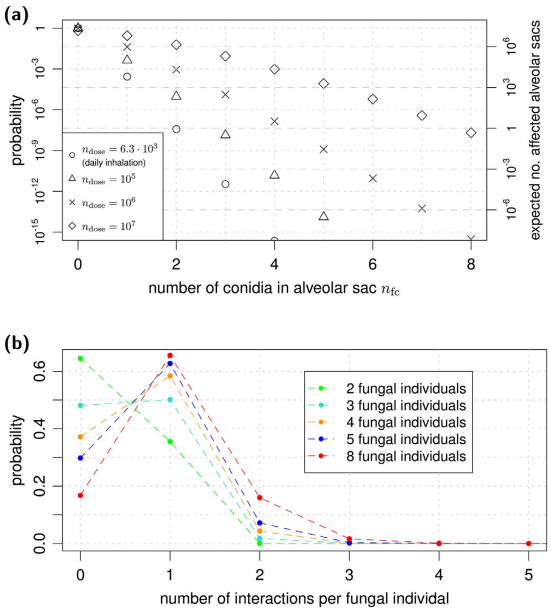

Figure 2. Number of conidia and their interactions per alveolar sac. (**a**) Dose-dependent probability distribution for the number of conidia entering the alveolar sac. Rescaling of the probability values were used to determine the expected number of affected alveolar sacs in the human lung, as shown by the scale on the right hand side. (**b**) Probability distribution for the number of interactions per fungal individual depending on the number of conidia inserted into the alveolar sac. Distributions were obtained from 10^6 interaction graphs.

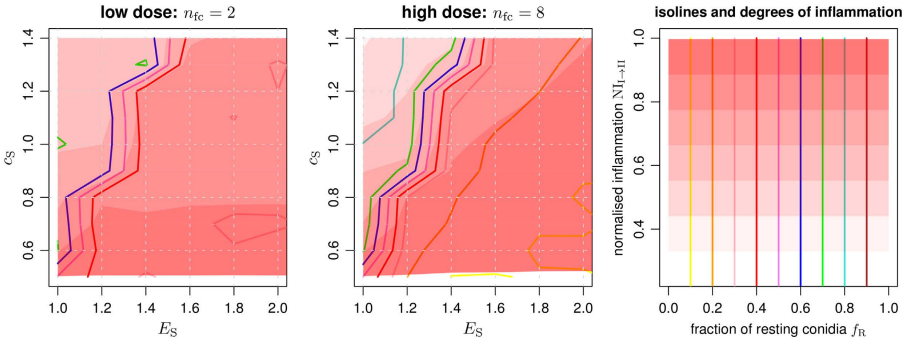

Figure 3. Fractions of *A. fumigatus* morphotypes and degrees of inflammation in response to the complement system. Equilibrium fractions of conidia in the resting state were determined from averaging over 100 repetitions per parameter configuration. Parameters were scanned in a lattice-based fashion at distinct points of the parameter space. Isolines (*colored lines*) for fractions of conidia in the resting state and isobands (*red shaded areas*) for different degrees of inflammation were generated using a modified version of the marching-squares algorithm for bilinear interpolation over rectangular grids. Parameters $E_R = 1$, $c_R = 0.5$ were kept fixed.

Alveolar macrophages reach phagocytic limits for high fungal doses. We performed simulations of Game II to identify the most relevant parameters under the impact of the immune response by AM. Using the concept of mutual information, as explained in the Methods section, we found that the activity of AM was of central importance regarding the infection score IS_{II} (see Eq. (6) and Table S2). Our investigations revealed that AM were in the position to keep the fungal cells in check for low infection-doses of fungal cells and for sufficiently high phagocytosis activity of AM. However, as shown in Fig. 4, AM were not able to remove the infectious agents in high-dose scenarios due to their inability to counteract hyphal cells appropriately. It can be expected that their function regarding elevation of the immune response via inflammatory and chemoattracting signals plays an important role in this case.

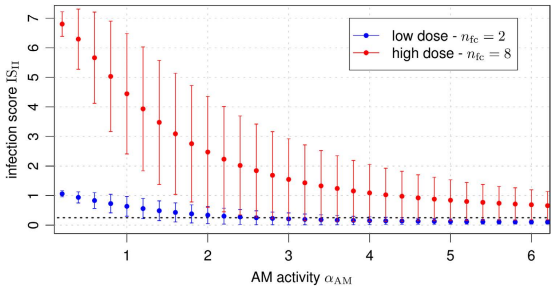

Figure 4. Dose-dependent infection scores according to simulations of Game II. The average infection score IS_{II} over all parameter combinations shown as a function of AM activity. Error bars denote one standard deviation. The *black short-dashed line* marks the infection score threshold IS = 0.25 below which clearance of infection is achieved.

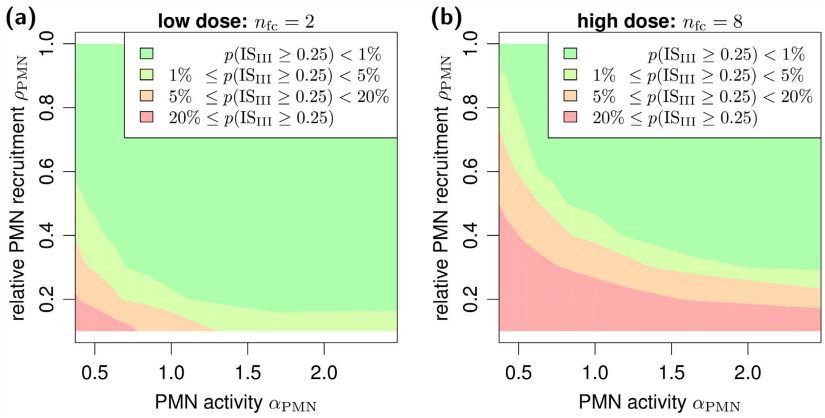

Figure 5. Dose-dependent connection between infection score and PMN parameters. Landscape of the persistent infection probability for different fungal doses in scenarios with (**a**) low and (**b**) high infection-doses. Isobands (*colored areas*) for different probability ranges were generated using a modified version of the marching-squares algorithm for bilinear interpolation over rectangular grids.

Recruitment of neutrophils can be essential for successful clearance. In Game III, *A. fumigatus* conidia were faced with the professional phagocytes PMN. First, we identified the most relevant parameters by computing the mutual information between each of the game's parameters and the infection score (see Eq. 6). The PMN recruitment ρ_{PMN} and phagocytosis activity α_{PMN} against live fungal cells were found to be most relevant for the outcome of the infection (see Table S2). We further analysed these parameters for low and high infection-doses and the results are shown in Fig. 5. It should be noted that the infection score $IS_{III} = 0.25$ represented the special case of one resting conidium in the AS that survived the immune response of the host. Consequently, infection scores $IS_{III} < 0.25$ and $IS_{III} \geq 0.25$ represent, respectively, clearance and persistence of the *A. fumigatus* infection. The measure $p(IS_{III} \geq 0.25)$, plotted in Fig. 5, denotes the fraction of parameter combinations over all performed simulations for which the fungal infection persisted in the host. We identified the most important parameters for infection clearance and found that, for a low number of infectious agents, PMN were able to clear the infection in most of the cases, whereas reduced recruitment and activity of PMN eventually led to the persistence of infection. In the limit of high infection-dose, PMN activity and a sufficiently high recruitment were pivotal to remove *A. fumigatus*. We further found that a reduced PMN activity could be partly compensated by an increase in the PMN recruitment. Moreover, independent of the precise value of PMN activity, sufficient PMN recruitment was generally found to be an essential prerequisite for successful infection clearance.

Infection-inflammation scenarios reveal regulatory role of alveolar macrophages. Going beyond the separated analysis of evolutionary games for the three distinct stages of the innate immune response against the human-pathogenic fungus *A. fumigatus*, we linked the games in a time-ordered fashion to simulate infection-inflammation scenarios in the human host. Thus, starting with Game I, we determined the infection score IS_I (see Eq. 6) due to the immune response by the complement system. Next, we linked Game I to Game II by computing the normalised inflammation $NI_{I \to II}$ (see Eq. (7)), which determined AM activity in the second stage of the immune response. The infection-inflammation scenario at this stage was evaluated by the infection

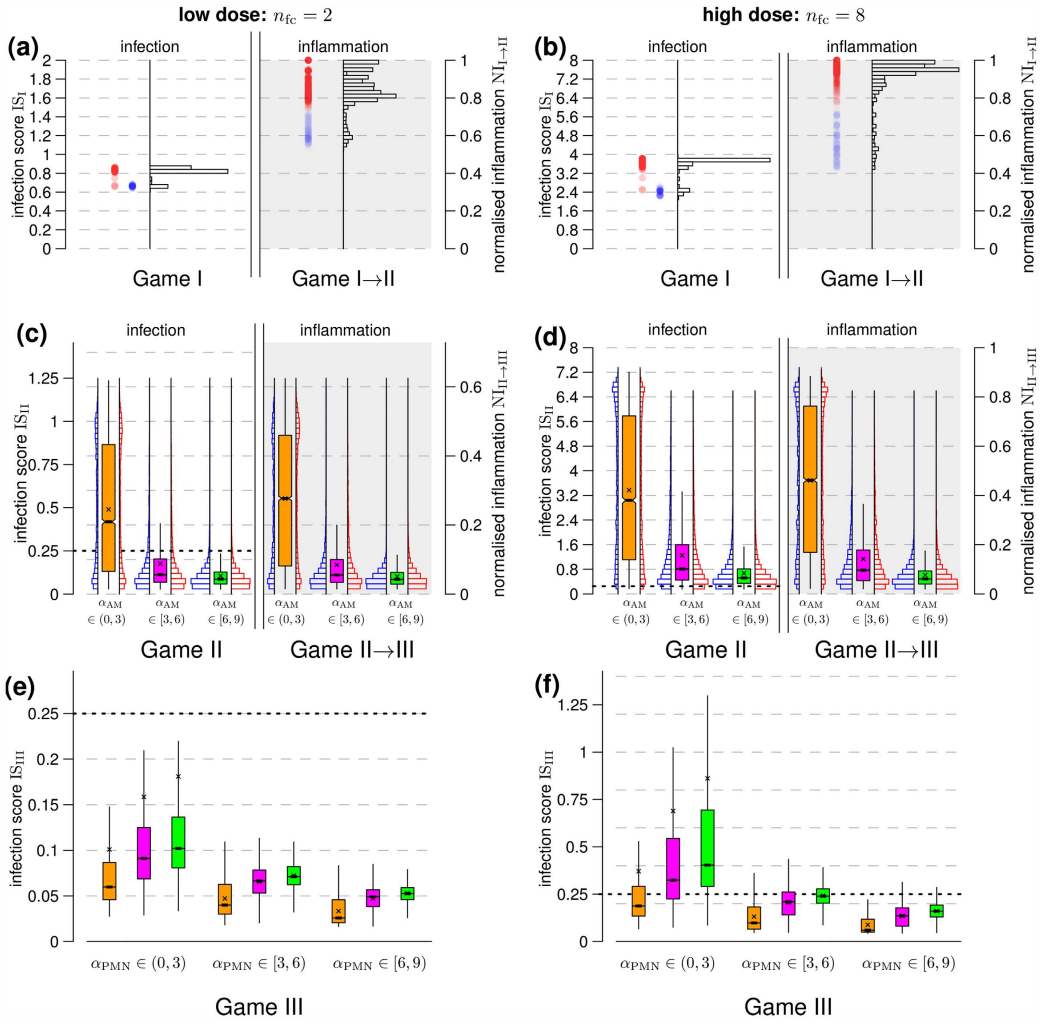

Figure 6. Dose-dependent relation between infection and inflammation across the consecutive sequence of evolutionary games. Two infection-inflammation scenarios were simulated: low infection-dose in (**a**,**c**,**e**) and high infection-dose in (**b**,**d**,**f**). In (**a**,**b**) the distribution of infection scores and corresponding values for the normalised inflammation are shown as *black histograms*. The distribution of higher (lower) values for the normalised inflammation with $NI_{I\to II} \geq 0.75$ ($NI_{I\to II} < 0.75$) are shown by circles colored in *red* (*blue*). The inflammatory signal $NI_{I\to II}$ was fed into Game II scaling AM activity. The effects of high and low values for the normalised inflammation are shown in (**c**,**d**) using *red* and *blue* inline histograms grouped by different levels of AM activity. The *red* and *blue* inline histograms were combined in the *notched box plots* and shown in *orange*, *violet* and *green* color, respectively, for low, medium and high AM activity with average values marked by (×). (**e**,**f**) Connection between Game II and Game III was set by the recruitment parameter $\rho_{PMN} = NI_{II\to III}$. Distributions for the different AM activities are presented in the same colors as in (**d**,**e**) grouped by PMN activities. The *black short-dashed lines* in (**c**–**f**) mark the infection score threshold IS = 0.25 below which clearance of infection is achieved.

score IS_{II} (see Eq. 6) and linking to Game III was realised by the normalised inflammation $NI_{II\to III}$ (see Eq. (8)), which determined PMN recruitment in the third stage of the immune response and gave rise to the infection score IS_{III} (see Eq. 6 and Fig. 1(b)).

The simulation results for low and high infection-doses as well as for varying AM and PMN activities are presented in Fig. 6. The counterplay between *A. fumigatus* infection and the complement system (Game I) yielded values for the infection score and the normalised inflammation that are shown in Fig. 6 for (a) low ($n_{fc} = 2$) and (b) high ($n_{fc} = 8$) infection-doses. The infection score IS_I resulting from Game I is depicted on the left-hand side in the black histograms in Fig. 6(a,b), while the corresponding normalised inflammation $NI_{I\to II}$ is shown on the

right-hand side. The normalised inflammation revealed a bimodal distribution that subdivides all simulations into infection-inflammation scenarios with low (blue) and high (red) NI-values. Interestingly, a comparison with the corresponding classes for the infection score did not show this clear separation. This result was observed for both low and high infection-doses and an in-depth analysis revealed that, while low (blue) inflammation values were associated with lower infection scores, higher (red) inflammation values were not only associated with higher infection scores but, quite unexpectedly, also with lower infection scores. It turned out that the reason for this behavior is in the effect that the complement system exerted on resting and swollen conidia. As can be observed in Fig. 3, high inflammation (dark red areas) exist for $f_R > 0.5$ and corresponds indeed to lower infection scores where the fraction of resting conidia is larger than that of swollen conidia. Furthermore, it could be observed that these cases were associated with approximately equal complement activity against resting and swollen conidia ($c_R \approx c_S$) in combination with only small differences between the nutrient contributions E_R and E_S.

The normalised inflammation $NI_{I\to II}$ that was induced by the response of the complement system (Game I) had direct impact on AM activity in Game II. The corresponding results are depicted in Fig. 6 for (c) low and (d) high infection-doses. In both cases, the highest impact on the infection scores could be attributed to the AM activity α_{AM}, where higher AM activity was associated with more strongly reduced infection and vice versa. Interestingly, only marginal differences were induced by low (blue) and high (red) infection-inflammation scenarios from the complement response with regard to the resulting distributions of infection scores after AM response in Game II (see Fig. 6(c,d), blue and red inline histograms). Of note, we generally observe that the level of infection is reflected by the level of inflammation (see Fig. 6(c,d)). In scenarios with low infection-dose, as shown in Fig. 6(c), AM with high activity were in the position to clear the infection in most of the cases ($p(IS_{II} < 0.25) = 95\%$), in contrast to scenarios with high infection-dose (see Fig. 6(d)), where even high AM activity could only reduce but not entirely clear the infection in most of the cases ($p(IS_{II} < 0.25) = 10\%$). In both infection scenarios and irrespective of AM activity, a statistically relevant number of different parameter configurations resulted in the PMN recruitment by AM to support in the elimination of the infectious agents. Interestingly, distributions of infection scores in Game II (IS_{II}) generally induced qualitatively comparable distributions for the normalised inflammation ($NI_{II\to III}$).

Linking Game II and Game III by the normalised inflammation $NI_{II\to III}$, we found that, since AM with lower activity induced on average higher infection scores, they gave rise to increased levels of inflammation associated with increased PMN recruitment. In general, low infection-doses were found to be cleared for a wide range of PMN activities as indicated by infection score $IS_{III} < 0.25$ in Fig. 6(e). This implies, in agreement with our earlier observations (see Fig. 5(a)), that the amount of recruited PMN was always sufficient and could even compensate lower PMN activities. The situation is different for the case of high infection-doses, where a minimum-activity of PMN was required to ensure statistically firm clearance of infection (see Fig. 6(f)). Interestingly, we observed an advantageous effect for fungal clearance by PMN for AM with reduced activity in counteracting the fungal pathogens and consequently higher production of inflammatory signals increasing PMN recruitment. As can for example be seen for high PMN activity and high infection-dose, the probability for a persistent infection rose from $p(IS_{III} \geq 0.25) = 0.7\%$ in cases with low AM activity to $p(IS_{III} \geq 0.25) = 2.5\%$ in cases with high AM activity. This stresses once again the pivotal role of AM with regard to PMN recruitment. For low and medium PMN activity, the probability for a persistent infection $p(IS_{III} \geq 0.25)$ was ranging, respectively, from 32% to 86% and from 12% to 43%. For pathogen removal, high PMN activity was required the higher the infection-dose and the lower the AM induced inflammatory signal produced for PMN recruitment.

Discussion

In this study, we applied EGT on graphs to investigate the dynamic counterplay between pathogens and the human immune system in various infection-inflammation scenarios. For illustrative purposes we focused on the concrete example of *A. fumigatus* infection, because even though this human-pathogenic fungus constitutes a common challenge, its potential threat can obviously be permanently managed under physiological immune conditions. Our virtual infection-inflammation model combined the three temporally distinct stages of the innate immune response against this fungal pathogen, *i.e.* the direct and immediate response by the complement system (Game I), followed by the phagocytic activity of AM (Game II) and the subsequent recruitment and immune response by PMN (Game III). Thus, going beyond separate *in silico* experiments of the three stages, we linked the three individual games in a time-ordered fashion. This is achieved by accounting for the quantitative elevation in the host inflammation, depending on the evolution of the various morphotypes that *A. fumigatus* can exhibit in the course of an infection. We performed stochastic computer simulations of various infection-inflammation scenarios scanning the parameter space of the model to identify and predict the relative importance of specific mechanisms in the innate immune response against *A. fumigatus*.

The activity of the complement system and the availability of nutrients determine the evolution of the fungal morphotypes, *i.e.* how the population of fungal cells is composed of resting and swollen conidia. In line with earlier experiments in mice, where a major inflammatory complement component (C5a) was depleted inducing a higher virulence of the pathogen[45], it was observed in the model that conidia did shift from the resting state to the swollen state associated with a higher infection potential. It can be concluded, that in this case the pressure of the complement system became so low that the uptake of nutrients made this state transition beneficial. We also found this effect to be increased in the limit of high infection-doses.

While the complement system is believed not to contribute to direct killing of this fungus, in agreement with previous experimental investigations[29,30,46], our simulations predicted a substantial contribution of the complement system to AM activity in AS via inflammatory signalling. Interestingly, on the one hand, it is well-known that AM comprise the largest population of resident cells in the respiratory tract[47] and that impairment of their function is one of the risk factors for invasive mycoses[43]. On the other hand, based on experiments with mice, Mircescu *et al.* claimed that PMN but not AM play the essential role in the immune response against

A. fumigatus[44]. Our simulations revealed that these seemingly contradictory view points could be reconciled by accounting for the impact of the infection-dose on the time course of the infection-inflammation scenario. In particular, we observed in the *in silico* experiments that AM have a key role in the regulation of the immune response and that this regulatory effect depended on the strength of the infection-dose. As a matter of fact, infections could generally be cleared by AM alone and without considerable PMN recruitment in the limit of low infection-doses corresponding to the typical dose of daily inhalation, where AM were mainly confronted with conidia in the resting and swollen state. In contrast, higher infection-doses were associated with higher inflammation and, consequently, inflammation-dependent PMN recruitment by AM was pronounced, such that PMN but not AM were ultimately playing the essential role in the phagocytosis of the fungal cells. This simulation-derived interpretation is in agreement with the fact that the study by Mircescu *et al.* was indeed performed with infection-doses that were orders of magnitude above the dosis of daily inhalation[44].

The regulatory function of AM was of paramount importance in the simulations, due to the quantitative and qualitative limitations of AM to phagocytose and kill *A. fumigatus* in the hyphal state[39]. However, apart from AM activities directed against the pathogen itself, these immune cells do also play an important role in shutting down inflammation and in initiating tissue recovery at sites of damage in later stages[48–50]. PMN are essential and highly skilled phagocytes that are equipped with various antifungal capabilities that can be fungicidal and/or fungistatic[30,34,39]. Our simulation results confirmed the importance of PMN, however, their recruitment and defensive function were most important in the limit of high infection-doses. Interestingly, impairment of PMN function in the scenarios with low infection-doses was compensated by an increased recruitment of these cells, however, this could consequently imply an increase in self-damage of tissue, *e.g.* by neutrophilic respiratory burst, which constitutes a threat for the host itself[51]. Nevertheless, PMN recruitment was found to play an important factor across all possible infection-doses, because lack of PMN function was associated with increased probabilities for pathogen persistence, as could be expected from findings in previous experimental studies[52]. Even though beyond the scope of the current modelling approach, it is very well conceivable that PMN recruitment by AM-induced inflammation occurs more quickly in the limit of high infection-doses.

Systems biology relies on the cross-fertilisation between theory and experiment. While uncertain or even unknown biological parameters can only be determined in wet-lab experiments, theoretical approaches can direct this exploration by generating concrete hypotheses. Obviously, parameters in the payoff matrices of EGT relate to the abstract concept of reproductive fitness in terms of nutrient uptake and immune response and, therefore, may be difficult and/or impossible to be separately measured in experiment. However, our study suggests that quantitative insights about the metabolic activities of different *A. fumigatus* morphotypes would narrow down the range of relevant nutrient contributions in the model and by that render scanning of several parameters obsolete. In turn, the model could be refined, extended and reviewed to focus investigations on particular aspects in the reduced parameter space with higher attention to details. Furthermore, guided by the outcome of our simulations, we suggest experimental investigations that may clarify the dependence between the infection-dose and the inflammatory signalling, *e.g.* by determining the cytokine profile secreted from AM and/or PMN. Similarly, *A. fumigatus* infection in mice with fully and/or partly impaired AM and/or PMN populations could as well be systematically investigated as a function of the infection-dose to specify the model dynamics of infection-inflammation scenarios. These investigations could be performed using different microscopy techniques: light-sheet microscopy could reveal cellular distributions, i.e. of conidia, AM and PMN, in the lung, whereas multi-photon microscopy could even allow monitoring dynamical aspects of cells in the lung. Furthermore, processes like phagocytosis of fungal cells by AM and PMN as well as recruitment of PMN could be quantified using fluorescence-activated cell sorting (FACS) at different time points and as a function of the infection-dose. Spatial-temporal insights from imaging experiments will support realistic mathematical modeling within the image-based systems biology approach[11].

The current version of the virtual infection-inflammation model captures the most relevant aspects of the innate immune response against *A. fumigatus*, but could be extended by other mechanisms, even including aspects of adaptive immunity, to more comprehensively resemble the full complexity of the infection process. For example, the first cells getting into physical contact with inhaled conidia are AEC of type I and type II, where type II cells were reported to internalise conidia and to generate inflammatory signals[38]. In this study, we intentionally omitted responses by AEC due to considerable gaps in our knowledge about type I AEC[53] that, in fact, make up the alveolar surface almost entirely[54]. Dendritic cells were also shown to contribute to fungal clearance[55] and a dysregulation in Th1/Th2 responses lead to invasive pulmonary aspergillosis despite a non-neutropenic status of the host[56], thus, revealing substantial evidence for the importance of adaptive immune responses in *A. fumigatus* infection. In future work, extensions of the virtual model might include responses mediated by adaptive immunity to study the relative contributions from innate and adaptive immune effectors and functions. This could be realised by a network of evolutionary games, where the immune response of the host is adapting regarding the activity against pathogenic attacks. The charming aspects of EGT lie, on the one hand, in the elegant reduction of model parameters to the ratios of parameters and, on the other hand, in the inherent extensibility that allows to realistically capture the characteristic features of complex host-pathogen interactions.

Methods

Modelling the dynamics of host-pathogen interactions by EGT on graphs. The game-theoretical description of the infection-inflammation scenario considered in this study is constructed as a consecutive sequence of three evolutionary games (see Fig. 1(b)). These games comprise the time course of the innate immune response and are played on graphs in order to perform *in silico* experiments of *A. fumigatus* infection using a pseudo-spatial representation of AS. Here, each fungal cell represents an infectious individual that interacts with other proximal fungal cells under the elevating inflammatory response of the host. In what follows, we present

a detailed description of the interaction graph construction, the distribution of different cell types in an AS, the design of the sequentially organised games and the evolutionary dynamics algorithm.

Environmental setting: alveolar sacs. Evolutionary dynamics take place in a typical AS. AS are organisational structures in the lower respiratory tract of the lung and are composed of 21 alveoli on average[33,57]. Alveoli in an AS are inter-connected via alveolar entrance rings and pores of Kohn[53,58], whereas different AS are considered as fairly independent units. In order to reflect connectivity properties between alveoli in a cylindrically shaped AS, we represent them by densely packed spheres as shown in Fig. 1(a). A relationship between any two neighbouring alveoli is assumed if their spheres touch each other.

Distribution of cells in alveolar sacs. Each alveolus represents a virtual site in which typical numbers of fungal and immune cells are placed. The number of fungal cells present in one AS emerges from a dose-dependent distribution over all AS upon inhalation or upon administration. The fungal dosis ranges from $n_{\mathrm{dose}} = 6.3 \cdot 10^3$ conidia (daily inhalation for humans) to $n_{\mathrm{dose}} = 10^7$ conidia (administration in experiments with mice). First, the number of fungal cells per AS, n_{fc}, is drawn from the Binomial distribution:

$$B_{\mathrm{fc/AS}}(n_{\mathrm{dose}}, p, n_{\mathrm{fc}}) = \binom{n_{\mathrm{dose}}}{n_{\mathrm{fc}}} p^{n_{\mathrm{fc}}} (1 - p)^{n_{\mathrm{dose}} - n_{\mathrm{fc}}}, \tag{1}$$

where $p = 1/n_{\mathrm{AS}}$ denotes the probability to choose the AS under consideration and the total number of AS is about $n_{\mathrm{AS}} = 2.3 \cdot 10^7$ in humans[33,57]. Second, the number of fungal cells per AS, n_{fc}, is uniformly distributed over the alveoli of the AS. Similarly, the number of resident AM (n_{AM}) and recruited PMN (n_{PMN}) follow the same distribution process over AS. In this case, n_{dose} in Eq. 1 is replaced by the total number of $2.1 \cdot 10^9$ macrophages in humans, whereas for PMN this number can be up to eight times higher depending on the strength of PMN recruitment[40].

Construction of the interaction graph. The interaction graph is based on the spatial proximity between *A. fumigatus* conidia in the AS. Interactions between the fungal cells of an AS are generated in a rule-based fashion: Two fungal cells interact,

1. If they are located in the same alveolus or
2. If they are randomly selected from two neighbouring alveoli and do not yet have another inter-alveolar interaction.

These rules give rise to a proximity-based interaction graph between all fungal cells in the same alveolus or fungal cells that are nearby in neighbouring alveoli, *e.g.* reflecting intra-alveolar localisation close to one of the pores of Kohn or the alveolar entrance ring. An example for a fungal interaction graph is shown in Fig. 1(a).

Sequential design of host-pathogen games. Fungal cells are viewed as infectious agents that play against each other for survival under the inflammatory pressure of the immune system. The different morphotypes that conidia of *A. fumigatus* can develop with time correspond to the strategies that the fungal cells may adopt in each game and are summarised in Table S1. We consider three different stages of innate immunity that are reflected by three distinct evolutionary games and that are played on the interaction graph of fungal individuals as depicted in Fig. 1(b).

In each of the three games, beneficial effects like the consumption of nutrients as well as the pressure of the immune system are aggregated in an utility function per individual, which contains quantitative information about the reproductive fitness of the fungal cell. This utility function has the general structure

$$U_i = (\text{nutrients})_i + (\text{immune response})_i , \tag{2}$$

where i denotes the i-th fungal individual. Nutrients generally increase the reproductive fitness and their contributions enter the expression with a positive sign, in contrast to payoffs associated with the immune response that have values below zero. The amount of nutrient uptake by fungal individuals depends on the strategy adopted by the cell, where E_{D}, E_{R}, E_{S} and E_{H} denote the nutrient contributions for fungal cells in the state "dead", "resting", "swollen" and "hyphal", respectively. Since the reproductive fitness of hyphae is higher than for swollen conidia and swollen conidia outperform resting conidia, we set the relation between the nutrient contributions to $E_{\mathrm{D}} < E_{\mathrm{R}} \leq E_{\mathrm{S}} \leq E_{\mathrm{H}}$ with $E_{\mathrm{D}} = 0$ for dead cells. Reduction of reproductive fitness induced by immune responses either acts on single fungal individuals or on pairs of individuals that are interacting with each other in a game-specific context.

Game I–Complement system. The proteins of the complement system are always present in the alveolar lining layer (surfactant) and immediately surround each fungal cell starting from its entry into the AS. Opsonisation of conidia induces inflammation and phagocyte attraction to the site of infection. This is the predominant immune response in the first minutes. At this stage, conidia of *A. fumigatus* may either stay in the "resting" state or initiate radial growth and switch to the "swollen" state. This game is restricted to these two states, because, during the first hour after entry into the lower respiratory tract, conidia do not germinate. Opsonisation and chemoattraction are represented by morphotype-specific negative payoffs as a function of the complement responses c_{R} and c_{S} that are associated with resting and swollen conidia, respectively. These effects are taken into account for each fungal individual irrespective of alveolar localisation and interaction partners. Both, resting and swollen conidia, can not evade opsonisation by the complement, but swollen conidia do activate the complement system more intensively, implying that $c_{\mathrm{S}} \geq c_{\mathrm{R}}$[36]. In addition, proximal fungal individuals interfere with each other due

$P_1^G(s_1, s_2)$		s_2			
		R	**S**	**H**	**D**
Game I					
s_1	R	$-c_R/2$	$-c_S/2$	–	–
	S	$-c_R/2$	$-c_S/2$	–	–
	H	–	–	–	–
	D	–	–	–	–
Game II					
s_1	R	$-1/2\times m_R$	$-\frac{m_R}{m_R+m_S}\times m_R$	$-\frac{m_R}{m_R+m_H}\times m_R$	$-m_R$
	S	$-\frac{m_S}{m_S+m_R}\times m_S$	$-1/2\times m_S$	$-\frac{m_S}{m_S+m_H}\times m_S$	$-m_S$
	H	$-\frac{m_H}{m_H+m_R}\times m_H$	$-\frac{m_H}{m_H+m_S}\times m_H$	$-1/2\times m_H$	$-m_H$
	D	0	0	0	0
Game III					
s_1	R	$-1/2\times g_R$	$-\frac{g_R}{g_R+g_S}\times g_R$	$-\frac{g_R}{g_R+g_H}\times g_R$	$-g_R$
	S	$-\frac{g_S}{g_S+g_R}\times g_S$	$-1/2\times g_S$	$-\frac{g_S}{g_S+g_H}\times g_S$	$-g_S$
	H	$-\frac{g_H}{g_H+g_R}\times g_H$	$-\frac{g_H}{g_H+g_S}\times g_H$	$-1/2\times g_H$	$-g_H$
	D	0	0	0	0

Table 1. Payoff matrices for Game I, II and III. Payoffs $P_1^I(s_1, s_2)$, $P_1^{II}(s_1, s_2)$ and $P_1^{III}(s_1, s_2)$ of Game I, Game II and Game III are shown for fungus 1 interacting with fungus 2. R, S, H and D denote resting, swollen, hyphal and dead fungal cells, respectively. The complement response for resting and swollen fungal cells in the Game I are represented by c_R and c_S, respectively. m_H, m_R, m_S and g_R, g_S, g_H are the responses by AM or PMN on encounter of resting condia, swollen conidia or hyphae. The complement responses satisfy the condition $c_R \leq c_S$ as well as the AM responses $m_H \leq m_R \leq m_S$ and the PMN responses $g_R \leq g_S \leq g_H$, which determine the payoffs.

to superimposed inflammatory and chemoattracting complement signals and by that induce further negative payoffs P^I that depend on the number of interaction partners.

The utility function of fungal cell i in this game is described as

$$U_i^I = E_{s_i} - c_{s_i} + \sum_{j\in\mathcal{N}_i} P_i^I(s_i, s_j), \tag{3}$$

where $s_i \in \{R, S\}$ is the morphotypic strategy of fungal individual i, c_{s_i} is the complement response associated with strategy s_i, $\mathcal{N}_i$ are the interaction partners of fungal cell i and $P_i^I(s_i, s_j)$ the payoffs as defined by the payoff matrix for Game I in Table 1. The utility function indicates that the more interaction partners a fungal individual has, the more it will be under pressure by complement activity.

Game II–Alveolar macrophages. The second game refers to the time scale of a few hours after entrance of conidia in the AS, which is the phase where germination of conidia becomes possible. In this phase, *A. fumigatus* conidia get into contact with professional phagocytes, *i.e.* AM being resident in alveoli. They are able to phagocytose conidia and have the potential to kill swollen conidia, while they fail to phagocyte fungal cells that filamented and have hyphae. The AM activity α_{AM} measures the ability to phagocytose and kill the fungal cells. At this stage of the immune response, conidia are enabled to adopt the four strategies "resting", "swollen", "hyphal" and "dead", where the latter strategy is preferred in the case of a strong immune response that is not compensated by a nutrient contribution ($E_D = 0$). The number of AM present in an alveolus is drawn from a Binomial distribution, as was done previously in our agent-based virtual *A. fumigatus* infection models[16,17] and as described before.

In this game, pairs of fungal cells are interacting under the pressure of the immune response mediated by AM. Each fungal cell of a pair aims to adopt a strategy that improves its reproductive fitness, at the risk of increasing the pressure by the immune system for both fungal cells. Fungal cells with no interaction partner receive the full immune exertion by AM, as if they would interact with a dead fungal cell. Thus, in the simulation algorithm a solitary fungal cell was virtually connected with a fungal cell in the state "dead".

AM respond with morphotype-specific activities, including phagocytosis, killing, inflammation and recruitment, which are summarised in the immune responses m_R, m_S, m_H against resting, swollen and hyphal fungal cells, respectively. Dead fungal cells receive a zero payoff from immune activities by AM (AM response $m_D = 0$). The response of AM against swollen conidia m_S is set to be strongest, followed by resting conidia m_R and the hyphal morphotype m_H, *i.e.*, the relation between the AM responses is given by $m_D < m_H \leq m_R \leq m_S$, which is in line with experimental observations[39].

The utility function of fungal cell i is defined as follows:

$$U_i^{\mathrm{II}} = E_{s_i} + \sum_{j \in \mathcal{R}_i^{\mathrm{AM}}} P_i^{\mathrm{II}}(s_i, s_j), \tag{4}$$

where $\mathcal{R}_i^{\mathrm{AM}} \subset \mathcal{N}_i$ denotes the set of interactors for which the fungal pair (i, j) with $j \in \mathcal{R}_i^{\mathrm{AM}}$ is randomly selected for AM–*A. fumigatus* interaction. The payoffs related to the AM immune response, $P_i^{\mathrm{II}}(s_i, s_j)$, are defined in the payoff matrix shown in Table 1.

Game III–Polymorphonuclear neutrophils. AM have important immune regulatory functions for the recruitment of cells from the bloodstream. For example, once recruited to the site of infection, PMN have an armory of weapons to attack pathogens. They can kill the fungus intracellularly after successful phagocytosis or extracellularly by the secretion of reactive oxygen species. Furthermore, they can undergo NETosis by committing an altruistic suicide in which they release their DNA and by that trap the fungus to prevent it from further spreading. After the recruitment of PMN to lung alveoli, these phagocytes govern the immune response and their overall activity is measured by the parameter α_{PMN}.

We introduce the parameter ρ_{PMN} to control the relative number of recruited PMN to the site of infection, where we impose – in agreement with observations in wet-lab experiments[40] – an upper PMN recruitment limit of eight times the number of present AM. As in Game II, pairs of conidia interact with PMN in a randomised fashion and can adopt the four strategies "resting", "swollen", "hyphal" and "dead" in this game. However, in contrast to Game II, the various defence mechanisms of PMN give rise to different relations in their specific responses. The relations between the PMN responses g_{R}, g_{S} and g_{H} against fungal cells in the resting, swollen and hyphal state are given by $g_{\mathrm{R}} \leq g_{\mathrm{S}} \leq g_{\mathrm{H}}$[29]. The utility function of fungal cell i in Game III is given by

$$U_i^{\mathrm{III}} = E_{s_i} + \sum_{j \in \mathcal{R}_i^{\mathrm{PMN}}} P_i^{\mathrm{III}}(s_i, s_j), \tag{5}$$

where $j \in \mathcal{R}_i^{\mathrm{PMN}}$ defines the interaction pairs (i, j), which randomly interact with a PMN. $P_i^{\mathrm{III}}(s_i, s_j)$ is the payoff imposed by interaction with a PMN as defined in Table 1.

The three games are linked in sequential order – Game I → Game II → Game III – to investigate the counterplay of *A. fumigatus* infection and host inflammation. Game linking is associated with the inflammatory signalling in response to the infectious agent, initiating the next higher instance along the cascade of the innate immune response. To this end, we introduce measures that enable quantifying the degree of infection and inflammation.

Quantification of infection and inflammation for game linking. To quantify the degree of infection induced by the human-pathogenic fungus *A. fumigatus* we define the infection score (IS) that is computed after execution of game G:

$$\mathrm{IS}_G = n_{\mathrm{fc}}\left(\frac{f_{\mathrm{R}} + 2f_{\mathrm{S}} + 4f_{\mathrm{H}}}{4}\right). \tag{6}$$

Here n_{fc} denotes the number of fungal cells in the AS and $f_{\mathrm{R}}, f_{\mathrm{S}}, f_{\mathrm{H}}$ and f_{D} with $f_{\mathrm{R}} + f_{\mathrm{S}} + f_{\mathrm{H}} + f_{\mathrm{D}} = 1$ refer to the fractions of fungal cells in the resting, swollen, hyphal and dead state, respectively. By construction, the infection score assumes increasing values $\mathrm{IS}_G = n_{\mathrm{fc}}/4$, $\mathrm{IS}_G = n_{\mathrm{fc}}/2$ and $\mathrm{IS}_G = n_{\mathrm{fc}}$ for populations consisting of increasingly challenging morphotypes $f_{\mathrm{R}} = 1$, $f_{\mathrm{S}} = 1$ and $f_{\mathrm{H}} = 1$, respectively. Furthermore, particular infection scores IS_G correspond to specific numbers of persisting fungal cells, irrespective of the infection-dose. For example, $\mathrm{IS}_G = 0.5$ either corresponds to one fungal cell in the swollen state or to two conidia in the resting state, whereas $\mathrm{IS}_G = 0.25$ represents one remaining fungal cell that is in the resting state. This threshold, $\mathrm{IS}_G = 0.25$, is set in the further analysis to distinguish between persistent ($\mathrm{IS}_G \geq 0.25$) and cleared ($\mathrm{IS}_G < 0.25$) infections.

Game linking is associated with the inflammatory signalling in response to the infectious agent. In particular, we link the complement system (Game I) with AM response (Game II) by the normalised inflammation (NI) measure that is defined as

$$\mathrm{NI}_{\mathrm{I}\to\mathrm{II}} = f_{\mathrm{S}} + \frac{c_{\mathrm{R}}}{c_{\mathrm{S}}} f_{\mathrm{R}} \in \left[\frac{c_{\mathrm{R}}}{c_{\mathrm{S}}}, 1\right]. \tag{7}$$

Based on literature data[36], this measure accounts for the relative difference in the complement response against the fractions of resting (f_{R}) and swollen (f_{S}) conidia. Furthermore, $\mathrm{NI}_{\mathrm{I}\to\mathrm{II}}$ accounts for relative differences in the complement response against resting and swollen conidia by the scaling factor $c_{\mathrm{R}}/c_{\mathrm{S}}$. The normalised infection value $\mathrm{NI}_{\mathrm{I}\to\mathrm{II}}$ regulates the response of AM in Game II by scaling the AM activity α_{AM}: $\tilde{\alpha}_{\mathrm{AM}} = \mathrm{NI}_{\mathrm{I}\to\mathrm{II}} \times \alpha_{\mathrm{AM}}$. Similarly, we link Game II to Game III by modelling PMN recruitment to depend on AM-secretion of the PMN-chemoattractant MIP-1. The secretion of MIP-1 is known to depend on the different *A. fumigatus* morphotypes[40]. Thus, we consider the relative recruitment number $\rho_{\mathrm{PMN}} = \mathrm{NI}_{\mathrm{II}\to\mathrm{III}}$, with the normalised inflammation:

$$\mathrm{NI}_{\mathrm{II}\to\mathrm{III}} = f_{\mathrm{H}} + \frac{11}{18} f_{\mathrm{S}} + \frac{1}{6} f_{\mathrm{R}} \in [0, 1], \tag{8}$$

where the coefficients conserve the relative responses of AM to MIP-1 for the different *A. fumigatus* morphotypes, as deduced from Ref. 40. Note that, in case the *A. fumigatus* infection can be cleared by AM, *i.e.* all fungal cells are dead $f_{\mathrm{D}} = 1$ and $f_{\mathrm{R}} = f_{\mathrm{S}} = f_{\mathrm{H}} = 0$ after Game II was played, no PMN-chemoattractant would be secreted and no PMN would be recruited.

Evolutionary dynamics. In each game, iterations over repetitive evolutionary steps t_{evo} are performed as depicted in Fig. S1. To ensure equilibration of the evolutionary dynamics, we set the number of iterations to 10^4. In each iteration step fungal cells receive nutrients and are confronted with the respective immune response. Each individual fungal cell evaluates its utility function in every time step t_{evo} containing the information on its reproductive fitness. Mutation and adaptation are evolutionary mechanisms performed in response to differences in the utility functions of individuals in the following way.

Mutation. Random change between strategies with probability $p = 0.01$.

Adaptation. Probabilistic change of an individual's current strategy s_i into a strategy s' applied by at least one fungal individual in the neighbourhood with higher reproductive fitness. Proportional imitation is applied as microscopic update rule and a distinction is drawn between the strategy "dead" (s_{dead}) and strategies related to individuals that are alive:

Case $s' \neq s_{dead}$: if strategy s' is played in the neighbourhood $\mathcal{N}_i$ of individual i, it adopts strategy s' with probability:

$$p(s_i \to s') = \frac{1}{\lambda |\mathcal{N}_i \cap \mathcal{I}(s')|} \sum_{j \in \mathcal{N}_i \cap \mathcal{I}(s')} \max(U_j^G - U_i^G, 0) \tag{9}$$

where $\mathcal{I}(s')$ is the set of all individuals playing strategy s' and λ a normalisation factor to ensure $p(s_i \to s') \in [0, 1]$.

Case $s' = s_{dead}$:

$$p(s_i \to s_{dead}) = \frac{1}{\lambda} \max(-U_i^G, 0). \tag{10}$$

Statistical measures. In order to distinguish parameters of the games by their relevance for the outcome of the infection-inflammation scenarios, we compute the mutual information (MI) as follows:

$$\mathrm{MI}(X, Y) = \sum_{x \in X} \sum_{y \in Y} p(x, y) \log_2 \left(\frac{p(x, y)}{p(x) p(y)} \right). \tag{11}$$

Here, X is the set of values related to one unknown parameter and Y the corresponding set of infection scores IS_G of game G. Furthermore, $p(x, y)$ denotes the joint probability function, $p(x)$ and $p(y)$ are marginal probability distributions of X and Y, respectively[59]. Since IS_G is a continuous measure, Y is discretised using different bin sizes for the calculation of MI(X, Y). We checked that the dependence of the mutual information MI(X, Y) on the binning of the infection score IS_G does not affect the ranking of the most important parameters. These are the AM activity α_{AM} in Game II (see Table S2 and Fig. S2 (a)) and both PMN activity α_{PMN} and PMN recruitment ρ_{PMN} in Game III (see Table S2 and Fig. S2 (b)).

Implementation and Simulation. All parameters used in the evolutionary games are scanned in reasonable ranges to capture their influence on the outcome of each game and the ultimate outcome of the infection. The evolutionary game-theoretical algorithm is implemented in the object-oriented programming language C++ and simulations are performed by the simulation algorithm depicted in Fig. S1. Statistical analyses are carried out using R. To reduce effective runtime, the algorithm is parallelised and is executed on a SUSE Linux Enterprise Server version 11 based on a x86-64 architecture with 512 GB RAM and 48 AMD Opteron processors, each running on 1781 MHz.

Virtual infection-inflammation scenarios were performed for different fungal doses and varied parameter configurations. To account for the stochastic nature of the *in silico* experiments, 100 repetitions were executed and from each simulation long-term density distributions of resting and swollen conidial fractions with their related averages and standard deviations were extracted.

References

1. Murphy, K. P., Janeway, C., Travers, P. & Walport, M. *Janeway's Immunobiology* (Garland Science, New York and London, 2008), 7 edn.
2. McLennan, I. C. M. Germinal centers. *Annual Review of Immunology* **12,** 117–139 (1994).
3. Zipfel, P. F. & Skerka, C. Complement regulators and inhibitory proteins. *Nature Reviews Immunology* **9,** 729–40 (2009).
4. Angus, D. C. & van der Poll, T. Severe sepsis and septic shock. *New England Journal of Medicine* **369,** 840–51 (2013).
5. Chi, H. *et al.* Dynamic regulation of pro- and anti-inflammatory cytokines by MAPK phosphatase 1 (MKP-1) in innate immune responses. *Proceedings of the National Academy of Sciences of the United States of America* **103,** 2274–2279 (2006).
6. Clermont, G. *et al. In silico* design of clinical trials: a method coming of age. *Critical Care Medicine* **32,** 2061–2070 (2004).
7. Kumar, R., Clermont, G., Vodovotz, Y. & Chow, C. C. The dynamics of acute inflammation. *Journal of Theoretical Biology* **230,** 145–55 (2004).
8. Day, J. *et al.* A reduced mathematical model of the acute inflammatory response II. Capturing scenarios of repeated endotoxin administration. *Journal of Theoretical Biology* **242,** 237–56 (2006).
9. Kumar, R., Chow, C. C., Bartels, J. D., Clermont, G. & Vodovotz, Y. A mathematical simulation of the inflammatory response to anthrax infection. *Shock (Augusta, Ga.)* **29,** 104–11 (2008).
10. Tanaka, R. J. *et al. In silico* modelling of spore inhalation reveals fungal persistence following low dose exposure. *Scientific Reports* **I,** 13958 (2015).
11. Medyukhina, A., Timme, S., Mokhtari, Z. & Figge, M. T. Image-based systems biology of infection. *Cytometry Part A* **87,** 462–70 (2015).

12. An, G. *In silico* experiments of existing and hypothetical cytokine-directed clinical trials using agent-based modeling. *Critical Care Medicine* **32,** 2050–60 (2004).
13. Hünniger, K., Lehnert, T., Bieber, K., Martin, R., Figge, M. T. & Kurzai, O. A Virtual Infection Model Quantifies Innate Effector Mechanisms and *Candida albicans* Immune Escape in Human Blood. *PLOS Computational Biology* **10,** e1003479 (2014).
14. Lehnert, T. *et al.* Bottom-up modeling approach for the quantitative estimation of parameters in pathogen-host interactions. *Frontiers in Microbiology* **6,** 1–15 (2015).
15. Tokarski, C. *et al.* Agent-Based Modeling Approach of Immune Defense Against Spores of Opportunistic Human Pathogenic Fungi. *Frontiers in Microbiology* **3,** 129 (2012).
16. Pollmächer, J. & Figge, M. T. Agent-based model of human alveoli predicts chemotactic signaling by epithelial cells during early *Aspergillus fumigatus* infection. *PLOS ONE* **9,** e111630 (2014).
17. Pollmächer, J. & Figge, M. T. Deciphering chemokine properties by a hybrid agent-based model of *Aspergillus fumigatus* infection in human alveoli. *Frontiers in Microbiology* **6,** 503 (2015).
18. von Neumann, J. & Morgenstern, O. *Theory of Games and Economic Behavior* (Princeton University Press, Princeton, 1944), 2nd edn.
19. Szabó, G. & Fáth, G. Evolutionary games on graphs. *Physics Reports* **446,** 97–216 (2007).
20. Hummert, S. *et al.* Evolutionary game theory: cells as players. *Molecular BioSystems* **10,** 3044–3065 (2014).
21. Nowak, M. A. *Evolutionary Dynamics* (Harvard University Press, 2006).
22. Epstein, J. M. Prisoner's dilemma and public goods games in different geometries: Compulsory versus voluntary interactions. *Complexity* **8,** 31–38 (2003).
23. Renaud, F. & de Meeüs, T. A simple model of host-parasite evolutionary relationships. Parasitism: compromise or conflict? *Journal of theoretical biology* **152,** 319–27 (1991).
24. Hummert, S., Hummert, C., Schröter, A., Hube, B. & Schuster, S. Game theoretical modelling of survival strategies of *Candida albicans* inside macrophages. *Journal of Theoretical Biology* **264,** 312–8 (2010).
25. Tyc, K. M., Kühn, C., Wilson, D. & Klipp, E. Assessing the advantage of morphological changes in *Candida albicans*: A game theoretical study. *Frontiers in Microbiology* **5,** 1–11 (2014).
26. Bohl, K. *et al.* Evolutionary game theory: molecules as players. *Molecular BioSystems* **10,** 3066–74 (2014).
27. Latgé, J.-P. *Aspergillus fumigatus* and Aspergillosis. *Clinical Microbiology Reviews* **12,** 310–350 (1999).
28. Codina, R., Fox, R. W., Lockey, R. F., DeMarco, P. & Bagg, A. Typical levels of airborne fungal spores in houses without obvious moisture problems during a rainy season in Florida, USA. *Journal of Investigational Allergology and Clinical Immunology* **18,** 156–162 (2008).
29. Brakhage, A. A., Bruns, S., Thywissen, A., Zipfel, P. F. & Behnsen, J. Interaction of phagocytes with filamentous fungi. *Current Opinion in Microbiology* **13,** 409–415 (2010).
30. Heinekamp, T. *et al.* Interference of *Aspergillus fumigatus* with the immune response. *Seminars in immunopathology* **37,** 141–52 (2015).
31. Aimanianda, V. *et al.* Surface hydrophobin prevents immune recognition of airborne fungal spores. *Nature* **460,** 1117–1121 (2009).
32. Brakhage, A. A. & Langfelder, K. Menacing Mold: The Molecular Biology of *Aspergillus fumigatus*. *Annual Review of Microbiology* **56,** 433–455 (2002).
33. Weibel, E. R. *Morphometry of the Human Lung* (Springer Berlin Heidelberg, 1963).
34. Hasenberg, M., Stegemann-Koniszewski, S. & Gunzer, M. Cellular immune reactions in the lung. *Immunological Reviews* **251,** 189–214 (2013).
35. Alonso, C., Waring, A. & Zasadzinski, J. A. Keeping lung surfactant where it belongs: protein regulation of two-dimensional viscosity. *Biophysical Journal* **89,** 266–73 (2005).
36. Kozel, T. R., Wilson, M. A., Farrell, T. P. & Levitz, S. M. Activation of C3 and binding to *Aspergillus fumigatus* conidia and hyphae. *Infection and Immunity* **57,** 3412–7 (1989).
37. Levitz, S. M. Overview of host defenses in fungal infections. *Clinical Infectious Diseases* **14,** S37–S42 (1992).
38. Osherov, N. Interaction of the pathogenic mold *Aspergillus fumigatus* with lung epithelial cells. *Frontiers in Microbiology* **3,** 1–9 (2012).
39. Margalit, A. & Kavanagh, K. The innate immune response to *Aspergillus fumigatus* at the alveolar surface. *FEMS Microbiology Reviews* **11,** 1–18 (2015).
40. Steele, C. *et al.* The Beta-Glucan Receptor Dectin-1 Recognizes Specific Morphologies of *Aspergillus fumigatus*. *PLOS Pathogens* **1,** e42 (2005).
41. Bruns, S. *et al.* Production of extracellular traps against *Aspergillus fumigatus in vitro* and in infected lung tissue is dependent on invading neutrophils and influenced by hydrophobin RodA. *PLOS Pathogens* **6,** e1000873 (2010).
42. Hillmann, F. *et al.* Virulence determinants of the human pathogenic fungus *Aspergillus fumigatus* protect against soil amoeba predation. *Environmental Microbiology* **17,** 2858–2869 (2015).
43. Roilides, E., Katsifa, H. & Walsh, T. J. Pulmonary host defences against *Aspergillus fumigatus*. *Research in Immunology* **149,** 454–65; discussion 523–4 (1998).
44. Mircescu, M. M., Lipuma, L., van Rooijen, N., Pamer, E. G. & Hohl, T. M. Essential Role for Neutrophils but not Alveolar Macrophages at Early Time Points following *Aspergillus fumigatus* Infection. *The Journal of Infectious Diseases* **200,** 647–656 (2009).
45. Hector, R. F., Yee, E. & Collins, S. Use of DBA/2N Mice in Models of Systemic Candidiasis and Pulmonary and Systemic Aspergillosis. *Infection and Immunity* **58,** 1476–1478 (1990).
46. Speth, C., Rambach, G., Lass-Flörl, C., Dierich, M. P. & Würzner, R. The role of complement in invasive fungal infections. *Mycoses* **47,** 93–103 (2004).
47. Philippe, B. *et al.* Killing of *Aspergillus fumigatus* by alveolar macrophages is mediated by reactive oxidant intermediates. *Infection and Immunity* **71,** 3034–3042 (2003).
48. Lambrecht, B. N. Alveolar Macrophage in the Driver's Seat. *Immunity* **24,** 366–368 (2006).
49. Segal, B. H. Role of macrophages in host defense against aspergillosis and strategies for immune augmentation. *The Oncologist* **12,** 7–13 (2007).
50. Bowden, D. H. The alveolar macrophage. *Environmental Health Perspectives* **55,** 327–341 (1984).
51. Butterfield, T. A., Best, T. M. & Merrick, M. A. The Dual Roles of Neutrophils and Macrophages in Inflammation: A Damage and Repair. *Journal of Athletic Training* **41,** 457–465 (2006).
52. Meier, A. *et al.* Toll-like receptor (TLR) 2 and TLR4 are essential for *Aspergillus*-induced activation of murine macrophages. *Cellular Microbiology* **5,** 561–570 (2003).
53. Herzog, E. L., Brody, A. R., Colby, T. V., Mason, R. & Williams, M. C. Knowns and unknowns of the alveolus. *Proceedings of the American Thoracic Society* **5,** 778–782 (2008).
54. McCormick, A., Loeffler, J. & Ebel, F. *Aspergillus fumigatus*: Contours of an opportunistic human pathogen. *Cellular Microbiology* **12,** 1535–1543 (2010).
55. Bozza, S. *et al.* Dendritic cells transport conidia and hyphae of *Aspergillus fumigatus* from the airways to the draining lymph nodes and initiate disparate Th responses to the fungus. *Journal of Immunology (Baltimore, Md.: 1950)* **168,** 1362–1371 (2002).
56. Roilides, E., Sein, T., Roden, M., Schaufele, R. L. & Walsh, T. J. Elevated serum concentrations of interleukin-10 in nonneutropenic patients with invasive aspergillosis. *The Journal of Infectious Diseases* **183,** 518–20 (2001).

57. Parker, H., Horsfield, K. & Cumming, G. Morphology of distal airways in the human lung. *Journal of Applied Physiology (Bethesda, Md.: 1985)* **31,** 386–391 (1971).
58. Bastacky, J. & Goerke, J. Pores of Kohn are filled in normal lungs: low-temperature scanning electron microscopy. *Journal of Applied Physiology (Bethesda, Md.: 1985)* **73,** 88–95 (1992).
59. MacKay, D. J. C. *Information theory, inference, and learning algorithms* vol. 7 (Cambridge University Press, Cambridge, 2003), 4th edn.

Acknowledgements
We thank Carl-Magnus Svensson for valuable discussions regarding the statistical evaluation of the results. This work was financially supported by the excellence graduate school Jena School for Microbial Communication (JSMC) and the CRC/TR124 FungiNet (Projects A1, B1, B4 and C6) that are both funded by the Deutsche Forschungsgemeinschaft (DFG).

Author Contributions
J.P., P.F.Z. and M.T.F. conceived and designed the study. M.T.F. contributed materials and computational resources. J.P. processed the data, implemented and applied the computational algorithm. J.P., S.T., S.S., A.A.B., P.F.Z. and M.T.F. evaluated and analysed the results. J.P., S.T., S.S., A.A.B., P.F.Z. and M.T.F. wrote the manuscript and revised it critically.

Additional Information
Supplementary information accompanies this paper at http://www.nature.com/srep

Competing financial interests: The authors declare no competing financial interests.

How to cite this article: Pollmächer, J. *et al.* Deciphering the Counterplay of *Aspergillus fumigatus* Infection and Host Inflammation by Evolutionary Games on Graphs. *Sci. Rep.* **6**, 27807; doi: 10.1038/srep27807 (2016).

Supplementary Information

Deciphering the Counterplay of *Aspergillus fumigatus* Infection and Host Inflammation by Evolutionary Games on Graphs

Johannes Pollmächer[1,2], Sandra Timme[1,2], Stefan Schuster[3], Axel A. Brakhage[2,4], Peter F. Zipfel[2,5], and Marc Thilo Figge[1,2,*]

[1]Research Group Applied Systems Biology, Leibniz Institute for Natural Product Research and Infection Biology – Hans Knöll Institute, Jena, Germany
[2]Faculty of Biology and Pharmacy, Friedrich Schiller University Jena, Germany
[3]Department of Bioinformatics, Faculty of Biology and Pharmacy, Friedrich Schiller University Jena, Germany
[4]Department of Molecular and Applied Microbiology, Leibniz Institute for Natural Product Research and Infection Biology – Hans Knöll Institute, Jena, Germany
[5]Department of Infection Biology, Leibniz Institute for Natural Product Research and Infection Biology – Hans Knöll Institute, Jena, Germany
[*]E-mail: thilo.figge@leibniz-hki.de

Table S1: Game-dependent morphotype options of *A. fumigatus*.

permitted morphotype (yes/no)	*A. fumigatus* strategy/morphotype			
	resting (R)	swollen (S)	hyphal (H)	dead (D)
Game I: complement system	yes	yes	no	no
Game II: AM	yes	yes	yes	yes
Game III: PMN	yes	yes	yes	yes

Possible strategies for fungal cells in the three different games. In Game I only resting and swollen conidia occur, while in Game II and Game III all four strategies are possible.

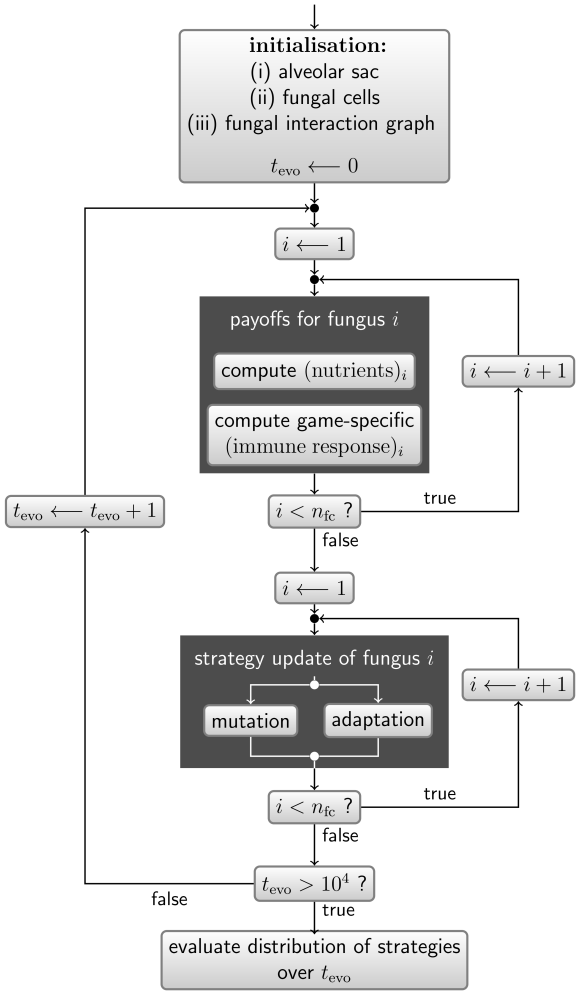

Figure S1: Simulation algorithm of each evolutionary game. Schematic overview of the simulation algorithm as applied for each evolutionary games on the fungal interaction graphs in alveolar sacs. Iterations over evolutionary steps t_{evo} include the computation of payoffs per fungus and microscopic strategy updates based on the concepts of mutation and adaptation. The number of fungal cells for which simulations are performed in the alveolar sac is denoted by n_{fc}.

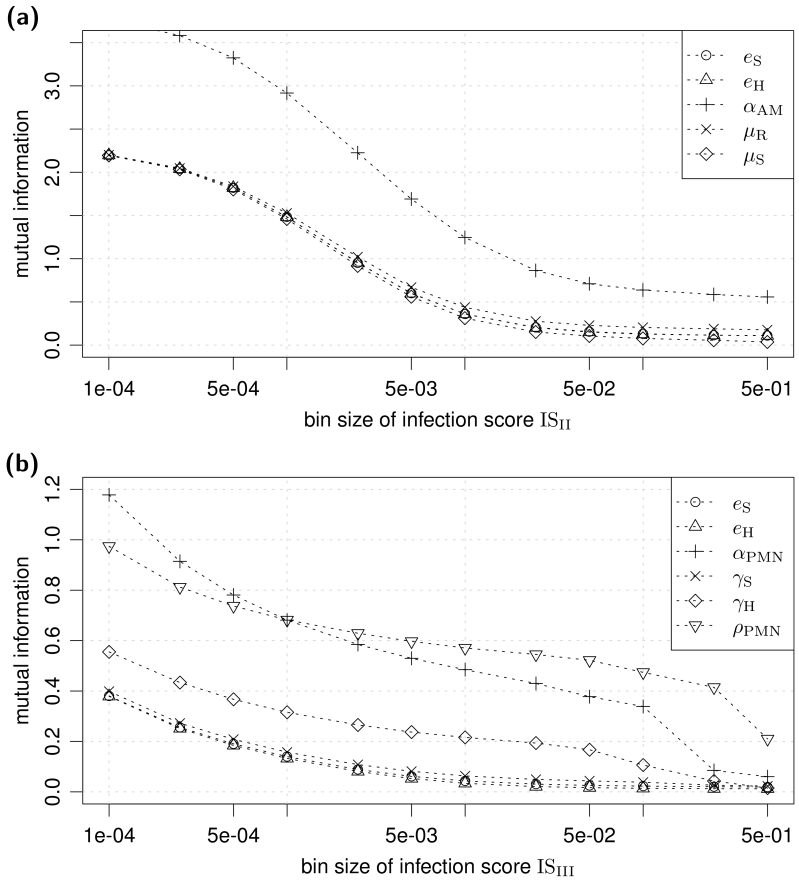

Figure S2: Dependence of mutual information on the bin size. Mutual information for the parameters of (a) Game II and (b) Game III as a function of the bin size of the infection score.

Table S2: Mutual information between infection score and parameters of Game II and Game III.

parameter	condition	MI (Game II)	MI (Game III)
$e_S = E_S/E_R$	$e_S \geq 1$	0.3679	0.0434
$e_H = E_H/E_S$	$e_H \geq 1$	0.3463	0.0338
$\alpha_{AM} = m_R/E_R$		**1.1439**	–
$\mu_R = m_R/m_H$	$\mu_R \geq 1$	0.3220	–
$\mu_S = m_S/m_R$	$\mu_S \geq 1$	0.3324	–
$\alpha_{PMN} = g_R/E_R$		–	**0.4847**
ρ_{PMN}	$\rho_{PMN} \in [0, 1]$	–	**0.5708**
$\gamma_S = g_S/g_R$	$\gamma_S \geq 1$	–	0.0632
$\gamma_H = g_H/g_S$	$\gamma_H \geq 1$	–	0.2161

The mutual information (MI) as a function of the infection score (IS) was computed for bin size 0.01 and for each of the games parameters. E_R, E_S, E_H describe the nutrient contributions for resting, swollen and hyphal fungal cells, respectively. μ_R, μ_S and γ_R, γ_S are fractions of response variables for the encounter of resting and swollen conidia and hyphae by either AM or PMN. *Bold* numbers denote the most relevant parameters of the respective evolutionary game, which are the AM activity α_{AM} in Game II and both PMN activity α_{PMN} and PMN recruitment ρ_{PMN} in Game III.

7. Predictive Virtual Infection Modeling of pathogen immune evasion in human whole-blood

frontiers in Immunology

ORIGINAL RESEARCH
published: 21 March 2018
doi: 10.3389/fimmu.2018.00560

Predictive Virtual Infection Modeling of Fungal Immune Evasion in Human Whole Blood

*Maria T. E. Prauße[1,2], Teresa Lehnert[1,3], Sandra Timme[1,2], Kerstin Hünniger[4,5], Ines Leonhardt[3,4], Oliver Kurzai[3,4,5] and Marc Thilo Figge[1,2,3]**

[1] Applied Systems Biology, Leibniz Institute for Natural Product Research and Infection Biology, Hans Knöll Institute (HKI), Jena, Germany, [2] Faculty of Biological Sciences, Friedrich Schiller University Jena, Jena, Germany, [3] Center for Sepsis Control and Care (CSCC), Jena University Hospital, Jena, Germany, [4] Fungal Septomics, Leibniz Institute for Natural Product Research and Infection Biology, Hans Knöll Institute (HKI), Jena, Germany, [5] Institute of Hygiene and Microbiology, University of Würzburg, Würzburg, Germany

frontiers in Immunology

ORIGINAL RESEARCH
published: 21 March 2018
doi: 10.3389/fimmu.2018.00560

Predictive Virtual Infection Modeling of Fungal Immune Evasion in Human Whole Blood

*Maria T. E. Prauße[1,2], Teresa Lehnert[1,3], Sandra Timme[1,2], Kerstin Hünniger[4,5], Ines Leonhardt[3,4], Oliver Kurzai[3,4,5] and Marc Thilo Figge[1,2,3]**

[1] Applied Systems Biology, Leibniz Institute for Natural Product Research and Infection Biology, Hans Knöll Institute (HKI), Jena, Germany, [2] Faculty of Biological Sciences, Friedrich Schiller University Jena, Jena, Germany, [3] Center for Sepsis Control and Care (CSCC), Jena University Hospital, Jena, Germany, [4] Fungal Septomics, Leibniz Institute for Natural Product Research and Infection Biology, Hans Knöll Institute (HKI), Jena, Germany, [5] Institute of Hygiene and Microbiology, University of Würzburg, Würzburg, Germany

Bloodstream infections by the human-pathogenic fungi *Candida albicans* and *Candida glabrata* increasingly occur in hospitalized patients and are associated with high mortality rates. The early immune response against these fungi in human blood comprises a concerted action of humoral and cellular components of the innate immune system. Upon entering the blood, the majority of fungal cells will be eliminated by innate immune cells, i.e., neutrophils and monocytes. However, recent studies identified a population of fungal cells that can evade the immune response and thereby may disseminate and cause organ dissemination, which is frequently observed during candidemia. In this study, we investigate the so far unresolved mechanism of fungal immune evasion in human whole blood by testing hypotheses with the help of mathematical modeling. We use a previously established state-based virtual infection model for whole-blood infection with *C. albicans* to quantify the immune response and identified the fungal immune-evasion mechanism. While this process was assumed to be spontaneous in the previous model, we now hypothesize that the immune-evasion process is mediated by host factors and incorporate such a mechanism in the model. In particular, we propose, based on previous studies that the fungal immune-evasion mechanism could possibly arise through modification of the fungal surface by as of yet unknown proteins that are assumed to be secreted by activated neutrophils. To validate or reject any of the immune-evasion mechanisms, we compared the simulation of both immune-evasion models for different infection scenarios, i.e., infection of whole blood with either *C. albicans* or *C. glabrata* under non-neutropenic and neutropenic conditions. We found that under non-neutropenic conditions, both immune-evasion models fit the experimental data from whole-blood infection with *C. albicans* and *C. glabrata*. However, differences between the immune-evasion models could be observed for the infection outcome under neutropenic conditions with respect to the distribution of fungal cells across the immune cells. Based on these predictions, we suggested specific experimental studies that might allow for the validation or rejection of the proposed immune-evasion mechanism.

Keywords: *Candida albicans*, *Candida glabrata*, immune evasion, state-based model, innate immune response, polymorphonuclear neutrophils, whole-blood infection assay

OPEN ACCESS

Edited by:
Lars Kaderali, Universitätsmedizin Greifswald, Germany

Reviewed by:
Stefan Klumpp, Georg-August-Universität Göttingen, Germany
Julio Vera González, Universitätsklinikum Erlangen, Germany

****Correspondence:***
Marc Thilo Figge
thilo.figge@leibniz-hki.de

Specialty section:
This article was submitted to Microbial Immunology, a section of the journal Frontiers in Immunology

Received: *20 December 2017*
Accepted: *06 March 2018*
Published: *21 March 2018*

Citation:
Prauße MTE, Lehnert T, Timme S, Hünniger K, Leonhardt I, Kurzai O and Figge MT (2018) Predictive Virtual Infection Modeling of Fungal Immune Evasion in Human Whole Blood. Front. Immunol. 9:560. doi: 10.3389/fimmu.2018.00560

INTRODUCTION

Even though pathogenic microbes constantly colonize the human skin or are inhaled, the human immune system is usually able to protect the body against infections. Thus, immunocompromised individuals have an increased risk for infections by opportunistic pathogens (1). In case of injuries or disturbed cellular integrity, the pathogens can easily overcome physical skin barriers and/or mucosal surfaces, and enter the host tissue or the blood stream (2, 3). Innate immune responses defend the host against microbial invaders (4–6), however, the exact interplay between pathogens and the immune defense is in many cases not fully resolved (7, 8). In order to investigate such unknown mechanisms, mathematical modeling is an appropriate approach to investigate complex biological systems at a quantitative level. Furthermore, mathematical models allow for hypothesis testing by varying single parameters or comparing various possible scenarios. This approach allows going beyond experimental limitations, for example, by quantifying biological processes that are not amenable to a direct measurement in experiment. Moreover, ethical concerns and financial efforts of experimental studies can be considerably reduced by computer simulations, because systematic variations of model parameters allow narrowing down the number and kind of further experimental investigations necessary to identify causal relationships responsible for experimentally observed effects (9). The iterative cycle of such a systems biology approach combines wet-lab and dry-lab experiments to their best advantage (10, 11).

In previous studies, we have applied a systems biology approach to investigate the complex interaction of the human-pathogenic fungus, *Candida albicans* with innate immune cells in human whole blood (12, 13). Interestingly, we observed that a relatively high proportion of *C. albicans* can survive in human blood and evades the immune response by a so far unknown mechanism. The experimental part of this study comprised human whole-blood infection assays, where blood samples from healthy donors were infected with fungal cells to acquire time-resolved data on the interaction of *C. albicans* with immune cells as well as fungal survival over the course of infection. Based on these experimental results, a bio-mathematical model was developed using a state-based modeling approach (12, 13). The model is composed of states that represent different *C. albicans* cell populations of the biological system. These include alive and killed *C. albicans* cells, which are either in extracellular space or phagocytosed by the immune cells, i.e., PMN or monocytes. Moreover, the model represents a population of fungal cells that can evade the immune defense, since these cells appear to be neither phagocytosed by immune cells nor killed extracellularly. Transitions between various states of cell populations can occur and these state changes represent biological processes like phagocytosis and killing. In the original state-based model (SBM), transition rates were defined to characterize the different transitions between the states, which represent the biological processes. The *a priori* unknown values for these transition rates were evaluated by applying the global parameter estimation algorithm *Simulated Annealing* that is based on the *Metropolis Monte Carlo* scheme (12, 13). This algorithm explores the space of transition rates and searches for the global minimum of the fitting error, i.e., the deviation between the simulated and experimentally measured kinetics, and by that yields values for the transition rates that together achieve optimal agreement between these kinetics. The resulting rates indicated that the larger number of *C. albicans* cells inside PMN, in comparison to the much smaller number of fungal cells inside monocytes, is not merely a consequence of the higher number of PMN than monocytes, but is also due to a larger phagocytosis rate of PMN compared to monocytes. This quantification, which is not directly accessible from the experimental data alone, allowed us to generally conclude that elimination of *C. albicans* cells in human blood is governed by PMN.

In the SBM, fungal cells that evaded the immune response were assumed to undergo a spontaneous process with a constant transition rate and we will refer to it as *spon-IE model* from now on (see **Figure 1A**). While the exact mechanism causing immune evasion of *C. albicans* in human blood has not been identified yet, our previous studies already allowed for the rejection of various hypotheses. In the work by Hünniger et al. (12) it has been shown that the non-filamentous *efg1*Δ, *cph1*Δ mutant of *C. albicans,* and even thimerosal-killed *C. albicans* yeast cells are both able to evade the immune response. These observations imply that the fungal cells do not play an active role in the acquisition of immune-evasive properties. Therefore, we addressed aspects of the host. However, we found that the addition of fresh blood of the same donor to an infected blood sample after 2 h did not result in higher elimination of fungal cells, implying that the hypothesis of early PMN exhaustion in the infection assay could be rejected. Additionally, we observed that during the 4 h of whole-blood infection the number of immune cells remained fairly constant. Thus, acquisition of immune evasion by fungal cells inside the phagocytes, which might then be followed by the destruction of phagocytic immune cells, appears to be unlikely. This lytic escape mechanism, which has been observed for macrophages (14), has not been reported for human PMN in *C. albicans* infection.

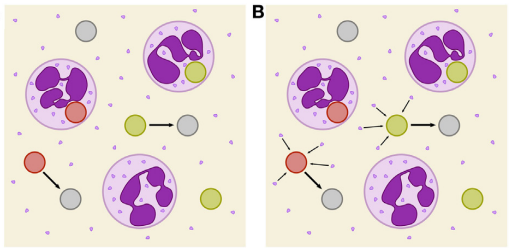

FIGURE 1 | Schematic depiction of two immune-evasion mechanisms. PMN (purple) with granula and fungal cells are either alive (green), killed (red), or immune evasive (gray). **(A)** Illustration of spontaneously evading fungal cells. **(B)** Illustration of the PMN-mediated immune-evasion mechanism, which is associated with degranulation on first-time phagocytosis of fungal cells by PMN. Degranulation is assumed to mediate the release of proteins into extracellular space that enables fungal cells to evade subsequent killing and phagocytosis by modification of their surface.

In this study, we investigate the unresolved mechanism of immune evasion by pathogens in human whole blood. This is realized by making predictions based on mathematical modeling of the infection kinetics and by comparing various infection scenarios that may be tested in experiment. Based on our previously developed state-based virtual infection model (12, 13), we hypothesize that the immune-evasion process is mediated by host factors and incorporate such a mechanism in the model. Our hypothesis is motivated by the experimental observation that even thimerosal-killed *C. albicans* cells can acquire immune-evasive properties. Thus, pathogen immune evasion may be actively driven by the host. Although PMN are the main actors in the defense against *C. albicans,* immune cells also have been shown to cause remodeling of the *C. albicans* cell wall (15). However, while it is known that PMN degranulation is associated with the release of antimicrobial effector proteins that can kill *C. albicans* cells in extracellular space (16, 17), the consequences of the cell wall remodeling is yet not clear, e.g., whether or not it enables the immune evasion by the pathogen. We here consider the possibility that PMN degranulation is associated with the secretion of effector molecules that may cause immune evasion. We investigate the possibility that these PMN-derived molecules may change the pathogen surface and thereby render the pathogen undetectable for immune cells (see **Figure 1B**). We will refer to the model that assumes a PMN-mediated evasion mechanism as *PMNmed-IE model* in the following.

The PMNmed-IE model will be compared with the spon-IE model by simulating the immune response to pathogens in healthy individuals as well as in virtual patients with neutropenia. Furthermore, we also extend this analysis to the fungus *C. glabrata*, which attributes to the rise of microbial infection in the clinics, especially in elderly individuals and immunocompromised patients (18). The two fungal pathogens are part of the normal microbial flora of the majority of people and remain in a commensal state under healthy conditions (19). *C. albicans* and *C. glabrata*, respectively, rank first and second in isolation frequency in humans (20) and in immunocompromised patients can switch into a pathogenic state, overcome physical barriers, enter the bloodstream, and disseminate throughout the body (4, 7). In blood, the microorganisms are attacked and cleared by the innate immune response. However, we find that both pathogens—albeit to a different quantitative extent—have the ability to evade the immune response. This emphasizes once more the importance of investigating immune-evasion mechanisms by mathematical modeling in order to generate testable hypothesis that may be checked in experiment and ultimately enable medical intervention that cuts the pathogen escape route in and subsequent dissemination from human whole blood.

MATERIALS AND METHODS

Ethics Statement

This study was conducted according to the principles expressed in the Declaration of Helsinki. All protocols were approved by the Ethics Committee of the University Hospital Jena (permit number: 273-12/09). Written informed consent was obtained from all blood donors.

Fungal Strains and Culture

The GFP expressing *C. albicans* strain was constructed as described in Hünniger et al. (12) and grown in liquid yeast extract-peptone-dextrose (YPD) medium at 30°C. The GFP expressing *C. glabrata* strain (21) was incubated at 37°C in YPD medium. After overnight culture both strains were reseeded in fresh YPD medium followed by growing at 30 and 37°C, respectively, until they reached the mid-log-phase. Finally, the fungal cells were washed and harvested in HBSS until use.

Human Whole Blood Infection Assay

Human peripheral blood samples from healthy individuals were infected with either *C. albicans* or *C. glabrata*. The assay was performed as described previously (12). In short, $1{\cdot}10^6$ *Candida* cells were added per ml of anti-coagulated blood and incubated at 37°C with gentle rotation for indicated time points. Subsequent to the confrontation, samples were maintained at 4°C and further analyzed by flow cytometry. Flow cytometry gating strategy was performed as previously described using FlowJo 7.6.4 software to investigate the distribution of fungal cells in human blood (12). Survival of fungal cells was determined in a plating assay by analysis of recovered colony forming units after plating appropriate dilutions of all time points on YPD agar plates.

SBM of Whole-Blood Infection

Recently, we established a virtual infection model to simulate the immune response against the fungal pathogen *C. albicans* in human whole blood (12, 13). This enabled us to quantify innate effector mechanisms as well as *C. albicans* immune evasion based on experimental data as obtained by FACS analysis and survival assays during a time course of 4 h. The time-resolved data comprised *C. albicans* viability as well as its association to innate immune cells, i.e., monocytes and PMN. In the SBM, immune cells and fungal cells can populate specific states. We identified five combined units of these states that could be directly compared with the experimentally measured cell populations. The combined unit P_E involves all extracellular pathogens and is given by

$$P_E \equiv P_{AE} + P_{KE} + P_{AIE} + P_{KIE} \tag{1}$$

Here, the states P_{AE} and P_{KE} represent extracellular cells that are alive and killed, respectively. The states P_{AIE} and P_{KIE} describe pathogens that are either alive and evade the immune response or kill and evade the immune response. Note that alive extracellular cells do not comprise alive immune-evasive cells and that these combined units are excluding each other.

Pathogens P_{AE} and P_{KE} can be phagocytozed by immune cells and in the SBM we account for phagocytosis by monocytes (M) and PMN (N), where the latter may also be referred to as

neutrophils and are, therefore, labeled with N. An intracellular pathogen is either phagocytosed by a PMN

$$P_N \equiv \sum_{i\geq 0}\sum_{j\geq 0}(i+j)N_{i,j}, \quad (2)$$

or by a monocyte

$$P_M \equiv \sum_{i\geq 0}\sum_{j\geq 0}(i+j)M_{i,j}. \quad (3)$$

Here, the indices i and j refer to the immune cell state that is defined by the number of internalized alive and killed pathogens, respectively. The combined unit of killed pathogens is given by

$$P_K \equiv P_{KE} + P_{KIE} + \sum_{i\geq 0}\sum_{j\geq 0}(M_{i,j}+N_{i,j})j, \quad (4)$$

whereas the combined unit of alive pathogens is defined by

$$P_A \equiv P_{AE} + P_{AIE} + \sum_{i\geq 0}\sum_{j\geq 0}(M_{i,j}+N_{i,j})i. \quad (5)$$

Note that the total number of pathogens is given by $P \equiv P_E+P_N+P_M+P_{KIE}$ or $P \equiv P_K+P_A$.

The states are connected by transitions that indicate possible state changes and thereby enable to simulate the dynamics of the model (see Figure S1 in Supplementary Material). Transition rates characterize these state changes and are defined as the probability of a transition per simulation time step Δt. The SBM by Hünniger et al. (12) and Lehnert et al. (13) distinguished a rate for first and subsequent phagocytosis events by PMN, since it was assumed that a phagocytosis event activates the PMN and leads to a higher phagocytosis rate. Since this fact is not experimentally validated for whole-blood infection with *C. glabrata*, we here implement a single phagocytosis rate of PMN that accounts for both, first and subsequent phagocytosis events. Therefore, the SBM of whole-blood infection comprises seven different transition rates that are given by the phagocytosis rate ϕ_M of monocytes, the phagocytosis rate ϕ_N of PMN, the intracellular killing rates κ_M and κ_N of both monocytes and PMN, the transition rates γ and $\bar{\kappa}_{EK}$, which define the extracellular killing, and the spontaneous immune-evasion rate ρ (see Table S1 in Supplementary Material). As already noted in our previous study (12), occasional filamentation of fungal cells but no budding could be observed in samples of blood smears. Therefore, proliferation of fungal cells is not included in the SBM. An overview of the SBM simulation algorithm is briefly described in Section S1 in Supplementary Material and schematically illustrated in Figure S1 in Supplementary Material. For a detailed description of the SBM, including the definition of rates for state transitions and their estimation by the *Simulated Annealing* algorithm that is based on the *Metropolis Monte Carlo* scheme (22, 23), we refer to our previous studies by Hünniger et al. (12) and Lehnert et al. (13). Here, we briefly mention that the values of the transition rates in the virtual infection model were estimated such that deviations from the kinetics of the combined units as obtained from the experiments are minimized. A brief overview of the parameter estimation algorithm is given in Section S2 and Figure S2 in Supplementary Material.

Our object-oriented framework combining the SBM simulation algorithm and the parameter estimation is implemented in the programming language C++ and available for download from https://asbdata.hki-jena.de/publidata/PrausseEtAl2018_FrontImmunol/.

Modeling of Immune Evasion by Pathogens

As was observed in our previous analysis for *C. albicans*, pathogens can evade the immune response in the states alive (P_{AIE}) or killed (P_{KIE}), i.e., these cells can neither be phagocytosed nor killed by PMN and monocytes, and their total number is denoted by $P_{IE} \equiv P_{KIE} + P_{AIE}$ (12). Note that immune evasion of *C. albicans* in human whole blood was first predicted by our state-based virtual infection model and then also verified experimentally. Since the mechanisms of the immune evasion could not be identified yet, this process was assumed to occur spontaneously with time-independent transition rate

$$\rho = \text{constant} \quad (6)$$

and we refer to this model as spon-IE model. In this study, spontaneous immune evasion of pathogens (see **Figure 1A**) was compared to an immune-evasion mechanism, which was assumed to be mediated by PMN. Since PMN secrete antimicrobial peptides upon initial phagocytosis of pathogens, we speculated that these pathogens may also secrete proteins that can mediate the immune evasion (see **Figure 1B**), e.g., inducing alterations of pathogens by modulating its molecular surface. We accounted for this mechanism in the SBM by replacing the constant transition rate of the spon-IE model with the time-dependent rate

$$\rho(t = n\Delta t) = \bar{\rho}\sum_{m=0}^{n}\frac{N_{NP}(t' = m\Delta t)}{G_{(0,0)}(0)}\cdot\exp(-\gamma_R\cdot\Delta t(n-m)) \quad (7)$$

in the PMNmed-IE model. In close analogy to the rate of extracellular killing of pathogens by antimicrobial peptide-release from PMN (1), Eq. 7 represents the rate of pathogen immune evasion at time t as mediated by the sum of PMN-released proteins upon first phagocytosis events (N_{NP}) up to time point t. Note that the simulation algorithm performs n simulation steps with step size Δt to calculate the system dynamics at time point $t = n\Delta t$. The impact of secreted molecules is determined by the parameters $\bar{\rho}$ and γ_R, where the latter describes the half-life associated with the molecular degradation, such that the molecules' immune-evasive effect is exponentially decreasing after their release at time $t' = m\Delta t$. Therefore, the PMNmed-IE model comprises eight parameters, i.e., one more rate than the spon-IE model for spontaneous immune-evasion processes.

Simulation of Virtual Patients With Neutropenia

In order to study the difference between the two models, spon-IE and PMNmed-IE, we simulated infection scenarios in human whole blood under neutropenic conditions. More specifically, virtual patients were considered with gradually decreasing amounts of PMN within the range of medically established severity levels of neutropenia (24) (see **Table 1**) and the impact of these conditions was compared with regards to the two mechanisms of immune evasion. The simulation algorithm described in Lehnert et al. (13) was applied to human whole-blood samples of 1 ml containing $5\cdot10^5$ monocytes and $1\cdot10^6$ pathogens. For each infection

TABLE 1 | Number of PMN per ml blood for different severity levels of neutropenia.

State of disease	PMN (1/ml)
Healthy	$1.8 \cdot 10^6$–$8 \cdot 10^6$
Mild neutropenia	$<1.5 \cdot 10^6$
Moderate neutropenia	$<1 \cdot 10^6$
Severe neutropenia	$<5 \cdot 10^5$

scenario, we performed 50 simulations with transition rate values that were randomly sampled within their respective SD.

RESULTS

Whole-Blood Infection Show Pathogen-Specific Immune Response Kinetics

Whole-blood infection assays were performed for the two fungal pathogens, *C. albicans* and *C. glabrata*. At specific time points, whole-blood samples were analyzed using flow cytometry and survival assays to acquire time-resolved data for the association between pathogens and immune cells as well as viability of the pathogens. **Figures 2A,B,D,E** depict these experimental data (dashed lines) for *C. albicans* and *C. glabrata*, respectively.

Comparing the two pathogens, the fraction of extracellular fungal cells at 4 h post infection was highest for *C. albicans* with 15 ± 5.8%and lowest for *C. glabrata* with 8.9 ± 7.5%, where the sub-populations of alive and killed cells are comparable in size (see **Figures 2A,B,D,E**). In the case of an infection with *C. albicans*, a fraction of 6.5 ± 4.2% cells still remained alive at 4 h post infection, whereas survival assays revealed that 1.3 ± 1.5% of *C. glabrata* cells were not killed at that time point. Interestingly, the association of fungal cells to monocytes was markedly higher for *C. glabrata* with a fraction of 10.1 ± 2.7% compared to *C. albicans* with a fraction of 2.7 ± 1.9%. Furthermore, *C. albicans* showed only a slightly higher association of 82.3 ± 7.0% to PMN than *C. glabrata* (81.0 ± 8.1%), as was previously observed by Duggan et al. (25). Nevertheless, for both pathogens, the fraction of association to PMN was dominant over association to monocytes, i.e., by a factor eight for *C. glabrata* and by a factor 30 for *C. albicans*. Furthermore, Hopke et al. showed that degranulation of PMN has an impact on cell wall modulation in fungi, but whether this could enable pathogenic immune evasion is still unclear (15). These findings motivated our decision to focus on a PMN-mediated immune-evasion mechanism in comparison to spontaneous immune evasion.

Spontaneous and PMN-Mediated Immune Evasion in Agreement With Experimental Data

We investigated the possibility that PMN secrete upon initial phagocytosis of pathogen proteins that can mediate immune evasion, e.g., inducing alterations of the surface of pathogens (15) (see **Figure 1B**). This mechanism was studied by applying mathematical modeling for hypothesis testing, i.e., we compared the impact of spontaneous versus PMN-mediated immune evasion on the infection outcome. To this end, we modified a previously implemented state-based virtual infection model (12, 13) to realize the PMN-mediated evasion mechanism. We refer to this model as *PMNmed-IE model* to distinguish it from the previously modeled spontaneous immune evasion, which we refer to as *spon-IE model*.

The transition rate values of the SBM were determined by the global parameter estimation algorithm *Simulated Annealing* based on *Metropolis Monte Carlo* scheme. This algorithm aims at searching for the optimal agreement between the simulated kinetics and the experimental data obtained from the whole-blood infection assays. The resulting transition rate values of both models are given in the Tables S2 and S3 in Supplementary Material and the corresponding simulated kinetics are depicted in **Figure 2**. Here, the experimental kinetics correspond to the combined units introduced in the Section "Materials and Methods" plotted in **Figure 2**. The excellent agreement between experiment and simulation can be seen for the whole-blood infection assays with either *C. albicans* (see **Figures 2A,B**) or *C. glabrata* (see **Figures 2D,E**) with their transition rate values in **Figures 2C,F**.

For *C. albicans* infection, the comparison between the spon-IE model and the PMNmed-IE model revealed comparable values for most transition rates, such as ϕ_N, ϕ_M, κ_N, and $\bar{\kappa}_{EK}$ (see **Figure 2C**; Table S2 in Supplementary Material). The largest differences were observed for intracellular killing in monocytes $\left(\kappa_M^{\text{PMNmed-IE}} / \kappa_M^{\text{spon-IE}} = 1.66\right)$ and the decrease of the antimicrobial effect $\left(\gamma^{\text{PMNmed-IE}} / \gamma^{\text{spon-IE}} = 1.26\right)$. However, the whole-blood infection assay does not allow to directly measure differences in these values in order to distinguish between the two immune-evasion models. Similarly, quantitative differences could also be observed for the kinetics of extracellular killing due to antimicrobial peptides (see **Figure 3A**) as well as for the kinetics of immune evasion (see **Figure 3B**). However, these readouts of the simulations either yield only small quantitative differences (time-dependent killing by antimicrobial peptides) or are, despite the qualitatively different time course, again not directly accessible in experiment (time-dependent immune-evasion rate). Thus, while it is possible to reconcile both models with the experimental data, differences in directly measurable quantities could not be identified (see Figures S3 and S4 in Supplementary Material for *C. albicans*).

While the experimental kinetics for *C. glabrata* infection were also found to be in excellent agreement with both the spon-IE and the PMNmed-IE models (see **Figures 2D,E**), differences between the estimated transition rate values were relatively large with up to 23% (see **Figure 2F**; Table S3 in Supplementary Material). The time-dependent extracellular killing due to antimicrobial factors was found to be strongly different between the two models, i.e., the peak values were six times higher for spon-IE model than PMNmed-IE model (see **Figure 3A**) and also the kinetics of immune-evasion were indicative for a larger effect in the spon-IE model than the PMNmed-IE model (see **Figure 3B**). The amount of fungal cells that became immune-evasive increased until 45 min post infection and then leveled off at the predicted

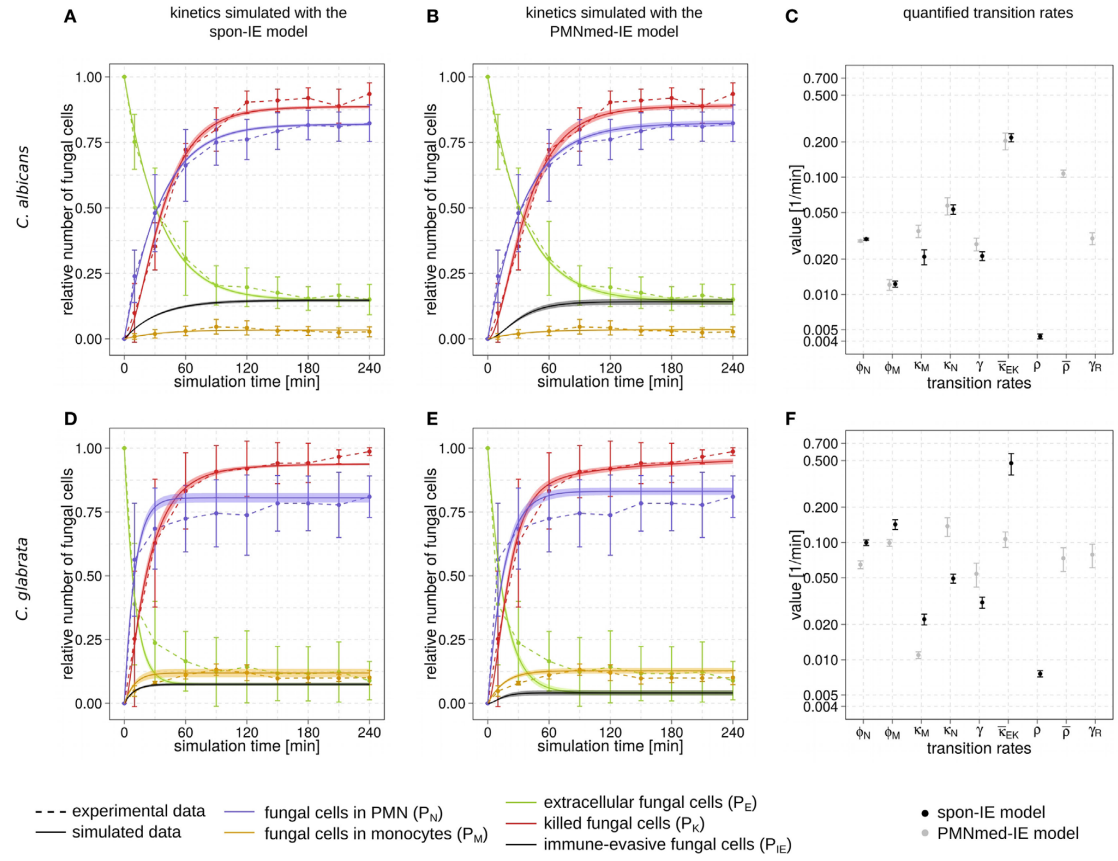

FIGURE 2 | Kinetics of combined units and corresponding transition rate values of the spon-IE model and the PMNmed-IE model. Experimental data from whole-blood infection assays (dashed lines) with corresponding SDs are compared to the simulated data (solid lines) by the spon-IE model (left column) and the PMNmed-IE model (middle column). The thickness of solid lines indicates the mean ± SD of 50 simulations with transition rate values that were randomly sampled within their corresponding SD. Mean values (data points) and SDs (error bars) of transition rates (right column) were quantified by the global parameter estimation algorithm *Simulated Annealing* based on *Metropolis Monte Carlo* scheme for the spon-IE model (black data points) and PMNmed-IE model (gray data points). The transition rates are given by the phagocytosis rate ϕ_N of PMN and the phagocytosis rate ϕ_M of monocytes, the intracellular killing rates κ_M and κ_N of both monocytes and PMN, the transition rates γ and $\bar{\kappa}_{EK}$ which define the extracellular killing, and the spontaneous immune-evasion rate ρ and the PMN-mediated immune-evasion rates $\bar{\rho}$ and γ_R, respectively. The time-course of the relative number of killed pathogens (P_K), which are indicated by red dashed lines, were experimentally measured by survival assays. The relative number of fungal cells that were associated with monocytes (P_M), PMN (P_N), or in extracellular space (P_E) were measured by association assays and indicated by orange, blue, or green dashed lines, respectively. The experimental results were compared with the corresponding combined units calculated for the simulated data. Black solid lines refer to the simulated time-course of immune-evasive fungal cells (P_{IE}). Kinetics of a *Candida albicans* infection simulated by **(A)** the spon-IE model and **(B)** the PMNmed-IE model. **(C)** Transition rates quantified by both models for a *C. albicans* infection. Kinetics of a *Candida glabrata* infection simulated by **(D)** the spon-IE model and **(E)** the PMNmed-IE model. **(F)** Transition rates quantified by both models for a *C. glabrata* infection.

value 7.47 ± 0.58% in the spon-IE model and 4.09 ± 1.0% in the PMNmed-IE model.

The comparison of whole-blood infections with the two pathogens revealed the estimated phagocytosis rate values ϕ_N and ϕ_M to be in both immune-evasion models lower for *C. albicans* than the phagocytosis rates of *C. glabrata*. Furthermore, for *C. albicans*, we found that $\phi_N > \phi_M$, whereas this relation is reversed for *C. glabrata*, reflecting the observed higher association of this pathogen to monocytes. Interestingly, the spon-IE model for infection with *C. glabrata* in comparison to infection with *C. albicans* predicted a higher peak value of the antimicrobial effect by a factor three (see **Figure 3A**). In contrast, the PMNmed-IE model predicted a peak value of the antimicrobial effect that is lower by a factor 0.5 for infection with *C. glabrata* compared to *C. albicans*. Apart from these observations, the two immune-evasion models could equally well explain the experimental

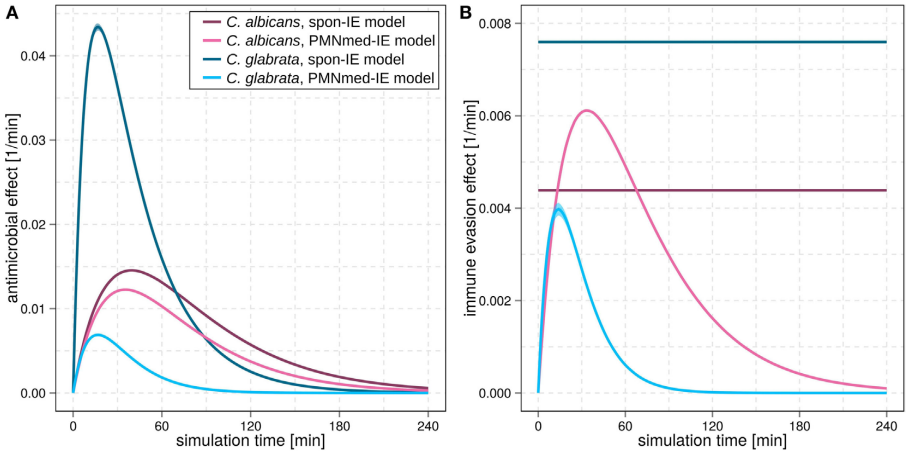

FIGURE 3 | Kinetics of the extracellular killing rate **(A)** and immune-evasion rate **(B)** predicted by spon-IE model and PMNmed-IE model. In both subfigures, purple lines represent results of infection with *Candida albicans* and blue lines depict results of infection with *Candida glabrata*. Predictions by the spon-IE model and PMNmed-IE model are indicated by dark colored lines and pale colored lines, respectively.

kinetics of infection in whole-blood samples as obtained from the healthy blood donors. To work out differences between the two immune-evasion models, we addressed the question how the models differ in their predictions on the infection kinetics for virtual patients with varying severity levels of neutropenia.

Simulations for Virtual Patients With Neutropenia Reveal Differences Between Immune-Evasion Models

The main difference between the spon-IE model and the PMNmed-IE model is that immune evasion in the latter is mediated by PMN and, therefore, is directly associated with the number of PMN in whole blood. Although most patients with candidemia are non-neutropenic, it is well known that neutropenia results in an impaired prognosis and facilitates disseminated infection and organ manifestation (16). Taking the previously estimated transition rate values for healthy blood donors as a reference, we gradually decreased the PMN number in the simulations within the range of medically established severity levels of neutropenia (see **Table 1**) and kept the number of monocytes and fungal cells fixed at $5 \cdot 10^5$ cells and $1 \cdot 10^6$ cells per milliliter, respectively. The predictions of simulations at 4 h post infection for the two immune-evasion models and for each of the two fungal pathogens are shown in **Figure 4**. As could be expected, an increase in the severity level of neutropenia was accompanied by a decreased interaction of fungal cells with PMN.

Virtual infections with *C. albicans* cells under neutropenic conditions revealed clear differences between the spon-IE model (see **Figure 4A**) and the PMNmed-IE model (see **Figure 4B**) at 240 min post infection. Differences in the models could be observed at the transition from moderate to severe neutropenia, where the fraction of immune-evasive fungal cells increased to 25.2 ± 1.0% in the spon-IE model and decreased to 10.4 ± 1.1% in PMNmed-IE model. These values for immune-evasive cells changed to 42.7 ± 1.6% for the spon-IE model and 0.24 ± 0.03% for the PMNmed-IE model in the simulations with the lowest PMN number ($5 \cdot 10^3$ cells/ml). Even though the latter immune-evasion model predicted the number of immune-evasive *C. albicans* cells after 240 min post infection to be vanishingly small, the fraction of extracellular alive fungal cells was larger with 24.5 ± 5.6% for the PMNmed-IE model than for the spon-IE model with 9.7 ± 1.1%. In the simulations with the lowest PMN number, the spon-IE model predicted an association of 46.4 ± 1.9% fungal cells to monocytes, which is clearly lower compared to 73.3 ± 5.8% in the PMNmed-IE model. Furthermore, the number of killed *C. albicans* cells differs between the two models with being predicted as 41.2 ± 2.3% in the spon-IE model and 67.1 ± 5.5% in the PMNmed-IE model. In general, we observed that the differences in various fractions of *C. albicans* cells between the two immune-evasion models clearly increase with progressing simulation time under neutropenic conditions. This can be seen in Video S1 in the Supplementary Material showing the development of the various fungal cell fractions at specific time points between time point 0 and 240 min post infection. Furthermore, differences between the models were observed for the distribution of fungal cells in immune cells for the condition of severe neutropenia with $5 \cdot 10^3$ PMN per milliliter. As shown in (**Figures 5A,B**), the distribution of alive and killed fungal cells across immune cells revealed differences between the immune-evasion models. Here it can be seen that the maximum of the distribution refers to PMN that contain two *C. albicans* cells for the spon-IE model (see **Figure 5A**) and three *C. albicans* cells for the PMNmed-IE model (see **Figure 5B**). Regarding the distribution of fungal cells in monocytes, the spon-IE model and the PMNmed-IE

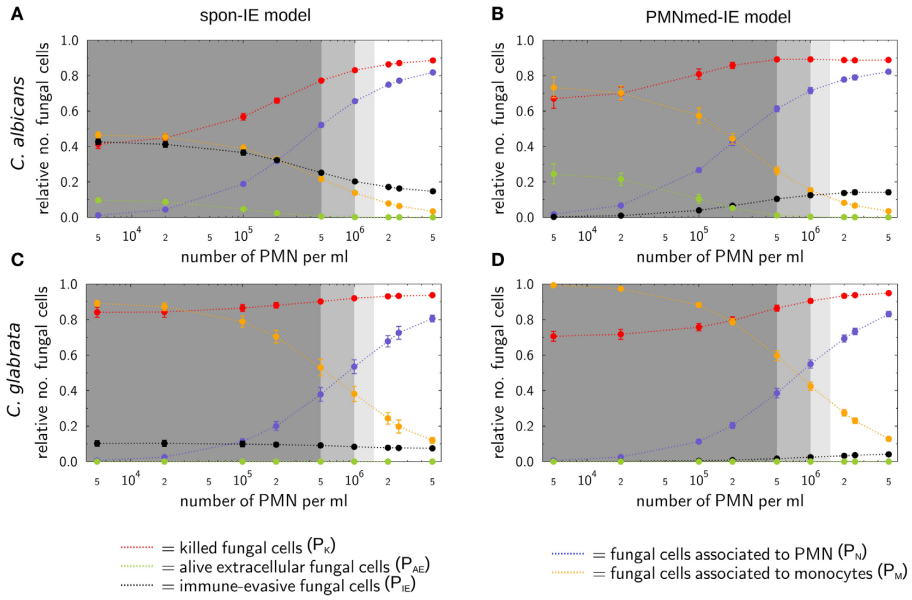

FIGURE 4 | Simulation results of the spon-IE model and of the PMNmed-IE model for different severity levels of neutropenia at the time point 240 min. The white region represents the physiological concentration of a whole-blood sample with $5{\cdot}10^5$ monocytes per milliliter and $5 \cdot 10^6$ PMN per milliliter. The PMN concentration declines with increasing severity levels of neutropenia: light gray area represents mild neutropenia ($<1.5{\cdot}10^6$ PMN/ml), medium gray area represents moderate neutropenia ($<1{\cdot}10^6$ PMN/ml), and dark gray area represents severe neutropenia ($<5{\cdot}10^5$ PMN/ml). The error bars indicate SDs of 50 simulations with transition rate values that were randomly sampled within their corresponding SD. **(A,B)** Depict simulation results of a virtual *Candida albicans* infection, respectively, for the spon-IE model and of the PMNmed-IE model and **(C,D)** accordingly for *Candida glabrata* infection. The relative numbers of killed fungal cells (red), alive extracellular fungal cells (green), phagocytosed fungal cells by monocytes (yellow), and by PMN (blue), as well as fungal cells which evaded the immune defense (black) are depicted. Note that alive extracellular cells do not comprise alive immune-evasive cells and that these combined units are excluding each other.

model predicted that the maximum number of monocytes which contained no fungal cells (see **Figure 5C**) and one fungal cell (see **Figure 5D**), respectively. These differences are accompanied by an overall shift of the distributions to higher numbers of phagocytes with more fungal cells in the PMNmed-IE model relative to the spon-IE model (see **Figures 5A–D**). In addition, the spon-IE model predicted a fraction of $7.0 \pm 0.5\%$ PMN that contain alive *C. albicans* cells (see **Figure 5A**), whereas this fraction of PMN was predicted to be more than two times larger in the PMNmed-IE model ($19.9 \pm 1.5\%$) (see **Figure 5B**).

Simulations for *C. glabrata* infection revealed as well differences between the spon-IE model and the PMNmed-IE model (see **Figures 4C,D**). The fraction of immune-evasive cells attained the value $10.2 \pm 1.6\%$ for the spon-IE model and $0.02 \pm 0.00\%$ for the PMNmed-IE model in the limit of lowest PMN number ($5 \cdot 10^3$ cells/ml). While these fractions reached different values, the fractions of extracellular alive cells were found to be vanishingly small in both models. At the PMN number of $5 \cdot 10^3$ cells/ml, the spon-IE model predicted $84.1 \pm 1.6\%$ of *C. glabrata* cells to be killed and the majority of cells were phagocytosed by monocytes ($89.2 \pm 1.7\%$). Analysis of simulations of the PMNmed-IE model revealed that $70.6 \pm 2.8\%$ of *C. glabrata* cells were killed and the majority of cells were phagocytosed by monocytes ($99.3 \pm 0.06\%$).

The time courses of each of these *C. glabrata* fractions at specific time points between 0 and 240 min post infection are shown in Video S2 in the Supplementary Material. Here it can be seen that at early time points post infection, the differences between the immune-evasion models is clearly visible. But with increasing simulation time these differences become smaller. While the distribution of killed and alive *C. glabrata* cells in PMN was similar for both immune-evasion models (see **Figures 5E,F**), differences in the distributions of fungal cells in monocytes, and their state of viability were observed (see **Figures 5G,H**). As can be seen in **Figure 5G**, the spon-IE model predicted that monocytes contained one to six fungal cells, where only a small fraction of fungal cells was alive, i.e., up to $7.1 \pm 0.9\%$ of monocytes contained alive fungal cells. This is in contrast to the PMNmed-IE model (see **Figure 5H**), which predicted a four times larger fraction of monocytes containing alive fungal cells ($31.7 \pm 1.0\%$). Thus, under severe neutropenic conditions, the most remarkable differences between the immune-evasion models were obtained with regard to the distribution of alive *C. glabrata* cells in monocytes.

Taken together, comparing the simulations of virtual patients under neutropenic conditions for the two immune-evasion models revealed, except for the number of immune-evaded cells,

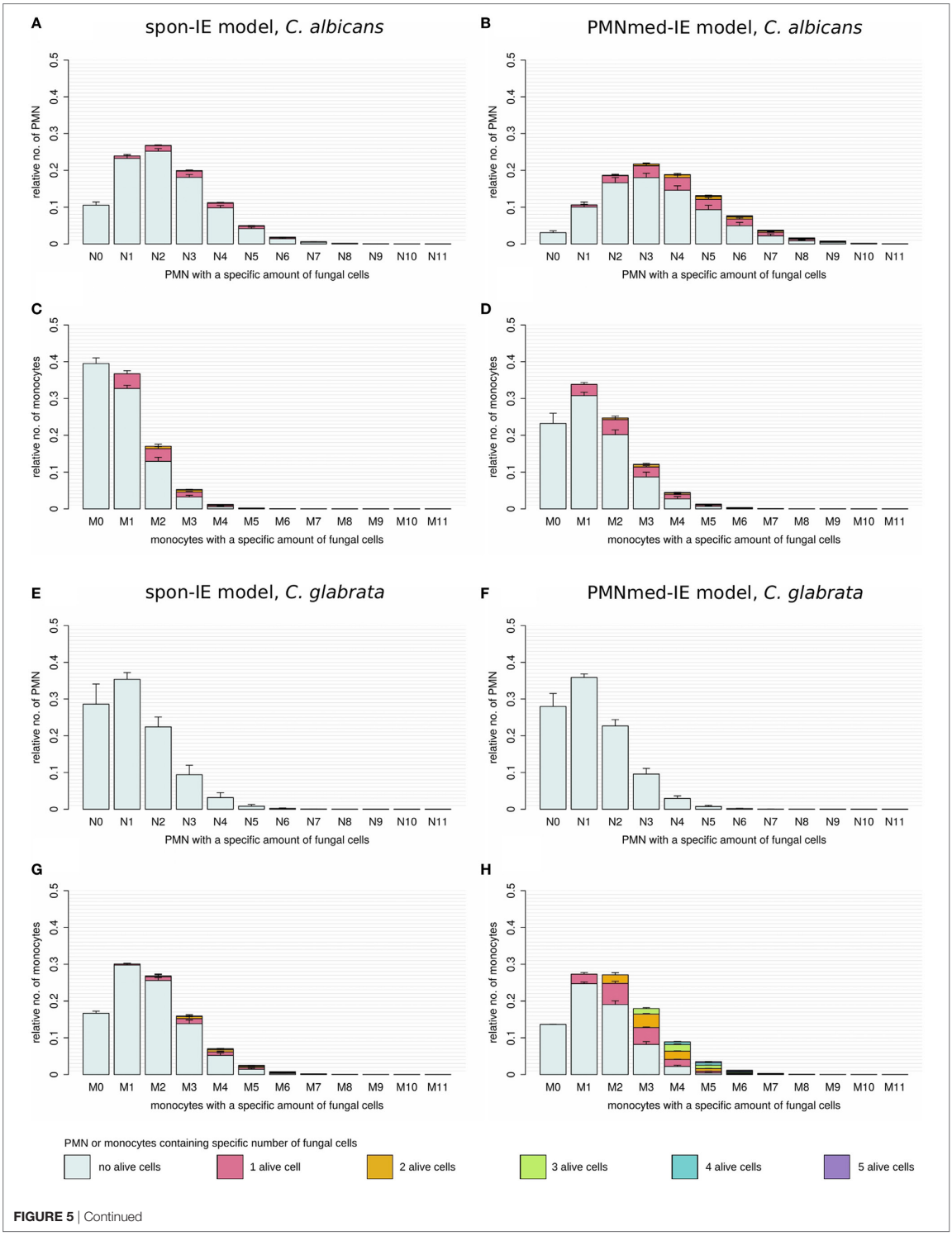

FIGURE 5 | Continued

FIGURE 5 | Distribution of total and alive fungal cells in PMN and monocytes for the most severe neutropenic condition 500 PMN/ml for the spon-IE model (left column) and PMNmed-IE model (right column). Relative numbers of PMN and monocytes are depicted corresponding to their association with fungal cells while each bar represents the immune cell type with the total number (0–11) of phagocytosed fungal cells. The error bars refer to SDs of 50 simulations with transition rate values that were randomly sampled within their corresponding SD. Gray-colored bars refer to "no alive" fungal cells, i.e., phagocytes contain killed cells only, bars in pink color refer to phagocytes with one alive fungal cell, orange bars refer to two alive fungal cells, green bars refer to phagocytes with three alive fungal cells, blue bars refer to phagocytes with four alive fungal cells, and purple bars refer to phagocytes with five alive fungal cells. **(A–D)** *Candida albicans* cell distribution for a virtual infection under the condition of severe neutropenia. **(E–H)** *Candida glabrata* cell distribution for a virtual infection under the condition of severe neutropenia.

a qualitative agreement for both pathogens (see **Figure 4**). Comparing the infection outcome between the two pathogens for each immune-evasion models revealed qualitative agreement, except for the alive extracellular fungal cells that increase (decrease) in the case of *C. albicans* (*C. glabrata*) with higher severity levels of neutropenia. As previously observed for whole blood from healthy donors, the fraction of immune-evasive cells for neutropenic patients was predicted to be higher for *C. albicans* than for *C. glabrata* in the spon-IE model. In contrast, the PMNmed-IE model predicted for both pathogens a quantitatively comparable fraction of immune-evasive cells that vanishes with the severity level of neutropenia. The phagocytosis by monocytes was found to be much lower for *C. albicans* than for *C. glabrata*, for both immune-evasion models, as previously observed for whole blood from healthy donors. This observation was also reflected by the distribution of fungal cells in immune cells (see **Figure 5**). *C. glabrata* was also represented by relatively large numbers of alive cells in monocytes at 4 h post infection. These findings indicate that infection in neutropenic whole blood could shed light on the mechanism of immune evasion by pathogens.

DISCUSSION

In this study, we applied mathematical modeling to investigate the yet unresolved mechanism of immune evasion by pathogens in human blood. The mechanism of immune evasion was first described in a systems biology study that quantified the immune response to *C. albicans* in human whole blood using a state-based virtual infection model (12, 13). Since the mechanism of immune evasion has not been identified so far, the immune evasion was assumed to occur spontaneously with a time-independent rate in the SBM (spon-IE model). In this study, we modified the spon-IE model by implementing a time-dependent immune-evasion mechanism mediated by PMN and refer to this virtual infection model as PMNmed-IE model. This is based on experimental findings, which show that neutrophils can modulate the composition of the fungal cell surface (15). The state-based modeling approach enables realization of such a process by a transition rate that is time-dependent and reflects PMN dynamics of phagocytosis and release of neutrophilic peptides. In order to verify the PMNmed-IE model and the spon-IE model, we estimated the *a priori* unknown transition rates of these models by fitting the simulated kinetics to the experimental data from human whole-blood infection assays with either *C. albicans* or *C. glabrata*. To further work out differences between the immune-evasion models, we simulated infection scenarios with reduced numbers of PMN that correspond to the range of medically established severity levels of neutropenia.

The comparison of the simulated kinetics for infections of blood with physiological and reduced numbers of PMN, the estimated transition rate values, as well as the pathogen distribution across immune cells revealed pathogen-specific differences between the two immune-evasion models. Based on these results, we suggest future experiments that could be performed to distinguish between the two immune-evasion mechanisms. While the kinetics of the experimental whole-blood infection assays for both pathogens could be reconciled with the virtual infection kinetics for both immune-evasion models, simulations for reduced PMN numbers revealed differences between the two immune-evasion models. These differences were largest for *C. albicans* infection and relatively small for infections with *C. glabrata*. In particular, the fractions of fungal cells that were killed, associated with monocytes or that became immune-evasive in simulations with reduced numbers of PMN, showed deviations between the two immune-evasion models most clearly for *C. albicans* (see **Figures 4A,B**). With decreasing PMN number, the PMNmed-IE model for this pathogen predicted that the fraction of immune-evasive pathogens remarkably decreased. Instead of becoming immune-evasive, *C. albicans* cells were mainly phagocytosed by monocytes and killed in this model. Furthermore, a significant fraction of fungal cells ($24.5 \pm 5.6\%$) was still alive and in extracellular space at 240 min post infection. In contrast to the PMNmed-IE model, the spon-IE model predicted the fractions of *C. albicans* cells that are (i) phagocytosed by monocytes, (ii) killed, or (iii) remained viable in extracellular space to be notably smaller, whereas the fraction of immune-evasive *C. albicans* cells is larger, because the constant rate of immune evasion does not depend on the decreasing number of PMN. Interestingly, both immune-evasion models predict even at 240 min post infection a remarkable fraction of *C. albicans* cells that are capable of dissemination. However, in the PMNmed-IE model these cells are mainly alive and extracellular due to absent phagocytosis whereas in the spon-IE model they are mostly immune-evasive fungal cells. Thus, both models would explain the observation that dissemination of *C. albicans* is more frequent in a neutropenic setting, albeit with different mechanisms (26–28). In order to verify the predicted differences for the two immune-evasion models, we suggest studying whole-blood infection assays either with depleted PMN numbers or with blood samples from neutropenic patients.

Regarding the pathogen distribution across immune cells, virtual infection scenarios for *C. albicans* with the low PMN number of $5 \cdot 10^3$ cells/ml revealed differences between the two immune-evasion models in the pathogen distributions within

PMN and monocytes as well as in the fraction of alive *C. albicans* cells in PMN (see **Figures 5A–D**). The experimental validation of the pathogen distribution in PMN and monocytes could be performed by Giemsa-stained blood smears obtained from *C. albicans*-infected blood samples of neutropenic patients. The overall distribution of *C. albicans* cells in PMN and monocytes could lead to further conclusions by comparing the experimental observations to simulated results, although information about viability cannot be obtained by Giemsa-stained blood smears. For the experimental validation of pathogen distribution across immune cells during infection of neutropenic blood samples it is necessary to differentiate between alive and killed fungal cells to unravel the immune-evasion mechanism of *C. glabrata*. The virtual infection of neutropenic blood by this pathogen showed clear differences between the immune-evasion models with regards to the distribution of alive pathogen cells in monocytes (see **Figures 5G,H**). The PMNmed-IE model predicted a relatively large fraction of alive fungal cells in monocytes at 240 min post infection. With increasing infection time in neutropenic patients, the high amount of alive fungal cells in monocytes may result in higher amounts of fungal cells in macrophages, which are professional phagocytes of the monocytic lineage. Since it is reported that *C. glabrata* cells are able to proliferate within macrophages and subsequently can leave these phagocytes (21, 29), this process could contribute to the increased risk for disseminated candidiasis in neutropenic patients (30).

Another suggestion for the experimental investigation of the immune-evasion mechanisms is to measure the activity of antimicrobial effector proteins inducing extracellular killing, because these kinetics are predicted to be different for the two immune-evasion models. This difference was observed to be relatively high for virtual *C. glabrata* infection at physiological numbers of PMN: in the spon-IE model the maximum value for the extracellular killing rate was much larger for *C. glabrata* infection compared to *C. albicans*, whereas in the PMNmed-IE model this peak value was predicted to be much smaller for *C. glabrata* infection (see **Figure 3A**). We, therefore, suggest measuring and comparing the activity of antimicrobial effector proteins inducing extracellular killing, such as lactoferrin, elastase 2 and myeloperoxidase, for both pathogens. In a previous study by Duggan et al. (25), where the differential recognition of *C. albicans* and *C. glabrata* by PMN was investigated, the concentration of these proteins were measured in supernatants of confrontation assays of PMN with the fungi 4 h after infection. For each of these antimicrobial proteins, the concentration in confrontation assays with *C. albicans* was observed to be higher than in confrontation assays with *C. glabrata*. We now suggest measuring not only the concentration of these antimicrobial peptides but also their fungicidal effect on the different pathogens in a comparative fashion. Moreover, our analysis predicts the time-window, where the largest difference for the kinetics of extracellular killing between both pathogens occurs, i.e., at 10 to 50 min post infection.

In future studies, the predictive power of virtual infection modeling can be further exploited by simulating infection scenarios with modified models that enable generating predictions for other hypotheses. For example, while the present study focused on the role of PMN-mediated immune evasion, a similar mechanism could be studied for monocytes, as well as a combination of contributions from both types of immune cells. Future computational studies could also benefit from spatial agent-based modeling. By applying a bottom-up approach, as previously performed by Lehnert et al. (13), the transition rate values of the SBM could be used as input for an agent-based model, where also spatial system properties are captured, such as the cells' morphology and/or migration pattern. This agent-based virtual infection model could, for example, be applied to investigate the impact of the various immune-evasion models on a hyper- and hypo-inflammatory immune response in human blood. In addition, the impact of the spatial distribution of PMN-secreted proteins causing immune evasion could be investigated by advancing the cellular agent-based virtual infection model to a hybrid agent-based model that simulates diffusion at the molecular level by partial differential equations. For example, in previous studies related to fungal infections, a hybrid agent-based model enabled to investigate the immune response against *Aspergillus fumigatus* in the alveoli of the human lung (31, 32). It could be shown that the migration pattern of immune cells is of high importance for the timely infection clearance and this lead to the prediction that chemotactic signaling molecules are essential for recruitment of phagocytes to the spatial position of fungal cells in the lung. Moreover, image-based systems biology approach combining mathematical modeling with microscopy experiments could be pursued (9, 33, 34). While imaging in whole blood is not performed today, host–pathogen interactions can be investigated by microscopy experiments under controlled conditions in a Petri dish. Recently, we have developed algorithms for the fully automated analysis of host–pathogen confrontation from microscopic endpoint experiments (33, 35–38), as well as from live cell imaging (39, 40). Similar to our recent comparative studies on *C. albicans* and *C. glabrata* phagocytosis (16, 41), host–pathogen confrontation assays could be performed and analyzed by automated image analysis to visualize surface alterations of immune-evading fungal cells.

ETHICS STATEMENT

This study was conducted according to the principles expressed in the Declaration of Helsinki. All protocols were approved by the Ethics Committee of the University Hospital Jena (permit number: 273-12/09). Written informed consent was obtained from all blood donors.

AUTHOR CONTRIBUTIONS

Conceived and designed this study: TL and MF. Provision of computational resources: MF. Provision of materials: OK. Data processing, implementation, and application of the computational algorithm: MP, TL, and MF. Performed experiments: KH and IL. Evaluation and analysis of the results: MP, TL, ST, KH, IL, OK, and MF. Draft and revision of the manuscript: MP, TL, ST, KH, IL, OK, and MF.

ACKNOWLEDGMENTS

The authors thank all anonymous blood donors.

FUNDING

This work was financially supported by the Center for Sepsis Control and Care (CSCC) (FKZ 01EO1502, project Quantim to MTF and OK) that is funded by the Federal Ministry for Education and Research, and by the CRC/TR124 FungiNet (project B4 to MTF and project C3 to OK) that is funded by the Deutsche Forschungsgemeinschaft (DFG).

SUPPLEMENTARY MATERIAL

The Supplementary Material for this article can be found online at https://www.frontiersin.org/articles/10.3389/fimmu.2018.00560/full#supplementary-material.

VIDEO S1 | Time-course of simulation results of both immune-evasion models for *C. albicans* infection for different severity levels of neutropenia. The error bars indicate standard deviations of 50 simulations with transition rate values that were randomly sampled within their corresponding standard deviation. The white region represents the physiological concentration of a whole-blood sample with $5{\cdot}10^5$ monocytes per milliliter and $5{\cdot}10^6$ PMN per milliliter. The PMN concentration declines with increasing severity levels of neutropenia: light gray area represents mild neutropenia ($<1.5{\cdot}10^6$ PMN/ml), medium gray area represents moderate neutropenia ($<1{\cdot}10^6$ PMN/ml) and dark gray area represents severe neutropenia ($<5{\cdot}10^5$ PMN/ml). **(A,B)** depict simulation results of a virtual *C. albicans* infection, respectively, for the spon-IE model and of the PMNmed-IE model. The relative numbers of killed fungal cells (red), alive extracellular fungal cells (green), phagocytosed fungal cells by monocytes (yellow) and by PMN (blue), as well as fungal cells which evaded the immune defense (black) are depicted. Note that alive extracellular cells do not comprise alive immune-evasive cells and that these combined units exclude each other.

VIDEO S2 | Time-course of simulation results of both immune-evasion models for *C. glabrata* infection for different severity levels of neutropenia. The error bars indicate standard deviations of 50 simulations with transition rate values that were randomly sampled within their corresponding SD. The white region represents the physiological concentration of a whole-blood sample with $5{\cdot}10^5$ monocytes per milliliter and $5{\cdot}10^6$ PMN per milliliter. The PMN concentration declines with increasing severity levels of neutropenia: light gray area represents mild neutropenia ($<1.5{\cdot}10^6$ PMN/ml), medium gray area represents moderate neutropenia ($<1{\cdot}10^6$ PMN/ml) and dark gray area represents severe neutropenia ($<5{\cdot}10^5$ PMN/ml). **(A,B)** depict simulation results of a virtual *C. glabrata* infection, respectively, for the spon-IE model and of the PMNmed-IE model. The relative numbers of killed fungal cells (red), alive extracellular fungal cells (green), phagocytosed fungal cells by monocytes (yellow) and by PMN (blue), as well as fungal cells which evaded the immune defense (black) are depicted. Note that alive extracellular cells do not comprise alive immune-evasive cells and that these combined units exclude each other.

REFERENCES

1. Kabir MA, Hussain MA, Ahmad Z. *Candida albicans*: a model organism for studying fungal pathogens. *ISRN Microbiol* (2012) 2012:1–15. doi:10.5402/2012/538694
2. Kühbacher A, Burger-Kentischer A, Rupp S. Interaction of *Candida* species with the skin. *Microorganisms* (2017) 5(2):32. doi:10.3390/microorganisms5020032
3. Lee SH, Jeong SK, Ahn SK. An update of the defensive barrier function of skin. *Yonsei Med J* (2006) 47(3):293–306. doi:10.3349/ymj.2006.47.3.293
4. Turvey SE, Broide DH. Innate immunity. *J Allergy Clin Immunol* (2010) 125 (2 Suppl 2):S24–32. doi:10.1016/j.jaci.2009.07.016
5. Cheng S-C, Sprong T, Joosten LAB, van der Meer JWM, Kullberg B-J, Hube B, et al. Complement plays a central role in *Candida albicans*-induced cytokine production by human PBMCs. *Eur J Immunol* (2012) 42(4):993–1004. doi:10.1002/eji.201142057
6. Beutler BA. TLRs and innate immunity. *Blood* (2009) 113(7):1399–407. doi:10.1182/blood-2008-07-019307
7. Mogensen TH. Pathogen recognition and inflammatory signaling in innate immune defenses. *Clin Microbiol Rev* (2009) 22(2):240–73. doi:10.1128/CMR.00046-08
8. Cheng SC, Joosten LAB, Kullberg BJ, Netea MG. Interplay between *Candida albicans* and the mammalian innate host defense. *Infect Immun* (2012) 80(4):1304–13. doi:10.1128/IAI.06146-11
9. Medyukhina A, Timme S, Mokhtari Z, Figge MT. Image-based systems biology of infection. *Cytometry A* (2015) 87(6):462–70. doi:10.1002/cyto.a.22638
10. Chavali AK, Gianchandani EP, Tung KS, Lawrence MB, Peirce SM, Papin JA. Characterizing emergent properties of immunological systems with multi-cellular rule-based computational modeling. *Trends Immunol* (2008) 29:589–99. doi:10.1016/j.it.2008.08.006
11. Materi W, Wishart DS. Computational systems biology in drug discovery and development: methods and applications. *Drug Discov Today* (2007) 12:295–303. doi:10.1016/j.drudis.2007.02.013
12. Hünniger K, Lehnert T, Bieber K, Martin R, Figge MT, Kurzai O. A virtual infection model quantifies innate effector mechanisms and *Candida albicans* immune escape in human blood. *PLoS Comput Biol* (2014) 10(2):e1003479. doi:10.1371/journal.pcbi.1003479
13. Lehnert T, Timme S, Pollmächer J, Hünniger K, Kurzai O, Figge MT. Bottom-up modeling approach for the quantitative estimation of parameters in pathogen-host interactions. *Front Microbiol* (2015) 6:608. doi:10.3389/fmicb.2015.00608
14. Erwig LP, Gow NAR. Interactions of fungal pathogens with phagocytes. *Nat Rev Microbiol* (2016) 14:163–76. doi:10.1038/nrmicro.2015.21
15. Hopke A, Nicke N, Hidu EE, Degani G, Popolo L, Wheeler RT. Neutrophil attack triggers extracellular trap-dependent *Candida* cell wall remodeling and altered immune recognition. *PLoS Pathog* (2016) 12(5):e1005644. doi:10.1371/journal.ppat.1005644
16. Duggan S, Leonhardt I, Hünniger K, Kurzai O. Host response to *Candida albicans* bloodstream infection and sepsis. *Virulence* (2015) 6(4):316–26. doi:10.4161/21505594.2014.988096
17. Gazendam RP, van de Geer A, Roos D, van den Berg TK, Kuijpers TW. How neutrophils kill fungi. *Immunol Rev* (2016) 273(1):299–311. doi:10.1111/imr.12454
18. Low C-Y, Rotstein C. Emerging fungal infections in immunocompromised patients. *F1000 Med Rep* (2011) 3(14). doi:10.3410/M3-14
19. Falagas ME, Roussos N, Vardakas KZ. Relative frequency of albicans and the various non-albicans *Candida* spp among candidemia isolates from inpatients in various parts of the world: a systematic review. *Int J Infect Dis* (2010) 14(11):e954–66. doi:10.1016/j.ijid.2010.04.006
20. Brunke S, Hube B. Two unlike cousins: *Candida albicans* and *C. glabrata* infection strategies. *Cell Microbiol* (2013) 15(5):701–8. doi:10.1111/cmi.12091
21. Seider K, Brunke S, Schild L, Jablonowski N, Wilson D, Majer O, et al. The facultative intracellular pathogen *Candida glabrata* subverts macrophage cytokine production and phagolysosome maturation. *J Immunol* (2011) 187(6):3072–86. doi:10.4049/jimmunol.1003730
22. de Vries G, Hillen T, Lewis M, Müller J, Schonfisch B. *A Course in Mathematical Biology: Quantitative Modeling with Computational Methods (Monographs on Mathematical Modeling and Computation)*. Philadelphia Society for Industrial and Applied Mathematics (2006).
23. Press W, Teukolsky S, Vetterling WT, Flannery BP. *Numerical Recipies: The Art of Scientific Computing*. 3rd ed. New York: Cambridge University Press (2007). 1256 p.
24. Boxer LA. How to approach neutropenia. *Hematology Am Soc Hematol Educ Program* (2012) 2012:174–82. doi:10.1182/asheducation-2012.1.174
25. Duggan S, Essig F, Hünniger K, Mokhtari Z, Bauer L, Lehnert T, et al. Neutrophil activation by *Candida glabrata* but not *Candida albicans* promotes fungal uptake by monocytes. *Cell Microbiol* (2015) 17(9):1259–76. doi:10.1111/cmi.12443

26. Guiot HFL, Fibbe WE, van't Wout JW. Risk factors for fungal infection in patients with malignant hematologic disorders: implications for empirical therapy and prophylaxis. *Clin Infect Dis* (1994) 18(4):525–32. doi:10.1093/clinids/18.4.525
27. Bow EJ, Loewen R, Cheang MS, Schacter B. Invasive fungal disease in adults undergoing remission-induction therapy for acute myeloid leukemia: the pathogenetic role of the antileukemic regimen. *Clin Infect Dis* (1995) 21(2):361–9. doi:10.1093/clinids/21.2.361
28. Verduyn Lunel FM, Meis JF, Voss A. Nosocomial fungal infections: candidemia. *Diagn Microbiol Infect Dis* (1999) 34(3):213–20. doi:10.1016/S0732-8893(99)00035-8
29. Kasper L, Seider K, Hube B. Intracellular survival of *Candida glabrata* in macrophages: immune evasion and persistence. *FEMS Yeast Res* (2015) 15(5):1–12. doi:10.1093/femsyr/fov042
30. Perlroth J, Choi B, Spellberg B. Nosocomial fungal infections: epidemiology, diagnosis, and treatment. *Med Mycol* (2007) 45(4):321–46. doi:10.1080/13693780701218689
31. Pollmächer J, Figge MT. Agent-based model of human alveoli predicts chemotactic signaling by epithelial cells during early *Aspergillus fumigatus* infection. *PLoS One* (2014) 9(10):e111630. doi:10.1371/journal.pone.0111630
32. Pollmächer J, Figge MT. Deciphering chemokine properties by a hybrid agent-based model of *Aspergillus fumigatus* infection in human alveoli. *Front Microbiol* (2015) 6:503. doi:10.3389/fmicb.2015.00503
33. Mech F, Wilson D, Lehnert T, Hube B, Figge MT. Epithelial invasion outcompetes hypha development during *Candida albicans* infection as revealed by an image-based systems biology approach. *Cytometry A* (2014) 85(2):126–39. doi:10.1002/cyto.a.22418
34. Figge MT, Murphy RF. Image-based systems biology. *Cytometry A* (2015) 87:459–61. doi:10.1002/cyto.a.22663
35. Mech F, Thywißen A, Guthke R, Brakhage AA, Figge MT. Automated image analysis of the host-pathogen interaction between phagocytes and *Aspergillus fumigatus*. *PLoS One* (2011) 6(5):e19591. doi:10.1371/journal.pone.0019591
36. Kraibooj K, Schoeler H, Svensson C, Brakhage AA, Figge MT. Automated quantification of the phagocytosis of *Aspergillus fumigatus* conidia by a novel image analysis algorithm. *Front Microbiol* (2015) 6:549. doi:10.3389/fmicb.2015.00549
37. Cseresnyes Z, Kraibooj K, Figge MT. Hessian-based quantitative image analysis of host-pathogen confrontation assays authors. *Cytometry A* (2018). doi:10.1002/cyto.a.23201
38. Kraibooj K, Park H-R, Dahse H-M, Skerka C, Voigt K, Figge MT. Virulent strain of *Lichtheimia corymbifera* shows increased phagocytosis by macrophages as revealed by automated microscopy image analysis. *Mycoses* (2014) 57:56–66. doi:10.1111/myc.12237
39. Brandes S, Mokhtari Z, Essig F, Hünniger K, Kurzai O, Figge MT. Automated segmentation and tracking of non-rigid objects in time-lapse microscopy videos of polymorphonuclear neutrophils. *Med Image Anal* (2015) 20(1):34–51. doi:10.1016/j.media.2014.10.002
40. Brandes S, Dietrich S, Hünniger K, Kurzai O, Figge MT. Migration and interaction tracking for quantitative analysis of phagocyte-pathogen confrontation assays. *Med Image Anal* (2017) 36:172–83. doi:10.1016/j.media.2016.11.007
41. Essig F, Hünniger K, Dietrich S, Figge MT, Kurzai O. Human neutrophils dump *Candida glabrata* after intracellular killing. *Fungal Genet Biol* (2015) 84:37–40. doi:10.1016/j.fgb.2015.09.008

Conflict of Interest Statement: The authors declare that the research was conducted in the absence of any commercial or financial relationships that could be construed as a potential conflict of interest.

frontiers

Supplementary Material

Predictive Virtual Infection Modeling of Pathogen Immune Evasion in Human Whole Blood

Maria T. E. Praußе, Teresa Lehnert, Sandra Timme, Kerstin Hünniger, Ines Leonhardt, Oliver Kurzai, Marc Thilo Figge*

*** Correspondence:** Marc Thilo Figge: thilo.figge@leibniz-hki.de

1 Supplementary Data

1.1 Supplementary Information

S1. Simulation algorithm of the state-based whole-blood infection model.

The temporal evolution of the state-based model (SBM) within the simulation time $t = 0, \ldots, t_{end}$ is calculated for each simulation time step Δt (with $\Delta t = 1$ min) by updating all individuals of the system with respect to their current state. In particular, an individual of state *s* will be updated by testing for transition into another state *s'*. Each state transition is associated with a rate, $r^{s \to s'}$, and will be executed with probability $P_{s \to s'} = r^{s \to s'} \Delta t$. The system is updated accordingly. As schematically depicted in Figure S1 in Supplementary Material, the simulation of the SBM for whole-blood infection comprises updating individuals of the states P_{AE} and P_{KE}, which are respectively alive extracellular pathogens and killed extracellular pathogens, as well as individuals of the states $M_{i,j}$ and $N_{i,j}$, which respectively represent monocytes and neutrophils containing i alive and j killed pathogens. Individuals of the states P_{AE} and P_{KE} are tested for extracellular killing and immune evasion, whereas individuals of the states $M_{i,j}$ and $N_{i,j}$ are tested for phagocytosis and intracellular killing. A description of the transition rates of the SBM and the respective state transitions are given in Table S1 in Supplementary Material.

This SBM simulation algorithm was implemented in the programming language C++ and is available for download from https://asbdata.hki-jena.de/publidata/PrausseEtAl2018_FrontImmunol/ .

S2. Parameter estimation by the global optimization method Simulated Annealing based on the Metropolis Monte Carlo scheme.

By randomly exploring the parameter space of transition rates used in the spon-IE model and PMNmed-IE model, the algorithm is able to find the global minimum of the least-square error (LSE) between the simulated data of the models and the experimental data acquired from the whole-blood infection assays. The flowchart of this algorithm is depicted in Figure S2 in Supplementary Material. The time-evolution of the state-based model kinetics, referred to as *combined units*, is simulated using parameter set $\vec{p}$ and compared with the experimental data by calculating the weighted sum of LSE ($E(\vec{p})$). This is followed by choosing a parameter set $\vec{p}'$ within a pre-defined range of ±10% from $\vec{p}$. Next, the model is simulated with the parameter set $\vec{p}'$ and the corresponding score $E(\vec{p}')$ is calculated. If $E(\vec{p}')$ attains a smaller value than $E(\vec{p})$, the new parameter set $\vec{p}'$ is accepted because of

the better fitting result. However, $\vec{p}'$ may also be accepted for $E(\vec{p}')$ larger than $E(\vec{p})$ with a probability that depends on the Boltzmann distribution (Metropolis Monte Carlo Step, see Step 3 in Figure S2 in Supplementary Material). This probability is decreased with progressing number of fitting steps f, simulating the system's annealing by a decreasing of temperature parameter $\tau(f)$ in the Boltzmann distribution. Thus the risk to accept an unfavorable parameter set $\vec{p}'$ decreases with the ongoing fitting procedure by the system's temperature decrease. The choice of a new parameter set $\vec{p}'$, its evaluation and acceptance or rejection is repeated for a specific number of fitting steps making up one fitting run. Fitting runs are repeated as wells starting from different initial parameter sets and the means and standard deviations of the determined optimal parameter sets resulting from these repetitions are calculated. Due to large numbers of fungal cells (P), monocytes (M) and polymorphonuclear neutrophils (N) in infected whole-blood samples, the state-based model simulation of such a system size is accompanied with large computation times. Therefore, the fitting procedure is designed in a step-wise fashion: The system size is gradually increased by factors of ten starting at $P = 100$, $M_{0,0} = 50$ and $N_{0,0} = 500$ up to $P = 10^6$, $M_{0,0} = 5 \cdot 10^5$ and $N_{0,0} = 5 \cdot 10^6$. *i.e.* keeping the ratio of cell numbers constant. Here, the optimal parameter values of a model system as determined by the above described estimation procedure serves as start values in fitting the state-based model for the next in size system.

This framework for parameter estimation of the state-based whole-blood infection model was implemented in the programming language C++ and is available for download from https://asbdata.hki-jena.de/publidata/PrausseEtAl2018_FrontImmunol/ .

1.2 Supplementary Videos

Video S1. Time-course of simulation results of both immune-evasion models for *C. albicans* infection for different severity levels of neutropenia. The error bars indicate standard deviations of 50 simulations with transition rate values that were randomly sampled within their corresponding standard deviation. The white region represents the physiological concentration of a whole-blood sample with $5 \cdot 10^5$ monocytes per milliliter and $5 \cdot 10^6$ PMN per milliliter. The PMN concentration declines with increasing severity levels of neutropenia: light gray area represents mild neutropenia ($< 1.5 \cdot 10^6 \frac{PMN}{ml}$), medium gray area represents moderate neutropenia ($< 1 \cdot 10^6 \frac{PMN}{ml}$) and dark gray area represents severe neutropenia ($< 5 \cdot 10^5 \frac{PMN}{ml}$). (**A**) and (**B**) depict simulation results of a virtual *C. albicans* infection, respectively, for the spon-IE model and of the PMNmed-IE model. The relative numbers of killed fungal cells (red), alive extracellular fungal cells (green), phagocytosed fungal cells by monocytes (yellow) and by PMN (blue), as well as fungal cells which evaded the immune defense (black) are depicted. Note that alive extracellular cells do not comprise alive immune-evasive cells and that these combined units exclude each other.

Video S2. Time-course of simulation results of both immune-evasion models for *C. glabrata* infection for different severity levels of neutropenia. The error bars indicate standard deviations of 50 simulations with transition rate values that were randomly sampled within their corresponding standard deviation. The white region represents the physiological concentration of a whole-blood sample with $5 \cdot 10^5$ monocytes per milliliter and $5 \cdot 10^6$ PMN per milliliter. The PMN concentration declines with increasing severity levels of neutropenia: light gray area represents mild neutropenia ($< 1.5 \cdot 10^6 \frac{PMN}{ml}$), medium gray area represents moderate neutropenia ($< 1 \cdot 10^6 \frac{PMN}{ml}$) and dark gray area represents severe neutropenia ($< 5 \cdot 10^5 \frac{PMN}{ml}$). (**A**) and (**B**) depict simulation results of a virtual *C. glabrata* infection, respectively, for the spon-IE model and of the PMNmed-IE model. The relative numbers of killed fungal cells (red), alive extracellular fungal cells (green), phagocytosed fungal cells by monocytes (yellow) and by PMN (blue), as well as fungal cells which evaded the immune defense (black) are depicted. Note that alive extracellular cells do not comprise alive immune-evasive cells and that these combined units exclude each other.

2 Supplementary Figures and Tables

2.1 Supplementary Tables

rate	description	state transition
$\boldsymbol{\phi_N}$	phagocytosis by neutrophils	$N_{i,j} + P_{AE} \rightarrow N_{i+1,j}$ $N_{i,j} + P_{KE} \rightarrow N_{i,j+1}$
$\boldsymbol{\phi_M}$	phagocytosis by monocytes	$M_{i,j} + P_{AE} \rightarrow M_{i+1,j}$ $M_{i,j} + P_{KE} \rightarrow M_{i,j+1}$
$\boldsymbol{\kappa_N}$	intracellular killing by neutrophils	$N_{i,j} \rightarrow N_{i-1,j+1}$
$\boldsymbol{\kappa_M}$	intracellular killing by monocytes	$M_{i,j} \rightarrow M_{i-1,j+1}$
$\boldsymbol{\kappa_{EK}(t)}$	extracellular killing by antimicrobial peptides released upon first-time PMN phagocytosis with decreasing activity rate depends on the activity of antimicrobial peptides, characterized by the rate $\bar{\kappa}_{EK}$, and the decay of their antimicrobial activity, characterized by γ, as defined in Hünniger et al. (2014) (1) and Lehnert et al. (2015) (2)	$P_{AE} \rightarrow P_{KE}$
$\boldsymbol{\rho}$	constant rate for the acquisition of immune evasion for spon-IE model	$P_{AE} \rightarrow P_{AIE}$ $P_{KE} \rightarrow P_{KIE}$
$\boldsymbol{\rho(t)}$	time dependent rate for the acquisition of immune evasion for PMNmed-IE model rate depends on the activity of effector molecules, characterized by $\bar{\rho}$ and the decay of their activity as characterized by γ_R (see Eq. (7) in the manuscript)	$P_{AE} \rightarrow P_{AIE}$ $P_{KE} \rightarrow P_{KIE}$

Table S1. Transition rates of the PMNmed-IE model and the spon-IE model for modeling the whole-blood infection assays. For details of the latter model, see Hünniger et al. (2014) (1) and Lehnert et al. (2015) (2).

C. albicans	mean $\times 10^{-2}$ $[min^{-1}]$ $\pm$ SD $\times 10^{-2}$ $[min^{-1}]$ (CV [%])	
rate	**spon-IE model**	**PMNmed-IE model**
ϕ_N	$2.97 \pm 0.061(2.1)$	$2.86 \pm 0.054(1.9)$
ϕ_M	1.23 ± 0.075 (6.1)	1.2 ± 0.13 (10.6)
κ_M	2.1 ± 0.31 (14.6)	3.5 ± 0.42 (12.2)
κ_N	5.3 ± 0.49 (9.2)	5.7 ± 0.97 (16.9)
$\bar{\kappa}_{EK}$	21.8 ± 1.8 (8.0)	20.44 ± 3.33 (16.3)
γ	2.13 ± 0.19 (8.8)	2.69 ± 0.34 (12.5)
ρ	0.44 ± 0.021 (4.8)	
$\bar{\rho}$		10.75 ± 0.34 (7.1)
γ_R		3.0 ± 0.35 (11.6)

Table S2. The transition rates of a virtual whole-blood infection with *C. albicans* for the spon-IE and PMNmed-IE model are given by the phagocytosis rate ϕ_N of PMN and the phagocytosis rate ϕ_M of monocytes, the intracellular killing rates κ_M and κ_N of both monocytes and PMN, the transition rates γ and $\bar{\kappa}_{EK}$ which define the extracellular killing and the spontaneous immune evasion rate ρ and the PMN-mediated immune evasion rates $\bar{\rho}$ and γ_R, respectively. The mean values and standard deviations (SD) were obtained by several repetitions of the parameter estimation procedure which is described in the work of Lehnert et al. (2014) (1,2). CV refers to the coefficient of variation which defines the ratio of SD to the mean.

C. glabrata	**mean $\times 10^{-2}$ $[min^{-1}]$ $\pm$ SD $\times 10^{-2}$ $[min^{-1}]$ (CV [%])**	
rate	**spon-IE model**	**PMNmed-IE model**
ϕ_N	10.0 ± 0.55 (5.5)	6.5 ± 0.49 (7.6)
ϕ_M	14.3 ± 1.4 (9.6)	9.9 ± 0.64 (6.5)
κ_M	2.2 ± 0.23 (10.6)	1.10 ± 0.073 (6.6)
κ_N	4.9 ± 0.43 (8.7)	13.8 ± 2.5 (18.3)
$\bar{\kappa}_{EK}$	47.5 ± 9.9 (20.8)	10.7 ± 1.6 (15.1)
γ	3.1 ± 0.34 (10.9)	5.4 ± 1.3 (23.1)
ρ	0.76 ± 0.047 (6.2)	
$\bar{\rho}$		7.3 ± 1.7 (22.8)
γ_R		7.9 ± 1.8 (22.7)

Table S3. The transition rates of a virtual whole-blood infection with *C. glabrata* for the spon-IE (left column in each split) and PMNmed-IE model (right column in each split) are given by the phagocytosis rate ϕ_N of PMN and the phagocytosis rate ϕ_M of monocytes, the intracellular killing rates κ_M and κ_N of both monocytes and PMN, the transition rates γ and $\bar{\kappa}_{EK}$ which define the extracellular killing and the spontaneous immune evasion rate ρ and the PMN-mediated immune evasion rates $\bar{\rho}$ and γ_R, respectively. The mean values and standard deviations (SD) were obtained by several repetitions of the parameter estimation procedure which is described in the work of Lehnert et al. (2014) (1,2). CV refers to the coefficient of variation which defines the ratio of SD to the mean.

2.2 Supplementary Figures

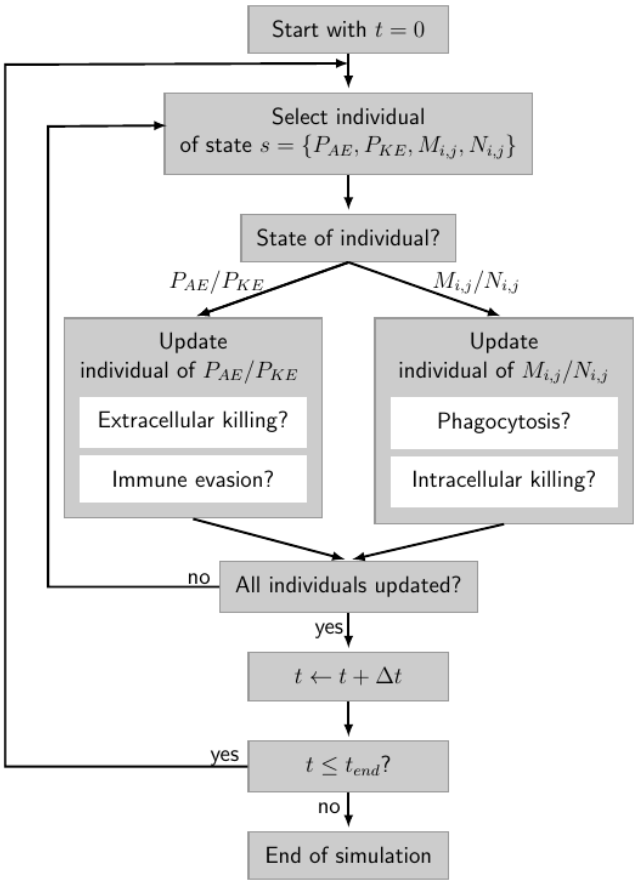

Figure S1. Flowchart of the simulation algorithm for the state-based whole-blood infection model. This algorithm is explained in detail in section S1 in Supplementary Material. The flowchart is adapted from Lehnert et al. (2015) (2).

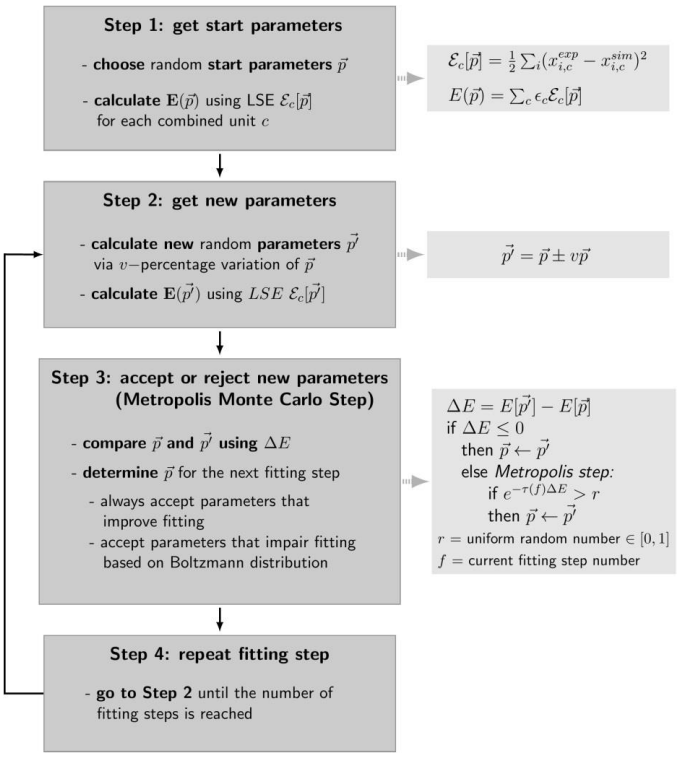

Figure 2. Flowchart of the parameter estimation algorithm. The algorithm is explained in detail in Section S2 in Supplementary Material. The flowchart is adapted from Lehnert et al. (2015) (2).

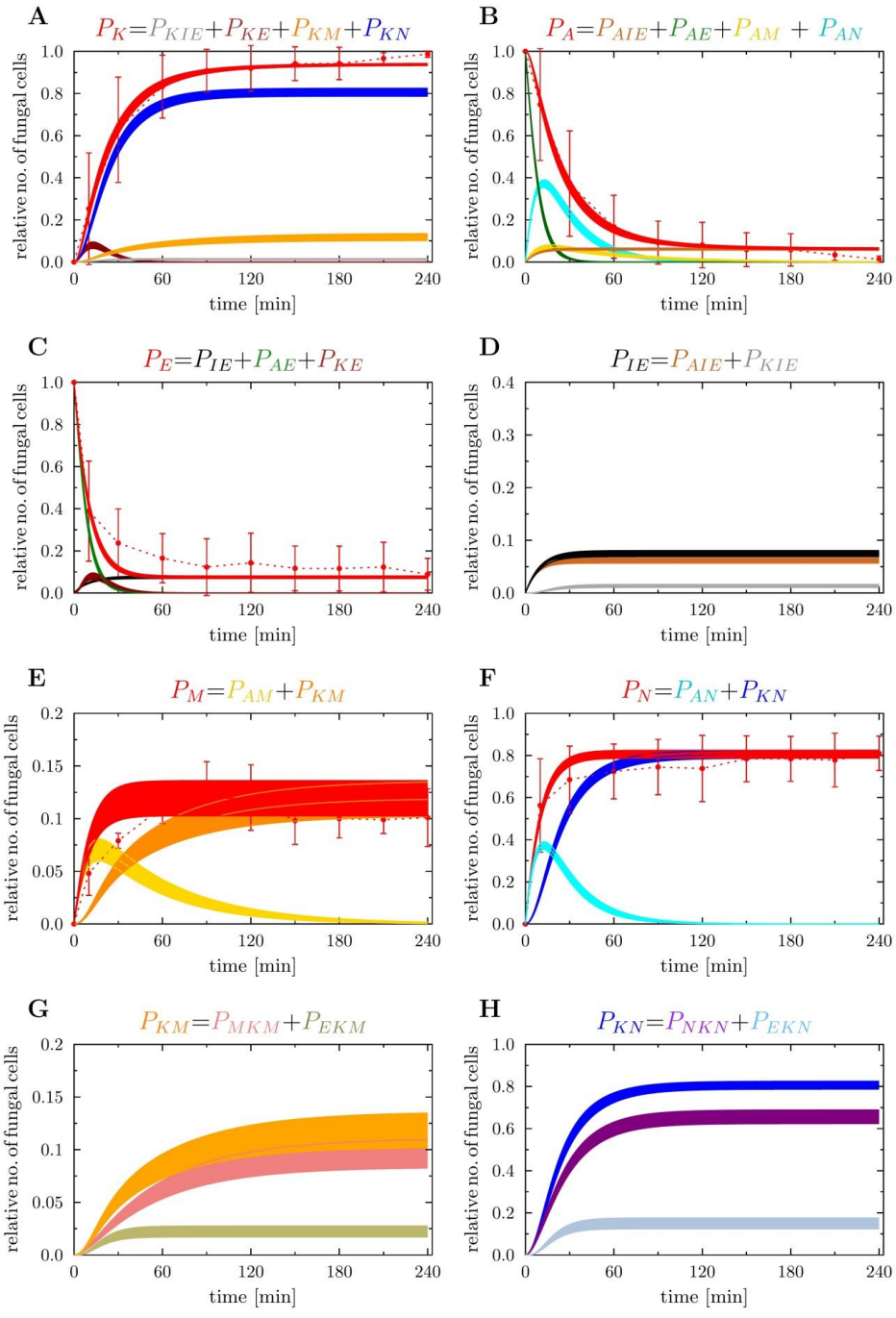

Figure S3. Kinetics of Combined Units of the spon-IE model by the use of the computed transition rates. Experimental data from whole-blood infection assays (red dotted lines) with corresponding

standard deviations are compared to the simulated data by the spontaneous evasion model. The thickness of solid lines indicates the mean ± standard deviation of 50 simulations with transition rate values that were randomly sampled within their corresponding standard deviation. The breakdown of each combined unit is depicted the following way. (**A**) Time-dependent relative number of killed *C. albicans* cells (P_K) that were experimentally measured by survival plates. The experimental results were compared with the total number of simulated killed *C. albicans* cells. P_K is defined as the sum of killed immune-evasive *C. albicans* (P_{KIE}), extracellularly killed *C. albicans* (P_{KE}), and killed *C. albicans* in monocytes (P_{KM}) and PMN (P_{KM}) (**B**) Alive *C. albicans* (P_A) were also measured by survival plates. The simulated result was then compared to the experimental data. (**C**) Time course of *C. albicans* cells that are in extracellular space in the blood. Here, experimental data was gathered via FACS analysis and compared to the simulated data. (**D**) Simulated immune-evasive *C. albicans* cells (P_{IE}) are the sum of alive and killed *C. albicans* cells, which are able to evade the immune defense, over the time course of the simulation. (**E**) Time course of the total number of alive and killed *C. albicans* cells that were phagocytosed by monocytes (P_M). (**F**) Relative number of *C. albicans* cells in PMN (P_N) during the whole-blood infection assay and comparison to the simulated result. (**G**) Simulation result of killed *C. albicans* cells within monocytes (P_{KM}), that is defined as the sum of internalized *C. albicans* that were intracellularly killed (P_{MKM}) and those who were extracellularly killed (P_{EKM}). (**H**) simulated time course of killed cells in PMN (P_{KN}), that is composed of intracellularly killed *C. albicans* cells (P_{NKN}) and extracellularly killed *C. albicans* cells (P_{EN}) in PMN.

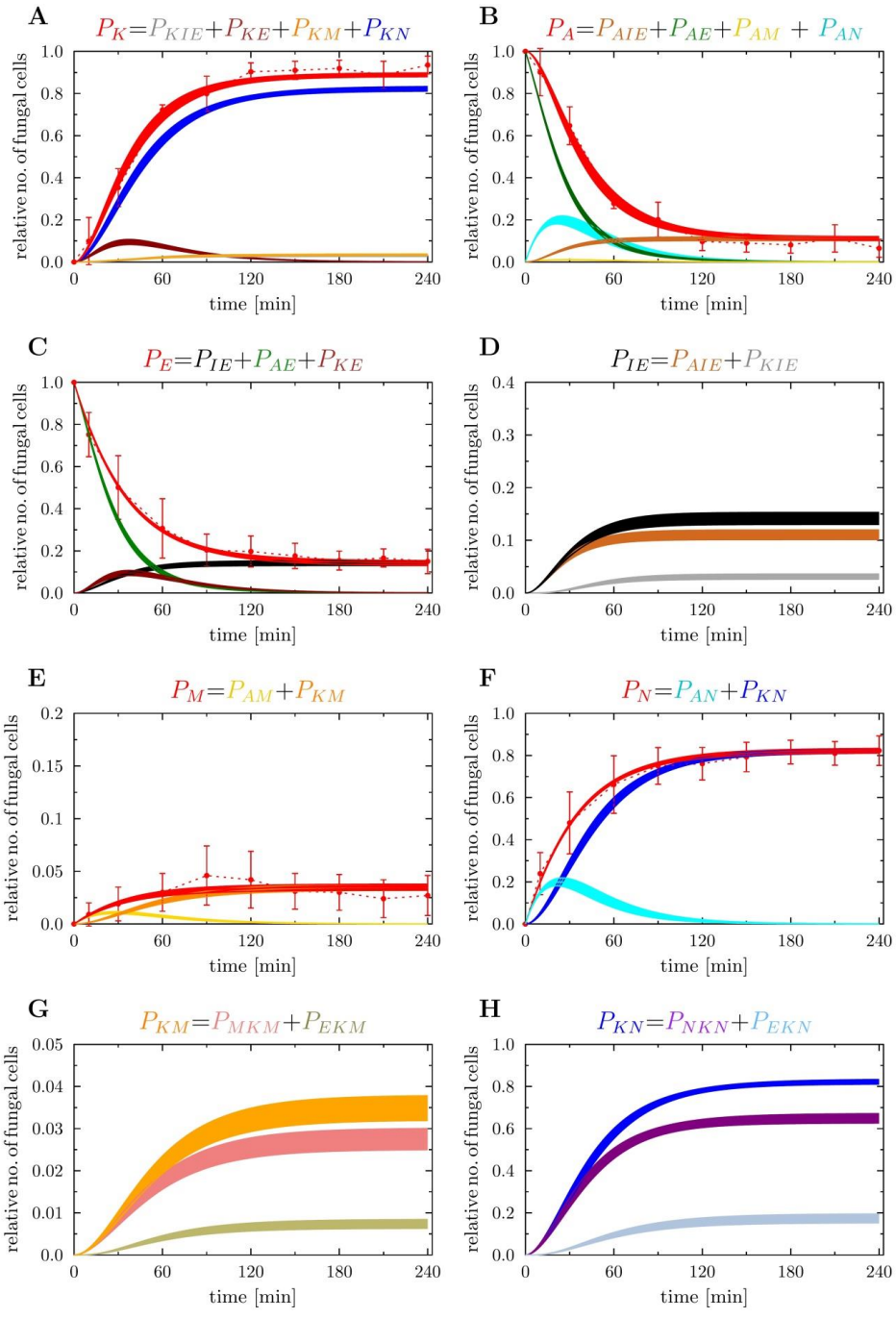

Figure S4. As in Figure S3 in Supplementary Material but for PMNmed-IE model in the case of *C. albicans* infection.

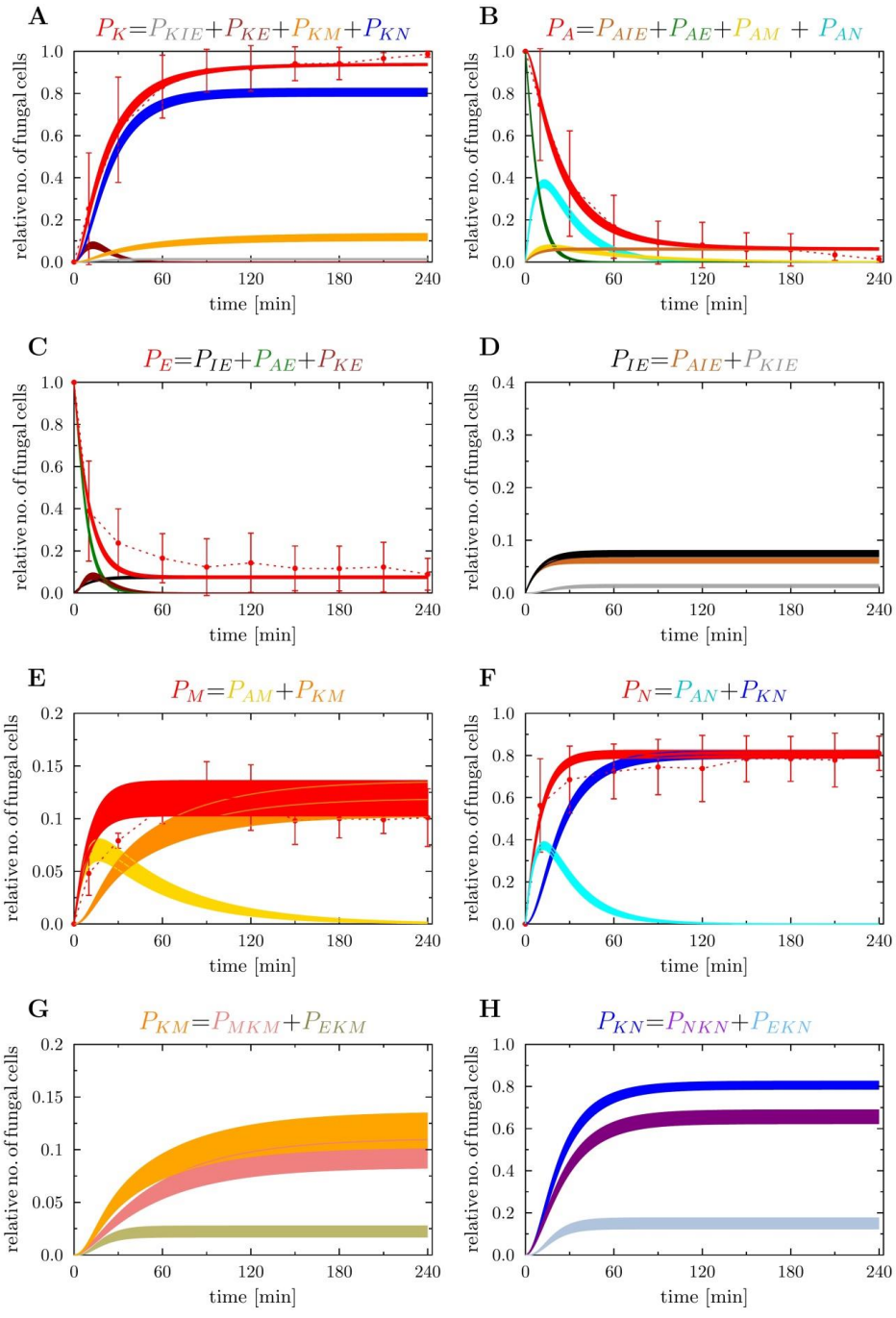

Figure S5. As in Figure S3 in Supplementary Material but for spon-IE model in the case of *C. glabrata* infection.

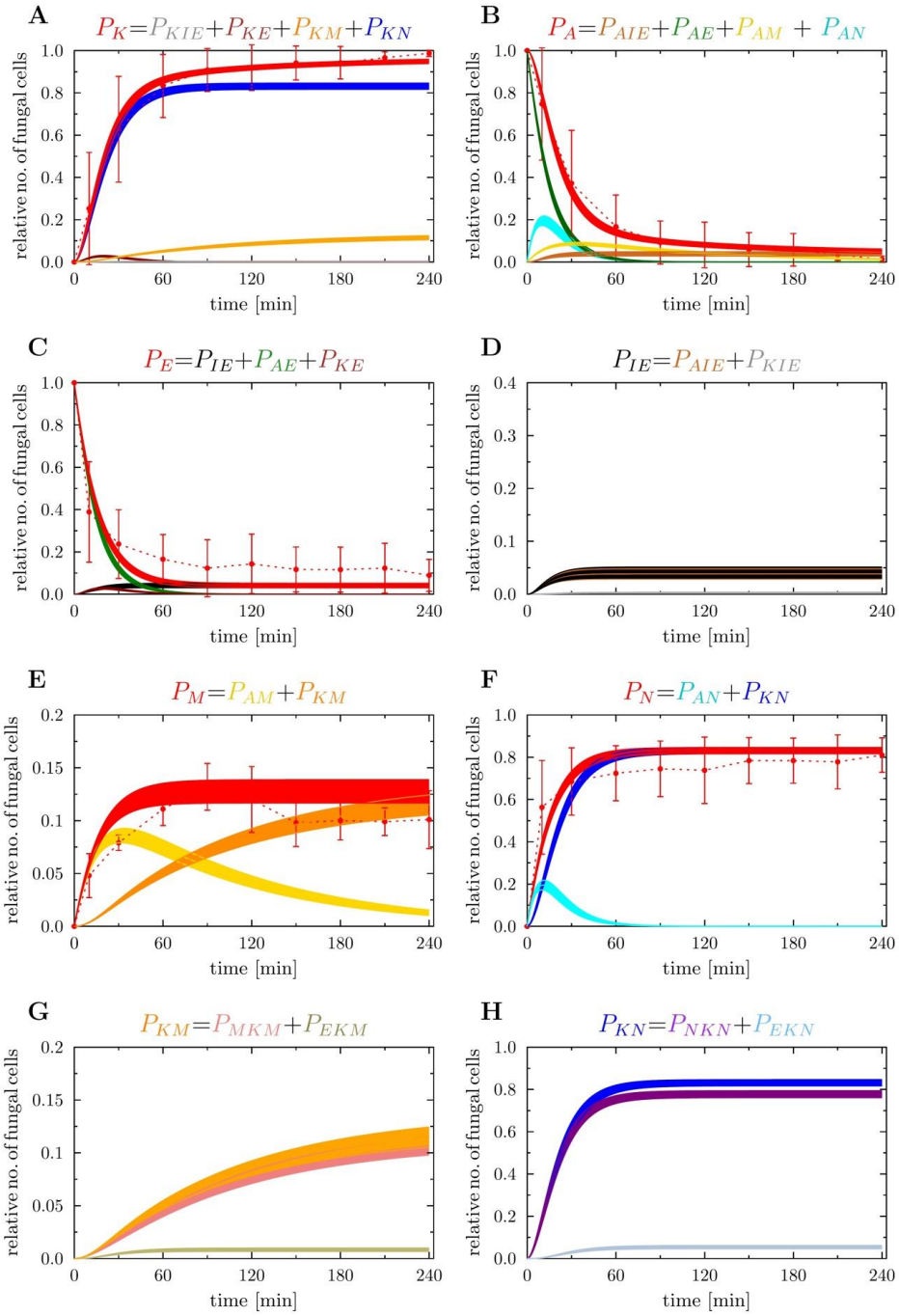
A
$P_K = P_{KIE} + P_{KE} + P_{KM} + P_{KN}$
B
$P_A = P_{AIE} + P_{AE} + P_{AM} + P_{AN}$
C
$P_E = P_{IE} + P_{AE} + P_{KE}$
D
$P_{IE} = P_{AIE} + P_{KIE}$
E
$P_M = P_{AM} + P_{KM}$
F
$P_N = P_{AN} + P_{KN}$
G
$P_{KM} = P_{MKM} + P_{EKM}$
H
$P_{KN} = P_{NKN} + P_{EKN}$
relative no. of fungal cells
time [min]

Figure S6. As in Figure S3 in Supplementary Material but for PMNmed-IE model in the case of *C. glabrata* infection.

3 References

1. Hünniger K, Lehnert T, Bieber K, Martin R, Figge MT, Kurzai O. A Virtual Infection Model Quantifies Innate Effector Mechanisms and Candida albicans Immune Escape in Human Blood. *PLoS Comput Biol* (2014) **10**:e1003479. doi:10.1371/journal.pcbi.1003479

2. Lehnert T, Timme S, Pollmächer J, Hünniger K, Kurzai O, Figge MT. Bottom-up modeling approach for the quantitative estimation of parameters in pathogen-host interactions. *Front Microbiol* (2015) **6**: doi:10.3389/fmicb.2015.00608

8. Quantitative simulations predict treatment strategies against fungal infections in virtual neutropenic patients

frontiers in Immunology

ORIGINAL RESEARCH
published: 04 April 2018
doi: 10.3389/fimmu.2018.00667

Quantitative Simulations Predict Treatment Strategies Against Fungal Infections in Virtual Neutropenic Patients

*Sandra Timme[1,2], Teresa Lehnert[1,3], Maria T. E. Praße[1,2], Kerstin Hünniger[4,5], Ines Leonhardt[3,4], Oliver Kurzai[3,4,5] and Marc Thilo Figge[1,2,3]**

[1]*Research Group Applied Systems Biology, Leibniz Institute for Natural Product Research and Infection Biology—Hans Knöll Institute, Jena, Germany,* [2]*Faculty of Biological Sciences, Friedrich Schiller University Jena, Jena, Germany,* [3]*Center for Sepsis Control and Care (CSCC), Jena University Hospital, Jena, Germany,* [4]*Fungal Septomics, Septomics Research Center, Leibniz Institute for Natural Product Research and Infection Biology—Hans Knöll Institute, Friedrich Schiller University, Jena, Germany,* [5]*Institute for Hygiene and Microbiology, University of Würzburg, Würzburg, Germany*

frontiers in Immunology

ORIGINAL RESEARCH
published: 04 April 2018
doi: 10.3389/fimmu.2018.00667

Quantitative Simulations Predict Treatment Strategies Against Fungal Infections in Virtual Neutropenic Patients

*Sandra Timme[1,2], Teresa Lehnert[1,3], Maria T. E. Praße[1,2], Kerstin Hünniger[4,5], Ines Leonhardt[3,4], Oliver Kurzai[3,4,5] and Marc Thilo Figge[1,2,3]**

[1]*Research Group Applied Systems Biology, Leibniz Institute for Natural Product Research and Infection Biology—Hans Knöll Institute, Jena, Germany,* [2]*Faculty of Biological Sciences, Friedrich Schiller University Jena, Jena, Germany,* [3]*Center for Sepsis Control and Care (CSCC), Jena University Hospital, Jena, Germany,* [4]*Fungal Septomics, Septomics Research Center, Leibniz Institute for Natural Product Research and Infection Biology—Hans Knöll Institute, Friedrich Schiller University, Jena, Germany,* [5]*Institute for Hygiene and Microbiology, University of Würzburg, Würzburg, Germany*

The condition of neutropenia, i.e., a reduced absolute neutrophil count in blood, constitutes a major risk factor for severe infections in the affected patients. *Candida albicans* and *Candida glabrata* are opportunistic pathogens and the most prevalent fungal species in the human microbiota. In immunocompromised patients, they can become pathogenic and cause infections with high mortality rates. In this study, we use a previously established approach that combines experiments and computational models to investigate the innate immune response during blood stream infections with the two fungal pathogens *C. albicans* and *C. glabrata.* First, we determine immune-reaction rates and migration parameters under healthy conditions. Based on these findings, we simulate virtual patients and investigate the impact of neutropenic conditions on the infection outcome with the respective pathogen. Furthermore, we perform *in silico* treatments of these virtual patients by simulating a medical treatment that enhances neutrophil activity in terms of phagocytosis and migration. We quantify the infection outcome by comparing the response to the two fungal pathogens relative to non-neutropenic individuals. The analysis reveals that these fungal infections in neutropenic patients can be successfully cleared by cytokine treatment of the remaining neutrophils; and that this treatment is more effective for *C. glabrata* than for *C. albicans*.

Keywords: fungal infections, neutropenia, treatment strategies, bottom-up modeling approach, computer simulations

OPEN ACCESS

Edited by:
Lars Kaderali, Universitätsmedizin Greifswald, Germany

Reviewed by:
Joshua J. Obar, Dartmouth College, United States
Hauke Busch, University of Lübeck, Germany

***Correspondence:**
Marc Thilo Figge
thilo.figge@leibniz-hki.de

Specialty section:
This article was submitted to Microbial Immunology, a section of the journal Frontiers in Immunology

Received: *18 December 2017*
Accepted: *19 March 2018*
Published: *04 April 2018*

Citation:
Timme S, Lehnert T, Praße MTE, Hünniger K, Leonhardt I, Kurzai O and Figge MT (2018) Quantitative Simulations Predict Treatment Strategies Against Fungal Infections in Virtual Neutropenic Patients. Front. Immunol. 9:667. doi: 10.3389/fimmu.2018.00667

INTRODUCTION

The human immune system protects the body against various environmental cues, such as microorganisms. It covers mechanisms on different levels ranging from physical barriers, like the skin and mucosal surfaces, down to cellular and molecular components of the innate and adaptive immune system (1). However, congenital or acquired diseases as well as medical treatments may impair proper functioning of the immune system, which can result in the loss of its protective ability. Neutrophils constitute the highest fraction of blood leukocytes, as they make up over 70% of all blood leukocytes (2). Since they can migrate to sites of infection and clear the organism from pathogens, they constitute an important part of the immune system.

Candida spp. cause 5–15% of all bloodstream infections and are associated with high mortality rates of 30–40% (3). A significant proportion (>50%, depending on the study setting) of the human population is colonized with *Candida* spp. The most prevalent species are *Candida albicans* and *Candida glabrata* that are both human commensals and reside predominantly on the human skin and mucosal surfaces (4–6). *C. albicans* is a morphotype-switching yeast, which in its commensal state exhibits the typical yeast form, while it forms hyphae when switching to its pathogenic state (7, 8). By contrast, *C. glabrata* does not form hyphae, neither in the commensal nor in the pathogenic state and is smaller than *C. albicans* (4, 9). In healthy people, both species usually stay in their commensal state. However, in immunocompromised patients, these human-pathogenic fungi can switch to their pathogenic state and cause superficial as well as systemic infections that are associated with high mortality rates.

To investigate host–pathogen interactions between the human innate immune system and these fungal pathogens, we applied a systems biology approach, where wet-lab experiments were combined with virtual infection models (10–13). Such virtual infection models have the great advantage of allowing for the identification and quantification of essential parameters that govern the biological system under consideration. This also makes them a powerful tool for hypothesis generation and uncovering new mechanisms, which consequently allows for minimizing the amount of animal experiments (14). Depending on the purpose, such *in silico* models can be built with different modeling techniques, such as *differential equations*, *state-based models* (SBMs) or spatial modeling techniques such as *cellular automata*, *cellular Potts models* or *agent-based models* (ABMs) (15). In a previous systems biology study, we established a human whole-blood infection assay (16), where blood was taken from healthy volunteers and infected with *C. albicans* cells. Then, subpopulations of alive, killed and extracellular fungal cells as well as fungal cells phagocytosed by monocytes and neutrophils were measured by association assays and survival assays. Based on these experimental data, we implemented an SBM that allowed for the quantification of immune-reaction rates, such as phagocytosis and killing rates, by fitting the simulated kinetics to the experimental data. In a subsequent study, we developed a bottom-up modeling approach that enabled not only quantification of immune-reaction rates but also the investigation of spatial aspects (17). Since the SBM simulates the temporal but not the spatial dynamics, we also developed an ABM that was based on a previous ABM implementation (18, 19). We combined both models in a bottom-up modeling approach (17): the SBM was used to determine non-spatial rates that were afterward transformed and used in the ABM to fit migration parameters of immune cells in human whole blood. We found that the *in silico* infection outcome for *C. albicans* was sensitive to changes in the diffusion coefficient of neutrophils, whereas that of monocytes had only minor impact on the system dynamics. This result reflected the more prominent role of neutrophils over monocytes in fighting *C. albicans* infection of human whole blood. Furthermore, immune dysregulation was investigated using the ABM, and the results showed that a reduced diffusion coefficient for neutrophils resembled conditions of neutropenia (17). This important observation is the main motivation of the present study, because it suggests how neutropenic patients may be treated to cope with bloodstream infections. Thus, increasing neutrophil activation in terms of phagocytic activity as well as migration strength is hypothesized to have the potential of balancing neutropenic conditions and clearance of infection. Based on this reasoning, we address infections in human whole blood by *C. albicans* and *C. glabrata* under neutropenic conditions in this study.

Diseases or medical treatments can evoke a reduced absolute neutrophil count (ANC) in blood and result into a condition called *neutropenia*. Neutropenia may result from congenital or acquired impairments, where the latter case is more frequent. A reduced ANC may arise due to a disturbed development of neutrophils in the bone marrow, a disturbed migration to the blood stream or a rapid consumption during an infection (20). In anti-cancer chemotherapy, neutropenia is the most abundant disorder of the immune system due to the relatively short lifespan of these terminally differentiated cells (21). Neutropenia emerges in different degrees of severity that are classified by the *Severe Chronic Neutropenia International Registry* (SCNIR) (20). The SCNIR distinguishes three degrees of severity: mild neutropenia with an ANC of 1,000–1,500 neutrophils/µl, moderate neutropenia with an ANC of 500–1,000 neutrophils/µl and severe neutropenia with an ANC of <500 neutrophils/µl. In this study, we focus on neutropenia treatment by stimulation and activation of present neutrophils by inflammatory cytokines and quantitatively investigate the impact on fungal infections by computer simulations. Thus, we aim to investigate a possible treatment strategy where the neutrophil activity is increased by a higher diffusion coefficient and/or phagocytosis rate. For this purpose, we apply the previously established protocol for whole-blood infection assays and perform the bottom-up modeling approach for the two human-pathogenic fungi. As is schematically shown in **Figure 1**, we first determine quantitative values for the immune-reaction rates as well as for diffusion coefficients of monocytes and neutrophils as the key immune cells of innate immunity in whole blood. Furthermore, we use this modeling approach to simulate neutropenia *in silico* and compare effects on the infection outcome between the different pathogens. To evaluate a possible treatment strategy, we simulate virtual neutropenic patients (VNP) with different degrees of severity and increase stepwise the phagocytosis rate and/or the diffusion coefficient of neutrophils to classify the infection outcome. Taken together, we could show that the increase of the phagocytosis rate and/or the migration parameter of neutrophils generally allowed balancing neutropenic conditions and clearance of infection. Furthermore, we predict that *C. albicans* compared with *C. glabrata* always requires stronger increases in the phagocytosis rate and the diffusion coefficient for the same conditions of neutropenia.

MATERIALS AND METHODS

Ethics Statement

This study was conducted according to the principles expressed in the Declaration of Helsinki. All protocols were approved by the Ethics Committee of the University Hospital Jena (permit number: 273-12/09). Written informed consent was obtained from all blood donors.

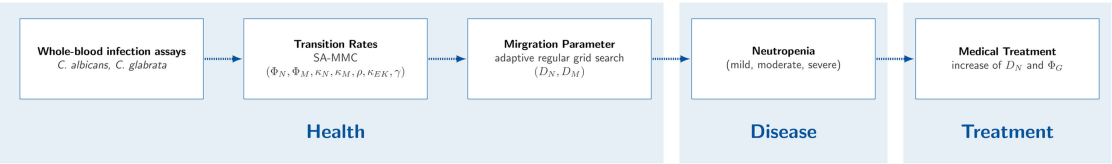

FIGURE 1 | Workflow for studying neutropenia *in silico*. First, whole-blood infection assays with *Candida albicans* and *Candida glabrata* were performed in wet lab. Second, non-spatial immune-reaction rates were fitted using the state-based model. Third, the agent-based model (ABM) was used to estimate migration parameters for neutrophils and monocytes. Based on the fitted non-spatial immune-reaction rates and the fitted migration parameters, virtual neutropenic patients were simulated in the ABM by gradually reducing the neutrophil count. Eventually, a medical treatment of the virtual patients was simulated by increasing the diffusion coefficient and/or the phagocytosis rate of neutrophils.

Fungal Strains and Culture

GFP expressing *C. albicans* strain [constructed as described in Ref. (16)] was grown in liquid yeast extract–peptone–dextrose (YPD) medium at 30°C. *C. glabrata* expressing GFP (22) was incubated at 37°C in YPD. In preparation for the whole-blood assay, both strains were reseeded after overnight culture in YPD medium and grown at 30 and 37°C, respectively, until they reached the mid-log-phase and finally harvested in HBSS until use.

Whole-Blood Infection Assay

Human peripheral blood from healthy individuals was infected with either of the two fungi *C. albicans* and *C. glabrata*, respectively. The assay was performed as described previously (16). In short, 1×10^6 *Candida* cells were added per ml of anti-coagulated blood and incubated at 37°C with gentle rotation for time points indicated. Following the incubation, cells were maintained at 4°C and analyzed immediately *via* flow cytometry. Flow cytometry gating strategy to investigate the distribution of fungal cells in human blood was performed as previously described (16) using FlowJo 7.6.4 software. Survival of fungal cells was determined in a plating assay by analysis of recovered colony-forming units after plating appropriate dilutions of all time points on YPD agar plates.

Bottom-Up Modeling Approach

We established a bottom-up modeling approach for simulation and fitting of whole-blood infection assays in a previous study (17). This bottom-up modeling approach incorporates models with increasing complexity that build on one another, where each model focuses on different aspects of the infection process.

SBM—Immune-Reaction Rates

First, we applied the SBM to quantify and characterize immune-reaction rates for discrete entities of pathogens and innate immune cells. Therefore, the populations of innate immune cells, i.e., neutrophils and monocytes, as well as the pathogens were modeled by different states in the SBM. For the comparison with experimentally measured cell populations, we identified five combined units that are composed of specific states. The states representing extracellular cells are combined in the combined unit P_E that is given by the following equation:

$$P_E \equiv P_{AE} + P_{KE} + P_{AIE} + P_{KIE}, \tag{1}$$

where the states P_{AE} and P_{KE} represent extracellular cells that are alive and killed, respectively. The states P_{AIE} and P_{KIE} describe pathogens that are either alive and evading the immune response or killed and evading the immune response. Pathogens that are in extracellular space and either alive (P_{AE}) or killed (P_{KE}) can be phagocytosed by two different immune cells, i.e., neutrophils (N) and monocytes (M). The combined unit P_N comprises pathogens that are phagocytosed by neutrophils and is given by the following equation:

$$P_N \equiv \sum_{i\geq 0} \sum_{j\geq 0} (i+j)\, N_{i,j}. \tag{2}$$

Similarly, pathogens that are phagocytosed by monocytes are combined in P_M that is given by the following equation:

$$P_M \equiv \sum_{i\geq 0} \sum_{j\geq 0} (i+j)\, M_{i,j}. \tag{3}$$

In Eqs 2 and 3, the indices i and j refer to the immune cell state that is defined by the number of internalized alive and killed pathogens, respectively.

Furthermore, the states representing alive and killed pathogens are combined in P_K and P_A, respectively, that are defined by the following equations:

$$P_K \equiv P_{KE} + P_{KIE} + \sum_{i\geq 0} \sum_{j\geq 0} (M_{i,j} + N_{i,j})\, j, \tag{4}$$

$$P_A \equiv P_{AE} + P_{AIE} + \sum_{i\geq 0} \sum_{j\geq 0} (M_{i,j} + N_{i,j})\, i. \tag{5}$$

The total number of pathogens is given by $P \equiv P_E + P_N + P_M$ or $P \equiv P_K + P_A$.

Transitions between these states are characterized by so-called *transition rates* and allow for dynamic state changes over time. The SBM of whole-blood infection comprises seven different transition rates that are given by the phagocytosis rate ϕ_M of monocytes, the phagocytosis rate ϕ_N of neutrophils, the intracellular killing rates κ_M and κ_N of both monocytes and neutrophils, the transition rates γ and $\bar{\kappa}_{EK}$, which define the extracellular killing by antimicrobial peptides, and the spontaneous immune evasion rate ρ. Note that, in the previous study by Lehnert et al. (17), a distinction between first and subsequent phagocytosis events by neutrophils was made, where the first phagocytosis event was assumed to activate the neutrophils and induce granulation. Since this fact is not experimentally validated for whole-blood infection with *C. glabrata*, we here did not distinguish between these two

processes and used only one transition rate (ϕ_N) referring to both first and subsequent phagocytosis events. To determine *a priori* unknown transitions rates, the *in silico* data were fitted to the experimental data by applying the method of *Simulated Annealing* based on the *Metropolis Monte Carlo* scheme (SA-MMC). For a more detailed description of the model and the parameter estimation method, we refer to Hünniger et al. (16) and Lehnert et al. (17).

ABM—Immune Cell Migration

The ABM is based on a previous ABM implementation (18, 19) and was already used in the previous study by Ref. (17). In contrast to the SBM, it allows studying spatial aspects, such as immune cell migration, in whole-blood infection assays. The ABM simulates all cell types, i.e., pathogens as well as immune cells, as individual spherical objects that are referred to as *agents*. All agents migrate, act and interact in a rule-based fashion within a spatially continuous, three-dimensional environment that represents 1 µl of blood.

Furthermore, the ABM was fitted to the experimental data to determine diffusion coefficients of neutrophils (D_N) and monocytes (D_M). This was done by the bottom-up modeling approach, where the previously determined transition rates from the SBM were used in the ABM. However, space-dependent rates, like phagocytosis rates, had to be adequately transformed (17). Regarding the fitting procedure, we used an *adaptive regular grid search* that scans the parameter space within reasonable ranges and uses a more fine-grained grid in regions with relatively small least squares errors (LSEs).

Simulation Workflow

The work flow of this study, comparing wet-lab and *in silico* experiments with different models is displayed in **Figure 1**. First, we performed whole-blood infection assays for the two fungal pathogens *C. albicans* and *C. glabrata*. Afterward, we applied for each of the two pathogens the following steps. The results from association and survival assays were used to fit the model parameters of the SBM to these data. The transition rates of the fit with the lowest LSE were then appropriately transformed and fed into the ABM. Subsequently, the grid search in the parameter space was applied to fit the ABM to the experimental data and, in this way, to estimate the diffusion coefficients of neutrophils and monocytes. The determined transition rates and migration parameters form the basis for all following investigations on neutropenia and possible treatment strategies in virtual patients with varying degree of neutropenia. In the following, each step of this work flow is described in more detail.

Infection in Virtual Patients With Normal Neutrophil Counts

For the quantification of the immune response against the human-pathogenic fungi *C. albicans* and *C. glabrata* with normal neutrophil counts, we first determined the transition rates by fitting the SBM to the corresponding data from whole-blood experiments. These rates were used in the ABM and diffusion coefficients for neutrophils D_N and monocytes D_M were determined by fitting the ABM to the experimental data.

Infection in Virtual Patients Under Neutropenic Condition

To examine the immune response of virtual patients under conditions of neutropenia, we performed simulations with the immune-reaction rates and migration parameters that were identified under non-neutropenic conditions and gradually decreased the number of neutrophils. Subsequently, we compared the infection outcome at 4 h post infection for varying degrees of severity of neutropenia.

Patterns and Classification of Simulations

Since the health of a patient is critically determined by the amount of killed pathogens P_K as well as by the amount of alive and immune-evasive pathogens P_{AIE}, we used these measures to characterize the infection outcome for the virtual patients.

We distinguish four different cases C for the infection outcome: an infection outcome corresponding to non-neutropenic immune conditions as well as the infection outcome under mild, moderate or severe neutropenia, i.e., $C = \{\text{non–neutropenic, mild, moderate, severe}\}$. To discriminate these classes, we calculated the patterns $\psi = (\mu(P_K) \pm \sigma(P_K),\ \mu(P_{AE}) \pm \sigma(P_{AE}),\ \mu(P_{AIE}) \pm \sigma(P_{AIE}))$ at the transition between consecutive degrees of neutropenia severity, in terms of the mean and SD. This resulted in the three patterns $\psi = \{\psi^{nm}, \psi^{mm}, \psi^{ms}\}$ at the transitions between two neutropenia severity levels: non-neutropenic–mild (nm), mild–moderate (mm), and moderate–severe (ms). For the classification of a particular simulation, we calculated the class of the values P_K^{sim} and P_{AIE}^{sim} at 4 h post infection. Then, we classified each of the three values of $v(P_K) = (\mu(P_K) + \sigma(P_K),\ \mu(P_K),\ \mu(P_K) - \sigma(P_K))$ and $v(P_{AIE}) = (\mu(P_{AIE}) + \sigma(P_{AIE}),\ \mu(P_{AIE}),\ \mu(P_{AIE}) - \sigma(P_{AIE}))$ separately. Thus, for each of the three values v_i, we set:

$$C(v_i(P_K)) = \begin{cases} \mu(P_K^{nm}) - \sigma(P_K^{nm}) \le v_i \le 1, & C = \text{non-neutropenic} \\ \mu(P_K^{mm}) - \sigma(P_K^{mm}) \le v_i \le \mu(P_K^{nm}) + \sigma(P_K^{nm}), & C = \text{mild} \\ \mu(P_K^{ms}) - \sigma(P_K^{ms}) \le v_i \le \mu(P_K^{mm}) + \sigma(P_K^{mm}), & C = \text{moderate} \\ 0 \le v_i \le \mu(P_K^{ms}) + \sigma(P_K^{ms}), & C = \text{severe} \end{cases} \quad (6)$$

$$C(v_i(P_{AIE})) = \begin{cases} 0 \le v_i < \mu(P_{AIE}^{nm}) + \sigma(P_{AIE}^{nm}), & C = \text{non-neutropenic} \\ \mu(P_{AIE}^{nm}) - \sigma(P_{AIE}^{nm}) \le v_i \le \mu(P_{AIE}^{mm}) + \sigma(P_{AIE}^{mm}), & C = \text{mild} \\ \mu(P_{AIE}^{mm}) - \sigma(P_{AIE}^{mm}) \le v_i \le \mu(P_{AIE}^{ms}) + \sigma(P_{AIE}^{ms}), & C = \text{moderate} \\ \mu(P_{AIE}^{ms}) - \sigma(P_{AIE}^{ms}) \le v_i < 1, & C = \text{severe} \end{cases} \quad (7)$$

The simulation's infection outcome C is then assigned to the class that received the highest number of votes from the nine values of $v_i(P_K)$ and $v_i(P_{AIE})$.

In Silico Treatment of Neutropenia and Identification of Optimal Treatment Strategies

After the simulation of VNP, we simulated the medical treatment of these patients. Therefore, we selected virtual patients with certain degrees of severity of neutropenia. These are the number of neutrophils that are specific for a transition between

two degrees of severity as well as the number of neutrophils between these transitions. Therefore, we simulate the following five VNP that are characterized by specific ANC: VNP-1 with 1,250 neutrophils/µl, VNP-2 with 1,000 neutrophils/µl, VNP-3 with 750 neutrophils/µl, VNP-4 with 500 neutrophils/µl, VNP-5 with 250 neutrophils/µl. Thus, the ANC of these VNP corresponds to a decrease in neutrophil number from the standard value by VNP-1: 75%, VNP-2: 80%, VNP-3: 85%, VNP-4: 90%, and VNP-5: 95%. Since the treatment with different drugs might improve the phagocytic activity and/or the migration parameter of neutrophils, we performed simulations with the ABM where the phagocytosis rate of neutrophils ϕ_N as well as their diffusion coefficient D_N was increased. In the following, we refer to these parameters that are affected by the treatment as ϕ_N^T and D_N^T.

For the sake of comparability of both values, we increased both values in a stepwise fashion. The increase of these values lead to an improvement in the infection outcome. For example, a virtual patient with moderate neutropenia and a simulated treatment might attain an infection outcome that corresponded to that of a patient with mild neutropenia or even to an infection outcome for an individual with a non-neutropenic immune status. Therefore, after simulating with a certain parameter set $(\phi_N^T,\ D_N^T)$ we classified the simulation outcome as described earlier.

The stepwise increase of the parameters was continued until a parameter configuration was found with an infection outcome for non-neutropenic individuals. For quantification of the improvement of the infection outcome, we fitted an exponential function $f_{\phi_N} = 1 + a \cdot e^{-b \cdot f_{D_N}}$ at the transitions between two consecutive degrees of neutropenia severity. Here, the factors f_{ϕ_N} and f_{D_N} are given by $f_{\phi_N} = \phi_N^T/\phi_N^{min}$ and $f_{D_N} = D_N^T/D_N^{min}$, and denote the ratios between the treatment parameter values $(\phi_N^T,\ D_N^T)$ and the parameter values $(\phi_N^{min},\ D_N^{min})$ obtained from minimizing the LSE under non-neutropenic conditions.

RESULTS

Whole-Blood Infection Assays Differ for *C. albicans* and *C. glabrata*

In this study, we performed human whole-blood infection assays with *C. glabrata* and compared the measured data with experimental measurements for *C. albicans* by applying a previously established protocol (16). The kinetics of pathogens associated with either neutrophils or monocytes can be seen in **Figures 2A,B**, respectively. In case of *C. glabrata*, 81.0 ± 8.1% cells were associated with neutrophils, which is similar to *C. albicans* with 82.3 ± 7%. However, the experimental data show different kinetics for the two species, since *C. glabrata* is phagocytosed by neutrophils in a shorter time. By contrast, the association with monocytes is higher for *C. glabrata* with 10.1 ± 2.7%, while only 2.7 ± 1.9% *C. albicans* cells were associated with monocytes 4 h post infection. Due to the phagocytosis of the pathogens by the immune cells, 4 h post infection, 8.9 ± 7.5% cells remained extracellular for *C. glabrata* and 15.0 ± 5.8% for *C. albicans* (see **Figure 2C**). The remaining extracellular cells are referred to as *immune-evasive* cells, as already introduced in previous studies (16, 17). Furthermore, 1.3 ± 1.5% *C. glabrata* cells remained extracellular and alive 4 h post infection (see **Figure 2D**), which is lower compared with *C. albicans* with 6.5 ± 4.2%. In comparison with

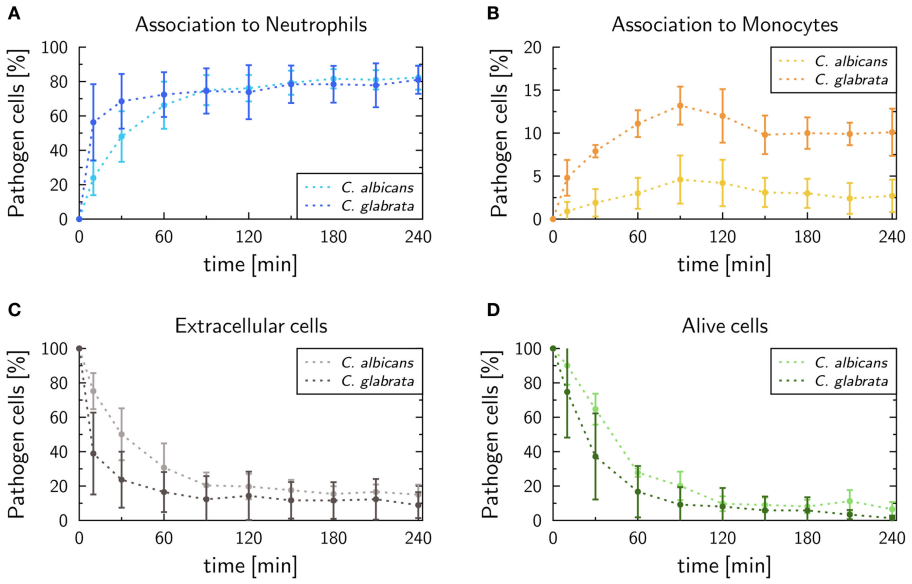

FIGURE 2 | Experimental data of whole-blood infection assays for *Candida albicans* (light color) and *Candida glabrata* (dark color), respectively. After incubation populations of extracellular cells **(A)**, alive cells **(B)**, as well as pathogens phagocytosed by either neutrophils **(C)** or monocytes **(D)**, were measured by flow cytometry and plating assays.

C. albicans, the decrease in alive *C. glabrata* cells mainly occurred during the first 2 h of the experiment exhibiting a much faster kinetics than for *C. albicans*.

Quantification of Immune-Reaction Rates Reveals Differences Between Pathogens

To quantify infection scenarios for the two pathogens, immune-reaction rates of the SBM were estimated by fitting to the experimental data as done previously for *C. albicans* in human whole blood (17). As explained in detail in Section "Material and Methods," this was done by computing the so-called *combined units*, which are combinations of different pathogen states and were directly accessible in experiment. In terms of these combined units, we evaluated the quality of a simulation by calculating the LSE between the experimental data and the *in silico* data. To determine the immune-reaction rates representing the best fit to the experimental data, i.e., that are associated with the lowest LSE, we applied the method of *Simulated Annealing* based on the *Metropolis Monte Carlo* scheme. The resulting immune-reaction rates from the fitting procedure where used to simulate the infection with the pathogens in 1 ml of blood, containing 5×10^6 neutrophils, 5×10^5 monocytes, and 1×10^6 cells, and are shown in **Figure 3** and in Table S1 in Supplementary Material.

The values of immune-reaction rates for *C. albicans* infection of whole blood are in line with our previous results (17). The reaction rate values for *C. glabrata* infection mostly differ in comparison to reaction rates for *C. albicans* infection (see **Figure 3**). The phagocytosis rate of neutrophils in the infection scenario with *C. glabrata* is $\phi_N = 10.11 \times 10^{-2}\,\mathrm{min}^{-1}$, which is 3.5 times higher than for *C. albicans* infection. The phagocytosis rate for monocytes

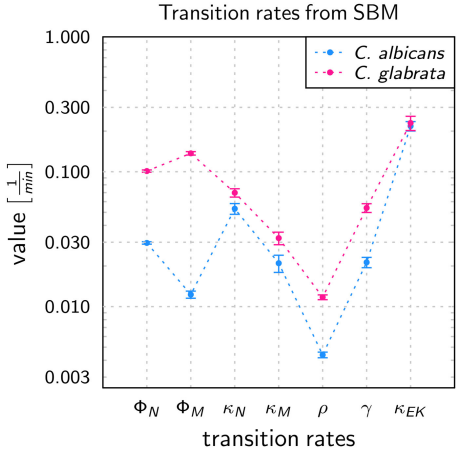

FIGURE 3 | Transition rates obtained from the calibration of the state-based model (SBM) to experimental data of the whole-blood infection assay for *Candida albicans* (blue) and *Candida glabrata* (pink), respectively. The values are compared for the phagocytosis rate for neutrophils (ϕ_N), and by monocytes (ϕ_M), killing rate for neutrophils (κ_N) and monocytes (κ_M), the rate at which the pathogens can evade the immune response with regard to phagocytosis and/or killing (ρ) as well as the rates that define the extracellular killing, i.e., γ and $\bar{\kappa}_{EK}$. Error bars correspond to SDs.

is with $\phi_M = 13.69 \times 10^{-2}\,\mathrm{min}^{-1}$ an order of magnitude higher than in the case of *C. albicans* infection. These higher phagocytosis rates arise due to the faster kinetics measured for *C. glabrata* in the experimental data (see **Figure 2**). Furthermore, the order in the magnitude of phagocytosis rates is reversed in comparison to *C. albicans* infection, because for *C. glabrata* the phagocytosis rate of monocytes is 1.4 times higher than that for neutrophils. The killing rate of neutrophils is for *C. glabrata* $\kappa_N = 6.98 \times 10^{-2}\,\mathrm{min}^{-1}$, which is only slightly higher than for *C. albicans* infection. Furthermore, differences between the fungal pathogens are again observed in the killing rate for monocytes, which is 1.5 times higher for *C. glabrata* with $\kappa_M = 3.22 \times 10^{-2}\,\mathrm{min}^{-1}$ compared with *C. albicans*. As was previously observed for *C. albicans* (16, 17), also *C. glabrata* was found to evade the immune response and to remain even hours post infection alive and non-phagocytosed in human whole blood (**Figures 2C,D**). The rate for fungal cells becoming evasive against the immune response is for both pathogens comparably low, i.e., $\rho = 1.173 \times 10^{-2}\,\mathrm{min}^{-1}$ for *C. glabrata* and $\rho = 0.439 \times 10^{-2}\,\mathrm{min}^{-1}$ for *C. albicans*. A comparison of both rates that define the extracellular killing by antimicrobial peptides ($\kappa_{EK}(t)$) showed that the value of $\bar{\kappa}_{EK}$ is similar for both pathogens (see Table S1 in Supplementary Material) and γ is 2.5 times larger for infection scenarios with *C. glabrata* ($\gamma = 5.39 \times 10^{-2}\,\mathrm{min}^{-1}$).

The time-resolved kinetics of the fits with the lowest LSE for the two fungal pathogens can be seen in Figures S1 and S2 in Supplementary Material, where the thickness of the simulation curves reflect random variations within the SDs of the immune-reaction rates. For both pathogens, the SBM adequately resembled the experimental data. Since the SBM neglects all spatial aspects of the infection scenarios, we performed a bottom-up modeling approach by combining the SBM with the ABM (17).

Migration Parameters of Phagocytes in Response to Various Pathogens Differ Quantitatively

To determine the migration parameters of neutrophils and monocytes in whole-blood infection scenarios with the respective pathogens, we used the experimentally measured data as well as the fitted immune-reaction rates from the SBM to perform stochastic spatiotemporal simulations by the ABM in 1 µl of blood. As a result of this bottom-up modeling approach for whole-blood infection assays, we obtained the diffusion coefficients of the immune cells in response to *C. albicans*. This can be seen in **Figure 4A**, where the best solution, i.e., the parameter configuration of (D_N, D_M) that resulted in the smallest LSE, was identified to be $\left(D_N^{\min}, D_M^{\min}\right) = \left(425\ \mu\mathrm{m}^2/\mathrm{min},\ 175\ \mu\mathrm{m}^2/\mathrm{min}\right)$. In line with our earlier findings (17), for *C. albicans* the LSE was sensitive for variations in D_N but not for variations in D_M. The range of D_M that still lead to comparably low LSE values spans from approximately 100 $\mu\mathrm{m}^2$/min up to 500 $\mu\mathrm{m}^2$/min, whereas the range with comparably low LSE for D_N was limited to 400–425 $\mu\mathrm{m}^2$/min. As shown in Figure S3 in Supplementary Material, the fitting results are in excellent agreement with the experimental data, and the stochasticity of the *in silico* experiments still give rise to low SDs in the simulation curves, as can be inferred from the thickness of the curves representing 30 runs.

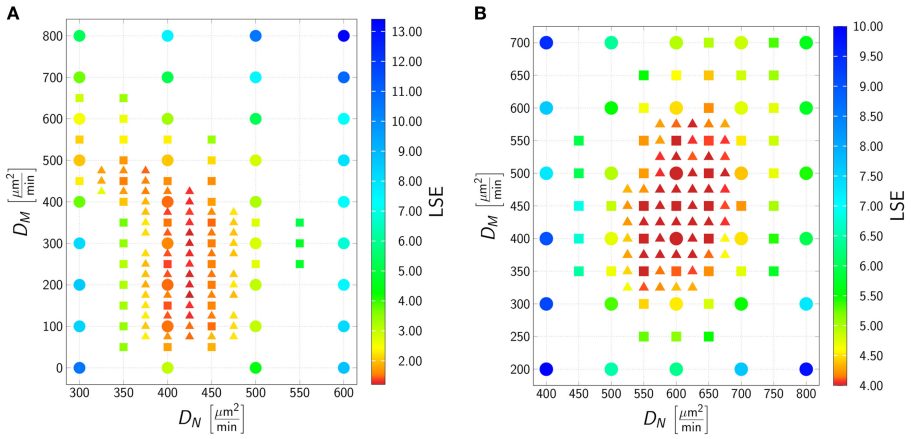

FIGURE 4 | Result of the agent-based model (ABM) parameter estimation for whole-blood infection assays with *Candida albicans* **(A)** and *Candida glabrata* **(B)**. Adaptive regular grid search was applied to fit the ABM to the experimental data and diffusion coefficients for neutrophils (D_N) and monocytes (D_M) were determined. At each grid point 1 µl blood was simulated, and 30 realizations for each parameter configuration were performed. Three different refinement levels were performed: simulations of the first level are represented as dots, simulations of the second level are represented as squares, and simulations of the third level are represented as triangles. The best fit to the experimental data was found at $(D_N^{min}, D_M^{min}) = (425\ \mu m^2/min,\ 175\ \mu m^2/min)$ for *C. albicans* and at $(D_N^{min}, D_M^{min}) = (600\ \mu m^2/min,\ 425\ \mu m^2/min)$ for *C. glabrata*.

The best fit of the simulation curves to the experimental data of whole-blood infection assays for *C. glabrata* was achieved for diffusion coefficients for neutrophils and monocytes with values $(D_N^{min}, D_M^{min}) = (600\ \mu m^2/min, 425\ \mu m^2/min)$ (see **Figure 4**). We note that the range in which the diffusion coefficient of monocytes can vary for comparable LSE values was found to be much more restricted than in the case of *C. albicans*, i.e., this range for D_M was from $350\,\mu m^2/min$ up to $575\,\mu m^2/min$ for fitting results with comparable LSE. However, in the case of *C. glabrata*, neutrophils were not found to be restricted to the small range of only $\pm 12\,\mu m^2/min$ as for *C. albicans*, but could vary in a range of $\pm\ 80\,\mu m^2/min$. As can be seen in Figure S4 in Supplementary Material, the experimentally determined kinetics of the infection scenario with *C. glabrata* is in excellent agreement with the simulation curves of the ABM.

Immune Response in Virtual Patients With Neutropenia Is Strongly Pathogen Dependent

Our previous considerations reveal that immune cells exhibit a qualitatively and quantitatively different response against *C. albicans* and *C. glabrata* in human whole-blood infection assays. Comparing *C. glabrata* to *C. albicans* infection, this is reflected by (i) increased phagocytosis rates and (ii) increased diffusion coefficients by factors of 1.4 and 2.4, respectively, for neutrophils and monocytes. In line with our previous work on the comparison between *C. glabrata* with *C. albicans* by live-cell imaging of phagocytosis assays (23–26), these quantitative differences are accompanied with the qualitative variation in the immune response that involves much stronger monocyte activation in the case of *C. glabrata*. Nevertheless, a prominent role is played by neutrophils that are quantitatively prevalent in cell number and qualitatively important in differently directing the immune response against these fungal pathogens (23).

To investigate the impact of neutropenia on the infection outcome with a specific pathogen, we simulated VNP using the ABM. Here, the optimal immune-reaction rates and diffusion coefficients were used as previously determined for normal ANC values. In the virtual patients, we stepwise decreased the number of neutrophils to resemble different degrees of severity of neutropenia and simulated the early immune response during 4 h post infection. The contributions of the combined units—such as killed, phagocytosed and immune-evasive *Candida* cells at 4 h post infection—are shown in **Figure 5**.

The phagocytosis by neutrophils is for both pathogens quite similar. For mild neutropenia the phagocytosis by neutrophils ranges for both fungal pathogens between ~40 and 50%, for mild neutropenia between ~25 and 40%, and is below ~25% for severe neutropenia. Interestingly, despite these similarities, the infection outcomes for the two pathogens under the condition of neutropenia are predicted to be remarkably different. As shown in **Figure 5A**, a stronger impact on the infection outcome can be observed for *C. albicans*, where in the scenario of severe neutropenia the number of killed fungal cells achieves only 10–45%. By contrast, killing of *C. glabrata* in severe neutropenia is more efficient, and the fraction of dead cells ranges between 45 and 60% of total fungal cells (see **Figure 5B**).

This difference is governed by the behavior of monocytes in response to the two fungal pathogens. Higher phagocytosis rates in case of *C. glabrata* compared with *C. albicans* enable monocytes to partially compensate for the loss of neutrophils under conditions of neutropenia. This compensatory effect is relatively low for *C. albicans*, where the fraction of cells that were phagocytosed by monocytes increased from 3% for normal ANC to only 12% under the condition of severe neutropenia (see **Figure 5A**). For

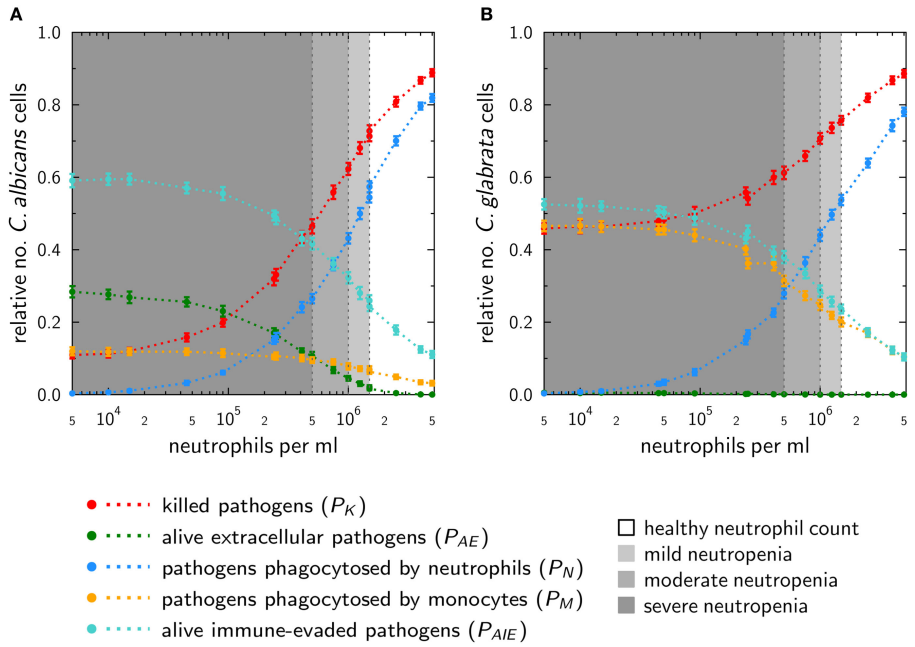

FIGURE 5 | *In silico* infections under neutropenic conditions with *Candida albicans* **(A)** and *Candida glabrata* **(B)** were performed by gradually decreasing the absolute neutrophil count in the agent-based model. Plots show the fraction of killed cells (red), alive and extracellular cells (green), phagocytosed cells by neutrophils (blue), and monocytes (yellow) as well as (alive) cells that are able to evade the immune system (turquoise) at 4 h post infection.

C. glabrata, this increase in monocyte phagocytosis rose from 10 to 46% of the *C. glabrata* cells (see **Figure 5B**). Furthermore, the infection outcome is also characterized by the number of cells that are able to evade the immune response. Immune evasion is more pronounced for *C. albicans*, where also for normal ANC 15% of all fungal cells are able to evade the immune response (see **Figure 5A**). However, with stronger degrees of neutropenia the fraction of these cells even increases to about 60%. In the case of *C. glabrata*, only 10% of the cells can evade the immune response for normal ANC, while this fraction rises up to 50% under conditions of severe neutropenia (see **Figure 5B**). As explained in Section "Materials and Methods," the infection outcome is mainly characterized by the fraction of killed as well as the fraction of alive and immune-evasive *Candida* cells. Therefore, we assigned the values of P_{K} and P_{AIE} at the boundaries to pattern that characterize the different degrees of severity of neutropenia (see Table S2 in Supplementary Material). Subsequently, with the help of these patterns, we were able to classify simulations of medical treatments in neutropenic patients.

Simulation of Medical Treatment for VNP

After we simulated the infection with the pathogens *C. albicans* and *C. glabrata* in VNP, we selected five types of VNP with different severity degrees of neutropenia for *in silico* treatment. The VNP-1 is characterized by an ANC of 1,250 neutrophils/µl representing patients with mild neutropenia. At the transition between mild and moderate, the ANC is 1,000 neutrophils/µl, and the corresponding VNP is referred to as VNP-2. Similarly, we defined VNP-3, VNP-4 and VNP-5 that are characterized, respectively, by ANC of 750 neutrophils/µl (moderate neutropenia), 500 neutrophils/µl (transition between moderate and severe neutropenia), and 250 neutrophils/µl (severe neutropenia). The *in silico* treatment involves the increase of neutrophil activation in terms of their phagocytosis rate and/or diffusion coefficient to quantitatively investigate its impact on the reduced numbers of neutrophils in these patients. Thus, increasing the phagocytosis rate and/or diffusion coefficient of neutrophils in a stepwise fashion, we simulated the infection with either of the two pathogens *C. albicans* and *C. glabrata* under neutropenic conditions. Afterward, the infection outcome of the simulation was classified according to the previously determined pattern (see Patterns and Classification of Simulations). To find a formal description of the increase of neutrophil phagocytosis rate and diffusion coefficient required for reaching the infection outcome for non-neutropenic individuals, we fitted an exponential function of the form $f_{\phi_{\mathrm{N}}} = 1 + a \cdot e^{-b \cdot f_{D_{\mathrm{N}}}}$ at the transition where the non-neutropenic infection outcome is reached. Here, the factors $f_{\phi_{\mathrm{N}}}$ and $f_{D_{\mathrm{N}}}$ are defined as $f_{\phi_{\mathrm{N}}} = \phi_{\mathrm{N}}^{\mathrm{T}}/\phi_{\mathrm{N}}^{\mathrm{min}}$ and $f_{D_{\mathrm{N}}} = D_{\mathrm{N}}^{\mathrm{T}}/D_{\mathrm{N}}^{\mathrm{min}}$, where $\phi_{\mathrm{N}}^{\mathrm{T}}$ and $D_{\mathrm{N}}^{\mathrm{T}}$ denote parameters that are affected by the treatment, and $\phi_{\mathrm{N}}^{\mathrm{min}}$ and $D_{\mathrm{N}}^{\mathrm{min}}$ refer to the parameter values obtained by minimizing the LSE under non-neutropenic conditions. We varied $\phi_{\mathrm{N}}^{\mathrm{T}}$ and $D_{\mathrm{N}}^{\mathrm{T}}$ over one order of magnitude, i.e., $f_{\phi_{\mathrm{N}}}, f_{D_{\mathrm{N}}} \in [1, 10]$, and plotted the resulting curves for each type of VNP in Figure S5 in Supplementary Material for the fitting parameters a and b as provided in Table S3 in Supplementary Material.

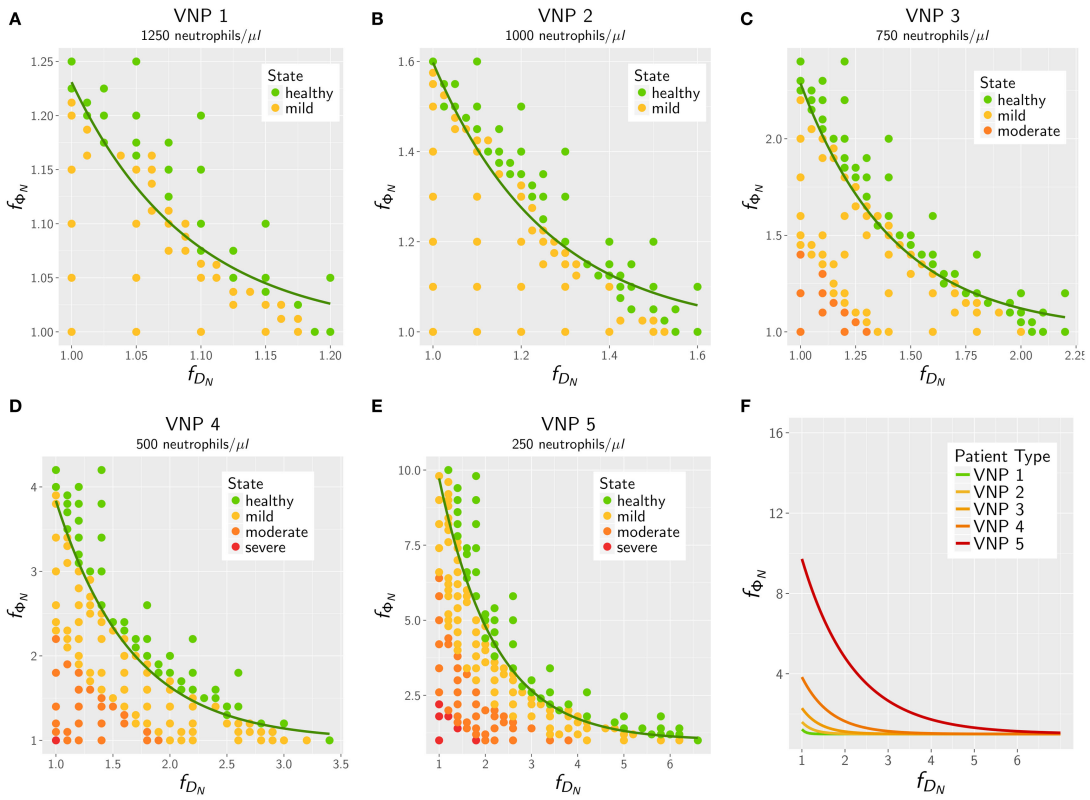

FIGURE 6 | *In silico* treatment of virtual neutropenic patients (VNP) infected with *Candida albicans* was simulated using the agent-based model. Stepwise increase of phagocytosis rate and diffusion coefficient of neutrophils was performed for VNP with various severity degrees of neutropenia: VNP1–5: 1,250 **(A)**, 1,000 **(B)**, 750 **(C)**, 500 **(D)**, and 250 **(E)** neutrophils/μl. Simulated points are classified according to the previously determined patterns: green points show a non-neutropenic infection outcome, yellow points show an infection outcome comparable to a mild neutropenia, orange points show an infection outcome comparable to a moderate neutropenia, and red points show an infection outcome comparable to a severe neutropenia. Solid lines depict the fitted exponential function $f_{\Phi_N} = 1 + a \cdot e^{-b \cdot f_{D_N}}$ at the transition to the non-neutropenic infection outcome. For comparison the fitted curves for the five VNP with their severity degrees of neutropenia are shown in panel **(F)**.

The results for the *in silico* treatment of VNP with *C. albicans* and *C. glabrata* infection are shown in detail in **Figures 6** and **7**, respectively. Performing more than 4×10^4 simulations, we generally found that all VNP do reach the infection outcome of non-neutropenic patients by increasing neutrophil activation in terms of phagocytosis rate and/or diffusion coefficient. As could be expected, the required increase in neutrophil activation depends on the severity degree of neutropenia in VNP. For VNP with severe neutropenia (VNP-5), reaching the infection outcome of non-neutropenic patients would require relatively high values for ϕ_N^T with $f_{\phi_N} > 10$, whereas the treatment was always successful for D_N^T with $f_{D_N} \ll 10$. To compare the two fungal pathogens with each other, we first fixed either $\phi_N^T = \phi_N^{min}$ $(f_{\phi_N} = 1)$ or $D_N^T = D_N^{min}$ $(f_{D_N} = 1)$ and varied only one parameter, respectively, D_N^T or ϕ_N^T. As can be seen in **Figure 8A**, for both fungal pathogens increasing the diffusion coefficient yields the infection outcome of non-neutropenic patients at smaller factors than increasing the phagocytosis rate, i.e., $f_{D_N} < f_{\phi_N}$. Interestingly, increasing only the neutrophil diffusion, the *in silico* treatment was found to be more effective for *C. glabrata*, whereas it turned out to be more effective for *C. albicans* if only the phagocytosis rate was increased. The combined impact of increasing ϕ_N^T and D_N^T yielded a pair $(f^*_{\phi_N}, f^*_{D_N})$ of optimal values with minimal distance from $(f_{\phi_N} = 1, f_{D_N} = 1)$ where the infection outcome of non-neutropenic patients was reached. The results are shown in **Figure 8B**, where the comparison between *C. albicans* and *C. glabrata* predicts that $f^*_{\phi_N} < f^*_{D_N}$ for the optimal *in silico* treatment, i.e., the required relative increase of the diffusion coefficient is larger than that for the phagocytosis rate. Moreover, the optimal *in silico* treatment was reached for factors $(f^*_{\phi_N}, f^*_{D_N})$ with lower values for all VNP in the case of *C. glabrata*.

DISCUSSION

In this study, we investigated bloodstream infections with the fungal pathogens *C. albicans* and *C. glabrata* in human whole

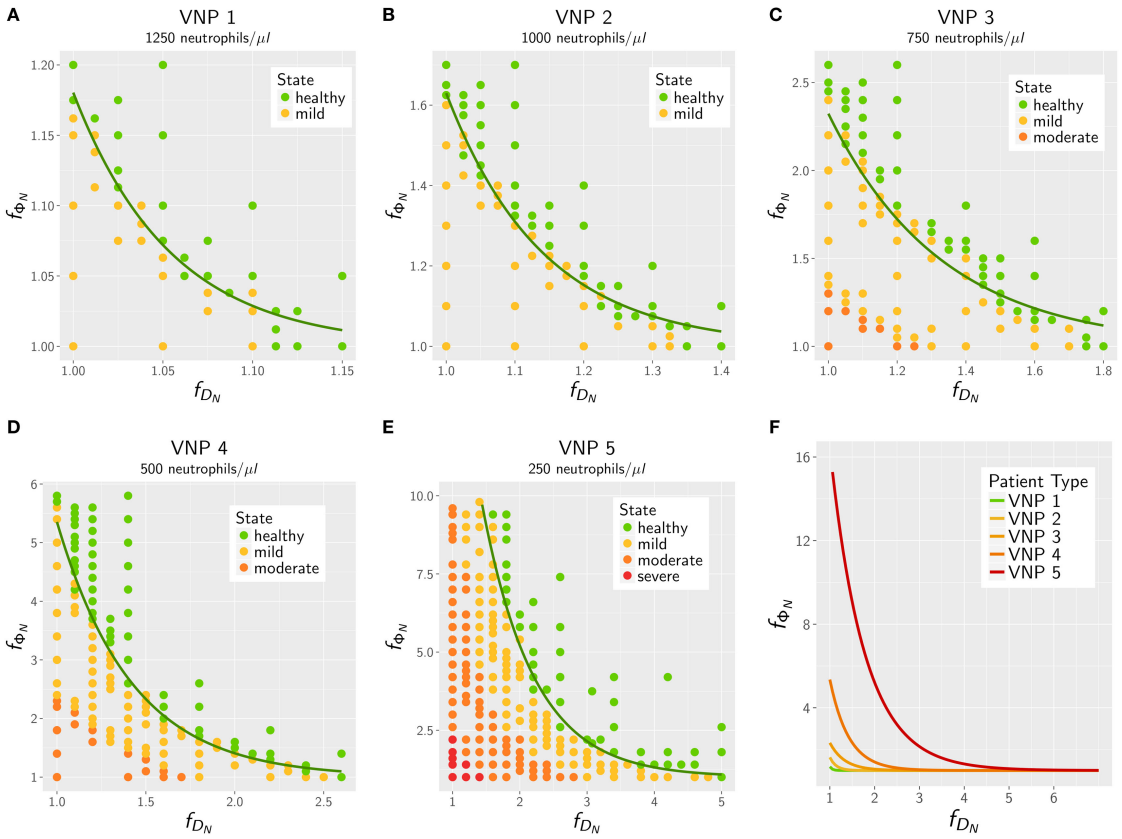

FIGURE 7 | *In silico* treatment of virtual neutropenic patients (VNP) infected with *Candida glabrata* was simulated using the agent-based model. Stepwise increase of phagocytosis rate and diffusion coefficient of neutrophils was performed for VNP with various severity degrees of neutropenia: VNP1–5: 1,250 **(A)**, 1,000 **(B)**, 750 **(C)**, 500 **(D)**, and 250 **(E)** neutrophils/μl. Simulated points are classified according to the previously determined patterns: green points show a non-neutropenic infection outcome, yellow points show an infection outcome comparable to a mild neutropenia, orange points show an infection outcome comparable to a moderate neutropenia, and red points show an infection outcome comparable to a severe neutropenia. Solid lines depict the fitted exponential function $f_{\Phi_N} = 1 + a \cdot e^{-b \cdot f_{D_N}}$ at the transition to the non-neutropenic infection outcome. For comparison, the fitted curves for the five VNP with their severity degrees of neutropenia are shown in panel **(F)**.

blood. Special focus was put on the infection scenario under neutropenic conditions as well as possible treatment strategies. These conditions are clinically relevant as it is well established that neutropenia promotes dissemination of *Candida* spp. during bloodstream infection and impairs prognosis. We used a previously established bottom-up modeling approach that combines different mathematical modeling approaches of increasing complexity based on wet-lab experiments (17). To investigate infection by different fungal pathogens, we first performed whole-blood infection assays using blood of healthy individuals. In the past, these whole-blood infection models have already been successfully applied to analyze the early immune response to clinically relevant pathogens (27–29) and to identify their virulence factors (30, 31). Furthermore, the influence of genetic polymorphisms on the immune response have been tested (32, 33) as well as potential therapeutic approaches and vaccine efficacy (34–38). In this study, we applied this experimental modeling approach to investigate early immune responses to the two *Candida* spp. in blood. The resulting experimental data showed that the immune response followed a faster kinetics for *C. glabrata* than for *C. albicans*, which is reflected by an earlier phagocytosis of this pathogen. In line with our previous studies (16, 17, 23), monocytes were found to contribute more to the immune response against *C. glabrata* compared with *C. albicans*.

The system behavior was quantified by estimating values for immune-reaction rates, such as phagocytosis and killing rates, based on fitting a SBM to the experimentally measured data (17). As expected from the observed difference in the kinetics of the immune response between *C. albicans* and *C. glabrata*, we found that the phagocytosis rates were orders of magnitude higher for *C. glabrata* with monocytes reaching the highest values (see Table S2 in Supplementary Material). Thus, for *C. glabrata* the

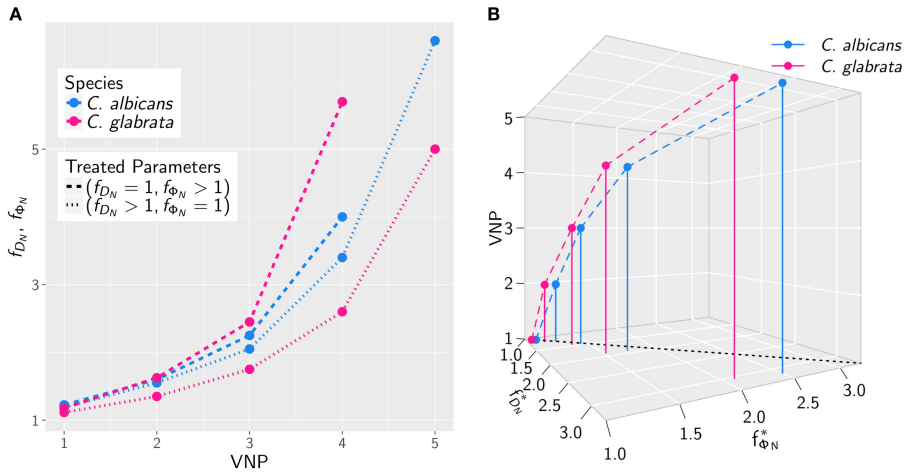

FIGURE 8 | The increase in neutrophil activation required to reach the infection outcome of non-neutropenic patients depends on the severity degree of neutropenia in VNP. **(A)** Comparison of *Candida albicans* (blue) and *Candida glabrata* (pink) infection for various VNP in terms of the factors f_{D_N} and f_{Φ_N} keeping either $f_{\Phi_N} = 1$ or $f_{D_N} = 1$ fixed. **(B)** The same as in panel **(A)** allowing both factors to vary to attain the optimal values $(f^*_{\Phi_N}, f^*_{D_N})$ with minimal distance from $(f_{\Phi_N} = 1, f_{D_N} = 1)$ at which the infection outcome of non-neutropenic patients is reached.

phagocytosis rate for monocytes is higher than for neutrophils and this relation is inverted for *C. albicans*. Applying a bottom-up modeling approach (17), we used an ABM to estimate migration parameters for neutrophils and monocytes in response to the two fungal species. For *C. glabrata* these migration parameter were higher than for *C. albicans*. As previously shown for *C. albicans* the outcome of the immune response was restricted to a narrow regime of migration parameters for the neutrophils (17), whereas these migration parameters in the case of *C. glabrata* infections could vary over a significantly wider range to fit the experimental data. This is another indication for the observable fact that monocytes play a more important role in the defense against *C. glabrata* compared with *C. albicans* (23, 39).

Since fungal infections by *Candida* spp. are a major risk for immunocompromised patients, we extended the computer simulations for normal ANC by numerically studying infection scenarios in virtual patients with different severity degrees of neutropenia. Due to the pronounced importance of neutrophils in the immune response against *C. albicans*, these computer simulations predicted a strong negative impact on the infection outcome for VNP depending on the severity degree of neutropenia. Although the impact of neutropenia on the infection outcome during *C. glabrata* infection was not as strong as for *C. albicans*, the immune response was still to a large extent impaired. For example, this was observed by the prediction that the fraction of killed pathogens at 4 h post infection decreased from around 90% for both species under normal ANC to about 50 and 10% for *C. glabrata* and *C. albicans* for severe neutropenic conditions, respectively. Moreover, at 4 h post infection, a fraction of 30% *C. albicans* cells are still alive and extracellular in human blood that could contribute to the dissemination to other body parts in real patients. While the fraction of alive and extracellular *C. glabrata* cells is negligible at 4 h post infection, a large fraction of about 50% is phagocytosed by monocytes including a few percent of fungal cells that are still alive and may disseminate by eventually escaping from the monocytes. These data again point toward different virulence traits in the two *Candida* spp. (40).

The bottom-up modeling approach for the simulation of infection scenarios under neutropenic conditions was established to simulate the effects of medical treatments. To date there exist three different ways to approach neutropenia in the clinical setting, which comprise (i) the stimulation and activation of remaining neutrophils by medical treatment of the patient, (ii) the internal stimulation of neutrophil maturation and release from the bone marrow by medication of patients with *granulocyte colony-stimulating factor* (G-CSF), and (iii) the transfusion of G-CSF/steroid mobilized neutrophils from a donor. The latter treatment of healthy donors leads to a vast increase of peripheral blood neutrophils (41–44), which are subsequently extracted from the donor by leukapheresis and administered to the patient to increase the ANC in blood. This therapy shows higher rates of patient survival in the context of bacterial infections (43), whereas improvement in patient survival was not consistently observed for fungal infections (45–47). In particular, Gazendam et al. (48) show that the G-CSF/dexamethasone stimulation of donor neutrophils leads to a change in their granular content, which impairs the fungal killing capacity with regard to *C. albicans*. The cytokine treatment with G-CSF to trigger the neutrophil release from the bone marrow in patients is mainly applied in congenital neutropenia and causes a significant increase of the ANC in blood (49, 50). Before effective drugs were available, children with congenital neutropenia typically died in their first year of life due to bacterial and fungal infections (51, 52). The G-CSF treatment makes use of the emergency mobilization of neutrophils in response to an inflammatory signal and the secretion of chemokines leading to neutrophil migration into blood vessels (53). However, patients

can be also *low-responders* or even *non-responders* exhibiting reduced effects of G-CSF (49, 54). Finally, instead of increasing the circulating number of neutrophils, the option to medically treat neutropenia by inflammatory cytokines, such as *interferon* γ and *tumor necrosis factor* α, yields a modulation of the immune response by the stimulation and activation of neutrophils in blood (41, 44). Both cytokines have been reported to enhance the neutrophil response against fungi, e.g., *Candida* spp. (55), *Aspergillus* spp. (56), and *Cryptococcus* spp. (57).

In this study, we focused on investigating the treatment of neutropenic patients by inflammatory cytokines to quantify the possibility of balancing neutropenic conditions and clearance of infection. The simulations of this *in silico* treatment revealed that an increase of the phagocytosis rate and/or the migration parameter of neutrophils generally improved the infection outcome. For both *Candida* spp. under investigation, conditions of mild neutropenia can be compensated resembling an infection outcome of non-neutropenic individuals by an increase in either the phagocytosis rate or the diffusion coefficient, or a combination of both, by less than 25% percent. The computer simulations allowed us to rigorously quantify the relative change in these parameters needed for any severity level of neutropenia. In the case of severe neutropenia, medical treatments would need to increase these parameters by at least 250% for the phagocytosis rate and at least 300% for the diffusion coefficient to reach infection outcomes in VNP comparable to individuals with normal ANC. It should be noted that the modulation of parameters has to be combined, because even a 10-fold increase of the phagocytosis rate alone would not recover the infection outcome of non-neutropenic individuals. Thus, the quantitative simulation of *in silico* treatments generates concrete predictions regarding the relative impact that treatments with inflammatory cytokines are required to exert on these two parameters. Moreover, our numerical experiments predict that *C. albicans* compared with *C. glabrata* always requires stronger increases in the phagocytosis rate and the diffusion coefficient for the same conditions of neutropenia.

Clearly, the underlying model assumptions (such as spatial homogeneity and absence of external forces) cannot be 1:1 translated into the *in vivo* situation—neither in small vessels nor in tissue. Despite this, several predictions resulting from the model could be confirmed *in vivo* or are in line with clinical findings (16). For this study, this also applies to the observations that (i) neutropenia may result in poor prognosis and a higher ratio of disseminated candidiasis [e.g., Ref. (58, 59)] and (ii) monocytes play a more important role in *C. glabrata* infection (23). Even though clinical studies will ultimately be required to validate our hypotheses, the first step would be to test these treatment strategies in whole-blood infection assays and our simulations for VNP can be used for this testing.

Our study may be extended in different ways. For example, computer simulations for various pathogens, such as *Staphylococcus* spp. and *Streptococcus* spp., which were shown to cause bacteremia and sepsis under conditions of neutropenia, could be performed (52, 60). Moreover, treatment strategies that lead to an increased ANC in neutropenic patients, like the transfusion therapy as well as the G-CSF treatment, could be simulated and compared with the cytokine treatment considered in this study. Furthermore, the bottom-up approach provides the possibility to investigate the impact of other immune disorders on the infection outcome with the pathogens under consideration. Moreover, the generated predictions of this study could be examined in future wet-lab experiments. Therefore, whole-blood infection assays with *C. albicans* or *C. glabrata* in human blood with reduced ANC could be performed. Such neutropenic blood samples could be taken from patients with neutropenia, where it should be considered that primary diseases of the patient may affect the experimental results. Another possibility may be to generate neutropenic blood samples in the wet lab by a controlled reduction of the neutrophil number. However, this poses a high challenge, since the remaining blood constituents will be affected by side effects that cannot be well controlled. Investigating such host–pathogen interactions by combining wet-lab and dry-lab studies is in the spirit of system biology. This approach provides a powerful tool to investigate biological systems in a qualitative as well as quantitative fashion and enables hypothesis generation in dry-lab as well as hypothesis testing in wet-lab studies.

ETHICS STATEMENT

Human peripheral blood was collected from healthy volunteers after informed consent. This study was conducted according to the principles expressed in the Declaration of Helsinki. All protocols were approved by the Ethics Committee of the University Hospital Jena (permit number: 273-12/09).

AUTHOR CONTRIBUTIONS

ST and MTF conceived and designed this study. MTF and OK provided computational resources and materials, respectively. Data processing, implementation, and application of the computational algorithm were done by ST, TL, MP, and MTF. Experiments were performed by KH and IL. ST, TL, MP, KH, IL, OK, and MTF evaluated and analyzed the results of this study; drafted the manuscript and revised it critically for important intellectual content and final approval of the version to be published; and agreed to be accountable for all aspects of the work in ensuring that questions related to the accuracy or integrity of any part of the work are appropriately investigated and resolved.

FUNDING

This work was financially supported by the Deutsche Forschungsgemeinschaft (DFG) through the excellence graduate school Jena School for Microbial Communication (JSMC), the CRC/TR124 FungiNet (project B4 to MTF and project C3 to OK), and the Center for Sepsis Control and Care (CSCC) (Project Quantim, FKZ 01EO1502 to MTF and OK) that is funded by the Federal Ministry for Education and Research (BMBF).

SUPPLEMENTARY MATERIAL

The Supplementary Material for this article can be found online at https://www.frontiersin.org/articles/10.3389/fimmu.2018.00667/full#supplementary-material.

REFERENCES

1. Murphy KP, Janeway C, Travers P, Walport M. *Janeway's Immunobiology*. 7th ed. New York, London: Garland Science (2008).
2. Schwartzberg LS. Neutropenia: etiology and pathogenesis. *Clin Cornerstone* (2006) 8:S5–11. doi:10.1016/S1098-3597(06)80053-0
3. Duggan S, Leonhardt I, Hünniger K, Kurzai O. Host response to *Candida albicans* bloodstream infection and sepsis. *Virulence* (2015) 6:316–26. doi:10.4161/21505594.2014.988096
4. Fidel PL Jr, Vazquez JA, Sobel JD. Candida glabrata: review of epidemiology, pathogenesis, and clinical disease with comparison to *C. albicans*. Clin Microbiol Rev (1999) 12:80–96.
5. Sardi JC, Scorzoni L, Bernardi T, Fusco-Almeida AM, Mendes Giannini MJ. *Candida* species: current epidemiology, pathogenicity, biofilm formation, natural antifungal products and new therapeutic options. *J Med Microbiol* (2013) 62:10–24. doi:10.1099/jmm.0.045054-0
6. Orasch C, Marchetti O, Garbino J, Schrenzel J, Zimmerli S, Mühlethaler K, et al. *Candida* species distribution and antifungal susceptibility testing according to European Committee on Antimicrobial Susceptibility Testing and new vs. old Clinical and Laboratory Standards Institute clinical breakpoints: a 6-year prospective candidaemia survey from the fungal infection network of Switzerland. *Clin Microbiol Infect* (2014) 20:698–705. doi:10.1111/1469-0691.12440
7. Mayer FL, Wilson D, Hube B, Article M. *Candida albicans* pathogenicity mechanisms. *Clin Infect Dis* (2002) 48105:119–28. doi:10.4161/viru.22913
8. Calderone RA, Clancy CJ, editors. *Candida and Candidiasis*. 2nd ed. Washington, DC: ASM Press (2002).
9. Rodrigues CF, Silva S, Henriques M. *Candida glabrata*: a review of its features and resistance. *Eur J Clin Microbiol Infect Dis* (2014) 33:673–88. doi:10.1007/s10096-013-2009-3
10. Kitano H. Systems biology: a brief overview. *Science* (2002) 295:1662–4. doi:10.1126/science.1069492
11. Aderem A. Systems biology: its practice and challenges. *Cell* (2005) 121:511–3. doi:10.1016/j.cell.2005.04.020
12. Bruggeman FJ, Westerhoff HV. The nature of systems biology. *Trends Microbiol* (2007) 15:45–50. doi:10.1016/j.tim.2006.11.003
13. Germain RN, Meier-Schellersheim M, Nita-Lazar A, Fraser IDC. Systems biology in immunology: a computational modeling perspective. *Annu Rev Immunol* (2011) 29:527–85. doi:10.1146/annurev-immunol-030409-101317
14. Horn F, Heinekamp T, Kniemeyer O, Pollmächer J, Valiante V, Brakhage AA. Systems biology of fungal infection. *Front Microbiol* (2012) 3:108. doi:10.3389/fmicb.2012.00108
15. Medyukhina A, Timme S, Mokhtari Z, Figge MT. Image-based systems biology of infection. *Cytometry A* (2015) 87:462–70. doi:10.1002/cyto.a.22638
16. Hünniger K, Lehnert T, Bieber K, Martin R, Figge MT, Kurzai O. A virtual infection model quantifies innate effector mechanisms and *Candida albicans* immune escape in human blood. *PLoS Comput Biol* (2014) 10:e1003479. doi:10.1371/journal.pcbi.1003479
17. Lehnert T, Timme S, Pollmächer J, Hünniger K, Kurzai O, Figge MT. Bottom-up modeling approach for the quantitative estimation of parameters in pathogen-host interactions. *Front Microbiol* (2015) 6:608. doi:10.3389/fmicb.2015.00608
18. Pollmächer J, Figge MT. Agent-based model of human alveoli predicts chemotactic signaling by epithelial cells during early *Aspergillus fumigatus* infection. *PLoS One* (2014) 9:e111630. doi:10.1371/journal.pone.0111630
19. Pollmächer J, Figge MT. Deciphering chemokine properties by a hybrid agent-based model of *Aspergillus fumigatus* infection in human alveoli. *Front Microbiol* (2015) 6:503. doi:10.3389/fmicb.2015.00503
20. Dale DC, Cottle TE, Fier CJ, Bolyard AA, Bonilla MA, Boxer LA, et al. Severe chronic neutropenia: treatment and follow-up of patients in the Severe Chronic Neutropenia International Registry. *Am J Hematol* (2003) 72:82–93. doi:10.1002/ajh.10255
21. Crawford J, Dale DC, Lyman GH. Chemotherapy-induced neutropenia. *Cancer* (2004) 100:228–37. doi:10.1002/cncr.11882
22. Seider K, Brunke S, Schild L, Jablonowski N, Wilson D, Majer O, et al. The facultative intracellular pathogen *Candida glabrata* subverts macrophage cytokine production and phagolysosome maturation. *J Immunol* (2011) 187:3072–86. doi:10.4049/jimmunol.1003730
23. Duggan S, Essig F, Hünniger K, Mokhtari Z, Bauer L, Lehnert T, et al. Neutrophil activation by *Candida glabrata* but not *Candida albicans* promotes fungal uptake by monocytes. *Cell Microbiol* (2015) 17:1259–76. doi:10.1111/cmi.12443
24. Essig F, Hünniger K, Dietrich S, Figge MT, Kurzai O. Human neutrophils dump *Candida glabrata* after intracellular killing. *Fungal Genet Biol* (2015) 84:37–40. doi:10.1016/j.fgb.2015.09.008
25. Brandes S, Mokhtari Z, Essig F, Hünniger K, Kurzai O, Figge MT. Automated segmentation and tracking of non-rigid objects in time-lapse microscopy videos of polymorphonuclear neutrophils. *Med Image Anal* (2015) 20(1):34–51. doi:10.1016/j.media.2014.10.002
26. Brandes S, Dietrich S, Hünniger K, Kurzai O, Figge MT. Migration and interaction tracking for quantitative analysis of phagocyte-pathogen confrontation assays. *Med Image Anal* (2017) 36:172–83. doi:10.1016/j.media.2016.11.007
27. Tena GN, Young DB, Eley B, Henderson H, Nicol MP, Levin M, et al. Failure to control growth of mycobacteria in blood from children infected with human immunodeficiency virus and its relationship to T cell function. *J Infect Dis* (2003) 187:1544–51. doi:10.1086/374799
28. Silva D, Ponte CGG, Hacker MA, Antas PRZ. A whole blood assay as a simple, broad assessment of cytokines and chemokines to evaluate human immune responses to *Mycobacterium tuberculosis* antigens. *Acta Trop* (2013) 127:75–81. doi:10.1016/j.actatropica.2013.04.002
29. Urrutia A, Duffy D, Rouilly V, Posseme C, Djebali R, Illanes G, et al. Standardized whole-blood transcriptional profiling enables the deconvolution of complex induced immune responses. *Cell Rep* (2016) 16:2777–91. doi:10.1016/j.celrep.2016.08.011
30. Echenique-Rivera H, Muzzi A, Del Tordello E, Seib KL, Francois P, Rappuoli R, et al. Transcriptome analysis of *Neisseria meningitidis* in human whole blood and mutagenesis studies identify virulence factors involved in blood survival. *PLoS Pathog* (2011) 7:e1002027. doi:10.1371/journal.ppat.1002027
31. Van Der Maten E, De Jonge MI, De Groot R, Van Der Flier M, Langereis JD. A versatile assay to determine bacterial and host factors contributing to opsonophagocytotic killing in hirudin-anticoagulated whole blood. *Sci Rep* (2017) 7:3–12. doi:10.1038/srep42137
32. Lin J, Yao YM, Yu Y, Chai JK, Huang ZH, Dong N, et al. Effects of CD14-159 C/T polymorphism on CD14 expression and the balance between proinflammatory and anti-inflammatory cytokines in whole blood culture. *Shock* (2007) 28:148–53. doi:10.1097/SHK.0b013e3180341d35
33. Duffy D, Rouilly V, Libri V, Hasan M, Beitz B, David M, et al. Functional analysis via standardized whole-blood stimulation systems defines the boundaries of a healthy immune response to complex stimuli. *Immunity* (2014) 40:436–50. doi:10.1016/j.immuni.2014.03.002
34. Deslouches B, Islam K, Craigo JK, Paranjape SM, Montelaro RC, Mietzner TA. Activity of the de novo engineered antimicrobial peptide WLBU2 against *Pseudomonas aeruginosa* in human serum and whole blood: implications for systemic applications. *Antimicrob Agents Chemother* (2005) 49:3208–16. doi:10.1128/AAC.49.8.3208-3216.2005
35. Jemmett K, Macagno A, Molteni M, Heckels JE, Rossetti C, Christodoulides M. A cyanobacterial lipopolysaccharide antagonist inhibits cytokine production induced by *Neisseria meningitidis* in a human whole-blood model of septicemia. *Infect Immun* (2008) 76:3156–63. doi:10.1128/IAI.00110-08
36. Li M, Xue J, Liu J, Kuang D, Gu Y, Lin S. Efficacy of cytokine removal by plasmodia filtration using a selective plasma separator: in vitro sepsis model. *Ther Apher Dial* (2011) 15:98–104. doi:10.1111/j.1744-9987.2010.00850.x
37. Plested JS, Welsch JA, Granoff DM. Ex vivo model of meningococcal bacteremia using human blood for measuring vaccine-induced serum passive protective activity. *Clin Vaccine Immunol* (2009) 16:785–91. doi:10.1128/CVI.00007-09
38. Sprong T, Brandtzaeg P, Fung M, Pharo AM, Høiby EA, Michaelsen TE, et al. Inhibition of C5a-induced inflammation with preserved C5b-9-mediated bactericidal activity in a human whole blood model of meningococcal sepsis. *Blood* (2003) 102:3702–10. doi:10.1182/blood-2003-03-0703
39. Jacobsen ID, Brunke S, Seider K, Schwarzmüller T, Firon A, D'Enfért C, et al. *Candida glabrata* persistence in mice does not depend on host immunosuppression and is unaffected by fungal amino acid auxotrophy. *Infect Immun* (2010) 78:1066–77. doi:10.1128/IAI.01244-09
40. Brunke S, Hube B. Two unlike cousins: *Candida albicans* and *C. glabrata* infection strategies. *Cell Microbiol* (2013) 15:701–8. doi:10.1111/cmi.12091
41. Posch W, Steger M, Wilflingseder D, Lass-Flörl C. Promising immunotherapy against fungal diseases. *Expert Opin Biol Ther* (2017) 17:861–70. doi:10.1080/14712598.2017.1322576

42. Marfin AA, Price TH. Granulocyte transfusion therapy. *J Intensive Care Med* (2015) 30:79–88. doi:10.1177/0885066613498045
43. Einsele H, Northoff H, Neumeister B. Granulocyte transfusion. *Vox Sang* (2004) 87:205–8. doi:10.1111/j.1741-6892.2004.00483.x
44. Armstrong-James D, Brown GD, Netea MG, Zelante T, Gresnigt MS, van de Veerdonk FL, et al. Immunotherapeutic approaches to treatment of fungal diseases. *Lancet Infect Dis* (2017) 17(12):e393–402. doi:10.1016/S1473-3099(17)30442-5
45. Strauss RG. Clinical perspectives of granulocyte transfusions: efficacy to date. *J Clin Apher* (1995) 10:114–8. doi:10.1002/jca.2920100303
46. Bhatia S, McCullough J, Perry EH, Clay M, Ramsay NK, Neglia JP. Granulocyte transfusions: efficacy in treating fungal infections in neutropenic patients following bone marrow transplantation. *Transfusion* (1994) 34:226–32. doi:10.1046/j.1537-2995.1994.34394196620.x
47. Safdar A, Hanna HA, Boktour M, Kontoyiannis DP, Hachem R, Lichtiger B, et al. Impact of high-dose granulocyte transfusions in patients with cancer with candidemia: retrospective case-control analysis of 491 episodes of *Candida* species bloodstream infections. *Cancer* (2004) 101:2859–65. doi:10.1002/cncr.20710
48. Gazendam RP, van de Geer A, van Hamme JL, Tool ATJ, van Rees DJ, Aarts CEM, et al. Impaired killing of *Candida albicans* by granulocytes mobilized for transfusion purposes: a role for granule components. *Haematologica* (2016) 101:587–96. doi:10.3324/haematol.2015.136630
49. Fioredda F, Calvillo M, Bonanomi S, Coliva T, Tucci F, Farruggia P, et al. Congenital and acquired neutropenias consensus guidelines on therapy and follow-up in childhood from the Neutropenia Committee of the Marrow Failure Syndrome Group of the AIEOP (Associazione Italiana Emato-Oncologia Pediatrica). *Am J Hematol* (2012) 87:235–8. doi:10.1002/ajh.22225
50. Palmblad J, Papadaki HA, Eliopoulos G. Acute and chronic neutropenias. What is new? *J Intern Med* (2001) 250:476–91. doi:10.1046/j.1365-2796.2001.00915.x
51. Zeidler C, Boxer L, Dale DC, Freedman MH, Kinsey S, Welte K. Management of Kostmann syndrome in the G-CSF era. *Br J Haematol.* (2000) 109:490–5. doi:10.1046/j.1365-2141.2000.02064.x
52. Newburger PE. Disorders of neutrophil number and function. *Hematology Am Soc Hematol Educ Program* (2006) 2006:104–10. doi:10.1182/asheducation-2006.1.104
53. Köhler A, De Filippo K, Hasenberg M, van den Brandt C, Nye E, Hosking MP, et al. G-CSF-mediated thrombopoietin release triggers neutrophil motility and mobilization from bone marrow via induction of Cxcr2 ligands. *Blood* (2011) 117:4349–57. doi:10.1182/blood-2010-09-308387
54. Berliner N, Horwitz M, Loughran TP. Congenital and acquired neutropenia. *Hematol Am Soc Hematol Educ Progr* (2004) 2004:63–79. doi:10.1182/asheducation-2004.1.63
55. Kullberg BJ, t Wout JW, Hoogstraten C, van Furth R. Recombinant interferon-gamma enhances resistance to acute disseminated *Candida albicans* infection in mice. *J Infect Dis* (1993) 168:436–43. doi:10.1093/infdis/168.2.436
56. Nagai H, Guo J, Choi H, Kurup V. Interferon-gamma and tumor necrosis factor-alpha protect mice from invasive aspergillosis. *J Infect Dis* (1995) 172:1554–60. doi:10.1093/infdis/172.6.1554
57. Clemons KV, Lutz JE, Stevens DA. Efficacy of recombinant gamma interferon for treatment of systemic cryptococcosis in SCID mice. *Society* (2001) 45:686–9. doi:10.1128/AAC.45.3.686
58. Dutta A, Palazzi DL. *Candida* non-albicans versus *Candida albicans* fungemia in the non-neonatal pediatric population. *Pediatr Infect Dis J* (2011) 30:664–8. doi:10.1097/INF.0b013e318213da0f
59. Delaloye J, Calandra T. Invasive candidiasis as a cause of sepsis in the critically ill patient. *Virulence* (2014) 5:154–62. doi:10.4161/viru.26187
60. Donadieu J, Fenneteau O, Beaupain B, Mahlaoui N, Chantelot CB. Congenital neutropenia: diagnosis, molecular bases and patient management. *Orphanet J Rare Dis* (2011) 6:26. doi:10.1186/1750-1172-6-26

Conflict of Interest Statement: The authors declare that the research was conducted in the absence of any commercial or financial relationships that could be construed as a potential conflict of interest.

Supplementary Material

Quantitative simulations predict treatment strategies against fungal infections in virtual neutropenic patients

Sandra Timme[1,2], Teresa Lehnert[1,3], Maria T. E. Praße[1,2], Kerstin Hünniger[4,5], Ines Leonhardt[3,4], Oliver Kurzai[3,4,5], and Marc Thilo Figge[1,2,3,*]

[1]Research Group Applied Systems Biology, Leibniz Institute for Natural Product Research and Infection Biology – Hans Knöll Institute, Jena, Germany

[2]Faculty of Biology and Pharmacy, Friedrich Schiller University Jena, Germany

[3]Center for Sepsis Control and Care (CSCC), Jena University Hospital, Jena, Germany

[4]Fungal Septomics, Septomics Research Center, Friedrich Schiller University and Leibniz Institute for Natural Product Research and Infection Biology – Hans Knöll Institute, Jena, Germany

[5]Institute for Hygiene and Microbiology, University of Würzburg, Würzburg, Germany

*** Correspondence:**
Marc Thilo Figge
thiol.figge@leibniz-hki.de

1 Supplementary Figures and Tables

1.1 Supplementary Figures

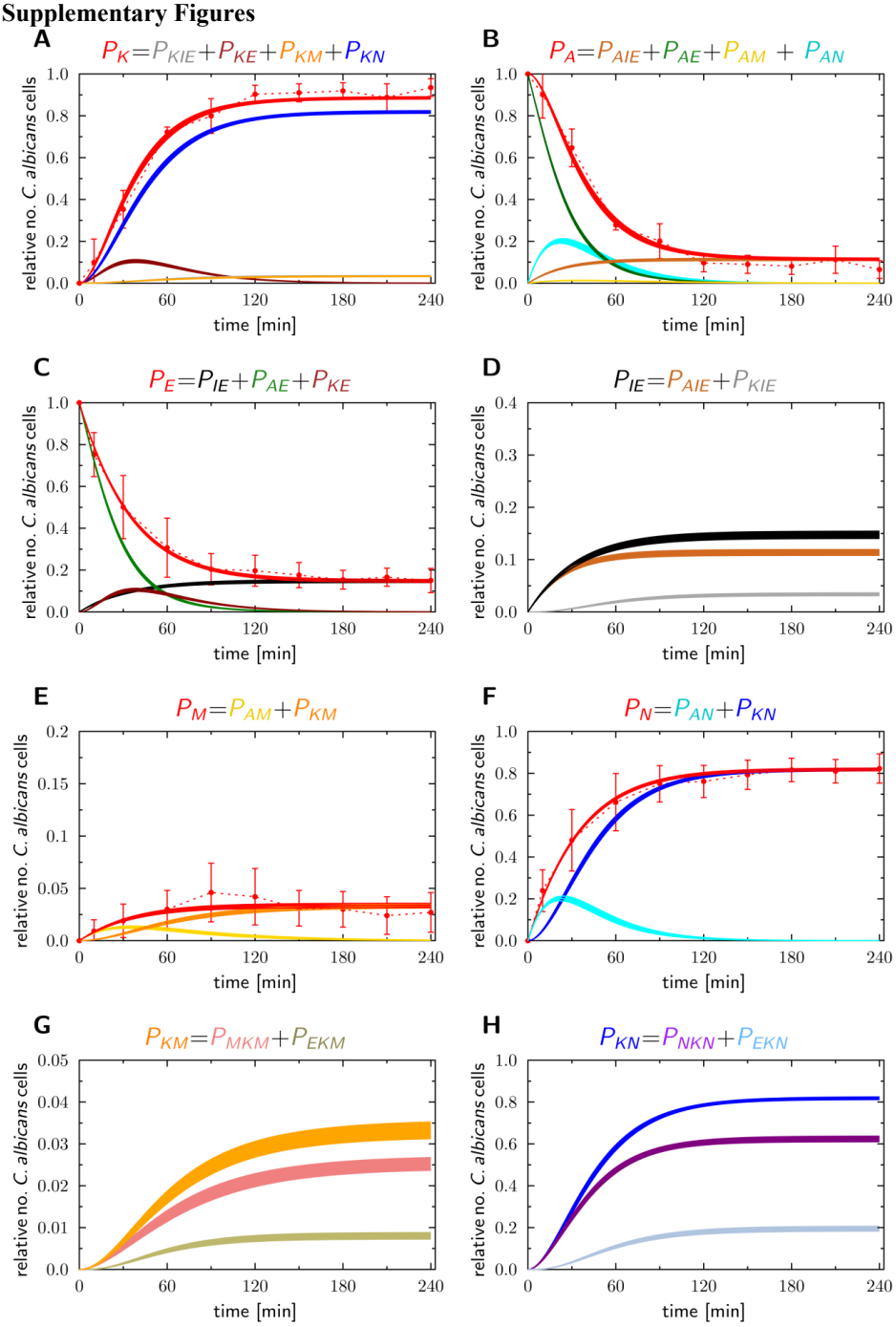

Supplementary Figure 1 Dynamics of combined units simulated by the SBM (red solid lines) with minimal least-squares error (LSE) to the experimental data from whole-blood infection assays with *C. albicans* (red dashed lines as guide for the eye). The error bars correspond to the standard deviations of five independent experiments. The thickness of the solid lines represents the standard deviation of the simulation results as obtained by 30 simulations for uniformly distributed transition rates as given in Table S1. The colored continuous lines represent the *in silico* kinetics of the fungal states that are referred to as the symbol with the same color. (A) The dynamics of killed fungal cells that were experimentally measured by survival assays. The corresponding combined unit P_K comprises the states of fungal cells that are killed and immune-evasive (P_{KIE}), killed and extracellular (P_{KE}), killed in monocytes (P_{KM}) and killed in neutrophils (P_{KN}). (B) Time course of alive fungal cells that were measured by survival assays and simulated by the combined unit P_A. This is calculated by the sum of all states representing alive fungal cells, *i.e.* fungal states that are alive and immune-evasive (P_{AIE}), alive and extracellular (P_{AE}), and alive and in monocytes (P_{AM}) or in neutrophils (P_{AN}). (C) Kinetics of extracellular fungal cells that were measured by FACS analysis. These are compared with the dynamics of the combined unit P_E that comprises states of fungal cells that are extracellular and alive (P_{AE}), extracellularly killed (P_{KE}) and immune-evasive (P_{IE}). (D) The *in silico* dynamics of fungal cells that are immune-evasive (P_{IE}) are the sum of alive (P_{AIE}) and killed (P_{KIE}) immune-evasive fungal cells at each time point of the simulation time. (E) The relative number of fungal cells in monocytes are experimentally measured by FACS analysis and simulated by the combined unit P_M that is defined by the sum of fungal states in monocytes that are alive or killed, *i.e.* P_{AM}, P_{KM}, respectively. (F) The kinetics of fungal cells in neutrophils were measured using FACS analysis and are comparable with *in silico* dynamics of the combined unit P_N. This is defined as the sum of all fungal states that are in neutrophils and either alive (P_{AN}) or killed (P_{KN}). (G) *In silico* kinetics of killed fungal cells in monocytes (P_{KM}) that are defined as the sum of intracellularly killed (P_{MKM}) and extracellularly killed (P_{EKM}) pathogens at each simulation time point. (H) *In silico* time course of fungal cells in neutrophils that were killed (P_{KN}). These cells were either killed intracellularly in neutrophils (P_{NKN}) or killed extracellularly (P_{EKN}).

Supplementary Material

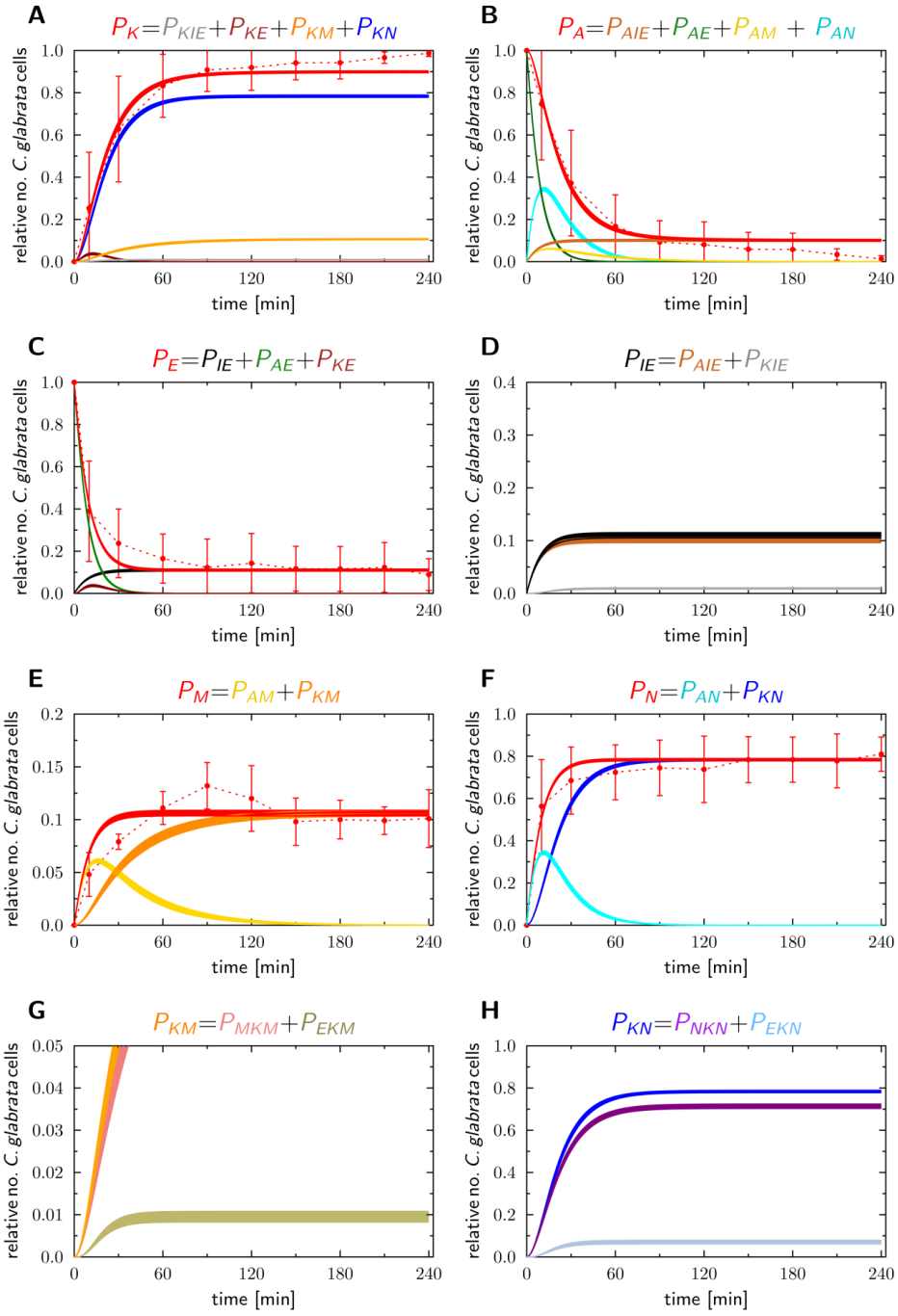

Supplementary Figure 2 Dynamics of combined units simulated by the SBM (red solid lines) with minimal least-squares error (LSE) to the experimental data from whole-blood infection assays with *C. glabrata* (red dashed lines as guide for the eye). The error bars correspond to the standard deviations of five independent experiments. The thickness of the solid lines represents the standard deviation of the simulation results as obtained by 30 simulations for uniformly distributed transition rates as given in Table S1. The colored continuous lines represent the *in silico* kinetics of the fungal states that are referred to as the symbol with the same color. (A) The dynamics of killed fungal cells that were experimentally measured by survival assays. The corresponding combined unit P_K comprises the states of fungal cells that are killed and immune-evasive (P_{KIE}), killed and extracellular (P_{KE}), killed in monocytes (P_{KM}) and killed in neutrophils (P_{KN}). (B) Time course of alive fungal cells that were measured by survival assays and simulated by the combined unit P_A. This is calculated by the sum of all states representing alive fungal cells, *i.e.* fungal states that are alive and immune-evasive (P_{AIE}), alive and extracellular (P_{AE}), and alive and in monocytes (P_{AM}) or in neutrophils (P_{AN}). (C) Kinetics of extracellular fungal cells that were measured by FACS analysis. These are compared with the dynamics of the combined unit P_E that comprises states of fungal cells that are extracellular and alive (P_{AE}), extracellularly killed (P_{KE}) and immune-evasive (P_{IE}). (D) The *in silico* dynamics of fungal cells that are immune-evasive (P_{IE}) are the sum of alive (P_{AIE}) and killed (P_{KIE}) immune-evasive fungal cells at each time point of the simulation time. (E) The relative number of fungal cells in monocytes are experimentally measured by FACS analysis and simulated by the combined unit P_M that is defined by the sum of fungal states in monocytes that are alive or killed, *i.e.* P_{AM}, P_{KM}, respectively. (F) The kinetics of fungal cells in neutrophils were measured using FACS analysis and are comparable with *in silico* dynamics of the combined unit P_N. This is defined as the sum of all fungal states that are in neutrophils and either alive (P_{AN}) or killed (P_{KN}). (G) *In silico* kinetics of killed fungal cells in monocytes (P_{KM}) that are defined as the sum of intracellularly killed (P_{MKM}) and extracellularly killed (P_{EKM}) pathogens at each simulation time point. (H) *In silico* time course of fungal cells in neutrophils that were killed (P_{KN}). These cells were either killed intracellularly in neutrophils (P_{NKN}) or killed extracellularly (P_{EKN}).

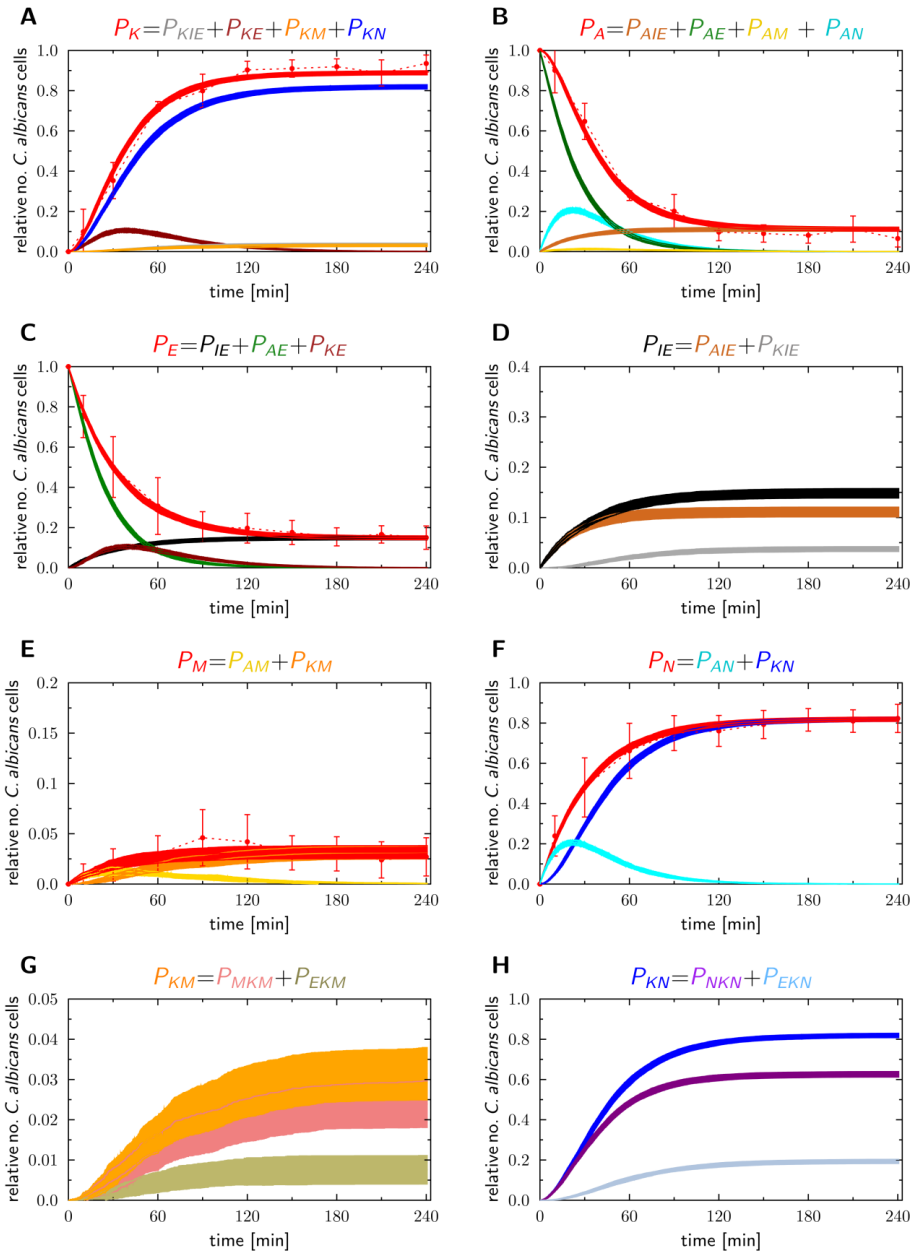

Supplementary Figure 3 Dynamics of combined units simulated by the ABM (red solid lines) with minimal least-squares error (LSE) to the experimental data from whole-blood infection assays with *C. albicans* (red dashed lines as guide for the eye). The error bars correspond to the standard deviations of five independent experiments. The thickness of the solid lines represents the standard deviation of the simulation results as obtained by 30 simulations for uniformly distributed transition

rates as given in Table S1. The colored continuous lines represent the *in silico* kinetics of the fungal states that are referred to as the symbol with the same color. (A) The dynamics of killed fungal cells that were experimentally measured by survival assays. The corresponding combined unit P_K comprises the states of fungal cells that are killed and immune-evasive (P_{KIE}), killed and extracellular (P_{KE}), killed in monocytes (P_{KM}) and killed in neutrophils (P_{KN}). (B) Time course of alive fungal cells that were measured by survival assays and simulated by the combined unit P_A. This is calculated by the sum of all states representing alive fungal cells, *i.e.* fungal states that are alive and immune-evasive (P_{AIE}), alive and extracellular (P_{AE}), and alive and in monocytes (P_{AM}) or in neutrophils (P_{AN}). (C) Kinetics of extracellular fungal cells that were measured by FACS analysis. These are compared with the dynamics of the combined unit P_E that comprises states of fungal cells that are extracellular and alive (P_{AE}), extracellularly killed (P_{KE}) and immune-evasive (P_{IE}). (D) The *in silico* dynamics of fungal cells that are immune-evasive (P_{IE}) are the sum of alive (P_{AIE}) and killed (P_{KIE}) immune-evasive fungal cells at each time point of the simulation time. (E) The relative number of fungal cells in monocytes are experimentally measured by FACS analysis and simulated by the combined unit P_M that is defined by the sum of fungal states in monocytes that are alive or killed, *i.e.* P_{AM}, P_{KM}, respectively. (F) The kinetics of fungal cells in neutrophils were measured using FACS analysis and are comparable with *in silico* dynamics of the combined unit P_N. This is defined as the sum of all fungal states that are in neutrophils and either alive (P_{AN}) or killed (P_{KN}). (G) *In silico* kinetics of killed fungal cells in monocytes (P_{KM}) that are defined as the sum of intracellularly killed (P_{MKM}) and extracellularly killed (P_{EKM}) pathogens at each simulation time point. (H) *In silico* time course of fungal cells in neutrophils that were killed (P_{KN}). These cells were either killed intracellularly in neutrophils (P_{NKN}) or killed extracellularly (P_{EKN}).

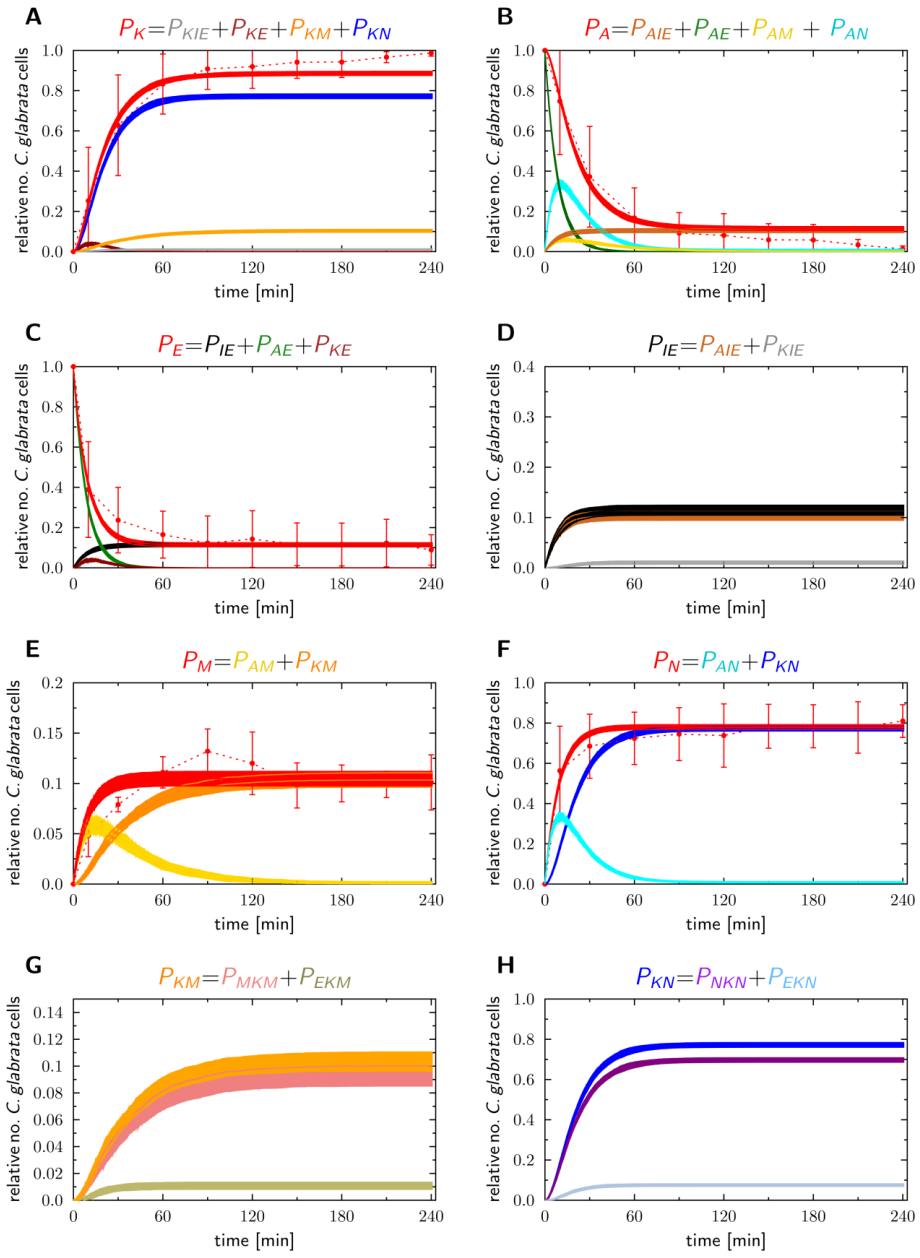

Supplementary Figure 4 Dynamics of combined units simulated by the ABM (red solid lines) with minimal least-squares error (LSE) to the experimental data from whole-blood infection assays with *C. glabrata* (red dashed lines as guide for the eye). The error bars correspond to the standard deviations of five independent experiments. The thickness of the solid lines represents the standard deviation of the simulation results as obtained by 30 simulations for uniformly distributed transition

rates as given in Table S1. The colored continuous lines represent the *in silico* kinetics of the fungal states that are referred to as the symbol with the same color. (A) The dynamics of killed fungal cells that were experimentally measured by survival assays. The corresponding combined unit P_K comprises the states of fungal cells that are killed and immune-evasive (P_{KIE}), killed and extracellular (P_{KE}), killed in monocytes (P_{KM}) and killed in neutrophils (P_{KN}). (B) Time course of alive fungal cells that were measured by survival assays and simulated by the combined unit P_A. This is calculated by the sum of all states representing alive fungal cells, *i.e.* fungal states that are alive and immune-evasive (P_{AIE}), alive and extracellular (P_{AE}), and alive and in monocytes (P_{AM}) or in neutrophils (P_{AN}). (C) Kinetics of extracellular fungal cells that were measured by FACS analysis. These are compared with the dynamics of the combined unit P_E that comprises states of fungal cells that are extracellular and alive (P_{AE}), extracellularly killed (P_{KE}) and immune-evasive (P_{IE}). (D) The *in silico* dynamics of fungal cells that are immune-evasive (P_{IE}) are the sum of alive (P_{AIE}) and killed (P_{KIE}) immune-evasive fungal cells at each time point of the simulation time. (E) The relative number of fungal cells in monocytes are experimentally measured by FACS analysis and simulated by the combined unit P_M that is defined by the sum of fungal states in monocytes that are alive or killed, *i.e.* P_{AM}, P_{KM}, respectively. (F) The kinetics of fungal cells in neutrophils were measured using FACS analysis and are comparable with *in silico* dynamics of the combined unit P_N. This is defined as the sum of all fungal states that are in neutrophils and either alive (P_{AN}) or killed (P_{KN}). (G) *In silico* kinetics of killed fungal cells in monocytes (P_{KM}) that are defined as the sum of intracellularly killed (P_{MKM}) and extracellularly killed (P_{EKM}) pathogens at each simulation time point. (H) *In silico* time course of fungal cells in neutrophils that were killed (P_{KN}). These cells were either killed intracellularly in neutrophils (P_{NKN}) or killed extracellularly (P_{EKN}).

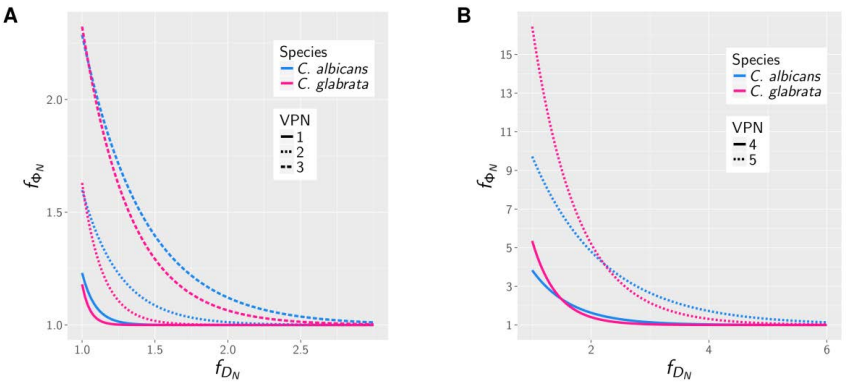

Supplementary Figure 5 The fitted curves $\boldsymbol{f_{\phi_N} = 1 + a \cdot e^{-b \cdot f_{D_N}}}$ at the transition to the non-neutropenic infection outcome with *C. albicans* (blue) or *C. glabrata* (pink) for VNP-1 – 3 (**A**) and VNP-4 and VNP-5 (**B**).

1.2 Supplementary Tables

Supplementary Table 1 Immune Reaction Rates estimated by fitting the state-based model (SBM) to the experimental data. The SBM comprises seven rates: the phagocytosis rate for neutrophils ($\boldsymbol{\Phi_N}$) and for monocytes ($\boldsymbol{\Phi_M}$), the rate for intracellular killing by neutrophils ($\boldsymbol{\kappa_N}$) and by monocytes ($\boldsymbol{\kappa_M}$), the rate for immune evasion by the pathogens ($\boldsymbol{\rho}$), the rates that define the extracellular killing by antimicrobial peptides, *i.e.* $\boldsymbol{\gamma}$ and $\boldsymbol{\bar{\kappa}_{EK}.\gamma}$).

Rate	***C. albicans***			***C. glabrata***		
	mean $10^{-2}\,min^{-1}$	sd $10^{-3}\,min^{-1}$	sd [%]	mean $10^{-2}\,min^{-1}$	sd $10^{-3}\,min^{-1}$	sd [%]
$\boldsymbol{\Phi_N}$	2.966	0.611	2.06	10.11	1.953	1.93
$\boldsymbol{\Phi_M}$	1.228	0.746	6.07	13.69	4.003	2.92
$\boldsymbol{\kappa_N}$	5.319	4.868	9.15	6.98	4.959	7.11
$\boldsymbol{\kappa_M}$	2.098	3.056	14.57	3.219	3.433	10.66
$\boldsymbol{\rho}$	0.439	0.211	4.81	1.173	0.481	4.1
$\boldsymbol{\gamma}$	2.129	1.868	8.77	5.389	4.028	7.47
$\boldsymbol{\bar{\kappa}_{EK}}$	21.78	17.46	8.02	22.98	27.74	12.07

Supplementary Table 2 Values for killed cells ($\boldsymbol{P_K}$) as well as alive and immune-evasive cells ($\boldsymbol{P_{AIE}}$) at the transitions between different severity degrees of neutropenia for *C. albicans* and *C. glabrata* infection at four hours post infection. These values are used as a pattern for classification of the outcome of *in silico* treatment of virtual neutropenic patients.

		mild	**moderate**	**severe**
C. albicans	P_K	0.713 ± 0.014	0.623 ± 0.017	0.464 ± 0.02
	P_{AIE}	0.26 ± 0.015	0.322 ± 0.016	0.417 ± 0.016
C. glabrata	P_K	0.757 ± 0.012	0.707 ± 0.015	0.612 ± 0.018
	P_{AIE}	0.236 ± 0.012	0.286 ± 0.015	0.38 ± 0.017

Supplementary Table 3 *In silico* treatment of VNP in infection with *C. albicans* and *C. glabrata* is predicted to reach the transition to the non-neutropenic infection outcome for VNP with various severity degrees of neutropenia. The function $\boldsymbol{f_{\phi_N} = 1 + a \cdot e^{-b \cdot f_{D_N}}}$ is fitted to this transition with the parameters $\boldsymbol{a}$ and $\boldsymbol{b}$.

Virtual Neutropenic Patient Type (VNP)	***C. albicans***		***C. glabrata***	
	a	b	a	b
1	12637.28	10.91	16974577.77	18.36
2	28.37	3.86	755.76	7.09
3	13.63	2.36	27.11	3.02
4	12.71	1.5	46.56	2.37
5	20	0.83	56.66	1.3

9. Comparative Assessment of Aspergillosis by Virtual Infection Modeling in Murine and Human Lung

frontiers in Immunology

ORIGINAL RESEARCH
published: 05 February 2019
doi: 10.3389/fimmu.2019.00142

Comparative Assessment of Aspergillosis by Virtual Infection Modeling in Murine and Human Lung

Marco Blickensdorf[1,2], *Sandra Timme*[1,2] *and Marc Thilo Figge*[1,2*]

[1] *Research Group Applied Systems Biology, Leibniz Institute for Natural Product Research and Infection Biology-Hans Knöll Institute, Jena, Germany,* [2] *Faculty of Biological Sciences, Friedrich Schiller University of Jena, Jena, Germany*

frontiers in Immunology

ORIGINAL RESEARCH
published: 05 February 2019
doi: 10.3389/fimmu.2019.00142

Comparative Assessment of Aspergillosis by Virtual Infection Modeling in Murine and Human Lung

Marco Blickensdorf[1,2], *Sandra Timme*[1,2] *and Marc Thilo Figge*[1,2]*

[1] *Research Group Applied Systems Biology, Leibniz Institute for Natural Product Research and Infection Biology-Hans Knöll Institute, Jena, Germany,* [2] *Faculty of Biological Sciences, Friedrich Schiller University of Jena, Jena, Germany*

Aspergillus fumigatus is a ubiquitous opportunistic fungal pathogen that can cause severe infections in immunocompromised patients. Conidia that reach the lower respiratory tract are confronted with alveolar macrophages, which are the resident phagocytic cells, constituting the first line of defense. If not efficiently removed in time, *A. fumigatus* conidia can germinate causing severe infections associated with high mortality rates. Mice are the most extensively used model organism in research on *A. fumigatus* infections. However, in addition to structural differences in the lung physiology of mice and the human host, applied infection doses in animal experiments are typically orders of magnitude larger compared to the daily inhalation doses of humans. The influence of these factors, which must be taken into account in a quantitative comparison and knowledge transfer from mice to humans, is difficult to measure since *in vivo* live cell imaging of the infection dynamics under physiological conditions is currently not possible. In the present study, we compare *A. fumigatus* infection in mice and humans by virtual infection modeling using a hybrid agent-based model that accounts for the respective lung physiology and the impact of a wide range of infection doses on the spatial infection dynamics. Our computer simulations enable comparative quantification of *A. fumigatus* infection clearance in the two hosts to elucidate (i) the complex interplay between alveolar morphometry and the fungal burden and (ii) the dynamics of infection clearance, which for realistic fungal burdens is found to be more efficiently realized in mice compared to humans.

Keywords: virtual infection modeling, *Aspergillus fumigatus* lung infection, mouse model, human model, hybrid agent-based computer simulations

OPEN ACCESS

Edited by:
Burkhard Ludewig, Kantonsspital St. Gallen, Switzerland

Reviewed by:
Lalit Kumar Dubey, Université de Lausanne, Switzerland
Joana Vitte, Aix-Marseille Université, France

***Correspondence:**
Marc Thilo Figge
thilo.figge@leibniz-hki.de

Specialty section:
This article was submitted to Molecular Innate Immunity, a section of the journal Frontiers in Immunology

Received: *25 October 2018*
Accepted: *17 January 2019*
Published: *05 February 2019*

Citation:
Blickensdorf M, Timme S and Figge MT (2019) Comparative Assessment of Aspergillosis by Virtual Infection Modeling in Murine and Human Lung. Front. Immunol. 10:142. doi: 10.3389/fimmu.2019.00142

INTRODUCTION

The concept of systems biology constitutes a powerful approach to investigate biological phenomena by combining wet-lab and dry-lab investigations that mutually support and complement each other (1–3). However, systems biology of infection faces problems that can interrupt the experiment-theory-cycle of systems biology (4–6). First, since *in vivo* experiments are predominantly conducted in animals, the general transferability of findings in the context of immunology to the human system is a matter of ongoing dispute (7, 8). Secondly, even in animal experiments it may be impossible to capture the spatio-temporal dynamics of infection processes. For example, in the case for lung infection *in vivo* time-lapse imaging is challenging due

to animal breathing. In these cases, virtual infection modeling is of particular importance, since it has the potential to advance our knowledge despite the aforementioned limitations and to generate hypotheses that direct future experiments in a targeted manner (9, 10). In particular, building *in silico* models of infection on the available experimental data basis, gives rise to realistic to-scale models that can be used to compare the outcome of computer simulations for animal and human systems.

In this study, we use virtual infection modeling to investigate *Aspergillus fumigatus* lung infections. *A. fumigatus* is an environmentally wide-spread fungus that is an opportunistic pathogen causing severe infections in immunocompromised patients (11–14). The fungal conidia are small in size of 2–3 μm (12, 13) and can reach the alveoli in the lower respiratory tract of the lung. Because alveoli make up about 50% of the lung volume and also make the largest contribution to lung surface area, they are by far the most likely niche for infection (15). If not efficiently removed by the innate immune system, *A. fumigatus* can cause invasive pulmonary aspergillosis (IPA) with high mortality rates of 30–90% (11). The resident immune cells in the lung are alveolar macrophages (AM) that constitute the first line of immune defense by phagocytosing the inhaled conidia (11, 14, 16). Without efficient clearing by innate immunity, *A. fumigatus* conidia can undergo morphological changes: Upon contact to the surfactant layer, which covers the alveolar epithelial cells (AEC) (15), resting conidia can swell and after $\sim$6 h start forming hyphae. These hyphae are able to penetrate the epithelial tissue of the alveolus and can thereby reach the bloodstream, from where they may disseminate and cause severe systemic infections (12, 13, 17). The first six hours after entrance of the conidia in the lung are therefore considered as a critical time frame, during which conidia need to be found in order to prevent damage of host tissue. This implies that the role of adaptive immunity can be neglected compared to a required rapid response by innate immunity, e.g., involving the complement system as well as phagocytic activity by AM and neutrophils. The condition of neutropenia, i.e., the considerable reduction in the absolute neutrophil count, poses a major risk factor for IPA (14, 18). Therefore, the nowadays increasing number of immunocompromised patients leads to a rising clinical prevalence, making *A. fumigatus* a relevant target for fungal infection research. Due to its complex interactions with the host immune system and its ability to adopt different morphologies, various levels of pathogenicity have to be considered in the development of effective therapy (13, 19).

Various mammalian species have been used for experimental research on *A. fumigatus* infection. Besides rats, rabbits, and guinea pigs, mice models have been used most extensively (20). It is important to note that—in order to provoke measurable numbers of interactions between pathogens and host cells—the experimentally applied infection doses typically are orders of magnitude higher compared to the natural inhalation dose for humans, which ranges between a few hundred and thousands of conidia per day (21–25). Thus, in addition to studying animal systems with host environments that are quite different from the human system, the significant differences in the applied infection doses need as well to be taken into consideration in the knowledge transfer from animals to humans. However, little is known about the comparability and transferability of mouse infection models in wet-lab and natural *A. fumigatus* infections in human. Therefore, in this study we compare *A. fumigatus* infection in mice and humans using virtual infection modeling to account for the respective lung morphologies and study the impact of the infection doses. In passing we note that, even though daily inhalation doses will be associated with homeostatic clearance and will typically pass unnoticed, we here use throughout the more general term infection clearance involving inflammation, tissue damage and a multifactorial host response in the case of high fungal doses.

In previous studies, we already implemented an infection model for the simulation of *A. fumigatus* infection in humans. The agent-based model (ABM) was built on an extensive experimental data basis available from literature and represents a typical human alveolus in three-dimensional continuous space (26, 27). The human alveolus was composed of AEC of type I and II, as well as of Pores of Kohn (PoK) representing connections between neighboring alveoli (28, 29). Our computer simulations revealed that AM performing random walk migration are not able to reliably detect a conidium in the alveolus before the onset of germination, i.e., before 6 h post infection (17, 26). This led to the hypothesis that a not yet experimentally identified chemotactic signal must exist that guides AM to the position of the conidium in the alveolus (26). The virtual infection model was then extended to explicitly incorporate chemokine secretion and diffusion by solving partial differential equations in a hybrid ABM (27). Scanning all unknown parameters within reasonable ranges, we determined those relevant for efficient pathogen clearance. For example, we found that a preferably high ratio of chemokine secretion by AEC with rate s_{AEC} over chemokine diffusion with diffusion coefficient D is required to establish a chemokine gradient that facilitates AM to detect a conidium before the onset of germination.

While these studies considered the immune response in human alveoli for daily inhalation doses of *A. fumigatus* conidia, the focus of the present study is on comparing *A. fumigatus* infections in mice and humans taking into account natural as well as experimental infection doses. Thus, we significantly adapted the agent-based virtual infection model to the to-scale morphometry of mouse alveoli. This enables generating comparative and quantitative predictions on the influence of morphological factors as well as dose-dependent effects during *A. fumigatus* infection in mice and humans.

RESULTS

Aspergillus fumigatus lung infection is commonly investigated using mouse models (20), where the pathogens can be administered in different ways (30): Intranasal deposition and intra-tracheal/intra-bronchial instillation bring the conidia directly in the nose or trachea/bronchia and are based on liquid solutions, while a more natural administration is realized in inhalation chambers with air-soluted conidia. All methods have in common that relatively high doses of $10^6 - 10^8$ conidia

are applied; however, the amount of conidia which is actually reaching the lower respiratory tract, i.e., the fungal burden in the alveoli of the mouse lung is found to be in the range of $10^3 - 10^5$ conidia (31, 32). On the other hand, it is reported that the distribution of conidia is fairly uniform only for administration by inhalation, whereas intranasal administration is accompanied with the accumulation of conidia in specific lung sections, i.e., inducing distributions with local variations in the fungal burden (33). This implies that our *in silico* experiments need to incorporate three major issues that differ from simulations of the human infection scenario: (i) implementing the differences in the morphometry of the lung for human and mouse, (ii) scanning for a larger range of infection doses, and (iii) studying the limit of high local fungal burdens due to the non-uniform distribution of conidia for administration based on liquid solutions.

As a measure of fungal clearance, we introduced an infection score $IS^{s=H,M}$, where the superscript refers to the human ($s = H$) or mouse ($s = M$) system and $IS^{s=H,M} = 0$ ($IS^{s=H,M} = 1$) implies that infections were cleared in each (none) simulations (for details see Materials and Methods section, Readout of Simulations).

Putative Morphology-Related Impact on Infection Clearance in Humans and Mice

As can be seen in **Figure 1**, the alveoli for human and mouse have been implemented as to-scale models that are composed of AEC of type I and II, as well as PoK. Given the differences in the size and composition of alveoli for the two organisms (see **Table 1** and **Supplementary Table 1**), it can be expected that infections may be cleared with different efficiency. For example, the surface area of the human alveolus is about 20 times larger compared to that of the murine alveolus and the number of AM per alveolus is about 6 times higher in the human alveoli. This gives rise to a scanning area per AM, which is about three times higher in humans suggesting that mice could cope much better with the detection of alveolar pathogens. However, the situation is complicated by the fact the number of PoK per alveolar area is higher by a factor 5.7 in the mouse alveolus, which together with the alveolar entrance ring gives rise to an increase of the relative alveolus' open boundary length by a factor 3.4 compared to the human alveolus. On the one hand, since AM can enter and leave the alveolus only across these boundaries (28, 29), this may result in a faster infection dynamics of the murine system. On the other hand, chemotactic signaling molecules can as well flow out of the alveolus via these boundaries implying that their increased length in the murine alveolus may be of disadvantage with regard to establishing an efficient chemokine gradient. Again, this argument may only be valid for a low pathogen density in the alveolus, because for high pathogen densities the induced chemokine profile may

TABLE 1 | Comparison of morphometric parameters and innate immune cells.

Parameter	Human alveolus	Mouse alveolus (references)
Radius of alveolus	116.5 μm	26.2 $\pm$ 7.2 μm (29, 34–41)
Number of type 1 AEC	48	4 (42)
Number of type 2 AEC	84	4 $\pm$ 2.4 (42–44)
Number of PoK	24	7 (45)
Type 1 AEC radius	27 μm	22 μm
Type 2 AEC edge length	9.34 μm	8.12 μm (42)
Number of alveoli per lung	4.8×10^8	$3.3 \pm 1.3 \times 10^6$ (34, 41)
Number of AM	2.1×10^9	$2.4 \pm 0.7 \times 10^6$ (42, 46)
Radius of AM	10.6 μm	9.5 μm (47)

The parameters of the human alveolus were taken from the literature search by Pollmächer et al. (26) and those of the mouse alveolus have been retrieved from the indicated references.

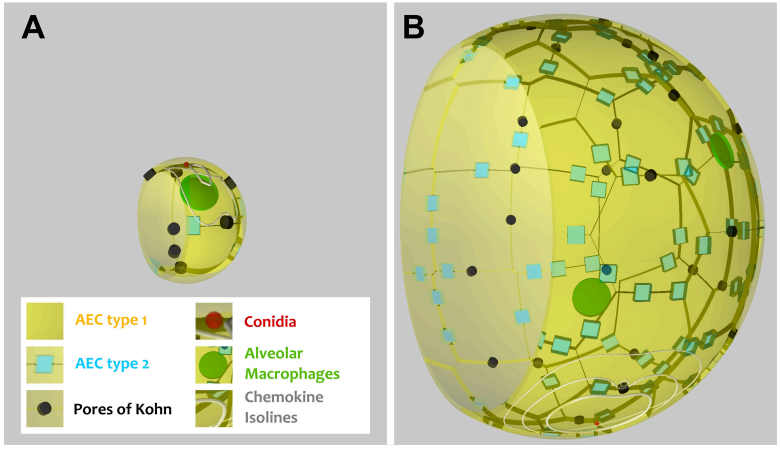

FIGURE 1 | Visualization of a to-scale alveolus in the hybrid agent-based model for mouse **(A)** and human **(B)**. The alveolar entrance ring (left) and Pores of Kohn (black) represent entry/exit points for AM (green) and chemokine flow (white isolines) induced by conidium (red). Alveolar surface is covered with epithelial cells of type 1 (yellow) and 2 (blue).

provide an ambiguous signal for AM guidance. For the same fungal burden in mice and humans, the pathogen density is much higher in the murine alveolus, due to their much lower number and smaller size. Therefore, *A. fumigatus* may be much more efficiently cleared from the human lung. Taken together, these considerations imply that the efficiency of the infection dynamics will depend on the combination of the alveolar morphometry and the fungal burden that together impact on the chemokine profile for AM migration in a way, which is impossible to quantitatively predict without performing comparative computer simulations of to-scale models.

Case of Low Fungal Burden: *A. fumigatus* Infection More Efficiently Cleared in Mice

We first consider the case of low fungal burden, which we define as the case where one *A. fumigatus* conidium per alveolus is the highest alveolar occupation number (AON) that is statistically expected to occur in the whole lung. The corresponding fungal burden can be derived from the binomial distribution (see Methods section for details) and is 2.5×10^3 in mice and 3×10^4 in humans (see **Figure 2**). This implies that the limit of low fungal burden covers the dose of daily inhalation for humans, but is relatively low for experimental conditions in typical mice experiments. Examples of the infection dynamics can be seen for humans and mice in **Supplementary Videos 1, 2**, respectively.

Our previous work on *A. fumigatus* infection in human alveoli for low fungal burden revealed that a high secretion rate s_{AEC} of chemotactic molecules combined with a low diffusion coefficient D of the chemokine is beneficial for a small infection score IS^H in humans (27). In the present study, we screened the diffusion coefficient and the secretion rate in the regimes, respectively, $D = [20, 6 \times 10^3]\ \mu m^2/\text{min}$ and $s_{AEC} = [1.5 \times 10^3, 5 \times 10^5]\ min^{-1}$ for alveoli of mice and humans. The numerical results for the quantitative comparison between human and mouse is shown by the infection scores $IS^{H,M}$ in **Figure 3A**. It can be observed that, for all combinations of D and s_{AEC}, the infection score in mice is significantly smaller: $IS^M < IS^H$. Furthermore, it can be seen that the relation of a high secretion rate and a low diffusion coefficient also leads to a more efficient infection clearance in mice. The relative difference in the infection scores of the two organisms, $\Delta IS = 1 - IS^M/IS^H$, is in the range $50 - 90$ %, indicating that the murine system performs always better than the human system in the limit of a low fungal burden.

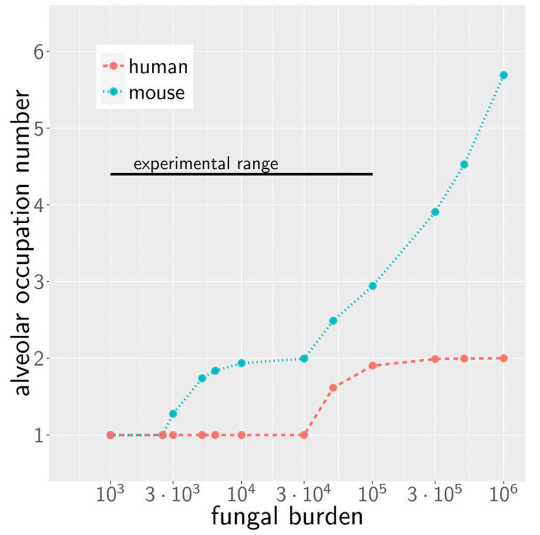

FIGURE 2 | Alveolar occupation number, the maximal expected number of present conidia per alveolus, as a function of the fungal burden in mouse (blue) and human (red). Black line represents the experimental range of fungal burden, which is reached in typical mice model experiment.

Case of Low Fungal Burden: Size of Alveolus Governs Infection Dynamics

To dissect whether the infection dynamics is governed by the chemotaxis or the alveolar size, we compared the probability of directed AM migration resulting from one conidium in the alveolus of mice and humans. The chemokine concentration itself falls off with the distance from the source AEC, i.e., the AEC in contact with the conidium. In order to avoid that AM perform mostly random walk migration, the chemokine gradient (i) must not exceed a certain value to avoid saturation of AM chemokine receptors and (ii) must not fall below a certain value to provide a detectable signal. As a qualitative measure of gradient efficiency we calculated the probability that AM follow the gradient depending on the distance to the source AEC. This probability reflects the impact of the chemokine gradient on AM migration and was computed as explained in **Supplemantary Methods** (see section on AM Migration) for optimal chemokine parameters $(\overline{D^s_{opt}}, \overline{s^s_{AEC_{opt}}})$ in the human (s=H) and mouse (s=M) system. The optimal parameters were computed from the 36 scanned parameter combinations, $\{D_1 \ldots D_6\} \times \{s_{AEC1} \ldots s_{AEC6}\}$, for the diffusion coefficient and the secretion rate as follows: Based on the simulation results in terms of the infection score $IS_{D_i,s_{AEC_i}}$ and the limits of its respective 95%-confidence interval, we computed the optimal diffusion coefficient as $\overline{D_{opt}} = \frac{1}{\sum_i w_i} \cdot \sum_i w_i \cdot D_i$ with weights $w_i = 1 - IS_{D_i,s_{AEC_i}}$ for all those parameter combinations that had infection scores not exceeding the minimal upper limit of all confidence intervals (see **Supplementary Video 3**). The optimal secretion rate $\overline{s_{AEC_{opt}}}$ was determined in the same way yielding for the human host $\overline{D_{opt}}^H = 34\mu m^2\,\text{min}^{-1}$ and $\overline{s^H_{AEC_{opt}}} = 1.5 \times 10^4\,\text{min}^{-1}$ and for the murine host $\overline{D_{opt}}^M = 61\mu m^2\,\text{min}^{-1}$ and $\overline{s^M_{AEC_{opt}}} = 4.9 \times 10^4\,\text{min}^{-1}$ as the optimal parameters in the limit of low fungal burden.

The probability of directed AM migration for both host systems and for their respective optimal chemokine parameters is plotted in **Figure 3B**. The two curves exhibit quantitative similarity suggesting that the infection dynamics in the case of a low fungal burden is mainly governed by the size of the alveolus rather than the chemokine profile itself. Thus, in contrast to the significantly larger human alveolus, AM in the murine

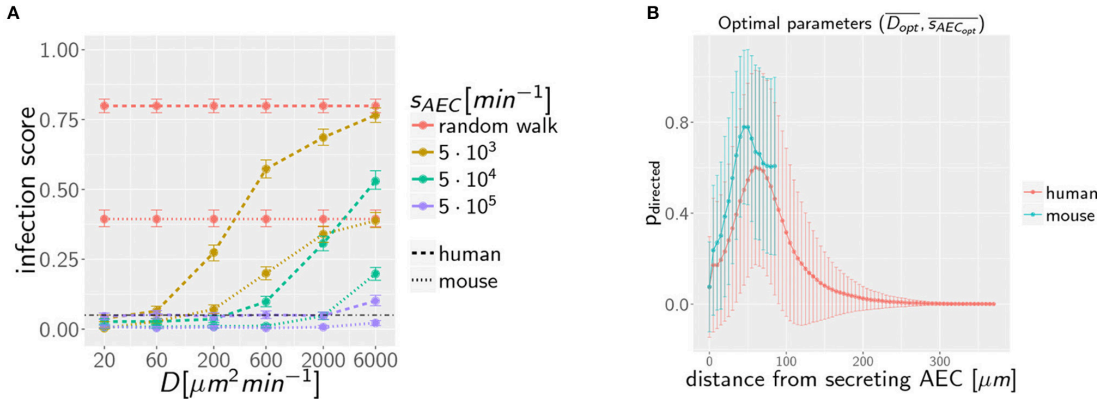

FIGURE 3 | (A) Infection scores *IS* for random walk migration and selected examples of chemokine parameters in the limit of low fungal burden with AON = 1. Dashed-dotted black line indicates the threshold infection score at $IS_t = 5\%$. Error bars represent 95%-confidence intervals received from bootstrapping. **(B)** Mean probability for directed AM migration $p_{directed}$ following the underlying chemokine gradient as a function of the distance from the source AEC. Chemokine parameters are set to the corresponding optima $\overline{D_{opt}}$ and $\overline{s_{AEC_{opt}}}$ in mice and men.

counterpart will typically perform directed migration across the entire alveolus.

A. fumigatus More Efficiently Cleared in Mice for Any Alveolar Occupation Number

Increasing the AON from one to higher conidia numbers, we again performed computer simulations for various infection scenarios that differ in the parameters for chemokine secretion s_{AEC} and diffusion coefficient D. However, multiple conidia within the alveolus can lead to more complex chemokine profiles derived from the various conidia-associated AEC that are simultaneously serving as sources of chemokine secretion. In **Figure 4A** the infection scores *IS* obtained from 10^3 simulations are summarized for AON between one and six and for selected secretion rates s_{AEC}, while the numerical results for the full range of studied parameter values is shown for human and mouse in **Supplementary Figure 1**. Parameter regimes of efficient infection clearance in these plots resemble those previously found for one conidium in the human alveolus (27), indicating that low ratios D/s_{AEC} are as well preferred in the mouse system.

Extending the computation of optimal chemokine parameters for one conidium to larger AON enables computing for both systems the average optimal parameter set (see **Supplementary Figure 2**). We obtain for one to six conidia per alveolus the averaged optimal values $\overline{D_{opt}{}^H} = 26 \pm 6.6\ \mu m^2 min^{-1}$ and $\overline{s^H_{AEC_{opt}}} = 1.1 \times 10^4 \pm 6 \times 10^3\ \text{min}^{-1}$ for the human host and $\overline{D_{opt}{}^M} = 74 \pm 22.4\ \mu m^2 min^{-1}$ and $\overline{s^M_{AEC_{opt}}} = 8.0 \times 10^4 \pm 4,1 \times 10^4\ \text{min}^{-1}$ for the murine host. In **Figure 4B**, we show that the resulting infection score *IS* as a function of the AON is always significantly lower in mice compared to humans.

Case of High Fungal Burden: Chemokine Profile Can Deteriorate Clearance Efficiency

Due to morphometric differences between the lungs of mice and humans, the AON is not directly related to the fungal burden. This follows from our earlier statistical considerations on the highest AON that is expected to occur in the whole lung for a given fungal burden (see **Figure 2**) exhibiting a significant quantitative difference between mice and humans. Since the number of more than 10^8 alveoli in the human lung exceeds that of mice by more than two orders of magnitude, even in the case of an extremely high fungal burden with 10^6 conidia in the lung, the maximal AON for humans does not exceed two. In contrast, the same fungal burden in the lung of mice yields a maximal AON between five and six conidia in one alveolus. It thus follows that a comparison between mice and humans for the same fungal burden requires contrasting infection scenarios with different AON. Of note, our analysis focuses on the maximal AON for a given fungal burden, because it is argued that this configuration will be directly correlated with the estimated time needed to clear all occupied alveoli from the pathogen. In **Figures 4C,D** the numerical results for the infection score *IS* are shown for mice and humans as a function of the fungal burden, respectively, for identical chemokine parameters and for the respective optimal chemokine parameters. **Supplementary Figure 3** shows the infection score *IS* as a function of the fungal burden for all the scanned parameter combinations. It can be seen by the smaller infection scores in the murine host that infections are still more efficiently cleared for the entire experimentally relevant range of $10^3 - 10^5$ conidia in the lung. In **Supplementary Video 3** we indicated all combinations of chemokine parameters for which the infection score reaches values below the threshold of $IS_t = 5\%$.

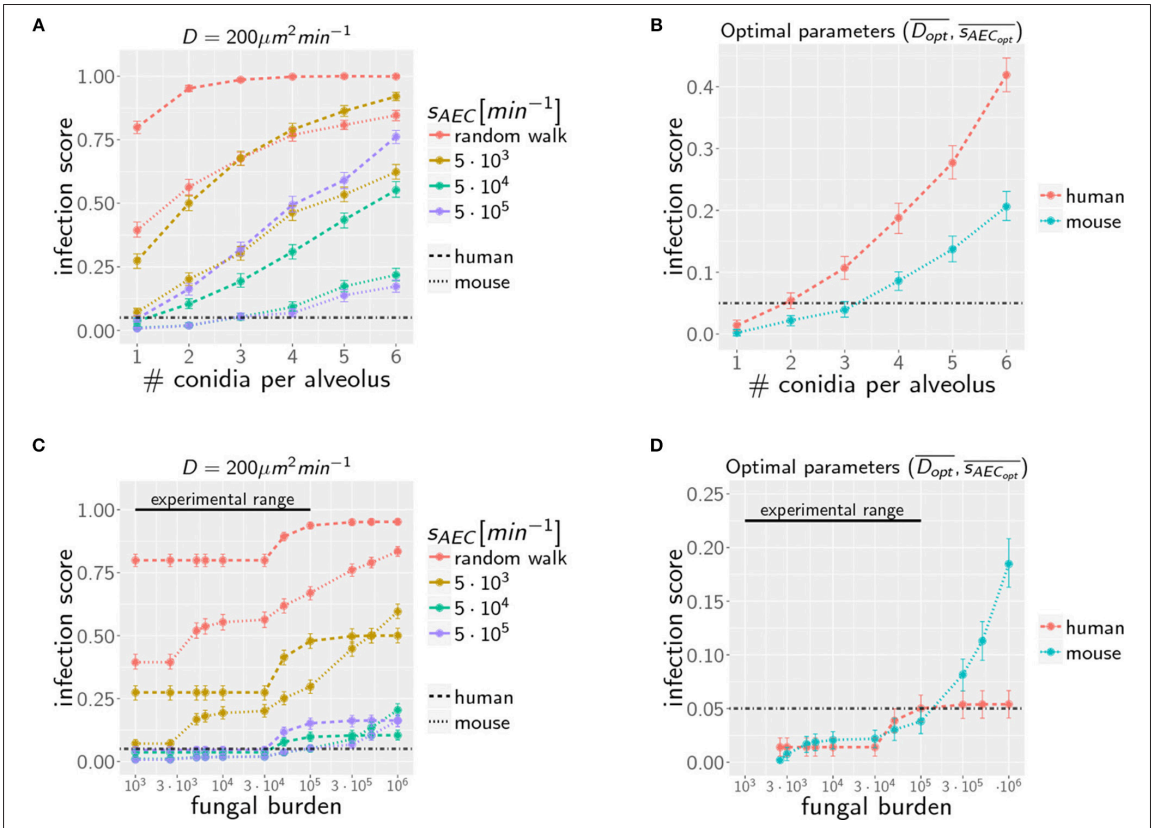

FIGURE 4 | Infection scores *IS* as a function of the AON **(A,B)** and the fungal burden **(C,D)** for selected secretion parameters with diffusion coefficient $D = 200\ \mu m^2\ \mathrm{min}^{-1}$ **(A,C)** and for optimal chemokine parameters $\overline{D_{opt}}$ and $\overline{s_{AEC_{opt}}}$ **(B,D)** in mice and men. Dashed-dotted black line indicates the threshold infection score at $IS_t = 5\%$. Error bars represent 95% confidence intervals. Black line represents the experimental range of fungal burden, which is reached in typical mice model experiment.

However, as we have mentioned before, administration of conidia based on liquid solutions is reported to be associated with higher local fungal burdens due to a more non-uniform distribution of conidia (33). It can be seen in **Figure 2** for a uniform distribution of conidia that a high fungal burden in the range $10^5 - 10^6$ conidia per lung is associated with an AON of two in the human system, whereas this value ranges between three and six for the murine system. Consequently, for a non-uniform distribution of conidia, such high AON can be reached in the murine lung and these can result in infection scores that are much higher than for the human system with AON of two, even if the respective optimal chemokine parameters are applied (see **Figure 4B**). Our spatio-temporal computer simulations of the infection scenarios reveal that higher AON are associated with chemokine profiles that deteriorate clearance efficiency. Since the mouse alveolus contains more than 10 times fewer AEC compared to the human alveolus (see **Table 1**), multiple randomly positioned conidia will occupy most of the alveolus' AEC associated with chemokine secretion from various source AEC. First of all, this can lead to chemokine saturation that will turn directed AM migration into random walk migration. Secondly, if the number of conidia is increased further, this will not alter the chemokine gradient anymore. Consequently, AM will perform the inefficient random walk migration until a sufficient number of conidia is detected, such that AM migration becomes again dominated by the chemokine gradient. Obviously, this complex interplay between the morphometry of the alveolus and the chemokine profile will be much less pronounced for the larger human alveolus that consists of many more AEC. To validate this hypothesis, we computed the mean values of the chemokine concentration across all alveolar surface grid points in the simulations and found that significant deviations arise between the human and mouse alveolus starting at AON of four. As can be seen in **Figure 5**, for AON above four the mean concentration value in the murine alveolus does change only slightly providing no additional chemotactic guidance to AM, whereas it is still increasing in the human alveolus and can provide chemotactic guidance associated with lower infection scores *IS* in the human alveolus and in the limit of fungal burdens well above the typical experimental range.

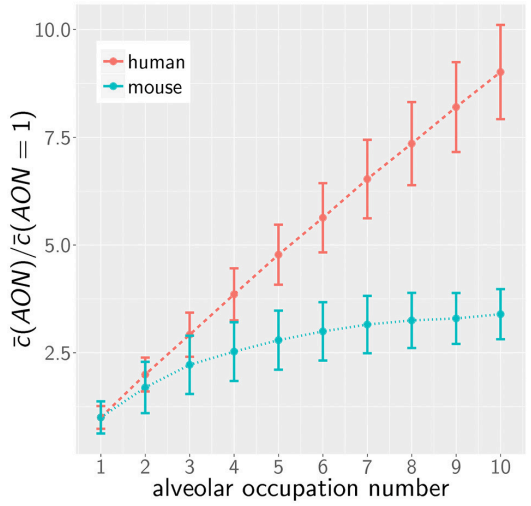

FIGURE 5 | Mean of the normalized alveolar chemokine concentration as a function of the AON in mice and men obtained from simulations. Error bars represent the standard deviation of this measurement.

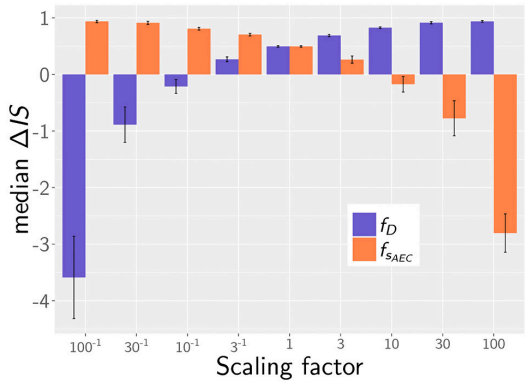

FIGURE 6 | Median of the relative infection score between human and mouse, $\Delta IS = 1 - IS^M/IS^H$, depending on the scaling factor for chemotaxis parameters: $f_D = D^H/D^M$ for the diffusion coefficient (purple) and $f_{s_{AEC}} = s^H_{AEC}/s^M_{AEC}$ for the secretion rate (orange). Error bars represent the standard errors.

Simulation Results Are Qualitatively Robust Against Variations of Model Parameters

In the quantitative comparison of infection scenarios in mice and humans, we so far assumed the same values for the model parameters. For example, we assumed that the chemokine secretion rates from human and murine alveolar epithelial cells are similar. However, it may be argued that this does not reflect the physiological reality correctly, since murine AEC are effectively about 33% smaller in area and may thus exhibit a reduced potential of chemokine secretion. Similarly, it is an open question today whether the postulated chemotactic signals in human and mice are transmitted by chemokines that are structural homologs and can therefore be expected to have similar diffusion coefficients in the surfactants of mice and humans. While these uncertainties cannot be avoided, we estimated the impact of variations in these parameters on the infection score in humans and mice. To this end, we calculated the relative infection score between the human and murine model $\Delta IS = 1 - IS^M/IS^H$, over all simulated parameter combinations in the experimental range of fungal burdens. Setting both diffusion parameters in humans and mice to identical values, the mouse shows lower relative infection scores with a median value of $\Delta IS = 0.49$.

Next, we analyzed the robustness of the infection outcome with regard to the diffusion coefficient and the secretion rate. To this end, we compared the infection scores for humans and mice for those simulated parameter combinations that obey the scaling factors $f_D = D^H/D^M$ for the diffusion coefficient and $f_{s_{AEC}} = s^H_{AEC}/s^M_{AEC}$ for the chemokine secretion rate. For example, comparing diffusion coefficients with scaling factor $f_D = 3^{-1}$ (i.e., $D^H = (20, 200, 2000)\ \mu m^2/\text{min}$, $D^M = (60, 600, 6000)\ \mu m^2/\text{min}$) revealed a reduction in the median value of the relative infection score to $\Delta IS = 0.27$ over the scanned fungal burdens. This indicates that the infection score in mice is higher in $> 50\%$ of all selected parameter combinations, even if the diffusion coefficient is three times higher in the murine alveolus (see **Figure 6**). The scaling factor of the secretion rate $f_{s_{AEC}}$ has a reversed impact on the relative infection score reflecting that a high ratio s_{AEC}/D induces low infection scores (see **Figure 6**).

Taken together, our simulation results imply that our main conclusions are qualitative robust against variations in the chemotaxis parameters. As long as the associated scaling factors have values $f_D > 10^{-1}$ or $f_{s_{AEC}} < 10$, the murine system still shows better infection scores in more than half of all screened fungal burdens, even if chemotactic signaling becomes deteriorated. We therefore conclude that within these limits our simulation results are qualitatively robust against variations in the chemotaxis parameters.

DISCUSSION

In this study, we investigated clearance of *Aspergillus fumigatus* infection from the lung of mice and humans by computer simulation of the complex interplay between alveolar morphometry and fungal burden in the dynamics of infection clearance. Since *in vivo* live cell imaging of these processes in the whole lung is still not possible today, we here extended a previously developed model of IPA in humans (25, 26) to the murine alveolus. The virtual infection model represents a realistic to-scale representation that was built on detailed experimental data available on the morphometry of the alveolus in the two hosts. Furthermore, alveolar macrophages as well as chemokine secretion and diffusion were incorporated into the model and we screened the physiologically relevant parameter ranges for as small as possible infection scores *IS*, which represent the

percentage of simulations for which clearance of all *A. fumigatus* conidia from the lung took longer than 6 h.

One important finding of this study is that, for realistic fungal burdens comprising daily inhalation doses in humans as well as typical doses in mice experiments, infection clearance is more efficiently realized in mice compared to humans. This result holds true in the limit of low fungal burden, where at most one conidium is present in the alveolus, as well as for larger fungal burdens with a maximal number of two and three conidia, respectively, in the alveolus of humans and mice. As we observed before for the human system (27), a low ratio of chemokine diffusion over secretion, D/s_{AEC}, leads to more efficient infection clearance in the murine system. However, our simulations revealed that in the limit of low fungal burden the dominating factor of efficient infection clearance in mice is the relatively short distances between AM and conidia in the relatively small murine alveolus. On the other hand, the chemokine profile played a dominant role in the limit of high fungal burden, because for four and more conidia in the relatively small murine alveolus this is associated with a featureless chemokine profile that cannot provide sufficient guidance to AM.

A quantitative comparison revealed that distinct optimal chemokine parameters exist that ensure minimal infection scores *IS* in the different alveoli of the two hosts. We therefore performed simulations comparing the infection results for both identical and optimal chemokine parameters. It should be noted that, even for the same chemotactic molecule in mice and humans, differences between optimal chemokine parameters can be induced by various factors that are different in the two hosts, such as the secretion competence of AEC and the viscosity of the alveolar surfactant. In any case, the importance of a well-established chemokine gradient as well as the functional sensing by AM is reflected by the fact that conidia, which are not detected within 6 h post infection, pose the risk of germination, invasion, and systemic infection. We also studied the case of non-uniform conidia distribution in the lung leading to locally high AON in alveoli. In this limit, which is more likely realized by the administration of conidia based on liquid solutions, our calculations predict that four and more conidia per alveolus can occur, leading to infection scores that are clearly higher in mice than in humans. However, in general, clearance of uniformly distributed conidia in the lung seems to be more efficiently realized in mice than in humans and we have demonstrated that this results are qualitatively robust over a broad range of variations in the chemokine parameters. These considerations are important with regard to the comparability and transferability of mouse infection models to the human system, e.g., with regard to estimating the efficiency of new therapeutics. Virtual infection modeling in the scope of systems biology has been applied to a broad range of biological systems and pathogens, such as bacteria (48) and fungi (9, 10, 49–53), since it provides a valuable tool to investigate infection processes that are not directly accessible in experiment. Moreover, this approach can direct future experiments by identifying key factors that govern the counterplay of infection and inflammation and require most attention. It should be mentioned that our results, indicating that AM are not able to clear the infection in the limit of a high fungal burden, are in line with previous findings based on a more phenomenological modeling approach. We applied evolutionary game theory on graphs to simulate several aspects of the immune response against *A. fumigatus* lung infection, including the complement system, phagocytosis by AM as well as recruitment and phagocytosis by neutrophils in one comprehensive model framework (54). This enabled us to reconcile the contradictory view on AM in the literature (55, 56) and predicted an infection dose-dependent switch in their function: While under low infection doses AM manage infection clearance, their role switches to a regulatory function under high infection doses by recruiting neutrophils (54).

In the future, validation of theoretical predictions needs to be addressed in experimental investigations. To date, one of the main limiting factors in understanding host response during *A. fumigatus* infections is the poor experimental accessibility and stable cultivation of alveolar tissue. However, new research approaches including organ-on-a-chip systems, which reduce the physiological complexity and bring nature closer to the simplifying virtual infection models, are promising for a better validation of e.g., alveolar epithelium properties or chemokine parameters (57–59). A lung-on-a-chip model will enable testing chemokine candidates for AM guidance, such as IL-8 that binds to the AM surface receptor CXCR2 (60). Similarly, the chemoattractant C5a is known to be activated by *A. fumigatus* conidia along the alternative pathway of the complement system (61, 62) and is able to trigger the secretion of macrophage inflammatory protein-2 and neutrophil chemoattractant-1 by AEC (63). Once chemokine parameters will have been identified and inflammatory conditions in terms of cytokine profiles will be accessible, the next step will be to extend the hybrid ABM toward neutrophil recruitment and an explicit phagocytosis model along the lines of our previous investigations based on evolutionary game theory (54). This will allow for the investigation of migration and phagocytic dynamics of AM, neutrophils and AEC in the alveolar environment during the interaction with pathogens. Furthermore, morphological changes of *A. fumigatus* including swelling and hyphae formation have a strong impact on phagocytosis of the fungus (17, 64) and can be included in such a virtual infection model. A further advancement will be in the scale-up of the alveolus to the higher organizational units of alveolar sacs for a more comprehensive simulation of infection scenarios.

MATERIALS AND METHODS

In this study, we extended our previously developed ABM of *in silico* infections by *Aspergillus fumigatus* in the human alveolus (26, 27) to the mouse alveolus in order to perform comparative analyses. The ABM is a spatio-temporal multi-scale model that simulates host-pathogen interactions on the cellular and molecular level. Thus, cells like the fungal conidia and AM are simulated as individual agents that migrate and interact in a rule-based fashion, while the chemokine secretion by AEC and the molecular diffusion of chemokines is simulated using partial differential equations. Chemokines are uniformly secreted with rate s_{AEC} at the surface of each AEC, which is associated with at least one conidium. The implementation of the ABM is described in more detail in the **Supplementary Material**, while here the

focus is on the main aspects associated with the extension to the mouse alveolus.

Morphometry of the Mouse Alveolus and Implementation

A comprehensive literature research was performed to design the virtual infection model of the mouse alveolus as realistic as possible. The most important morphology parameters are summarized and compared with the human alveolus in **Table 1**, from which other characteristics can be derived (see for examples **Supplementary Table 1**). For example, it can be seen that the radius (surface area) of a typical human alveolus is about 4.5 (20)-fold larger compared to a murine alveolus. The numbers of AEC of type 1 and 2 differ significantly in both organisms, i.e., a human alveolus contains about 12.0-fold more type 1 and 21-fold more type 2 AEC. Furthermore, the number of PoK is about 3.4 times higher in the human alveolus. A video of both model alveoli is provided in the (**Supplementary Videos 1, 2**).

Implementation of Mouse Alveolus in Virtual Infection Model

The ABM was adjusted for the implementation of the mouse alveolus with parameters as summarized in **Table 1** and **Supplementary Table 1**. This also required changes in the algorithm for cell positioning on the alveolar surface. Type 1 AEC were placed as described before around the three-quarter sphere (see **Supplementary Material** for details). Previously, type 2 AEC and PoK were placed at the borders between type 1 AEC. However, due to the larger ratio of type 2 AEC and PoK with respect to type 1 AEC in mice, the positioning of PoK and type 2 AEC had to be changed. We adjusted the position of type 2 AEC and PoK uniformly across the whole border of the type 1 AEC. While these changes in the cell positioning were required for realistic configurations of mouse alveolus morphometries, quantitative results of the ABM for the human alveolus remained within the 95%-confidence interval. Moreover, the smaller size of the mouse compared to the human alveolus required adjustment of the Delaunay-triangulated grid, on which the diffusion equation is solved (27). The number of grid points could be reduced from 10^4 in the human alveolus to only 5.1×10^2, keeping the spatial resolution in the mouse alveolus the same as in the human system (see **Supplementary Table 1**).

Readout of the Simulations

As a measure of fungal clearance we compute for various infection scenarios the first-passage-time (FPT) of AM, i.e., the time required for migrating AM to find all conidia in a particular alveolus (26, 27). The relation between the FPT and the time point of conidia germination, which corresponds to about 6 h post conidia arrival, is obtained from repeating the simulation of each infection scenario 10^3 times. From the corresponding FPT distribution, we then compute an infection score, *IS*, as the percentage p of simulations with FPT above 6 h: $IS^{s=H,M} = p(FPT > 6\,h)$, where the superscript refers to the human ($s = H$) or mouse ($s = M$) system and $IS^{s=H,M} = 0$ ($IS^{s=H,M} = 1$) implies that conidia were cleared in each (none) of the 10^3 simulations. The various infection scenarios correspond to scanning the parameter space in terms of AM migration, chemokine secretion, and diffusion, as well as conidia infection doses in alveoli of mice and humans.

Comparison of Fungal Burden

For a given fungal burden δ, the conidia are distributed across all alveoli n_{alv} of the host's lung. Assuming an independent and uniform distribution of these conidia, we can describe the probability of having n_{con} conidia present in one alveolus by the Binomial distribution $B_{con}\left(\delta, p, n_{con}\right)$ with probability of $p = \frac{1}{n_{alv}}$ for δ repeats. To estimate the maximal AON that is associated with a specific fungal burden, we computed n_{con} from the $1 - \frac{1}{n_{alv}}$-quantile of the distribution $B_{con}\left(\delta, p, n_{con}\right)$. The resulting number corresponds to the maximal AON that can be expected to occur in the whole lung for a specific fungal burden (see **Figure 2**). The corresponding *IS* was determined by linear interpolation of the results from our simulations for various AON.

DATA AVAILABILITY STATEMENT

The raw data supporting the conclusions of this manuscript will be made available by the authors, without undue reservation, to any qualified researcher.

AUTHOR CONTRIBUTIONS

MTF conceived and designed this study. MTF provided computational resources. Data processing, implementation and application of the computational algorithm were done by MB and ST. MB, ST, and MTF evaluated and analyzed the results of this study. MB, ST, and MTF drafted the manuscript and revised it critically for important intellectual content and final approval of the version to be published. MB, ST, and MTF agree to be accountable for all aspects of the work in ensuring that questions related to the accuracy or integrity of any part of the work are appropriately investigated and resolved.

FUNDING

This work was financially supported by the Deutsche Forschungsgemeinschaft (DFG) through the excellence graduate school Jena School for Microbial Communication (JSMC) the International Leibniz Research School for Microbial and Biomolecular Interactions (ILRS) and the CRC/TR124 FungiNet (project B4 to MTF).

ACKNOWLEDGMENTS

We acknowledge numerous helpful discussions with Johannes Pollmächer.

SUPPLEMENTARY MATERIAL

The Supplementary Material for this article can be found online at: https://www.frontiersin.org/articles/10.3389/fimmu.2019.00142/full#supplementary-material

REFERENCES

1. Kitano H. Systems biology: a brief overview. *Science* (2002) 295:1662–4. doi: 10.1126/science.1069492
2. Aderem A. Systems biology: its practice and challenges. *Cell* (2005) 121:511–513. doi: 10.1016/j.cell.2005.04.020
3. Ideker T, Galitski T, Hood L. A new approach to decoding life: systems biology. *Annu Rev Genomics Hum Genet.* (2001) 2:343–72. doi: 10.1146/annurev.genom.2.1.343
4. Horn F, Heinekamp T, Kniemeyer O, Pollmächer J, Valiante V, Brakhage AA. Systems biology of fungal infection. *Front Microbiol.* (2012) 3:108. doi: 10.3389/fmicb.2012.00108
5. Medyukhina A, Timme S, Mokhtari Z, Figge MT. Image-based systems biology of infection. *Cytom Part A* (2015) 87:462–70. doi: 10.1002/cyto.a.22638
6. Kreutz C, Timmer J. Systems biology: experimental design. *FEBS J.* (2009) 276:923–42. doi: 10.1111/j.1742-4658.2008.06843.x
7. Bart van der Worp H, Howells DW, Sena ES, Porritt MJ, Rewell S, O'Collins V, et al. Can animal models of disease reliably inform human studies? *PLoS Med.* (2010) 7:1–8. doi: 10.1371/journal.pmed.1000245
8. Mestas J, Hughes CCW. Of mice and not men: differences between mouse and human immunology. *J Immunol.* (2004) 172:2731–8. doi: 10.4049/JIMMUNOL.172.5.2731
9. Hünniger K, Lehnert T, Bieber K, Martin R, Figge MT, Kurzai O. A virtual infection model quantifies innate effector mechanisms and *Candida albicans* immune escape in human blood. *PLoS Comput Biol.* (2014) 10:e1003479. doi: 10.1371/journal.pcbi.1003479
10. Lehnert T, Timme S, Pollmächer J, Hünniger K, Kurzai O, Figge MT. Bottom-up modeling approach for the quantitative estimation of parameters in pathogen-host interactions. *Front Microbiol.* (2015) 6:1–15. doi: 10.3389/fmicb.2015.00608
11. Brakhage AA, Bruns S, Thywissen A, Zipfel PF, Behnsen J. Interaction of phagocytes with filamentous fungi. *Curr Opin Microbiol.* (2010) 13:409–15. doi: 10.1016/j.mib.2010.04.009
12. Latge J-P. *Aspergillus fumigatus* and Aspergillosis. *Clin Microbiol Rev.* (1999) 12:310–50.
13. Latgé J. The pathobiology of *Aspergillus fumigatus*. *Trends Microbiol.* (2001) 9:382–9. doi: 10.1016/S0966-842X(01)02104-7
14. Dagenais TRT, Keller NP. Pathogenesis of *Aspergillus fumigatus* in invasive Aspergillosis. *Clin Microbiol Rev.* (2009) 22:447–65. doi: 10.1128/CMR.00055-08
15. Weibel ER. *Morphometry of the Human Lung*. Berlin; Heidelberg: Elsevier Science (2013).
16. Balloy V, Chignard M, Margalit A, Kavanagh K, Balloy V, Chignard M. The innate immune response to *Aspergillus fumigatus* at the alveolar surface. *FEMS Microbiol Rev.* (2009) 11:919–27. doi: 10.1016/j.micinf.2009.07.002
17. Van De Veerdonk FL, Gresnigt MS, Romani L, Netea MG, Latgé JP. *Aspergillus fumigatus* morphology and dynamic host interactions. *Nat Rev Microbiol.* (2017) 15:661–74. doi: 10.1038/nrmicro.2017.90
18. Baddley JW. Clinical risk factors for invasive aspergillosis. *Med Mycol.* (2011) 49:7–12. doi: 10.3109/13693786.2010.505204
19. Latgé JP. Fungal immunology: from simple to very complex concepts. *Semin Immunopathol.* (2015) 37:81–2. doi: 10.1007/s00281-014-0474-0
20. Clemons KV., Stevens DA. The contribution of animal models of aspergillosis to understanding pathogenesis, therapy and virulence. *Med Mycol.* (2005) 43:51919. doi: 10.1080/13693780500051919
21. Sarfati J, Diaquin M, Debeaupuis JP, Schmidt A, Lecaque D, Beauvais A, et al. A new experimental murine aspergillosis model to identify strains of *Aspergillus fumigatus* with reduced virulence. *Nippon Ishinkin Gakkai Zasshi* (2002) 43:203–13. doi: 10.3314/jjmm.43.203
22. Lepak AJ, Marchillo K, Vanhecker J, Andes DR. Posaconazole pharmacodynamic target determination against wild-type and Cyp51 mutant isolates of *Aspergillus fumigatus* in an *in vivo* model of invasive pulmonary aspergillosis. *Antimicrob Agents Chemother.* (2013) 57:579–85. doi: 10.1128/AAC.01279-12
23. Tang CM, Cohen J, Krausz T, Van Noorden S, Holden ' DW. The alkaline protease of *Aspergillus fumigatus* is not a virulence determinant in two murine models of invasive pulmonary aspergillosis. *Infect Immun.* (1993) 61:1650–6.
24. Wong SSW, Rasid O, Laskaris P, Fekkar A, Cavaillon J-M, Steinbach WJ, et al. Treatment of Cyclosporin A retains host defense against invasive pulmonary aspergillosis in a non-immunosuppressive murine model by preserving the myeloid cell population. *Virulence* (2017) 8:1744–52. doi: 10.1080/21505594.2017.1339007
25. Codina R, Fox RW, Lockey RF, DeMarco P, Bagg A. Typical levels of airborne fungal spores in houses without obvious moisture problems during a rainy season in Florida, USA. *J Investig Allergol Clin Immunol.* (2008) 18:156–62.
26. Pollmächer J, Figge MT. Agent-based model of human alveoli predicts chemotactic signaling by epithelial cells during early *Aspergillus fumigatus* infection. *PLoS ONE* (2014) 9:e111630. doi: 10.1371/journal.pone.0111630
27. Pollmächer J, Figge MT. Deciphering chemokine properties by a hybrid agent-based model of *Aspergillus fumigatus* infection in human alveoli. *Front Microbiol.* (2015) 6:503. doi: 10.3389/fmicb.2015.00503
28. Peão M, Águas AP, de Sá CM, Grande NR. Morphological evidence for migration of particle-laden macrophages through the interalveolar pores of Kohn in the murine lung. *Cells Tissues Organs* (1993) 147:227–32. doi: 10.1159/000147509
29. Namati E, Thiesse J, De Ryk J, McLennan G. Alveolar dynamics during respiration: are the pores of Kohn a pathway to recruitment? *Am J Respir Cell Mol Biol.* (2008) 38:572–8. doi: 10.1165/rcmb.2007-0120OC
30. Desoubeaux G, Cray C. Rodent models of invasive aspergillosis due to *Aspergillus fumigatus*: Still a long path toward standardization. *Front Microbiol.* (2017) 8:1–31. doi: 10.3389/fmicb.2017.00841
31. Bowman JC, Abruzzo GK, Anderson JW, Flattery AM, Gill CJ, Pikounis VB, et al. Quantitative PCR assay to measure *Aspergillus fumigatus* burden in a murine model of disseminated aspergillosis: demonstration of efficacy of caspofungin acetate. *Antimicrob Agents Chemother.* (2001) 45:3474–81. doi: 10.1128/AAC.45.12.3474-3481.2001
32. Sheppard DC, Marr KA, Fredricks DN, Chiang LY, Doedt T, Filler SG. Comparison of three methodologies for the determination of pulmonary fungal burden in experimental murine aspergillosis. *Clin Microbiol Infect.* (2006) 12:376–80. doi: 10.1111/j.1469-0691.2005.01349.x
33. Steinbach WJ, Benjamin DK, Trasi SA, Miller JL, Schell WA, Zaas AK, et al. Value of an inhalational model of invasive aspergillosis. *Med Mycol.* (2004) 42:417–25. doi: 10.1080/13693780410001712034
34. Knust J, Ochs M, Gundersen HJG, Nyengaard JR. Stereological estimates of alveolar number and size and capillary length and surface area in mice lungs. *Anat Rec.* (2009) 292:113–22. doi: 10.1002/ar.20747
35. Irvin CG, Bates JHT. Measuring the lung function in the mouse: the challenge of size. *Respir Res.* (2003) 4:4. doi: 10.1186/rr199
36. Stone KC, Mercer RR, Freeman BA, Chang L-Y, Crapo JD. Distribution of lung cell numbers and volumes between alveolar and nonalveolar tissue. *Am Rev Respir Dis.* (1992) 146:454–6.
37. Chang S, Kwon N, Kim J, Kohmura Y, Ishikawa T, Rhee CK, et al. Synchrotron X-ray imaging of pulmonary alveoli in respiration in live intact mice. *Sci Rep.* (2015) 5:8760. doi: 10.1038/srep08760
38. Faffe DS, Rocco PRM, Negri EM, Zin WA. Comparison of rat and mouse pulmonary tissue mechanical properties and histology. *J Appl Physiol.* (2002) 92:230–4. doi: 10.1152/japplphysiol.01214.2000
39. Miller FJ, Mercer RR, Crapo JD. Lower respiratory tract structure of laboratory animals and humans: dosimetry implications. *Aerosol Sci Technol.* (1993) 18:257–71. doi: 10.1080/02786829308959603
40. Osmanagic E, Sukstanskii AL, Quirk JD, Woods JC, Pierce RA, Conradi MS, et al. Quantitative assessment of lung microstructure in healthy mice using an MR-based 3He lung morphometry technique. *J Appl Physiol.* (2010) 109:1592–9. doi: 10.1152/japplphysiol.00736.2010
41. Mercer RR, Russell ML, Crapo JD. Alveolar septal structure in different species. *J Appl Physiol.* (1994) 77:1060–6.
42. Stone KC, Mercer RR, Gehr P, Stockstill B, Crapo JD. Allometric relationships of cell numbers and size in the mammalian lung. *Am J Respir Cell Mol Biol.* (1992) 6:235–43. doi: 10.1165/ajrcmb/6.2.235
43. Huffman Reed JA, Rice WR, Zsengellér ZK, Wert SE, Dranoff G, Whitsett JA. GM-CSF enhances lung growth and causes alveolar type II epithelial cell hyperplasia in transgenic mice. *Am J Physiol.* (1997) 273:L715–25.
44. Jung K, Schlenz H, Krasteva G, Mühlfeld C. Alveolar epithelial type II cells and their microenvironment in the Caveolin-1-deficient mouse. *Anat Rec.* (2012) 295:196–200. doi: 10.1002/ar.21543

45. Henry MM, Ranga V. A Quantitative study of the development of interalveolar pores in the postnatal mouse. *Exp Lung Res.* (1985) 9:277–87. doi: 10.3109/01902148509057528
46. van oud Alblas AB, van Furth R. Origin, Kinetics, and characteristics of pulmonary macrophages in the normal steady state. *J Exp Med.* (1979) 149:1504–18. doi: 10.1084/jem.149.6.1504
47. Haley PJ, Muggenburg BA, Weissman DN, Bice DE. Comparative morphology and morphometry of alveolar macrophages from six species. *Am J Anat.* (1991) 191:401–7. doi: 10.1002/aja.1001910407
48. Wigginton JE, Kirschner D. A model to predict cell-mediated immune regulatory mechanisms during human infection with *Mycobacterium tuberculosis*. *J Immunol.* (2001) 166:1951–67. doi: 10.4049/jimmunol.166.3.1951
49. Prauße MTE, Lehnert T, Timme S, Hünniger K, Leonhardt I, Kurzai O, et al. Predictive virtual infection modeling of fungal immune evasion in human whole blood. *Front Immunol.* (2018) 9:1–13. doi: 10.3389/fimmu.2018.00560
50. Timme S, Lehnert T, Prauße MTE, Hünniger K, Leonhardt I, Kurzai O, et al. Quantitative simulations predict treatment strategies against fungal infections in virtual neutropenic patients. *Front Immunol.* (2018) 9:1–14. doi: 10.3389/fimmu.2018.00667
51. Tokarski C, Hummert S, Mech F, Figge MT, Germerodt S, Schroeter A, et al. Agent-based modeling approach of immune defense against spores of opportunistic human pathogenic fungi. *Front Microbiol.* (2012) 3:129. doi: 10.3389/fmicb.2012.00129
52. Oremland M, Michels KR, Bettina AM, Lawrence C, Mehrad B, Laubenbacher R. A computational model of invasive aspergillosis in the lung and the role of iron. *BMC Syst Biol.* (2016) 10:34. doi: 10.1186/s12918-016-0275-2
53. Tanaka RJ, Boon NJ, Vrcelj K, Nguyen A, Vinci C, Armstrong-James D, et al. *In silico* modeling of spore inhalation reveals fungal persistence following low dose exposure. *Sci Rep.* (2015) 5:13958. doi: 10.1038/srep 13958
54. Pollmächer J, Timme S, Schuster S, Brakhage AA, Zipfel PF, Figge MT. Deciphering the counterplay of Aspergillus fumigatus infection and host inflammation by evolutionary games on graphs. *Sci Rep.* (2016) 6:27807. doi: 10.1038/srep27807
55. Roilides E, Walsh TJ, Pizzo PA, Rubin M. Granulocyte Colony-Stimulating Factor enhances the phagocytic and bactericidal activity of normal and defective human neutrophils. *J Infect Dis.* (1991) 163:579–83. doi: 10.1093/infdis/163.3.579
56. Mircescu MM, Lipuma L, van Rooijen N, Pamer EG, Hohl TM. Essential role for neutrophils but not alveolar macrophages at early time points following *Aspergillus fumigatus* infection. *J Infect Dis.* (2009) 200:647–56. doi: 10.1086/600380
57. Huh D. A human breathing lung-on-a-chip. *Ann Am Thorac Soc.* (2015) 12:S42–4. doi: 10.1513/AnnalsATS.201410-442MG
58. Mosig AS. Organ-on-chip models: new opportunities for biomedical research. *Futur Sci. OA* (2016) 3:fsoa-2016-0038. doi: 10.4155/fsoa-201 6-0038
59. Benam KH, Villenave R, Lucchesi C, Varone A, Hubeau C, Lee HH, et al. Small airway-on-a-chip enables analysis of human lung inflammation and drug responses *in vitro*. *Nat Methods* (2016) 13:151–7. doi: 10.1038/nmet h.3697
60. Miller AL, Strieter RM, Gruber AD, Ho SB, Lukacs NW. CXCR2 regulates respiratory syncytial virus-induced airway hyperreactivity and mucus overproduction. *J Immunol.* (2003) 170:3348–56. doi: 10.4049/jimmunol.170.6.3348
61. Zipfel PF, Skerka C. Complement regulators and inhibitory proteins. *Nat Rev Immunol.* (2009) 9:729–40. doi: 10.1038/nri2620
62. Kozel TR, Wilson MA, Farrell TP, Levitz SM. Activation of C3 and binding to *Aspergillus fumigatus* conidia and hyphae. *Infect Immun* (1989) 57:3412–7.
63. Riedemann NC, Guo R-F, Sarma VJ, Laudes IJ, Huber-Lang M, Warner RL, et al. Expression and function of the C5a receptor in rat alveolar epithelial cells. *J Immunol.* (2002) 168:1919–25. doi: 10.4049/jimmunol.168.4.1919
64. McCormick A, Loeffler J, Ebel F. *Aspergillus fumigatus*: contours of an opportunistic human pathogen. *Cell Microbiol.* (2010) 12:1535–43. doi: 10.1111/j.1462-5822.2010.01517.x

Conflict of Interest Statement: The authors declare that the research was conducted in the absence of any commercial or financial relationships that could be construed as a potential conflict of interest.

frontiers

Supplementary Material

Comparative assessment of aspergillosis by virtual infection modeling in murine and human lung

Marco Blickensdorf, Sandra Timme and Marc Thilo Figge *

*** Correspondence:** Corresponding Author: thilo.figge@leibniz-hki.de

1 Supplementary Methods

In this study, we implemented a to-scale model of the murine alveolus following our previous work on the implementation of the human alveolus. For details on the hybrid agent-based model (ABM), the reader is referred to the extended description of this model in the work by Pollmächer *et al.*(Pollmächer and Figge, 2014, 2015). This Supplementary Information presents essential aspects of the algorithmic implementation that are important in view of the current study.

1.1 Alveolus Setup

In close analogy to our previous work(Pollmächer and Figge, 2014, 2015), the human and murine alveoli were modeled as three-dimensional three-quarter spheres, with radius $r_{Alv}^{H} = 116.5\ \mu m$ and $r_{Alv}^{M} = 26.2\ \mu m$, respectively. The polyhedral shape of the alveolus was approximated by a spherical representation with surface points $\vec{x} = c(r_{Alv}, \vartheta, \varphi)$ and an entrance ring at the lower threshold value of the polar angle $\vartheta_c \leq \vartheta \leq \pi$. Alveolar epithelial cells (AEC) of realistic dimensions were placed at the inner surface of the alveolus as follows: Centroids of type 1 AEC were placed in an equidistant fashion using a Voronoi tessellation to project cells on the curved geometry of the alveolus. Type 2 AEC were placed randomly on the border between two neighboring type 1 AEC. The same procedure was applied for the positioning of Pores of Kohn. All cells were represented with realistic cell sizes and in realistic amounts as obtained from an in-depth literature search (see Table 1 and Supplementary Table S1).

1.2 Chemokine Secretion and Diffusion

The hybrid ABM(Pollmächer and Figge, 2014, 2015) was used to simulate chemokine secretion and diffusion on an equidistant grid of points on the surface of the alveolus. Placing n points uniformly on a spherical surface is known as the Thompson problem(Thomson, 1904) and we used established algorithms(MacWilliam and Cecka, 2013) to generate a near-equidistant solution of a grid with 10000 points and 513 points, respectively, for the human and murine alveolus, *i.e.* keeping the same spatial resolution in both systems. Chemokine diffusion was modeled solving the reaction-diffusion equation on the grid. The reaction-diffusion equation

$$\frac{\delta c(\vec{r},t)}{\delta t} = D\Delta c(\vec{r},t) - \lambda c(\vec{r},t) + S(\vec{r},t) - Q(\vec{r},t)$$

describes molecule diffusion with diffusion coefficient D and molecule degradation with degradation rate λ of the concentration $c(\vec{r},t)$ at position $\vec{r}$ and time point t. Furthermore, the terms $S(\vec{r},t)$ and $Q(\vec{r},t)$ describe chemokine secretion and consumption at position $\vec{r}$ and time point t, where molecule consumption involves molecule-receptor binding by alveolar macrophages. Chemokine secretion was induced at all grid points on the surface of the AEC associated with a conidium. The reaction-diffusion equation was numerically integrated in time using a finite difference method for unstructured grids, as described by Sukumar(Sukumar, 2003). When multiple conidia were present in the alveolus, all associated cells secrete chemokines with the same secretion rate. When a conidium was found by an alveolar macrophage (AM) the associated cell stopped chemokine secretion.

1.3 AM Migration

Migration of AM was realized along surface vectors of length $v\Delta t$, where v denotes the macrophage speed and Δt refers to the time step of the simulation. A new migration direction was chosen after persistence time t_p, either randomly to simulate random walk migration or biased by chemotactic signals to simulate directed AM migration. AM sensing of the chemokine concentration was realized by the receptor-ligand model that was previously introduced by Guo and Tay (2008)(Guo et al., 2008) and Guo *et al.*(Guo and Tay, 2008) and applied here to the spherical alveolar surface. This model consisted of an independent system of three differential equations reflecting the state of ligands and receptors on the AM surface. In short, the chemokine receptors were able to bind free chemokines with binding rate k_b, building a receptor-ligand complex, which was internalized by the AM with rate k_i and finally recycled and re-expressed on the cellular surface with rate k_r. The most favorable direction of migrating AM was determined by computing the sum of weighted gradients over one period of directional persistence. Then, after each period of directional persistence, the respective AM migrates in the direction of the weighted cumulative gradient $\vec{g}_{AM}$ with probability $p_{directed} = \min(||\vec{g}_{AM}||\sigma_{AM}, 1)$, where the sensitivity factor σ_{AM} was determined by Tranquillo *et al.*(Tranquillo et al., 1988). For all simulations we assumed that AM migrate at speed of $v = 4\frac{\mu m}{min}$ and with persistence time $t_p = 1\ min$.

1.4 Agent Distribution

AM were placed randomly on the inner surface of the alveolus. Placing n_{AM} AM uniformly over n_{Alv} alveoli leads to the binomial distribution $B_{AM}(n_{AM}, p, k) = \binom{n_{AM}}{k} p^k (1-p)^{n_{AM}-k}$, where the probability $p = 1/n_{alv}$ refers to the probability to have k AM per alveolus. In close analogy, the probability to have j conidia present in one alveolus is $B_{con}(n_{con}, p, j)$. The alveolar system was implemented with absorbing boundaries, *i.e.* each agent that crosses a system boundary was taken out of the system. To account for these randomly exiting AM and to preserve the binomial distribution $B_{AM}(n_{AM}, p, k)$, new AM were inserted into the system with exponentially distributed waiting time $t_{wait} = \frac{1}{\lambda_{in}} \ln(\frac{1}{u})$, where u is uniformly distributed in $(0,1]$. The input rate λ_{in} is calibrated for each set of migration parameters (v and t_p) and alveolar system (murine and human). The entry point of newly entering macrophages was modeled to depend on gradient of the local chemokine concentration, $||\vec{g}^b_{AM,i}||$, with probability $p_i = \frac{||\vec{g}^b_{AM,i}||}{||\vec{g}^b_{AM,max}||}$ at entry point i and $||\vec{g}^b_{AM,max}||$ is the maximum gradient of all boundary points. The acceptance-rejection method is applied in the following way: An entry point is accepted if $p_i < l$ with a randomly chosen l in $[0,1]$ from a uniform

distribution for each candidate position; otherwise a new position is chosen randomly over all boundary points of the alveolus as the next candidate entry point.

1.5 Implementation

The simulation framework was implemented in *C++* to provide maximum expandability. Model dynamics as agent migration, interaction handling and diffusion were realized by asynchronous random-order updating for each time step independently. Two agents interact if their associated spheres were overlapping. In case of contact between an AM and a conidium, the conidium was assumed to be phagocytosed by the AM.

1.6 Simulation Result Robustness

We provide a statistical estimate on how reliable our results are. As explained before, we run each simulation for a particular set of model parameters 10^3 times. One option to estimate the robustness of the resulting readouts would be to repeat these 10^3 simulations multiple times and to calculate statistical measures. Since this would be very time consuming, we decided to bootstrap(Efron and Tibshirani, 1986) the simulation results as follows: We randomly chose a set of 10^3 simulations out of the 10^3 computed simulations with replacement and computed readouts like the infection score IS for a number B of repetitions. From the resulting IS distribution we calculated the 95%-confidence interval as an estimation of the real quantiles. We here chose $B = 300$ to produce stable results.

To evaluate the results of the bootstrapping procedure, we compared it to an estimated standard deviation, which we received from 10 repetitions of 10^3 simulations for the human and mouse system with 1 conidium for all parameter combinations of chemotactic signaling. The standard deviation in these 72 simulations differed on average by 6% between the bootstrapped and the repetition estimates, indicating that our bootstrapping procedure produced valid results.

1.7 References

Efron, B., and Tibshirani, R. (1986). Bootstrap Methods for Standard Errors, Confidence Intervals, and Other Measures of Statistical Accuracy. *Stat. Sci.* 1, 54–75. doi:10.1214/ss/1177013815.

Guo, Z., Sloot, P. M. A., and Tay, J. C. (2008). A hybrid agent-based approach for modeling microbiological systems. *J. Theor. Biol.* 255, 163–75. doi:10.1016/j.jtbi.2008.08.008.

Guo, Z., and Tay, J. C. (2008). *Granularity and the Validation of Agent-based Models*. San Diego, CA: Simulation Councils, Inc doi:10.1145/1400549.1400568.

MacWilliam, T., and Cecka, C. (2013). CrowdCL: Web-based volunteer computing with WebCL. in *2013 IEEE High Performance Extreme Computing Conference (HPEC)* (IEEE), 1–6. doi:10.1109/HPEC.2013.6670348.

Pollmächer, J., and Figge, M. T. (2014). Agent-based model of human alveoli predicts chemotactic signaling by epithelial cells during early Aspergillus fumigatus infection. *PLoS One* 9, e111630. doi:10.1371/journal.pone.0111630.

Pollmächer, J., and Figge, M. T. (2015). Deciphering chemokine properties by a hybrid agent-based model of Aspergillus fumigatus infection in human alveoli. *Front. Microbiol.* 6, 503. doi:10.3389/fmicb.2015.00503.

Sukumar, N. (2003). Voronoi cell finite difference method for the diffusion operator on arbitrary unstructured grids. *Int. J. Numer. Methods Eng.* 57, 1–34. doi:10.1002/nme.664.

Thomson, J. J. (1904). XXIV. *On the structure of the atom: an investigation of the stability and periods of oscillation of a number of corpuscles arranged at equal intervals around the circumference of a circle; with application of the results to the theory of atomic structure*. *London, Edinburgh, Dublin Philos. Mag. J. Sci.* 7, 237–265. doi:10.1080/14786440409463107.

Tranquillo, R. T., Lauffenburger, D. A., and Zigmond, S. H. (1988). A stochastic model for leukocyte random motility and chemotaxis based on receptor binding fluctuations. *J. Cell Biol.* doi:10.1083/jcb.106.2.303.

2 Supplementary Videos

2.1 Video S1 – Human Alveolus Model Video

The video shows one exemplary simulation in the to-scale hybrid ABM for the human alveolus. The video starts with a rotation of the alveolus. The simulation of an infection scenario with one conidium starts when the time stamp is visible. AM (green) migrating towards the conidium (red) along the chemokine gradient (white isolines) produced by the source AEC. The conidium is found by an AM after 55 minutes in this simulation.

2.2 Video S2 – Mouse Alveolus Model Video

The video shows one exemplary simulation in the to-scale hybrid ABM for the murine alveolus. The video starts with a rotation of the alveolus. The simulation of an infection scenario with one conidium starts when the time stamp is visible. AM (green) migrating towards the conidium (red) along the chemokine gradient (white isolines) produced by the source AEC. The conidium is found by an AM after 21 minutes in this simulation.

2.3 Video S3 – Infection scores and parameter optima

The video provides a slide show of simulation results for increasing alveolar occupation number comparing the human (left) and mouse (right) system. The infection score is represented in a color-coded fashion as a function of all chemokine parameter combinations. Small grey dots represent all those data points that did not exceed the minimal upper limit of all 95%-confidence intervals. Gold points indicate their respective weighted mean. A black border around a data point indicates an infection score below the threshold $IS_t = 5\%$.

3 Supplementary Figures

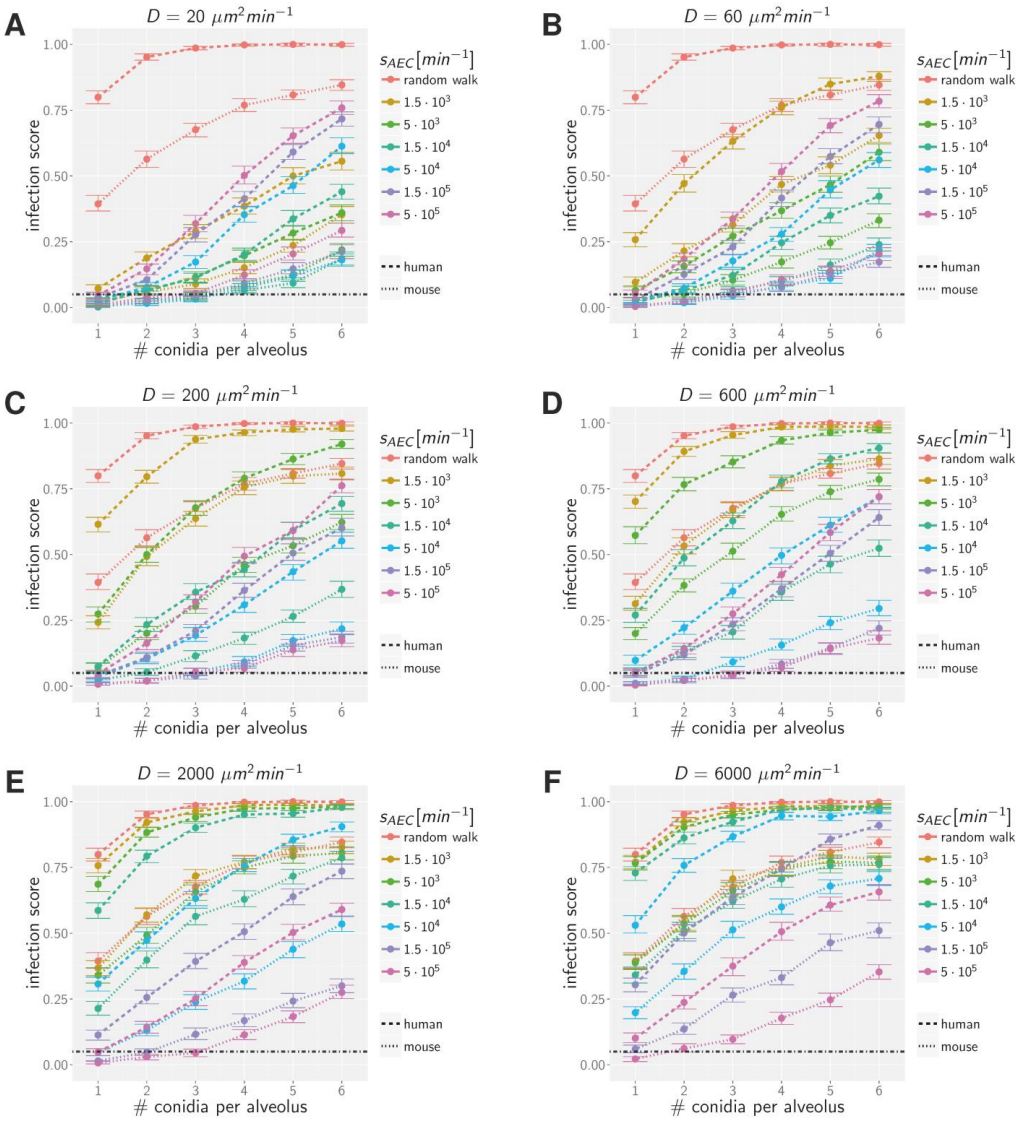

Supplementary Fig. S1: Infection scores for all scanned alveolar occupation numbers and all combinations of chemokine parameters in the human (dashed line) and mouse (dotted line) alveolus. Black dashed-dotted line indicates an infection score of $\boldsymbol{IS_t = 5\%}$. Error bars represent the 95%-confidence interval.

Supplementary Material

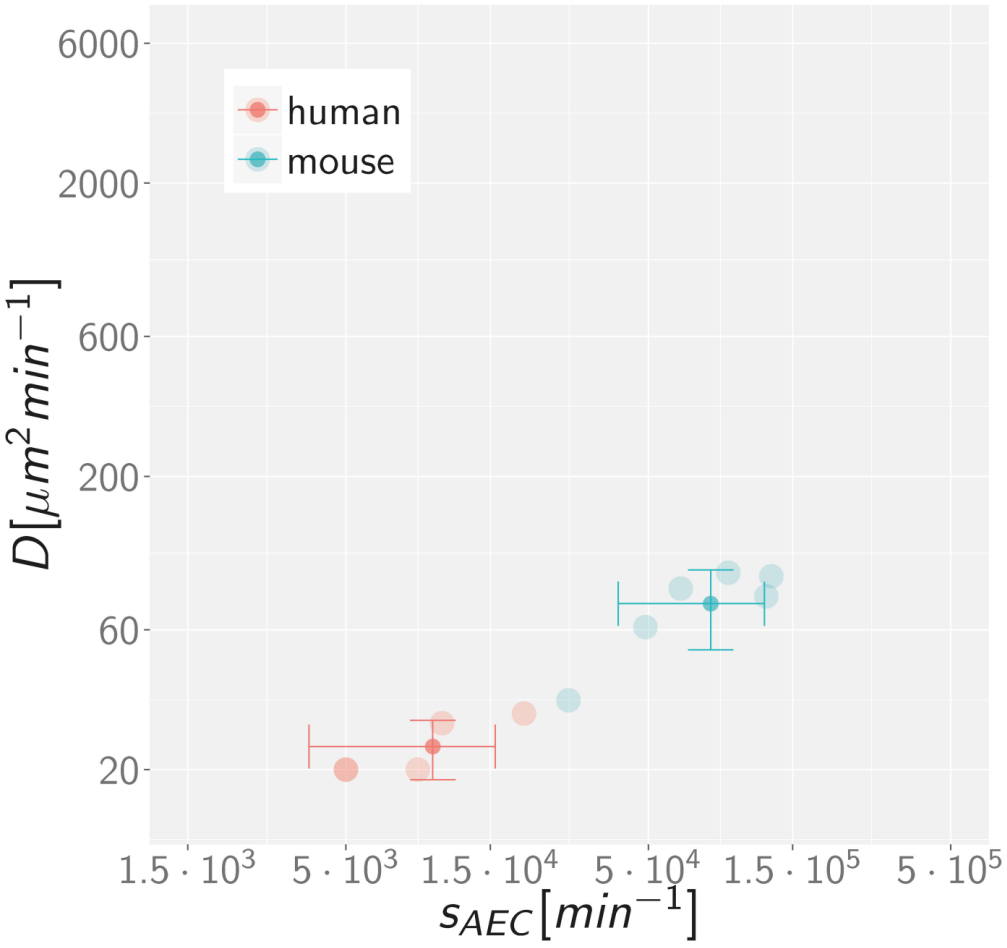

Supplementary Fig. S2: Optimal chemokine parameters for alveolar occupation numbers AON = [1,6] in the human and mouse system. For the respective mean with standard deviations across the six data points, we the values $\overline{D_{opt}{}^{H}} = 26 \pm 6.6\ \mu m^2 min^{-1}$ and $\overline{s^{H}_{AEC_{opt}}} = 1.1 \times 10^4\ \pm 6 \times 10^3\ min^{-1}$ for the human host and $\overline{D_{opt}{}^{M}} = 74 \pm 22.4\ \mu m^2 min^{-1}$ and $\overline{s^{M}_{AEC_{opt}}} = 8.0 \times 10^4 \pm 4{,}1 \times 10^4\ min^{-1}$ for the murine host.

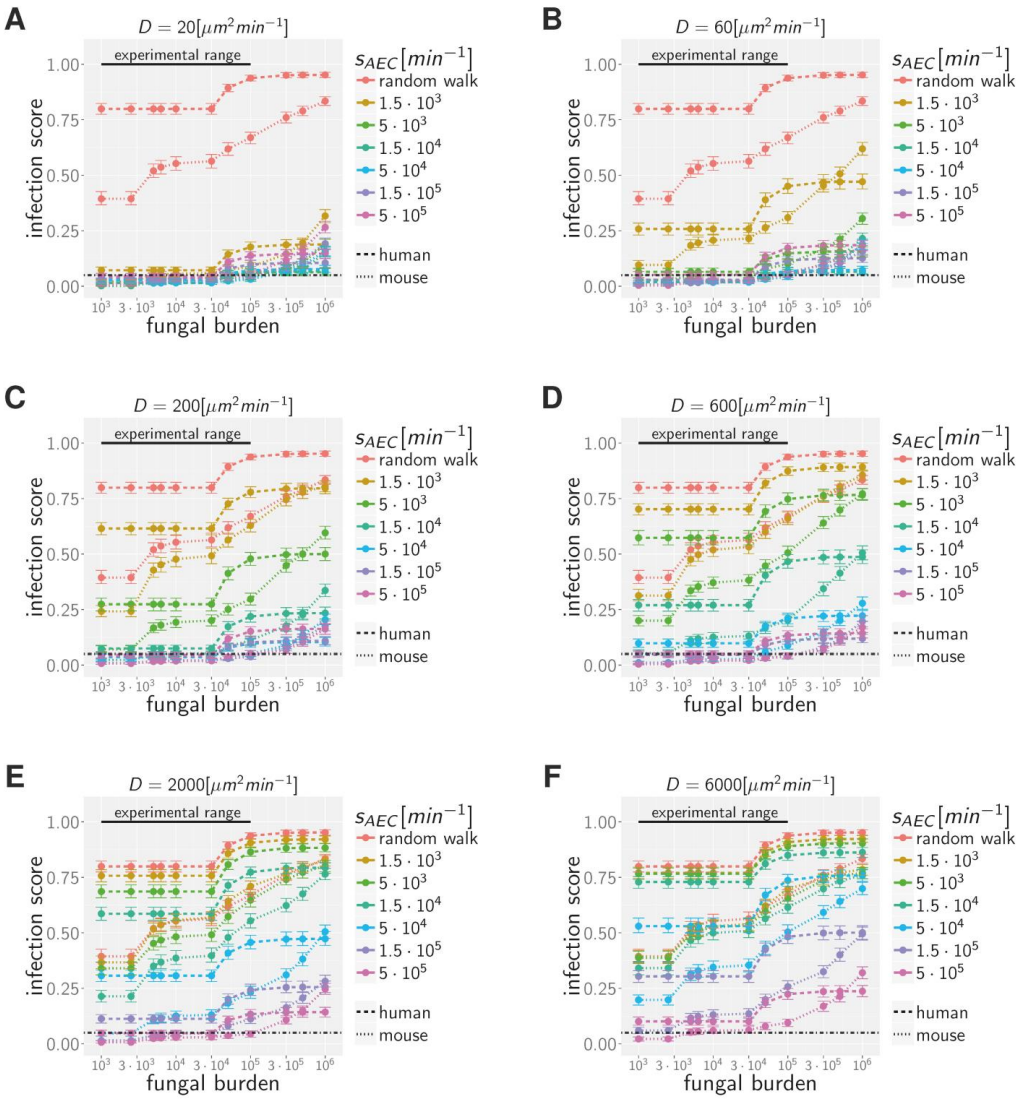

Supplementary Fig. S3: Infection scores for all scanned fungal burdens and all combinations of chemokine parameters in the human (dashed line) and mouse (dotted line) alveolus. Black dashed-dotted line indicates an infection score of $IS_t = 5\%$. Error bars represent the 95%-confidence interval.

Supplementary Material

4 Supplementary Tables

Supplementary Table 1: Average characteristics derived per alveolus for the human and murine system.

Parameter	Human	Mouse	Mouse/Human [%]
Surface area	$127 \times 10^3\ \mu m^2$	$6.5 \times 10^3\ \mu m^2$	5.1
Volume	$5\,588 \times 10^3\ \mu m^3$	$64 \times 10^3\ \mu m^3$	1.1
Length of boundary	$743.2\ \mu m$	$128.2\ \mu m$	17.2
Surface to boundary ratio	$170.1\ \mu m$	$50.7\ \mu m$	29.8
Mean AM number	4.38	0.74	16.9
Surface area per AM	$28.9 \times 10^3\ \mu m^2$	$8.8 \times 10^3\ \mu m^2$	30.4
Mean distance to boundary*	$95.4\ \mu m$	$21.3\ \mu m$	22.3
Surface grid points	10 000	513	5.13

*The mean distance to boundary was computed for random points in the respective alveolar systems measuring their distance to the closest border point from 1000 random realizations.

Part V.

Discussion

Human-pathogenic fungi constitute a serious problem in medical health care due to the increasing number of immunocompromised patients and are associated with high mortality rates [12]. Among others, the most prevalent fungal isolates associated with severe fungal infections are the human commensals *C. albicans* and *C. glabrata* as well as the airborne fungus *A. fumigatus* [7]. In this thesis, several individual-based virtual infection models have been developed and used to investigate host-pathogen interactions of the host immune system and the aforementioned human-pathogenic fungi. This cumulative dissertation comprises six manuscripts as depicted in Figure 6. These manuscripts belong to three main topics: (i) image-based systems biology, (ii) *Candida* bloodstream infection and (iii) *A. fumigatus* lung infection. The first topic (see Figure 6

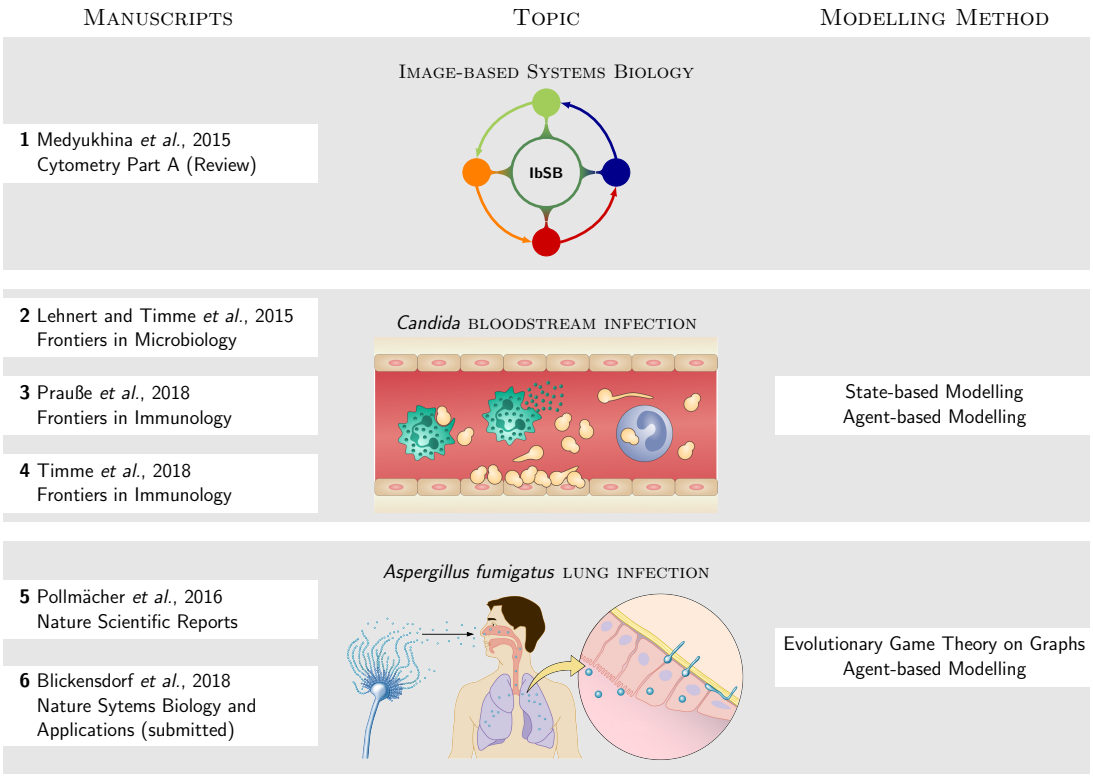

Figure 6.: Overview of Manuscripts. This thesis comprises six manuscripts that cover various topics in fungal infection biology combined with a number of state of the art modelling techniques. (1) The first manuscript reviews the workflow and techniques in image-based systems biology [143], (2-4) The first research topic on *Candida* whole blood infection comprises three publications [142, 144, 145] and (5-6) the second topic on *A. fumigatus* lung infection comprises one publication and one submitted manuscript [124].

upper panel) involves a publication that reviews the workflow, techniques and state of science in image-based systems biology [143].

The second topics (see Figure 6 middle panel) involves three publications, which address different aspects of the host-pathogen interactions of the innate immune response against the two *Candida* spp., *C. albicans* and *C. glabrata*, in human whole blood [142, 144, 145]. In particular, a bottom-up modelling approach was developed that combines modelling techniques of different complexity. This innovative multi-model approach allows

rigorous investigation of the infection-inflammation process of *Candida* spp. in human whole-blood and was used to predict immune reaction rates and migration parameters of immune cells. Furthermore, hypothesis testing of an immune evasion mechanisms of these fungal pathogens, which enables escape from killing and phagocytosis by immune cells, was performed. Additionally, the bottom-up modelling approach was used to simulate immune dysregulation, neutropenic conditions and *in silico* cytokine treatment of virtual neutropenic patients.

The third topic (see Figure 6 lower panel) involves two manuscripts on *A. fumigatus* lung infection. The first publication within this topic uses *evolutionary game theory* (EGT) to investigate innate immune processes under various infection doses and host immune states [124]. Furthermore, in a submitted manuscript we used a realistic to-scale hybrid agent-based model for comparative analysis between *A. fumigatus* lung infection in human and mice under natural daily inhalation and experimental inhalation doses.

Due to the modular structure of the developed virtual infection models, they feature a high degree of extensibility and flexibility that allows studying further aspects of the aforementioned human-pathogenic fungi as well as their adaptation to other biological systems. The results and generated hypotheses within this thesis add knowledge on host-pathogen interactions with human pathogenic fungi and will form the basis for future experimental and computational research initiating multiple cycles of systems biology. Chapter 10 and chapter 11 discuss the main results and outline perspectives on experimental validation, clinical relevance and future model developments of *Candida* bloodstream infections and *A. fumigatus* lung infections, respectively.

10. *Candida* bloodstream infection

Upon entering the bloodstream via catheters or a disturbed intestinal barrier the human commensals *C. albicans* and *C. glabrata* are able to cause severe systemic infections in immunocompromised individuals. Thus, research on the infection process and the immune response against these pathogens is of great importance.

Experimentally, this infection process can be investigated using human whole-blood infection assays as established by Hünniger *et al.* [141]. In this assay, human whole blood is infected with *Candida* yeast cells and incubated for four hours. At several time points post-infection *fluorescence-activated cell sorting* (FACS) analyses and survival assays are performed in order to measure pathogen killing and association to specific immune cells. Based on these temporal infection dynamics immune reactions can be investigated in a quantitative manner using state-based modelling. However, spatial aspects of these dynamics remain disguised, since imaging of whole blood is not possible to date. Virtual infection modelling allows to overcome this limitation by integrating experimental data and estimated immune reaction rates within a spatial model.

Bottom-up modelling enables efficient virtual infection modelling of *Candida* bloodstream infections

In the first publication within the topic of *Candida* bloodstream infections (see Figure 6 middle panel), a bottom-up modelling approach was developed, which enabled investigation of the host-pathogen interaction between innate immune mechanisms and *Candida* spp. by incorporating wet-lab experiments as well as multiple models with increasing complexity that build on one another [144]. With this sophisticated approach several non-spatial and spatial aspects of the biological system can be addressed and simultaneously computational costs remain manageable.

Non-spatial rates that quantify the immune reactions in human blood can be determined using a *state-based model* (SBM) that was previously developed by Hünniger *et al.* [141] and extended within this framework, in order to resolve also immune cell states. The higher degree of detail in the extended SBM enabled the transfer of estimated immune reaction rates to the spatial model within the bottom-up approach. Parameter estimation was performed using the global optimization method *simulated annealing*.

In order to resolve spatial dynamics of the biological system, we developed a spatial counterpart of the SBM. This spatial model is based on a previously established agent-based framework by Pollmächer and Figge [139] that was implemented using the object-oriented programming language `C++`, which features a high degree of flexibility. During my PhD project this framework was extended to model whole-blood infection assays with the human-pathogenic fungi *C. albicans* and *C. glabrata*. For cost-efficient parameter estimation, the ABM makes use of previously estimated immune reaction rates from the SBM. Therefore, *contact-independent* and *contact-dependent* processes have to be distinguished and transformed, *i.e.* event probabilities of contact-dependent processes, such as phagocytosis, have to be equalized. Thus, the dimensionality of the parameter

space in the ABM can be drastically reduced and values of diffusion coefficients of immune cells remain to be estimated. Since ABMs are cost-intensive in terms of computational runtime and diffusion coefficients can be restricted to biologically relevant ranges, the local optimization approach *adaptive regular grid search*, which requires comparably little simulations, was applied.

Typically, in systems biology, single-model approaches are applied in order to investigate a certain biological system. However, depending on the choice of modelling technique this approach can be limited by various complications. If the modelling technique is very general, such as ODEs, either the predictive potential may not be fully utilized, or when new types of data become available over time, they cannot be integrated into the model. In contrast, modelling techniques with a high degree of detail, such as ABMs, may be too complex to start with, since many parameters are not known in the beginning, leading to unreliable predictions. Combining several modelling techniques to simulate biological systems is already used in multi-scale modelling, where different modelling approaches are applied to represent different biological scales. For example, in hybrid agent-based modelling the ABM is typically used to simulate cells, while a PDE is used to account for molecule diffusion. However, such multi-scale models are even more complex than ABMs and, thus, rely on even more parameters. In the scope of the bottom-up modelling approach various modelling approaches with different complexity are combined within one framework, which allows investigation of biological systems in a systematic manner and generation of relevant predictions.

Immune reaction rates can be quantified by state-based modelling

Immune reaction rates, such as phagocytosis rates, intra- and extracellular killing rates as well as the effect rate of anti-microbial peptides, are not directly accessible in experiments. Simulation and fitting of the SBM to the underlying experimental data basis allows estimation of these rates. Additionally, temporal kinetics of pathogen subpopulations can be uncovered using this virtual infection model.

Within the bottom-up modelling approach we extended the SBM to additionally account for immune cell states and we repeated parameter estimation for *C. albicans* human whole-blood infection. The resulting immune reaction rates were to those previously estimated by Hünniger *et al.* [141] comparable, indicating the validity of both models and the robustness of the predicted solution. With this, we could further confirm the major role of neutrophils during the immune response against *C. albicans*.

In the third publication within this topic (see Figure 6 middle panel), we applied the bottom-up modelling approach also in the context of human whole-blood infection with *C. glabrata* [142]. Here, we observed pathogen-specific differences to *C. albicans* in the estimated immune reaction rates. On the one hand, phagocytosis rates of neutrophils and monocytes were higher for *C. glabrata*. On the other hand, monocytes showed a more important role in the immune response against *C. glabrata*, which is in line with experimental observations [146]. Duggan *et al.* [146] showed that *C. glabrata* is able to trigger neutrophils to secrete soluble factors leading to an increased monocyte recruitment as well as an increased anti-fungal activity of monocytes and, thus, higher phagocytosis. This is indicative for a fungal evasion strategy, since *C. glabrata* cells can survive and replicate intracellularly within monocytes [146], which increases the risk for dissemination.

Spatial modelling allows for prediction of immune cell migration

Live cell imaging of whole blood is not possible to date. Therefore, spatial properties of the host-pathogen interactions between the human immune system and the fungal pathogens *C. albicans* and *C. glabrata* remain disguised. However, virtual infection modelling has the potential to overcome this limitation by simulation of spatial models and the generation of predictions that can be tested in future experiments. Hence, we developed an ABM as spatial counterpart of the SBM that is able to resolve spatial dynamics of the system. Using transformed estimated non-spatial immune reaction rates from the SBM we performed simulations with the ABM in order to determine immune cell migration parameters. We estimated diffusion coefficients of the two immune cell types – monocytes and neutrophils – by fitting ABM simulations to the experimental data basis. We found that during *C. albicans* infection, large variations of the diffusion coefficient of monocytes have only a vanishingly low impact on the infection outcome. In contrast, the infection outcome was very sensitive to the diffusion coefficients of neutrophils, which has, therefore, to be fine-tuned in a narrow range. This further promotes the importance of neutrophils in response to *C. albicans* in human blood. In comparison to *C. albicans*, diffusion coefficients for both immune cell types in response to *C. glabrata* were in general higher. Interestingly, the diffusion coefficient for monocytes was much more restricted in case of *C. glabrata* infection. This is in line with previous findings that monocytes play a more important role during *C. glabrata* infections [146]. In contrast, the impact of the diffusion coefficients for neutrophils on the infection outcome with *C. glabrata* was smaller than for *C. albicans* and could vary in a significantly larger range.

State-based modelling enables hypothesis testing of *Candida* immune evasion mechanism

Hünniger *et al.* [141] detected a population of *C. albicans* cells during human whole-blood infection assays that was not phagocytosed. While some of these cells were killed extracellularly, others remained viable [141]. Since these alive cells that evade the immune system increase the risk for dissemination, it is important to unravel the underlying mechanisms leading to this immune evasive population.

In order to clarify this mechanism Hünniger *et al.* [141] performed several experiments, such as testing for immune cell exhaustion by reinoculation of new fungal cells and by adding fresh immune cells, respectively [141]. However, both experiments falsified the hypothesis of immune cell exhaustion. Furthermore, immune escape due to hyphae formation could be excluded, since an immune evasive population was also observed using a non-filamentous mutant [141]. Furthermore, after inoculation of killed fungal cells the same amount of immune evasive cells was detected.

Since the mechanism of fungal immune evasion could not be deciphered until now, we tested for several hypotheses and generated predictions that can be addressed in future experiments, using our previously established SBM. Therefore, we implemented two different mechanisms for immune evasion, which are: (i) a *spontaneous* mechanism and (ii) a *neutrophil-mediated* mechanism, that is based on the assumptions that neutrophils secrete peptides that (not on purpose) remodel fungal surface molecules by shaving or masking. Both models could be fitted to the experimental data with similar quality. For *C. albicans* major differences could be observed in the intracellular killing rates

intracellular killing in monocytes and the decrease of the anti-microbial killing effect, which are, however, not directly measurable in experiment. Furthermore, quantitative differences could also be observed for the kinetics of extracellular killing due to anti-microbial peptides and the kinetics of immune evasive cells, which are too small to distinguish both models using the experimental data. For *C. glabrata*, immune reaction rates for both mechanisms showed relatively large differences. Similar to *C. albicans* differences in the time-dependent extracellular killing due to antimicrobial factors were observed, which were much stronger for *C. glabrata*. Although, both mechanisms will not be distinguishable in experiment within one pathogen, the comparison of the relative differences in the pathogen-specific effect of anti-microbial peptides could be measured in future experiments. We predict that the strongest differences in the anti-microbial peptides will be visible at ten to 50 minutes post infection.

To more clearly distinguish both models, we simulated the condition of neutropenia, since the neutrophil-mediated mechanism is largely influenced by the number of neutrophils in the system. The infection outcome four hours post-infection showed clear differences between the two immune evasion mechanisms in the fractions of phagocytosed, alive, killed and immune-evasive fungal cells as well as in the distribution across immune cells. These differences were larger for *C. albicans*, since in the immune response against *C. glabrata* monocytes can partly compensate the loss of neutrophils.

IMMUNE DYSREGULATION RESEMBLES CONDITIONS OF NEUTROPENIA

We further used the established bottom-up approach and the previously determined immune reaction rates and migration parameters to vary specific parameters and investigate their impact on the infection outcome. We used the SBM in order to simulate the infection process with *C. albicans* during immune cell deficiency. Here we, according to medically relevant ranges, steadily decreased the number of monocytes or neutrophils, respectively. While we could not observe an effect on the infection outcome for monocytopenia, neutropenia led to a strong impairment in pathogen killing. This result is in line with the impaired prognosis of neutropenic patients during *C. albicans* infection [76].

Additionally, we varied immune cell migration parameters in the ABM to simulate immune dysregulation that can occur during hyper- and hypo-inflammation in sepsis. This *in silico* experiment revealed that an altered monocyte migration does not affect the infection outcome during *C. albicans* infection, which shows again the minor role of macrophages for *C. albicans* infections. In contrast, a reduced neutrophil migration led to a decrease in killed *C. albicans* cells and, thus, an increase in immune evasive *C. albicans* cells, which increases the risk for dissemination. Interestingly, we observed that neutrophil paralysis resembled the condition of neutropenia.

ENHANCED RISK FOR FUNGAL DISSEMINATION IN VIRTUAL NEUTROPENIC PATIENTS WITH *Candida* INFECTION

As described before, we developed a bottom-up modelling approach and predicted immune reaction rates and immune cell migration parameters on the basis of infection assays performed with whole-blood from healthy donors. However, patients with an underlying disease, associated with a compromised immune system, are often at high risk for infections. Thus, the goal in systems biology of infection is not only to understand

the infection process in health but also in disease, in order to develop new diagnostic and therapeutic approaches. Especially, the condition of neutropenia – a neutrophil deficiency – constitutes a major risk factor for candidiasis [72]. Thus, we addressed this important issue in the third publication within the context of whole-blood infections. Based on the afore-described observation that neutrophil paralysis resembles the infection outcome in neutropenic patients, we hypothesize that an improved neutrophil activation, in terms of phagocytosis and migration, is able to recover the infection outcome in these patients.

A great advantage of virtual infection modelling is that once a sound model has been developed and calibrated to experimental data, model parameters or mechanisms can be changed in a targeted manner and tested for their impact on the simulation outcome. Thus, we simulated *virtual neutropenic patients* (VNP) with various severity degrees of neutropenia by gradually decreasing the absolute number of neutrophils in the ABM. We then simulated the infection with *C. albicans* and *C. glabrata* in these VNP and compared the infection outcome four hours post-infection. The infection outcome in VNP with both pathogens was significantly impaired in severe neutropenia, since the number of killed fungal cells decreased from 90 % to 50 % and 10 % for *C. glabrata* and *C. albicans*, respectively. This shows that the impact of neutropenia on the infection outcome is much stronger in *C. albicans* infection, since neutrophils have a higher importance against this fungus. In contrast, in *C. glabrata* infections monocytes are more involved in the immune response. For this reason, they can counteract the loss of neutrophils to some extent and phagocytose up to 50 % of the fungal cells in severe neutropenia and nearly no fungal cells remain extracellular and alive. However, this still poses the possibility of dissemination, since *C. glabrata* has the ability to survive and replicate within monocytes [146]. In *C. albicans* monocytes can hardly counteract neutropenic conditions, which is why a fraction of 30 % is still alive and extracellular four hours post-infection. This subpopulation of *C. albicans* cells might disseminate in real patients. The fractions of fungal subpopulations present four hours post-infection in the different VNP allowed to calculate severity-degree specific patterns of the infection outcome.

In silico cytokine treatment recovers infection outcome in virtual neutropenic patients

The bottom-up modelling approach also allows testing of hypothetical treatments in VNP. Based on our hypothesis that neutrophil activation in terms of phagocytosis and migration may recover the infection outcome in VNP, we performed simulations in the ABM. We here systematically increased the phagocytosis rate and diffusion coefficient of neutrophils in all VNP. The previously determined severity-degree specific patterns allowed for classification of the infection outcome. This analysis revealed that the *in silico* treatment indeed improves the infection outcome in VNP. Depending on the severity degree of neutropenia different treatment strength was required. We could show that a combined treatment of both parameters is most efficient in infection treatment in VNP to reach infection outcomes comparable to individuals with normal neutrophil counts. For *C. glabrata* lower activation was required to recover the infection outcome in VNP, *i.e.* the treatment was more efficient compared to *C. albicans*.

In the clinical situation the treatment as simulated in the ABM could be realized by a *cytokine treatment*. Inflammatory cytokines such as IFNγ and TNFα were shown to enhance the neutrophil response against *Candida* spp. [147] and other fungal pathogens,

such as *Aspergillus* spp. [148] and *Cryptococcus* spp. [149]. Besides cytokine treatments, common methods to treat neutropenia are medication of patients with *granulocyte colony-stimulating factor* (G-CSF), which leads to internal stimulation of neutrophil maturation and release from the bone marrow, as well as the transfusion of G-CSF/steroid mobilized neutrophils from a donor. Internal stimulation with G-CSF leads to a vast increase of neutrophils in blood and is mainly applied in congenital neutropenia [150, 151]. Thereby, G-CSF provides an inflammatory signal, which initiates the emergency mobilization of neutrophils leading to their migration into blood vessels [152]. However, some patients are low- or no-responders of the G-CSF treatment [74, 150]. Furthermore, the transfusion therapy of mobilized neutrophils from donors is very effective against bacterial infections. However, Gazendam *et al.* [153] showed that in particular G-CSF/dexamethasone stimulation of donor neutrophils changes the granular content of neutrophils leading to an impaired fungal killing capacity of *C. albicans*. This is in line with the clinical observation that the transfusion therapy improves survival in case of bacterial infections, which could not consistently be observed for fungal infections [154–156]. This highlights the need for alternative treatment strategies, which improve survival also during fungal infections in neutropenic patients.

PERSPECTIVES ON EXPERIMENTAL VALIDATION AND CLINICAL RELEVANCE

Several predictions and new hypotheses could be generated within this thesis, which might be addressed in future wet-lab studies. Hence, this section outlines perspectives on future experimental studies as well as possible applications of the bottom-up modelling approach in the clinical context.

As new microscopy technologies will be available in the future, experimental validation of our predictions regarding diffusion coefficients can be performed. Such an experimental testing of predicted migration parameters and immune reaction rates might either confirm our model or raise the need for model improvement. Once these parameters can be experimentally determined, our model can be used to address further questions regarding the infection process and immune response in human blood against *C. albicans* and *C. glabrata*.

In our study on *Candida* immune evasion in whole-blood infection assays, we performed hypotheses testing of two mechanisms using the SBM. We predict differences in the effect of anti-microbial killing for both mechanisms and the two pathogens. Therefore, in experiment the fungicidal effect of antimicrobial effector proteins inducing extracellular killing, like lactoferrin, elastase 2 and myeloperoxidase [146], could be measured in the time-window of 10 to 50 minutes, where the difference was predicted to be largest. A subsequent comparison of the effect against both pathogens could provide indication for the underlying mechanism. Furthermore, under neutropenic conditions, large relative differences in the infection outcome between the two fungal pathogens and the two immune evasion mechanisms could be observed. Thus, blood from neutropenic patients or blood with depleted neutrophil numbers could be used in whole-blood infection assays. These experimental tests could verify or reject our hypotheses and might contribute to the clarification of the underlying mechanism that causes fungal immune evasion. If both mechanisms would be falsified, other hypotheses for the immune evasion mechanism can be tested *in silico* and *in vitro*. Conceivable immune evasion mechanisms might involve other immune components, such as the complement system, monocytes or parts

of the adaptive immune system. Another possibility is that the subpopulation of immune-evasive cells exists from the beginning and is a special phenotype within the population of *Candida* cells that does not arise due to specific mechanisms in blood. Therefore, the research on the immune evasion mechanism will initiate further experiment-theory cycles.

Furthermore, we simulated the infection with *C. albicans* and *C. glabrata* under neutropenic conditions, since these patient are at high risk for fungal infections. Since traditional treatment strategies during neutropenia either do not work properly for some patients or impair anti-fungal killing capacities of immune cells alternative treatment strategies need to be investigated. Therefore, we applied an *in silico* treatment of the virtual neutropenic patients, where we determined the required treatment strength that is needed to recover the infection outcome to that of an immunocompetent host. Experimentally, different cytokines, like IFNγ and TNFα, can be tested for their ability to increase phagocytic and migratory activity of neutrophils. If the activation effect appears to be as strong as the predicted required treatment strength, the molecule under investigation might be appropriate for further testing as a potential therapeutic drug in neutropenia.

Besides using the bottom-up modelling approach for simulating virtual patients and treatment testing, it could be also used to stratify the immune-state of sepsis patients in the clinical setting. Sepsis appears to be a multi-faceted syndrome with hypo- and hyper-inflammatory phases that often occur simultaneously [157]. Due to the heterogeneous phenotype of sepsis, there exists no established treatment to date. Classification of sepsis patients according to their current immune status is, however, not straightforward and appropriate treatment of these patients strongly depends on the correct assessment of their immune status. In the future, the bottom-up modelling approach could be of help in the immuno-profiling of sepsis patients. This could be realized by using blood samples from sepsis patients for whole-blood infection assays with pathogens, such as *Candida* spp. or *Staphylococcus aureus*. Fitting the SBM to results from whole-blood infection assays and estimation of immune reaction rates would allow to identify patterns of immune dysregulation. Furthermore, estimation of immune cell migration parameters would further support pattern identification. These patterns would allow to build functional classifiers that can be used in the future for patient stratification.

Perspectives on model developments

The bottom-up modelling approach is a modular and generalized framework that can be extended in various ways. Currently, it comprises an SBM and an ABM connected by a self-consistent parameter conversion. In the future, the bottom-up approach can be extended by a *hybrid agent-based model* (hABM), which allows simulation of molecule secretion and diffusion and thereby adds another level of complexity. Simulation of molecule diffusion, such as anti-microbial peptides or chemokines, could be realized by adding a molecule layer within the ABM. However, solving the diffusion equation analytically is not possible in the ABM due to the large amount of sources and sinks in the system, which are represented by migrating cells that secrete and consume molecules in the environment. Therefore, molecule diffusion needs to be solved numerically, which can be realized for example using the *forward-Euler approach*. However, this method restricts the simulation time-step to a certain value due to the *Courant-limit* [158, 159], which determines the stability of the solution, and thereby increases simulation runtime.

Another numerical method that can be used to solve the diffusion equation is the *Trotter-Suzuki-Matrix-Exponential approach*, which has the advantage that it is unconditionally stable. Furthermore, besides the parameter estimation methods *simulated annealing* based on the Metropolis Monte Carlo scheme and *adaptive regular grid search* other parameter estimation methods could be implemented within the bottom-up modelling approach for comparison and faster convergence to the optimum. Parameter validation methods such as parameter sensitivity analysis and parameter identifiability analysis methods can be used to identify key parameters of the virtual infection model and might improve the modelling and simulation process of the bottom-up approach.

To date, only temporal dynamics are used as input for the bottom-up approach. This input data pool could be extended in the future to other types of experimental data, such as image data, which would provide spatial information and would be especially valuable for spatial simulations using the ABM. Furthermore, large amounts of gene-expression data exist that could on the one hand provide additional information to the virtual infection model. On the other hand, the bottom-up model might help in assigning new gene functions by fitting the model to data of various experimental conditions.

Currently, the spatial environment within the ABM is represented by a cube, which is reasonable, since whole-blood infection assays are performed in a slowly rotating tube, where blood flow is neglected. However, in order to bring these studies closer to the clinical situation a more sophisticated environment could be implemented. For example, a torus or a more complex branched system with periodic boundaries can be used to represent blood vessels. The implementation of such a vascular system can be realized by implementing the respective spatial structures and blood flow. Furthermore, the simulation of blood flow within such a vessel system would require the implementation of physical forces, such as flow and shear forces. This could be realized by adding a mechanical flow field layer to the ABM, where the Navier-Stokes equation, which accounts for flow and shear forces, is solved using numerical approaches from computational fluid dynamics [160–163]. Since flow forces act on cell movement and molecule diffusion the implementation of appropriate mechanisms that can handle these forces within the ABM would be required. Moreover, this vascular system could be embedded within a tissue environment, which would allow for simulation of tissue invasion by fungal cells and immune cell recruitment and migration within the tissue. Here, a well-conceived handling of boundary conditions between tissue and blood vessels that allows for molecule diffusion and blood flow needs to be developed.

Furthermore, the bottom-up modelling approach that was developed within my PhD project can be applied to various other research questions. For example, it provides the possibility to investigate infection and immune processes in whole blood regarding various pathogens, such as the gram-positive coccal bacterium *Staphylococcus aureus*, which is a human commensal and resides predominantly on the human skin and mucosal surfaces [17, 164]. It is a major human pathogen and the leading cause for bacteremia. In industrial countries, per year 10 to 30 people out of 100 000 suffer from *S. aureus* bacteremia [164]. Moreover, neutropenia correlates not only with a higher risk for *Candida* infections but also for *Staphylocoocus* and *Streptococcus* infections [165–167].

Besides simulating whole-blood infections with other pathogens the bottom-up approach provides also the possibility to model and simulate completely different biological systems such as the formation of biofilms on surfaces of medical devices, like catheters, but also on epithelial cells. It could also be applied in the context of intraspecies interaction as is

the case in the human microbiota, which highly interacts with the human immune system and contributes to health and disease to a major extent. Both systems – biofilms and microbiota – are also very important in the context of fungal colonization and infection, since *Candida* spp. colonize large fractions of the world population [16–18] and cause severe bloodstream infections by entering blood vessels through catheters. Modelling these biological systems will also rely on extensions of the ABM with regard to molecule diffusion and blood flow and will further require the implementation of specific biological structures.

11. *Aspergillus fumigatus* LUNG INFECTION

Every human individual inhales several hundreds up to thousands airborne conidia of *A. fumigatus* every day [43]. Unnoticed, the immune system is able to clear the lung from the conidia in healthy individuals, while this fails in immunocompromised individuals, causing life-threatening infections. Research on the infection dynamics in the lung under physiological conditions poses a great challenge, since appropriate microscopy techniques that capture infection dynamics *in vivo* are not available to date. Even *in vitro* experiments cannot easily be conducted, since alveolar epithelial cells of type I, which make up approximately 95 % of the alveolar surface, are challenging to cultivate. Furthermore, natural daily inhalation and experimentally administered infection doses differ by several orders of magnitude and, typically, experiments are conducted using mice, which exhibit a different lung physiology and different cellular composition. In order to assess the impact of various infection doses as well as morphological differences in the murine and human lung during the infection process with *A. fumigatus* we applied virtual infection modelling.

First, we established a model using *evolutionary game theory* (EGT) on graphs that incorporates several immune mechanisms, such as the complement system, AM and neutrophils, and simulates the immune response in a broader context. Secondly, we extended a previously established hABM of a realistic to-scale representation of the human alveolus by Pollmächer and Figge [139, 140]. We simulated the infection process in a very detailed fashion in human and mice and focused on the immune response by *alveolar macrophages* (AM) as well as chemokine secretion and diffusion.

EVOLUTIONARY GAME THEORY DECIPHERS KEY IMMUNE PROCESSES AGAINST *A. fumigatus* FOR VARIOUS INFECTION DOSES AND IMMUNE CONDITIONS

The infection-inflammation process during *A. fumigatus* lung infections involves various immune effector mechanisms and cell types. Each of these processes relies on several rates that are often neither known from literature nor accessible in experiment, leading to the generation of unreliable predictions during modelling and simulation. Nevertheless, in EGT model parameters can be elegantly condensed, which still allows capturing characteristic features of the infection-inflammation process.

In the first study within the topic of *A. fumigatus* lung infections (see Figure 6 lower panel), we developed an EGT model, where fungal cells are simulated as individual entities that are able to adapt different morphologies, such as resting and swollen conidia as well as hyphae. These morphologies resemble strategies in the context of game theory and are assigned with certain abilities of the fungal cells. For example swollen conidia and hyphae can obtain more nutrients than resting conidia, which increases its reproductive fitness, while they are also better recognized by the immune system and, thus, face a stronger immune response. Hence, individual fungal cells choose their strategy in order to increase their payoff, which represents the utility they gain from higher nutrient availability and loose by stronger immune attacks. For each of the considered immune

components we created a game, where fungal cells play against each other under the pressure of the immune system. We modelled the interaction with the complement system in *Game I*, with alveolar macrophages in *Game II* and with neutrophils in *Game III*. During the simulation of these games the strategies of fungal cells evolve over iterative evolutionary steps. Thereby, fungal cells choose their strategy in order to optimize their reproductive fitness. However, strategies are also influenced by random mutation and adaptation events.

This approach allowed incorporation of several aspects of the immune response by simultaneously keeping the number of unknown parameters in the model feasible and simulation run times low. We used this model to simulate the counterplay of human immune processes against *A. fumigatus* under various infection doses and immune conditions. Each game was simulated for several parameters, such as the strength of the immune mechanisms. Furthermore, the infection outcome was quantified by calculation of an *infection score*, which considers the fractions of fungal morphologies when the steady state is reached.

First, we simulated the interaction with the complement system in Game I, which is at a time scale of the first seconds and minutes after entry of the condidia in the human lung. Therefore, fungal cell can only be resting or swollen, where the latter ones have a higher nutrient acquisition ability and a higher virulence but also attract stronger immune responses. As expected, weaker complement responses and higher nutrient availability led to increased fractions of swollen conidia. Next, in Game II we simulated the interaction of fungal cells under the immune response of AM, where we distinguished cases of low, moderate and high AM activity. Here, fungal cells could not only be resting and swollen, but also in a hyphal state. We found that for low infection doses AM were able to clear the infection, if AM activity was sufficiently high, which was not the case in high infection doses due to the inability of AM to phagocytose hyphae. Finally, in Game III fungal strategies evolved under the immune response by neutrophils, which could for most parameters clear the infection in low infection doses, given a minimum neutrophil recruitment. For high infection doses sufficiently high neutrophil activity and recruitment were crucial for fungal clearance. Interestingly, reduced neutrophil activity could be, to some extend, compensated by an increased recruitment. However, it is known that higher neutrophil recruitment contributes also to increased host cell damage [168]. Furthermore, AM regulate the immune response also during later stages by shutting down inflammation and by the initiation of tissue recovery at sites of damage [169–171].

In silico INFLAMMATORY CASCADE RECONCILES CONTRADICTORY VIEW ON ALVEOLAR MACROPHAGES IN THE LITERATURE

Immune effector mechanisms against infectious agents establish an inflammatory milieu that activates signalling cascades and leads to recruitment and activation of other players along the cascade of the immune system. In order to account for this inflammatory cascade we aligned the afore described games in a temporal sequence. Thereby, each game relied on the inflammation strength caused by the previous game, which is determined by the fractions of fungal cells with a certain morphology and the strength of the immune system against these morphologies.

The inflammation caused by the complement system in Game I determined directly the activity of AM in Game II. As expected, high AM activities led to an improved

fungal clearance in both, low and high infection dose scenarios. However, only in low infection doses AM with high activity were able to clear the infection completely, while this failed under high infection doses. Furthermore, AM with weak activity induced higher inflammatory signals, leading to increased neutrophil recruitment. As already the single-game simulation showed, neutrophils are able to clear the infection in almost all cases of low infection scenarios and lower neutrophils activation was compensated by higher recruitment. In high infection doses a minimum neutrophil activity was required for infection clearance. The regulatory role of AM during high infection doses was pronounced by the fact that AM with low activity caused higher inflammation and, thus, more neutrophil recruitment, which turned out to be beneficial for the infection clearance.

These results reconciled an existing contradictory view in the literature on the role of AM during the immune response against *A. fumigatus* in the lung. As AM are resident immune cells in the lung [172] they are the first immune cells to encounter inhaled conidia. Furthermore, it is well known that an impaired AM function is associated with an increased risk for invasive infections [173]. On the contrary, Mircescu *et al.* [174] performed experimental aspergillosis studies in mice and came to the conclusion that AM are not important, while neutrophils are the major players during fungal clearance.

Surprisingly, these contradictory observations are both in line with our results. We found that under low infection doses AM where able to clear the lung from the inhaled conidia by themselves, while under high infection doses their role switches towards a regulatory function. This regulatory function involves formation of an inflammatory milieu to recruit neutrophils from the blood stream to the site of infection, since they feature a broader spectrum of defence mechanisms than AM, especially, in response to hyphae. Mircescu *et al.* [174] administered infection doses in mice experiments that exceeded daily inhalation by several orders of magnitude. In line with our results, they observed that under high infection doses mainly neutrophils contribute to phagocytosis of *A. fumigatus*. Furthermore, our results indicate that during the normal daily inhalation, AM clear the lung from the inhaled conidia, which is in line with the observation that AM impairment increases the risk for invasive mycoses. Therefore, the EGT model predicts that the different views on the role of AM are not in conflict with each other, but rather describe the infection scenario under different infection doses.

Realistic to-scale hybrid agent-based modelling predicts chemokine properties in human and mice

Mice are the most commonly used model organism to investigate pulmonary aspergillosis. Besides differences in the lung morphometry also infection doses of natural inhalation in humans and experimentally administered doses in mice differ by several orders of magnitude. However, little is known to date concerning the comparability and transferability of experimental aspergillosis models in mice to the human system. We addressed this issue in the second publication within the topic of *A. fumigatus* infection (see Figure 6 lower panel).

Therefore, we adapted a previously established hABM of a realistic to-scale representation of the human alveolus by Pollmächer and Figge [139, 140] to the murine system. This model incorporates various cellular structures of the alveoli and the immune response by AM as well as chemokine secretion and diffusion, which we screened for physiological relevant parameter ranges. This allowed comparative analyses with respect to the different

lung physiology and infection doses. In our studies, we accounted for the actual *fungal burden* that reaches the alveoli given a certain infection dose.

First, we addressed the case of low fungal burden, where only one conidium is present in the alveolus. Here, we predict that optimal chemokine parameters, *i.e.* diffusion coefficient D and chemokine secretion by AEC s_{AEC} are are slightly higher in mice, compared to human. However, the ratio of chemokine parameters for both organisms are in agreement with the observation by Pollmächer and Figge [140] that a low ratio between diffusion coefficient and secretion rate leads to more efficient infection clearance. Furthermore, we found that this also holds true for mice, since this ratio allows maintenance of a pronounced chemokine gradient in the alveolus, while faster chemokine diffusion or lower secretion would result in a weaker gradient.

A. fumigatus INFECTION IS MORE EFFICIENTLY CLEARED IN MICE FOR NATURAL AND EXPERIMENTAL INFECTION DOSES

Typically, in experiment much higher infection doses compared to daily inhalation doses are administered, which leads to higher fungal burdens and, thus, higher alveolar occupation numbers in the alveoli. Therefore, in this second study within the topic of *A. fumigatus* lung infections (see Figure 6 lower panel), we further simulated the infection in human and mouse alveoi with more than one conidium per alveolus. Here, we observed in general higher infection scores compared to the case of low fungal burden. Similarly, low chemokine diffusion and high secretion led to more efficient fungal clearance, while higher chemokine diffusion and lower chemokine secretion led to deteriorated infection scores.

Similarly to low fungal burdens, a low ratio of chemokine diffusion and secretion contributed to more efficient fungal clearance. Interestingly, we found that in very high alveolar occupation numbers of more than four conidia per alveolus, which can arise due to non-uniform distributions of conidia during intranasal administration in liquid solution, the human system was more efficient in infection clearance. Contrary to the previous observation that the higher efficiency in mice is due to the shorter migration distances, in the limit of high fungal burdens we observed a more important role of the chemokine profile. For four and more conidia in the relatively small murine alveolus, chemokine is secreted by all AEC leading to a uniform chemokine distribution in the alveolus and, thus, inefficient random walk migration of AM.

The number of alveoli in the human lung outnumbers the number of alveoli in the murine lung by two order of magnitude and the surface area of human alveoli is approximately 20 times larger compared to murine alveoli. This is why the alveolar occupation number is not directly related to the fungal burden. Thus, we performed a statistical analysis that relates the alveolar occupation number to the fungal burden, which allows to compare the infection outcome for the same fungal burden in human and mice. We found that over a broad range of fungal burdens, including natural and experimental infection doses, the infection clearance was in most cases more efficient in mice.

Higher alveolar occupation numbers and non-optimal chemokine parameters increased the infection score values higher than 0.05, *i.e.* in more than 5% of all simulations the alveolus could not be cleared from the conidia. These undetected conidia pose the risk of germination and invasion in real patients, highlighting the importance of a well-established chemokine gradient and functional sensing by AM.

To conclude, we can state that conidia clearance seems to be more efficient in mice in relevant regimes of natural and experimental doses. Of note, results from mice experiments on the infection dynamics or treatment efficacies cannot be transferred 1:1 to the human system. It can be expected, that infection prognosis under a specific infection dose is impaired in humans and may require stronger treatments.

Perspectives on experimental validation and clinical relevance

In this theses several hypotheses could be generated by virtual infection modelling on the infection-inflammation process during *A. fumigatus* lung infections that may build the basis for future experimental studies. Both, the EGT model and the hABM rely on a spectrum of parameters that were screened in large ranges, since values from the literature were not available. Determining values or ratios of model parameters experimentally would open up new opportunities for model extensions to investigate additional aspects of the infection-inflammation process and to still generate reliable predictions.

The current EGT model comprises immune effector mechanisms of the complement system, AM as well as neutrophils and would benefit from experimental assessment of the strength of these effector mechanisms against different fungal morphologies. For example, the opsonization efficiency of different *A. fumigatus* morphologies by the complement molecules C3b and C5b could be measured and relative differences could be incorporated into Game I of the EGT model. Similarly, immune effector mechanisms of the fungal killing by alveolar macrophages and neutrophils could be experimentally assessed and incorporated in Game II and III, respectively.

Furthermore, in the EGT model we predict that the role of AM switches in an infection-dose dependent manner. However, validation of this observation remains an open issue. Therefore, confrontation assays could be performed, where AM are confronted with various infection doses and quantification of phagyocytosis and cytokine profiles could be measured. Confrontation assays of murine AM and *A. fumigatus* condia have been performend previously and phagocytosis was quantified by automated image analysis by Kraibooj *et al.* [175] and Cseresnyes *et al.* [176]. However, they did neither consider different infection doses nor cytokine secretion by AM, which could be addressed in future studies. The resulting quantities on AM dynamics could form the basis for model refinements, which is in the scope of image-based systems biology.

Furthermore, new experimental approaches, like lab-on-a-chip systems could be used to investigate chemokine parameters, surfactant properties, migration speed and directional persistence of AM and uptake of fungal cells by AEC [177–179]. Light-sheet microscopy of murine lungs could give further insights into the distribution of conidia, and neutrophils after administration of various infection doses in mice experiments.

Perspectives on model developments

Besides experimental validation of already generated predictions as outlined in the previous section, the developed virtual infection models provide also the basis for further dry-lab studies and model extensions. The current EGT model comprises the most important innate effector mechanisms against *A. fumigatus*. However, it is known that also dendritic cells initiate the activation of a T cell-mediated defence against *A. fumigatus* and Th1/Th2 dysregulation is associated with an increased risk for invasive aspergillosis

[41, 44, 173]. Therefore, the model can be extended by including various aspects of the adaptive immune response and their regulation through, for example, dendritic cells. This could be realized by incorporation of additional games that could be arranged in a network structure instead of a linear process, since innate and adaptive immune mechanisms are highly interwoven and regulate each other.

The hABM could be extended by simulating morphological changes of the fungus over time. Until now, only resting spores are considered within the model. However, especially in scenarios where AM fail to detect the conidia, time limits before the start of germination are exceeded. Therefore, swelling and hyphae formation should be considered, since virulence properties and the detection by immune cells and their effector mechanisms are very morphology specific.

Furthermore, the model can be extended by including neutrophil recruitment as well as an explicit phagocytosis model for AM, neutrophils and AEC [180], since until now only the time for first contact with the fungal cells is determined. However, this first contact does not necessarily lead to phagocytosis in reality. Thus, implementing a phagocytosis model would be essential to simulate infection dynamics. Neutrophil recruitment would rely on the simulation of chemokine secretion by AM, which could be realized by adding further molecules to the existing close-to-equidistant discretization of the three-quarter alveolus. Sensing of these molecules by the neutrophils would be implemented similar to the receptor-ligand model modeled with PDEs in AM.

Furthermore, the current hABM represents the most commonly observed alveolar morphometry, which is approximated as a three-quarter sphere. However, it is known that alveolar surfaces can adapt to various polyhedral shapes [83]. Therefore, in the future the model could be extended to other representations such as one-quarter spheres, as they make up about 44% of all alveoli in the human lung [181].

Additionally, the hABM provides also the possibility to scale up the environment to for example a whole alveolar sac to investigate the infection dynamics on tissue or even whole organ level. Since an alveolar sac comprises about 21 densely packed alveoli [83], they typically do not exhibit the rigid three-quarter shape, as currently implemented in the hABM, but rather involve several other morphometries of alveoli, which continuously change due to dynamic forces and breathing. Pollmächer and Figge [139] already simulated breathing within a single alveolus and found that this does not impact on the infection outcome with *A. fumigatus*. If this holds also true on the tissue scale could be tested in future *in silico* experiments. Simulating the infection process within these irregular alveolar shapes would require to develop an elaborate approach to calculate a close-to-equidistant grid representation for molecule diffusion along several alveoli. Furthermore, within the alveolar sac AM would be able to migrate through the Pores of Kohn and the alveolar entrance rings [182]. To sum up, these model developments would enormously increase the realism of the simulations. However, this detailed representation of alveolar morphometry as well as all consequences on the calculation of the grid-based molecule layer, numerical solution of the diffusion equation as well as AM migration along an irregular shape would also increase computational costs.

In addition, studies on lung infections using the developed virtual infection models could also be extended to other pathogens that are known to cause pulmonary infections, such as *Mycobacterium tuberculosis*, *Legionella* spp. and *Streptococcus pneumoniae* [183].

Bibliography

[1] Blackwell, M. **The fungi: 1, 2, 3 ... 5.1 million species?** In: *American journal of botany* 98.3 (2011), pp. 426–38. ISSN: 1537-2197. DOI: 10.3732/ajb.1000298.

[2] Ainsworth, G. C. **Ainsworth & Bisby's Dictionary of the Fungi**. 10th ed. Wallingford: TODO, 2008.

[3] Schmit, J. P. and Mueller, G. M. **An estimate of the lower limit of global fungal diversity**. In: *Biodiversity and Conservation* 16.1 (2007), pp. 99–111. ISSN: 0960-3115. DOI: 10.1007/s10531-006-9129-3.

[4] O'Brien, H. E., Parrent, J. L., Jackson, J. A., Moncalvo, J.-M., and Vilgalys, R. **Fungal Community Analysis by Large-Scale Sequencing of Environmental Samples**. In: *Applied and Environmental Microbiology* 71.9 (2005), pp. 5544–5550. ISSN: 0099-2240. DOI: 10.1128/AEM.71.9.5544-5550.2005.

[5] Fisher, M. C., Henk, D. A., Briggs, C. J., Brownstein, J. S., Madoff, L. C., McCraw, S. L., and Gurr, S. J. **Emerging fungal threats to animal, plant and ecosystem health**. In: *Nature* (2012). ISSN: 0028-0836. DOI: 10.1038/nature10947. arXiv: NIHMS150003.

[6] Pointing, S. B. **Feasibility of bioremediation by white-rot fungi**. In: *Applied Microbiology and Biotechnology* 57.1-2 (2001), pp. 20–33. ISSN: 01757598. DOI: 10.1007/s002530100745.

[7] Brown, G. D., Denning, D. W., Gow, N. A. R., Levitz, S. M., Netea, M. G., and White, T. C. **Hidden Killers: Human Fungal Infections**. In: *Science Translational Medicine* 4.165 (2012), pp. 1–9. ISSN: 1946-6242. DOI: 10.1126/scitranslmed.3004404. arXiv: arXiv:1011.1669v3.

[8] Köhler, J. R., Hube, B., Puccia, R., Casadevall, A., and Perfect, J. R. **Fungi that Infect Humans**. In: (2017), pp. 1–29. DOI: 10.1128/microbiolspec.FUNK-0014-2016.Correspondence.

[9] Wiemann, P. and Keller, N. P. **Strategies for mining fungal natural products**. In: *Journal of Industrial Microbiology and Biotechnology* 41.2 (2014), pp. 301–313. ISSN: 1367-5435. DOI: 10.1007/s10295-013-1366-3.

[10] Hohl, T. M., Rivera, A., and Pamer, E. G. **Immunity to fungi**. In: *Current Opinion in Immunology* 18.4 (2006), pp. 465–472. ISSN: 09527915. DOI: 10.1016/j.coi.2006.05.003.

[11] Brown, G. D., Denning, D. W., and Levitz, S. M. **Tackling Human Fungal Infections**. In: *Science* 336.6082 (2012), pp. 647–647. ISSN: 0036-8075. DOI: 10.1126/science.1222236.

[12] Erwig, L. P. and Gow, N. A. R. **Interactions of fungal pathogens with phagocytes**. In: *Nature Reviews Microbiology* 14.3 (2016), pp. 163–176. ISSN: 1740-1526. DOI: 10.1038/nrmicro.2015.21.

[13] Bianconi, E. *et al.* **An estimation of the number of cells in the human body**. In: *Annals of Human Biology* 40.6 (2013), pp. 463–471. ISSN: 0301-4460. DOI: 10.3109/03014460.2013.807878.

[14] Sender, R., Fuchs, S., and Milo, R. **Revised Estimates for the Number of Human and Bacteria Cells in the Body**. In: *PLoS Biology* 14.8 (2016), pp. 1–14. ISSN: 15457885. DOI: 10.1371/journal.pbio.1002533. arXiv: 036103.

[15] Underhill, D. M. and Iliev, I. D. **The mycobiota: interactions between commensal fungi and the host immune system**. In: *Nature Reviews Immunology* 14.6 (2014), pp. 405–416. ISSN: 1474-1741. DOI: 10.1038/nri3684.

[16] Calderone, R. A. and Clancy, C. J. **Candida and candidiasis**. Ed. by Calderone, R. A. and Clancy, C. J. 2nd ed. Washington DC: ASM Press, 2002, p. 524. ISBN: 9781555815394.

[17] Sardi, J. C. O., Scorzoni, L., Bernardi, T., Fusco-Almeida, A. M., Mendes Giannini, M. J. S., Bernardi, T., Scorzoni, L., Fusco-Almeida, A. M., and Sardi, J. C. O. **Candida species: current epidemiology, pathogenicity, biofilm formation, natural antifungal products and new therapeutic options**. In: *Journal of Medical Microbiology* 62.1 (2013), pp. 10–24. ISSN: 0022-2615. DOI: 10.1099/jmm.0.045054-0.

[18] Rodrigues, C. F., Silva, S., and Henriques, M. **Candida glabrata: a review of its features and resistance**. In: *European Journal of Clinical Microbiology & Infectious Diseases* 33.5 (2014), pp. 673–688. ISSN: 0934-9723. DOI: 10.1007/s10096-013-2009-3.

[19] Papon, N., Courdavault, V., Clastre, M., Bennett, R. J. R. R. J., and Bennett, R. J. R. R. J. **Emerging and emerged pathogenic Candida species: Beyond the Candida albicans paradigm**. In: *PLoS Pathogens* 9.9 (2013). Ed. by Heitman, J., e1003550. ISSN: 1553-7374. DOI: 10.1371/journal.ppat.1003550.

[20] Deorukhkar, S. C., Saini, S., and Mathew, S. **Non-albicans Candida Infection: An Emerging Threat.** In: *Interdisciplinary perspectives on infectious diseases* 2014 (2014), p. 615958. ISSN: 1687-708X. DOI: 10.1155/2014/615958.

[21] Lamoth, F., Lockhart, S. R., Berkow, E. L., and Calandra, T. **Changes in the epidemiological landscape of invasive candidiasis Incidence of invasive candidiasis: a research challenge**. In: *Journal of Antimicrobial Chemotherapy* 73.January (2018), pp. i4–i13. ISSN: 0305-7453. DOI: 10.1093/jac/dkx444.

[22] Sudbery, P. E. **Growth of Candida albicans hyphae.** In: *Nature Reviews Microbiology* 9.10 (2011), pp. 737–748. ISSN: 1740-1526. DOI: 10.1038/nrmicro2636.

[23] Sudbery, P. E., Gow, N., and Berman, J. **The distinct morphogenic states of Candida albicans.** English. In: *Trends in Microbiology* 12.7 (2004), pp. 317–24. ISSN: 0966-842X. DOI: 10.1016/j.tim.2004.05.008.

[24] Vila, T. V. M. and Rozental, S. **Biofilm Formation as a Pathogenicity Factor of Medically Important Fungi**. In: *Intech* 6 (2012), pp. 111–133. ISSN: 9789533070865. DOI: http://dx.doi.org/10.5772/62768. arXiv: 0803973233.

[25] Fidel, P. L. . L., Vazquez, J. A., and Sobel, J. D. **Candida glabrata: review of epidemiology, pathogenesis, and clinical disease with comparison to C. albicans**. In: *Clinical microbiology reviews* 12.1 (1999), pp. 80–96. ISSN: 0893-8512.

[26] Glöckner, A. and Cornely, O. A. **Candida glabrata - unique features and challenges in the clinical management of invasive infections**. In: *Mycoses* 58.8 (2015), pp. 445–450. ISSN: 14390507. DOI: 10.1111/myc.12348.

[27] Berman, J. and Sudbery, P. E. **Candida albicans: A molecular revolution built on lessons from budding yeast**. In: *Nature Reviews Genetics* 3.12 (2002), pp. 918–930. ISSN: 14710056. DOI: 10.1038/nrg948.

[28] Mayer, F. L., Wilson, D., Hube, B., and Article, M. **Candida albicans pathogenicity mechanisms**. In: *Virulence* 4.2 (2013), pp. 119–128. ISSN: 2150-5608. DOI: 10.4161/viru.22913.

[29] Brunke, S. and Hube, B. **Two unlike cousins: Candida albicans and C. glabrata infection strategies**. In: *Cellular Microbiology* 15.5 (2013), pp. 701–708. ISSN: 14625814. DOI: 10.1111/cmi.12091.

[30] Blankenship, J. R. and Mitchell, A. P. **How to build a biofilm: a fungal perspective**. In: *Current Opinion in Microbiology* 9.6 (2006), pp. 588–594. ISSN: 13695274. DOI: 10.1016/j.mib.2006.10.003.

[31] Nobile, C. J. and Johnson, A. D. **Candida albicans Biofilms and Human Disease**. In: *Annual Review of Microbiology* 69.1 (2015), pp. 71–92. ISSN: 0066-4227. DOI: 10.1146/annurev-micro-091014-104330.

[32] Ramage, G., Mowat, E., Jones, B., Williams, C., and Lopez-Ribot, J. **Our Current Understanding of Fungal Biofilms**. In: *Critical Reviews in Microbiology* 35.4 (2009), pp. 340–355. ISSN: 1040-841X. DOI: 10.3109/10408410903241436.

[33] Fanning, S. and Mitchell, A. P. **Fungal Biofilms**. In: *PLoS Pathogens* 8.4 (2012). Ed. by Heitman, J., e1002585. ISSN: 1553-7374. DOI: 10.1371/journal.ppat.1002585.

[34] da Silva Dantas, A., Lee, K. K., Raziunaite, I., Schaefer, K., Wagener, J., Yadav, B., and Gow, N. A. **Cell biology of Candida albicans–host interactions**. In: *Current Opinion in Microbiology* 34 (2016), pp. 111–118. ISSN: 18790364. DOI: 10.1016/j.mib.2016.08.006.

[35] Akpan, A. and Morgan, R. **Oral candidiasis**. In: *Postgraduate Medical Journal* 78.922 (2002), pp. 455–459. DOI: 10.1136/pmj.78.922.455.

[36] Cassone, A. **Vulvovaginal Candida albicans infections: Pathogenesis, immunity and vaccine prospects**. In: *BJOG: An International Journal of Obstetrics and Gynaecology* 122.6 (2015), pp. 785–794. ISSN: 14710528. DOI: 10.1111/1471-0528.12994.

[37] Kullberg, B. J. and Arendrup, M. C. **Invasive Candidiasis**. In: *New England Journal of Medicine* 373.15 (2015), pp. 1445–1456. ISSN: 0028-4793. DOI: 10.1056/NEJMra1315399.

[38] Lionakis, M. S. **New insights into innate immune control of systemic candidiasis**. In: *Medical Mycology* 52.6 (2014), pp. 555–564. ISSN: 14602709. DOI: 10.1093/mmy/myu029.

[39] Delaloye, J. and Calandra, T. **Invasive candidiasis as a cause of sepsis in the critically ill patient**. In: *Virulence* 5.1 (2014), pp. 154–162. ISSN: 21505608. DOI: 10.4161/viru.26187.

[40] Dagenais, T. R. T. and Keller, N. P. **Pathogenesis of Aspergillus fumigatus in invasive aspergillosis**. In: *Clinical Microbiology Reviews* 22.3 (2009), pp. 447–465. ISSN: 08938512. DOI: 10.1128/CMR.00055-08.

[41] Hohl, T. M. and Feldmesser, M. **Aspergillus fumigatus: Principles of pathogenesis and host defense**. In: *Eukaryotic Cell* 6.11 (2007), pp. 1953–1963. ISSN: 15359778. DOI: 10.1128/EC.00274-07.

[42] Latge, J.-P. **Aspergillus fumigatus and Aspergillosis**. In: *Clin. Microbiol. Rev.* 12.2 (1999), pp. 310–350.

[43] Van De Veerdonk, F. L., Gresnigt, M. S., Romani, L., Netea, M. G., and Latgé, J. P. **Aspergillus fumigatus morphology and dynamic host interactions**. In: *Nature Reviews Microbiology* 15.11 (2017), pp. 661–674. ISSN: 17401534. DOI: 10.1038/nrmicro.2017.90.

[44] Margalit, A. and Kavanagh, K. **The innate immune response to Aspergillus fumigatus at the alveolar surface**. In: *FEMS Microbiology Reviews* 39.5 (2015), pp. 670–687. DOI: 10.1093/femsre/fuv018.

[45] Shapiro, R. S., Robbins, N., and Cowen, L. E. **Regulatory Circuitry Governing Fungal Development, Drug Resistance, and Disease**. In: *Microbiology and Molecular Biology Reviews* 75.2 (2011), pp. 213–267. ISSN: 1092-2172. DOI: 10.1128/MMBR.00045-10.

[46] Latgé, J. P. and Beauvais, A. **Functional duality of the cell wall**. In: *Current Opinion in Microbiology* 20 (2014), pp. 111–117. ISSN: 18790364. DOI: 10.1016/j.mib.2014.05.009.

[47] Behnsen, J., Hartmann, A., Schmaler, J., Gehrke, A., Brakhage, A. A., and Zipfel, P. F. **The opportunistic human pathogenic fungus Aspergillus fumigatus evades the host complement system**. In: *Infection and Immunity* 76.2 (2008), pp. 820–827. DOI: 10.1128/IAI.01037-07.

[48] Beauvais, A., Fontaine, T., Aimanianda, V., and Latgé, J.-P. **Aspergillus cell wall and biofilm**. In: *Mycopathologia* 178.5-6 (2014). DOI: 10.1007/s11046-014-9766-0.

[49] Latgé, J.-P. **Tasting the fungal cell wall**. In: *Cellular Microbiology* 12.7 (2010), pp. 863–872. ISSN: 14625814. DOI: 10.1111/j.1462-5822.2010.01474.x.

[50] Chaplin, D. D. **Overview of the Immune Response**. In: *Journal of Allergy and Clinical Immunology* 5.2 (2010), pp. 1–34. ISSN: 22124152. DOI: 10.1016/B978-0-08-046884-6.00601-1. arXiv: NIHMS150003.

[51] Turvey, S. E. and Broide, D. H. **Innate immunity**. In: *Journal of Allergy and Clinical Immunology* 125.2 SUPPL. 2 (2010), S24–S32. ISSN: 00916749. DOI: 10.1016/j.jaci.2009.07.016.

[52] Murphy, K. **Janeway's Immunobiology**. 8th ed. New York, NY, USA: y Garland Science, Taylor & Francis Group, LLC, 2012. ISBN: 9780815342434.

[53] Merle, N. S., Church, S. E., Fremeaux-Bacchi, V., and Roumenina, L. T. **Complement system part I - molecular mechanisms of activation and regulation**. In: *Frontiers in Immunology* 6.JUN (2015), pp. 1–30. ISSN: 16643224. DOI: 10.3389/fimmu.2015.00262.

[54] Mathern, D. R. and Heeger, P. S. **Molecules great and small: The complement system**. In: *Clinical Journal of the American Society of Nephrology* 10.9 (2015), pp. 1636–1650. ISSN: 1555905X. DOI: 10.2215/CJN.06230614.

[55] Merle, N. S., Noe, R., Halbwachs-Mecarelli, L., Fremeaux-Bacchi, V., and Roumenina, L. T. **Complement system part II: Role in immunity**. In: *Frontiers in Immunology* 6.May (2015), pp. 1–26. ISSN: 16643224. DOI: 10.3389/fimmu.2015.00257.

[56] Trouw, L. A. and Daha, M. R. **Role of complement in innate immunity and host defense**. In: *Immunology Letters* 138.1 (2011), pp. 35–37. ISSN: 01652478. DOI: 10.1016/j.imlet.2011.02.014.

[57] Rodríguez De Córdoba, S., Esparza-Gordillo, J., Goicoechea De Jorge, E., Lopez-Trascasa, M., and Sánchez-Corral, P. **The human complement factor H: Functional roles, genetic variations and disease associations**. In: *Molecular Immunology* 41.4 (2004), pp. 355–367. ISSN: 01615890. DOI: 10.1016/j.molimm.2004.02.005.

[58] Carroll, M. V. and Sim, R. B. **Complement in Health and Disease**. In: *Advanced Drug Delivery Reviews* 63 (2011), 965–975 Contents. ISSN: 0169409X. DOI: 10.1016/B978-012455900-4/50273-7.

[59] Walport, M. J. **Complement - First of Two Parts**. In: *The New England Journal of Medicine* 344.14 (2001), pp. 1058–1066.

[60] Schwartzberg, L. S. **Neutropenia: Etiology and pathogenesis**. In: *Clinical Cornerstone* 8 (2006), S5–S11. ISSN: 10983597. DOI: 10.1016/S1098-3597(06)80053-0.

[61] Mayadas, T. N., Cullere, X., and Lowell, C. A. **The Multifaceted Functions of Neutrophils**. In: *Annual Review of Pathology: Mechanisms of Disease* 9.1 (2014), pp. 181–218. ISSN: 1553-4006. DOI: 10.1146/annurev-pathol-020712-164023.

[62] Soehnlein, O., Steffens, S., Hidalgo, A., and Weber, C. **Neutrophils as protagonists and targets in chronic inflammation**. In: *Nature Reviews Immunology* 17.4 (2017), pp. 248–261. ISSN: 14741741. DOI: 10.1038/nri.2017.10.

[63] Medzhitov, R., Preston-Hurlburt, P., and Janeway Jr, C. A. **A human homologue of the Drosophila Toll protein signals activation of adaptive immunity**. In: *Nature* 388.July (1997), pp. 6–9.

[64] Medzhitov, R. and Janeway Jr, C. A. **Innate immunity: impact on the adaptive immune response**. In: *Current Opinion in Immunology* 9.1 (1997), pp. 4–9. ISSN: 0952-7915. DOI: http://dx.doi.org/10.1016/S0952-7915(97)80152-5.

[65] Bonilla, F. A. and Oettgen, H. C. **Adaptive immunity**. In: *Journal of Allergy and Clinical Immunology* 125.2 SUPPL. 2 (2010), S33–S40. ISSN: 00916749. DOI: 10.1016/j.jaci.2009.09.017. arXiv: NIHMS150003.

[66] Späth, P. J. **Structure and function of immunoglobulins**. In: *Journal of Allergy and Clinical Immunology* 125.2 (2010), S41–S52. ISSN: 13850229. DOI: 10.1023/A:1009899803032. arXiv: NIHMS150003.

[67] Bousfiha, A. *et al.* **The 2017 IUIS Phenotypic Classification for Primary Immunodeficiencies**. In: *Journal of Clinical Immunology* 38.1 (2018), pp. 129–143. ISSN: 15732592. DOI: 10.1007/s10875-017-0465-8.

[68] Chinen, J. and Shearer, W. T. **Secondary immunodeficiencies, including HIV infection.** In: *The Journal of allergy and clinical immunology* 125.2 Suppl 2 (2010), pp. 195–203. ISSN: 1097-6825. DOI: 10.1016/j.jaci.2009.08.040.

[69] Notarangelo, L. D. **Primary immunodeficiencies**. In: *Journal of Allergy and Clinical Immunology* 125.2 SUPPL. 2 (2010), S182–S194. ISSN: 00916749. DOI: 10.1016/j.jaci.2009.07.053.

[70] Delano, M. J. and Ward, P. A. **The immune system's role in sepsis progression, resolution, and long-term outcome**. In: *Immunological Reviews* 274.1 (2016), pp. 330–353. ISSN: 1600065X. DOI: 10.1111/imr.12499.

[71] Delano, M. J. and Ward, P. A. **Sepsis-induced immune dysfunction: Can immune therapies reduce mortality?** In: *Journal of Clinical Investigation* 126.1 (2016), pp. 23–31. ISSN: 15588238. DOI: 10.1172/JCI82224.

[72] Zeidler, C., Boxer, L., Dale, D. C., Freedman, M. H., Kinsey, S., and Welte, K. **Management of Kostmann syndrome in the G-CSF era**. In: *British Journal of Haematology* 109.3 (2000), pp. 490–495. ISSN: 0007-1048. DOI: 10.1046/j.1365-2141.2000.02064.x.

[73] Crawford, J., Dale, D. C., and Lyman, G. H. **Chemotherapy-Induced Neutropenia: Risks, Consequences, and New Directions for Its Management**. In: *Cancer* 100.2 (2003), pp. 228–237. ISSN: 0008-543X. DOI: 10.1002/cncr.11882.

[74] Berliner, N., Horwitz, M., and Loughran, T. P. **Congenital and acquired neutropenia.** In: *Hematology. American Society of Hematology. Education Program* 2004.1 (2004), pp. 63–79. ISSN: 1520-4391. DOI: 10.1182/asheducation-2004.1.63.

[75] Gibson, C. and Berliner, N. **How we evaluate and treat neutropenia in adults**. In: *Blood* 124.8 (2014), pp. 1251–1258. ISSN: 1935-469X. DOI: 10.1200/JOP.091087.

[76] Duggan, S., Leonhardt, I., Hünniger, K., and Kurzai, O. **Host response to Candida albicans bloodstream infection and sepsis.** In: *Virulence* 6.4 (2015), pp. 316–26. ISSN: 2150-5608. DOI: 10.4161/21505594.2014.988096.

[77] Luo, S., Skerka, C., Kurzai, O., and Zipfel, P. F. **Complement and innate immune evasion strategies of the human pathogenic fungus Candida albicans**. In: *Molecular Immunology* 56.3 (2013), pp. 161–169. ISSN: 01615890. DOI: 10.1016/j.molimm.2013.05.218.

[78] Netea, M. G., B Joosten, L. A., M van der Meer, J. W., Kullberg, B.-J. J., Veerdonk, F. L. van de, Joosten, L. A., Meer, J. W. van der, Kullberg, B.-J. J., and Veerdonk, F. L. van de. **Immune defence against Candida fungal infections**. In: *Nature Reviews Immunology* 15.10 (2015), pp. 630–642. ISSN: 1474-1741. DOI: 10.1038/nri3897.

[79] Schmidt, S., Tramsen, L., and Lehrnbecher, T. **Natural killer cells in antifungal immunity**. In: *Frontiers in Immunology* 8.NOV (2017), pp. 1–10. ISSN: 16643224. DOI: 10.3389/fimmu.2017.01623.

[80] Zipfel, P. F., Skerka, C., Kupka, D., and Luo, S. **Immune escape of the human facultative pathogenic yeast Candida albicans: The many faces of the Candida Pra1 protein**. In: *International Journal of Medical Microbiology* 301.5 (2011), pp. 423–430. ISSN: 14384221. DOI: 10.1016/j.ijmm.2011.04.010.

[81] Hernández-Chávez, M., Pérez-García, L., Niño-Vega, G., and Mora-Montes, H. **Fungal Strategies to Evade the Host Immune Recognition**. In: *Journal of Fungi* 3.4 (2017), p. 51. ISSN: 2309-608X. DOI: 10.3390/jof3040051.

[82] Seider, K. *et al.* **Immune evasion, stress resistance, and efficient nutrient acquisition are crucial for intracellular survival of Candida glabrata within macrophages**. In: *Eukaryotic Cell* 13.1 (2014), pp. 170–183. ISSN: 15359778. DOI: 10.1128/EC.00262-13.

[83] Weibel, E. R. **Morphometry of the Human Lung**. Elsevier Science, 2013, p. 164. ISBN: 1483225798.

[84] Brakhage, A. A., Bruns, S., Thywissen, A., Zipfel, P. F., and Behnsen, J. **Interaction of phagocytes with filamentous fungi**. In: *Current Opinion in Microbiology* 13.4 (2010), pp. 409–415. ISSN: 13695274. DOI: 10.1016/j.mib.2010.04.009.

[85] McCormick, A., Loeffler, J., and Ebel, F. **Aspergillus fumigatus: Contours of an opportunistic human pathogen**. In: *Cellular Microbiology* 12.11 (2010), pp. 1535–1543. ISSN: 14625814. DOI: 10.1111/j.1462-5822.2010.01517.x.

[86] Westerhoff, H. V., Winder, C., Messiha, H., Simeonidis, E., Adamczyk, M., Verma, M., Bruggeman, F. J., and Dunn, W. **Systems Biology: The elements and principles of Life**. In: *FEBS Letters* 583.24 (2009), pp. 3882–3890. ISSN: 00145793. DOI: 10.1016/j.febslet.2009.11.018.

[87] Vidal, M. **A unifying view of 21st century systems biology**. In: *FEBS Letters* 583.24 (2009), pp. 3891–3894. ISSN: 00145793. DOI: 10.1016/j.febslet.2009.11.024.

[88] Kesić, S. **Systems biology, emergence and antireductionism**. In: *Saudi Journal of Biological Sciences* 23.5 (2016), pp. 584–591. ISSN: 1319562X. DOI: 10.1016/j.sjbs.2015.06.015.

[89] Kitano, H. **Systems biology: a brief overview.** In: *Science (New York, N.Y.)* 295.5560 (2002), pp. 1662–4. ISSN: 1095-9203. DOI: 10.1126/science.1069492.

[90] Aderem, A. **Systems biology: Its Practice and Challenges.** In: *Cell* 121.4 (2005), pp. 511–513. DOI: 10.1016/j.cell.2005.04.020.

[91] Ideker, T., Galitski, T., and Hood, L. **A new approach to decoding life: systems biology**. In: *Annu Rev Genomics Hum Genet* 2 (2001), pp. 343–372. DOI: 10.1146/annurev.genom.2.1.343.

[92] Siegfried, R. **Modeling and simulation of complex systems : a framework for efficient agent-based modeling and simulation**. ISBN: 3658075287.

[93] Kaderali, L. and Thiel, V. **Systems biology of viral infections**. In: *Virus Research* 218.1 (2016).

[94] Horn, F., Heinekamp, T., Kniemeyer, O., Pollmächer, J., Valiante, V., and Brakhage, A. A. **Systems biology of fungal infection.** In: *Frontiers in Microbiology* 3 (2012), p. 108. ISSN: 1664-302X. DOI: 10.3389/fmicb.2012.00108.

[95] An, G., Mi, Q., Dutta-Moscato, J., and Vodovotz, Y. **Agent-based models in translational systems biology**. In: *Wiley Interdisciplinary Reviews: Systems Biology and Medicine* 1.2 (2009), pp. 159–171. DOI: 10.1002/wsbm.45. arXiv: NIHMS150003.

[96] Vodovotz, Y., Csete, M., Bartels, J., Chang, S., and An, G. **Translational systems biology of inflammation and healing**. In: *PLoS Computational Biology* 4.4 (2008). ISSN: 10671927. DOI: 10.1111/j.1524-475X.2009.00566.x. arXiv: NIHMS150003.

[97] Sbalzarini, I. **Modeling and simulation of biological systems from image data**. In: *Bioessays* (2013), pp. 482–490. DOI: 10.1002/bies.201200051.

[98] Fonoberova, M., Fonoberov, V. A., and Mezić, I. **Global sensitivity/uncertainty analysis for agent-based models**. In: *Reliability Engineering and System Safety* 118 (2013), pp. 8–17. ISSN: 09518320. DOI: 10.1016/j.ress.2013.04.004.

[99] DiStefano, J. **Dynamic systems biology modeling and simulation**. Academic Press, 2013. ISBN: 978-0-12-410411-2. DOI: 10.1007/s13398-014-0173-7.2. arXiv: 9809069v1 [arXiv:gr-qc].

[100] Fisher, J., Harel, D., and Henzinger, T. A. **Biology as reactivity**. In: *Communications of the ACM* 54.10 (2011), p. 72. ISSN: 00010782. DOI: 10.1145/2001269.2001289.

[101] Rabin, M. O. **Probabilistic automata**. In: *Information and Control* 6.3 (1963), pp. 230–245. ISSN: 00199958. DOI: 10.1016/S0019-9958(63)90290-0.

[102] Bonabeau, E. **Agent-based methods and techniques for simulating human systems**. In: *Proceedings of the National Academy of Sciences of the USA* 99.10 (2002), pp. 7280–7287. ISSN: 00278424. DOI: 10.1073/pnas.082080899.

[103] Rapaport, D. **The Art of Molecular Dynamics Simulation**. Vol. 2. 2004, p. 549. ISBN: 0521825687. DOI: 10.2277/0521825687.

[104] Bauer, A. L., Beauchemin, C. A. A., and Perelson, A. S. **Agent-based modeling of host–pathogen systems: The successes and challenges**. In: *Information Sciences* 179.10 (2009), pp. 1379–1389. DOI: 10.1016/j.ins.2008.11.012.

[105] Bernaschi, M. and Castiglione, F. **Design and implementation of an immune system simulator**. In: *Computers in Biology and Medicine* 31.5 (2001), pp. 303–331. ISSN: 0010-4825. DOI: 10.1016/S0010-4825(01)00011-7.

[106] Kleinstein, S. H. and Seiden, P. E. **Simulating the immune system**. In: *Computer Simulations* (2000).

[107] Meier-Schellersheim, M. and Mack, G. **SIMMUNE, a tool for simulating and analyzing immune system behavior**. In: (2008), pp. 1–23. ISSN: 17417007. DOI: 10.1186/1741-7007-11-96. arXiv: 9903017 [cs].

[108] Meier-Schellersheim, M., Fraser, I., and Klauschen, F. **Multi-scale modeling in cell biology**. In: *Wiley interdisciplinary reviews. Systems biology and medicine* 1.1 (2009), pp. 4–14. ISSN: 1939-5094. DOI: 10.1002/wsbm.33.Multi-scale.

[109] Mata, J. and Cohn, M. **Cellular automata-based modeling program: Synthetic immune system**. In: *Immunological Reviews* 216.1 (2007), pp. 198–212. ISSN: 01052896. DOI: 10.1111/j.1600-065X.2007.00511.x.

[110] Wendelsdorf, K. V., Alam, M., Bassaganya-Riera, J., Bisset, K., Eubank, S., Hontecillas, R., Hoops, S., and Marathe, M. **Enteric immunity simulator: A tool for in silico study of gastroenteric infections**. In: *IEEE Transactions on Nanobioscience* 11.3 (2012), pp. 273–288. DOI: 10.1109/TNB.2012.2211891. arXiv: NIHMS150003.

[111] Warrender, C., Forrest, S., and Segel, L. **Homeostasis of peripheral immune effectors**. In: *Bulletin of Mathematical Biology* 66.6 (2004), pp. 1493–1514. DOI: 10.1016/j.bulm.2004.02.003.

[112] Warrender, C., Forrest, S., and Koster, F. **Modeling intercellular interactions in early Mycobacterium infection**. In: *Bulletin of Mathematical Biology* 68.8 (2006), pp. 2233–2261. arXiv: 33750735048.

[113] Shapiro, M., Duca, K. A., Lee, K., Delgado-Eckert, E., Hawkins, J., Jarrah, A. S., Laubenbacher, R., Polys, N. F., Hadinoto, V., and Thorley-Lawson, D. A. **A virtual look at Epstein-Barr virus infection: Simulation mechanism**. In: *Journal of Theoretical Biology* 252.4 (2008), pp. 633–648. DOI: 10.1016/j.jtbi.2008.01.032.

[114] Polys, N. F., Bowman, D. A., North, C., Laubenbacher, R., and Duca, K. **PathSim visualizer: an Information-Rich Virtual Environment Framework for Systems Biology**. In: *Proceedings of the ninth international conference on 3D Web technology* (2004), p. 7. ISSN: 15529886. DOI: 10.1145/985040.985042.

[115] Sklar, E. **NetLogo, a Multi-agent Simulation Environment**. In: *Artificial Life* 13.3 (2007), pp. 303–311. DOI: 10.1162/artl.2007.13.3.303.

[116] Tyc, K. M. **Modeling Dissemination of Pathogenic Fungi within a Host: A Cartoon for the Interactions of Two Complex Systems**. In: *Journal of Computer Science & Systems Biology* S1 (2011), pp. 1–8. ISSN: 09747230. DOI: 10.4172/jcsb.S1-001.

[117] Tokarski, C., Hummert, S., Mech, F., Figge, M. T., Germerodt, S., Schroeter, A., and Schuster, S. **Agent-based modeling approach of immune defense against spores of opportunistic human pathogenic fungi**. In: *Frontiers in Microbiology* 3.129 (2012), p. 129. ISSN: 1664-302X. DOI: 10.3389/fmicb.2012.00129.

[118] Neumann, J. von and Morgenstern, O. **Theory of Games and Economic Behavior**. 2nd. Princeton: Princeton University Press, 1944, p. 674. ISBN: 978-0691130613. DOI: 10.2307/j.ctt1r2gkx.

[119] Szabó, G. and Fáth, G. **Evolutionary games on graphs**. In: *Physics Reports* 446.4-6 (2007), pp. 97–216. ISSN: 03701573. DOI: 10.1016/j.physrep.2007.04.004. arXiv: 0607344 [cond-mat].

[120] Nash, J. F. **Equilibrium points in n-person games**. In: *Proceedings of the National Academy of Sciences* 36.1 (1950), pp. 48–49. ISSN: 0027-8424. DOI: 10.1073/pnas.36.1.48. arXiv: 1701.01724.

[121] Epstein, J. M. **Zones of Cooperation in Demographic Prisoner's Dilemma**. In: *Complexity* 4.2 (1998), pp. 36–48.

[122] Lieberman, E., Hauert, C., and Nowak, M. a. **Evolutionary dynamics on graphs.** In: *Nature* 433.7023 (2005), pp. 312–316. ISSN: 0028-0836. DOI: 10.1038/nature03204. arXiv: 0601031 [arXiv:q-bio.PE].

[123] Ohtsuki, H. and Nowak, M. a. **The replicator equation on graphs**. In: *Journal of Theoretical Biology* 243.1 (2006), pp. 86–97. ISSN: 00225193. DOI: 10.1016/j.jtbi.2006.06.004.

[124] Pollmächer, J., Timme, S., Schuster, S., Brakhage, A. A., Zipfel, P. F., and Figge, M. T. **Deciphering the counterplay of Aspergillus fumigatus infection and host inflammation by evolutionary games on graphs**. In: *Scientific Reports* 6.May (2016), p. 27807. ISSN: 2045-2322. DOI: 10.1038/srep27807.

[125] Fehler, M. "Kalibrierung Agenten-basierter Simulationen". PhD thesis. Julius-Maximilians-University Würzburg, 2010.

[126] Ashyraliyev, M., Fomekong-Nanfack, Y., Kaandorp, J. A., and Blom, J. G. **Systems biology: Parameter estimation for biochemical models**. In: *The FEBS journal* 276.4 (2008), pp. 886–902. DOI: 10.1111/j.1742-4658.2008.06844.x.

[127] Powell, M. J. D. **Direct search algorithms for optimization calculations**. In: *Ada Numerica* 287-336 (1998).

[128] Hooke, R. and Jeeves, T. A. **"Direct Search" Solution of Numerical and Statistical Problems**. In: *Journal of the ACM* 8.2 (1961), pp. 212–229. DOI: 10.1145/321062.321069.

[129] Nelder, J. A. and Mead, R. **A Simplex Method for Function Minimization**. In: *The Computer Journal* 7.4 (1965), pp. 308–313. ISSN: 0010-4620. DOI: 10.1093/comjnl/7.4.308.

[130] Kirkpatrick, S., Gelatt, C. D., and Vecchi, M. P. **Optimization by Simulated Annealing**. In: *Science* 220.4598 (1983), pp. 671–680. DOI: 10.1126/science.220.4598.671.

[131] Storn, R. and Price, K. **Differential evolution–A simple and efficient heuristic for global optimization over continuous spaces**. In: *Journal of Global Optimization* 11.4 (1997), pp. 341–359.

[132] Ólafsson, S. **Two-stage nested partitions method for stochastic optimization**. In: *Methodology and Computing in Applied Probability* 6.1 (2004), pp. 5–27. DOI: 10.1023/B:MCAP.0000012413.54789.cc.

[133] Kennedy, J. and Eberhart, R. **Particle swarm optimization**. In: *Proceedings IEEE International Conference on Neural Networks, 1995.* 4 (1995), 1942–1948 vol.4. DOI: 10.1109/ICNN.1995.488968. arXiv: 9780201398298.

[134] Rodriguez-Fernandez, M., Mendes, P., and Banga, J. R. **A hybrid approach for efficient and robust parameter estimation in biochemical pathways**. In: *BioSystems* 83.2-3 SPEC. ISS. (2006), pp. 248–265. DOI: 10.1016/j.biosystems.2005.06.016.

[135] McClatchey, K. D. **Clinical Laboratory Medicine**. Vol. 49. 2. Lippincott Williams & Wilkins, 2003, p. 807. ISBN: 0683307517.

[136] Whibley, N. and Gaffen, S. L. **Beyond Candida albicans: Mechanisms of immunity to non-albicans Candida species.** In: *Cytokine* 76.1 (2015), pp. 42–52. ISSN: 1096-0023. DOI: 10.1016/j.cyto.2015.07.025.

[137] Gow, N. A. R. and Hube, B. **Importance of the Candida albicans cell wall during commensalism and infection.** In: *Current Opinion in Microbiology* 15.4 (2012), pp. 406–12. ISSN: 1879-0364. DOI: 10.1016/j.mib.2012.04.005.

[138] Herzog, E. L., Brody, A. R., Colby, T. V., Mason, R., and Williams, M. C. **Knowns and unknowns of the alveolus.** In: *Proceedings of the American Thoracic Society* 5.7 (2008), pp. 778–82. ISSN: 1546-3222. DOI: 10.1513/pats.200803-028HR.

[139] Pollmächer, J. and Figge, M. T. **Agent-based model of human alveoli predicts chemotactic signaling by epithelial cells during early Aspergillus fumigatus infection.** In: *PLoS One* 9.10 (2014), e111630. DOI: 10.1371/journal.pone.0111630.

[140] Pollmächer, J. and Figge, M. T. **Deciphering chemokine properties by a hybrid agent-based model of Aspergillus fumigatus infection in human alveoli.** In: *Frontiers in microbiology* 6.May (2015), p. 503. ISSN: 1664-302X. DOI: 10.3389/fmicb.2015.00503.

[141] Hünniger, K., Lehnert, T., Bieber, K., Martin, R., Figge, M. T., and Kurzai, O. **A virtual infection model quantifies innate effector mechanisms and Candida albicans immune escape in human blood**. In: *PLoS Computational Biology* 10.2 (2014). Ed. by De Boer, R. J., e1003479. DOI: 10.1371/journal.pcbi.1003479.

[142] Timme, S., Lehnert, T., Prauße, M. T. E., Hünniger, K., Leonhardt, I., Kurzai, O., and Figge, M. T. **Quantitative Simulations Predict Treatment Strategies Against Fungal Infections in Virtual Neutropenic Patients**. In: *Frontiers in Immunology* 9.April (2018), pp. 1–14. ISSN: 1664-3224. DOI: 10.3389/fimmu.2018.00667.

[143] Medyukhina, A., Timme, S., Mokhtari, Z., and Figge, M. T. **Image-based systems biology of infection.** In: *Cytometry Part A* 87.6 (2015), pp. 462–470. ISSN: 1552-4930. DOI: 10.1002/cyto.a.22638.

[144] Lehnert, T., Timme, S., Pollmächer, J., Hünniger, K., Kurzai, O., and Figge, M. T. **Bottom-up modeling approach for the quantitative estimation of parameters in pathogen-host interactions**. In: *Frontiers in Microbiology* 6.June (2015), pp. 1–15. ISSN: 1664-302X. DOI: 10.3389/fmicb.2015.00608.

[145] Praußе, M. T., Lehnert, T., Timme, S., Hünniger, K., Leonhardt, I., Kurzai, O., and Figge, M. T. **Predictive virtual infection modeling of fungal immune evasion in human whole blood**. In: *Frontiers in Immunology* 9.MAR (2018), pp. 1–13. ISSN: 16643224. DOI: 10.3389/fimmu.2018.00560.

[146] Duggan, S. *et al.* **Neutrophil activation by Candida glabrata but not Candida albicans promotes fungal uptake by monocytes.** In: *Cellular microbiology* 17.May (2015), pp. 1259–1276. ISSN: 1462-5822. DOI: 10.1111/cmi.12443.

[147] Kullberg, B. J., van 't Wout, J. W., Hoogstraten, C., Furth, R. van, Wout, J. W. t, Hoogstraten, C., and Furth, R. van. **Recombinant interferon-gamma enhances resistance to acute disseminated Candida albicans infection in mice**. In: *The Journal of Infectious Diseases* 168.2 (1993), pp. 436–443.

[148] Nagai, H., Guo, J., Choi, H., and Kurup, V. **Interferon-gamma and tumor necrosis factor-alpha protect mice from invasive aspergillosis**. In: *The Journal of infectious diseases* 172.6 (1995), pp. 1554–60. ISSN: 0022-1899.

[149] Clemons, K. V., Lutz, J. E. O. N. E., and Stevens, D. A. **Efficacy of Recombinant Gamma Interferon for Treatment of Systemic Cryptococcosis in SCID Mice**. In: *Society* 45.3 (2001), pp. 686–689. DOI: 10.1128/AAC.45.3.686.

[150] Fioredda, F. *et al.* **Congenital and acquired neutropenias consensus guidelines on therapy and follow-up in childhood from the Neutropenia Committee of the Marrow Failure Syndrome Group of the AIEOP (Associazione Italiana Emato-Oncologia Pediatrica)**. In: *American Journal of Hematology* 87.2 (2012), pp. 235–238. ISSN: 03618609. DOI: 10.1002/ajh.22225.

[151] Palmblad, J., Papadaki, H. A., and Eliopoulos, G. **Acute and chronic neutropenias. What is new?** In: *Journal of Internal Medicine* 250.6 (2001), pp. 476–491. ISSN: 09546820. DOI: 10.1046/j.1365-2796.2001.00915.x.

[152] Köhler, A. *et al.* **G-CSF–mediated thrombopoietin release triggers neutrophil motility and mobilization from bone marrow via induction of Cxcr2 ligands**. In: *Blood* 117.16 (2011). DOI: 10.1182/blood-2010-09-308387.

[153] Gazendam, R. P. *et al.* **Impaired killing of Candida albicans by granulocytes mobilized for transfusion purposes: A role for granule components.** In: *Haematologica* 101.5 (2016), pp. 587–96. ISSN: 1592-8721. DOI: 10.3324/haematol.2015.136630.

[154] Bhatia, S., McCullough, J., Perry, E. H., Clay, M., Ramsay, N. K., and Neglia, J. P. **Granulocyte transfusions: efficacy in treating fungal infections in neutropenic patients following bone marrow transplantation**. In: *Transfusion* 34.3 (1994), pp. 226–232. ISSN: 0041-1132 (Print). DOI: 10.1046/j.1537-2995.1994.34394196620.x.

[155] Strauss, R. G. **Clinical perspectives of granulocyte transfusions: Efficacy to date**. In: *Journal of Clinical Apheresis* 10.3 (1995), pp. 114–118. ISSN: 10981101. DOI: 10.1002/jca.2920100303.

[156] Safdar, A., Hanna, H. A., Boktour, M., Kontoyiannis, D. P., Hachem, R., Lichtiger, B., Freireich, E. J., and Raad, I. I. **Impact of high-dose granulocyte transfusions in patients with cancer with candidemia: Retrospective case-control analysis of 491 episodes of candida species bloodstream infections**. In: *Cancer* 101.12 (2004), pp. 2859–2865. ISSN: 0008543X. DOI: 10.1002/cncr.20710.

[157] Hotchkiss, R. S., Monneret, G., and Payen, D. **Immunosuppression in sepsis: a novel understanding of the disorder and a new therapeutic approach**. In: *The Lancet Infectious Diseases* 13.3 (2013), pp. 260–8. ISSN: 1474-4457. DOI: 10.1016/S1473-3099(13)70001-X.

[158] Courant, R., Friedrichs, K., Lewy, H., and H, L. **Über die partiellen Differenzengleiehungen der**. In: *Mathematische Annalen* 100.1 (1928), pp. 32–74. DOI: 10.1007/BF01448839.

[159] Press, W., Flannery, B., Teukolsky, S., and Vetterling, W. **Numerical Recipes: The Art of Scientific Computing**. Vol. 29. 4. 1987, p. 501. ISBN: 0521431085. DOI: 10.2307/1269484. arXiv: arXiv:1011.1669v3.

[160] Guo, Z., Sloot, P. M. A., and Tay, J. C. **A hybrid agent-based approach for modeling microbiological systems.** In: *Journal of theoretical biology* 255.2 (2008), pp. 163–75. ISSN: 1095-8541. DOI: 10.1016/j.jtbi.2008.08.008.

[161] Fullstone, G., Wood, J., Holcombe, M., and Battaglia, G. **Modelling the transport of nanoparticles under blood flow using an agent-based approach**. In: *Scientific Reports* 5 (2015), pp. 1–13. ISSN: 20452322. DOI: 10.1038/srep10649.

[162] Behr, M., Arora, D., Coronado, O., and Pasquali, M. **Models and Finite Element Techniques for Blood Flow Simulation**. In: *International Journal for Computational Dynamics* 20 (2006), pp. 175–181. ISSN: 10618562. DOI: 10.1080/10618560600789776.

[163] Morris, P. D. *et al.* **Computational fluid dynamics modelling in cardiovascular medicine**. In: *Heart* 102.1 (2016), pp. 18–28. ISSN: 1468201X. DOI: 10.1136/heartjnl-2015-308044.

[164] Tong, S. Y. C., Davis, J. S., Eichenberger, E., Holland, T. L., and Fowler, V. G. **Staphylococcus aureus infections: epidemiology, pathophysiology, clinical manifestations, and management.** In: *Clinical microbiology reviews* 28.3 (2015), pp. 603–61. ISSN: 1098-6618. DOI: 10.1128/CMR.00134-14.

[165] Walsh, T. J. and Gamaletsou, M. N. **Treatment of fungal disease in the setting of neutropenia.** In: *Hematology / The Education Program of the American Society of Hematology* 2013.1 (2013), pp. 423–427. ISSN: 1520-4383. DOI: 10.1182/asheducation-2013.1.423.

[166] Donadieu, J., Fenneteau, O., Beaupain, B., Mahlaoui, N., and Chantelot, C. B. **Congenital neutropenia: diagnosis, molecular bases and patient management.** In: *Orphanet journal of rare diseases* 6 (2011), p. 26. ISSN: 1750-1172. DOI: 10.1186/1750-1172-6-26.

[167] Newburger, P. E. **Disorders of neutrophil number and function.** In: *The Education Program of the American Society of Hematology* 2006.1 (2006), pp. 104–10. ISSN: 1520-4391. DOI: 10.1182/asheducation-2006.1.104.

[168] Bardoel, B. W., Kenny, E. F., Sollberger, G., and Zychlinsky, A. **The balancing act of neutrophils**. In: *Cell Host and Microbe* 15.5 (2014), pp. 526–536. ISSN: 19346069. DOI: 10.1016/j.chom.2014.04.011.

[169] Lambrecht, B. N. **Alveolar Macrophage in the Driver's Seat**. In: *Immunity* 24.4 (2006), pp. 366–368. ISSN: 10747613. DOI: 10.1016/j.immuni.2006.03.008.

[170] Bowden, D. H. **The alveolar macrophage**. In: *Environmental Health Perspectives* 55 (1984), pp. 327–341. ISSN: 00916765. DOI: 10.1289/ehp.8455327.

[171] Segal, B. H. **Role of macrophages in host defense against aspergillosis and strategies for immune augmentation.** In: *The Oncologist* 12 Suppl 2 (2007), pp. 7–13. ISSN: 1083-7159. DOI: 10.1634/theoncologist.12-S2-7.

[172] Philippe, B., Ibrahim-Granet, O., Prévost, M. C., Gougerot-Pocidalo, M. a., Perez, M. S., Van der Meeren, a., and Latgé, J. P. **Killing of Aspergillus fumigatus by alveolar macrophages is mediated by reactive oxidant intermediates**. In: *Infection and Immunity* 71.6 (2003), pp. 3034–3042. ISSN: 00199567. DOI: 10.1128/IAI.71.6.3034-3042.2003.

[173] Roilides, E., Katsifa, H., and Walsh, T. J. **Pulmonary host defences against Aspergillus fumigatus.** In: *Research in Immunology* 149.4-5 (1998), 454–65, discussion 523–4. ISSN: 0923-2494. DOI: 10.1016/S0923-2494(98)80769-4.

[174] Mircescu, M. M. M. M., Lipuma, L., Rooijen, N. van, Pamer, E. G. G. G., and Hohl, T. M. M. M. **Essential Role for Neutrophils but not Alveolar Macrophages at Early Time Points following Aspergillus fumigatus Infection**. In: *The Journal of Infectious Diseases* 200.4 (2009), pp. 647–656. ISSN: 0022-1899. DOI: 10.1086/600380.

[175] Kraibooj, K., Schoeler, H., Svensson, C.-M., Brakhage, A. A., and Figge, M. T. **Automated quantification of the phagocytosis of Aspergillus fumigatus conidia by a novel image analysis algorithm**. In: *Frontiers in Microbiology* 6.June (2015), pp. 1–13. ISSN: 1664-302X. DOI: 10.3389/fmicb.2015.00549.

[176] Cseresnyes, Z., Kraibooj, K., and Figge, M. T. **Hessian-based quantitative image analysis of host-pathogen confrontation assays**. In: *Cytometry Part A* 93.3 (2018), pp. 346–356. ISSN: 15524930. DOI: 10.1002/cyto.a.23201.

[177] Huh, D. **A human breathing lung-on-a-chip**. In: *Annals of the American Thoracic Society* 12.March (2015), S42–S44. ISSN: 23256621. DOI: 10.1513/AnnalsATS.201410-442MG.

[178] Mosig, A. S. **Organ-on-chip models: new opportunities for biomedical research**. In: *Future Science OA* 3.2 (2016), fsoa–2016–0038. ISSN: 2056-5623. DOI: 10.4155/fsoa-2016-0038.

[179] Benam, K. H. *et al.* **Small airway-on-a-chip enables analysis of human lung inflammation and drug responses in vitro**. In: *Nature Methods* 13.2 (2016), pp. 151–157. ISSN: 15487105. DOI: 10.1038/nmeth.3697.

[180] Osherov, N. **Interaction of the pathogenic mold Aspergillus fumigatus with lung epithelial cells**. In: *Frontiers in Microbiology* 3 (2012), p. 346. ISSN: 1664-302X. DOI: 10.3389/fmicb.2012.00346.

[181] Hansen, J. E. and Ampaya, E. P. **Human air space shapes, sizes, areas, and volumes**. In: *Journal of Applied Physiology* 38.6 (1975), pp. 990–995. ISSN: 0021-8987.

[182] Standring, S. **Gray's anatomy : the anatomical basis of clinical practice**, p. 964. ISBN: 9780702068515.

[183] Kradin, R. L. and Mark, E. J. **Pulmonary infections**. Elsevier Inc., 2010, pp. 125–188. ISBN: 9781416034292. DOI: 10.1016/B978-1-4160-3429-2.00007-9.

Danksagung

Der lange Weg bis zur Fertigstellung dieser Arbeit ist mit vielen schönen Erinnerungen aber auch anstrengenden Phasen verbunden. Auf diesem Weg wurde ich von einigen besonderen Menschen begleiten und unterstützt, denen ich an dieser Stelle meinen herzlichen Dank aussprechen möchte.

Meinem Doktorvater, Prof. Dr. Marc Thilo Figge, gilt mein ganz besonderer Dank, da er mir die Promotion in der Arbeitsgruppe *Angewandte Systembiologie* ermöglicht hat. Bei seiner Betreuung ist es ihm stets gelungen, Zeit für die Entwicklung neuer Ideen, Lösungsansätze und die Bewältigung von inhaltlichen Schwierigkeiten zu finden. Durch seine Art die Arbeitsgruppe zu leiten, schaffte er die Basis für einen unkomplizierten und hilfsbereiten Umgang innerhalb der Arbeitsgruppe. Zudem räumte er mir die Möglichkeit ein, an zahlreichen Workshops und Symposien organisatorisch mitzuwirken und dabei sehr viel außerhalb der reinen Wissenschaft zu lernen.

Den aktuellen und ehemaligen Mitarbeitenden der Arbeitsgruppen *Angewandte Systembiologie* und *Systembiologie/ Bioinformatik* möchte ich für die gute Arbeitsatmosphäre danken. Insbesondere die Gespräche während der Kaffeepausen und auf dem Weg zur Mensa haben zur Lösung mancher wissenschaftlichen Probleme beigetragen oder durch gezielte Ablenkung den Kopf für frische Gedankengänge freigemacht. Dabei ist mir besonders der kreative Austausch mit Stefanie Dietrich über zahlreiche Projekte und private Belange in sehr guter Erinnerung geblieben. Bei Johannes Pollmächer möchte ich mich ganz besonders für seine Betreuung während meiner Masterarbeit und darüber hinaus bedanken. Durch seine sehr gute Anleitung, seine Geduld und viele Erklärungen hat er eine gelungene und konstruktive Zusammenarbeit an seinem Programmcode ermöglicht und zu einer reibungslosen Weiterführung meiner Arbeit am Programmcode, nach seinem Weggang aus der Arbeitsgruppe, beigetragen. Weiterhin möchte ich mich bei meiner Büronachbarin Teresa Lehnert für die schönen Jahre bedanken, in denen der Arbeitsalltag, durch inspirierende wissenschaftliche Gespräche und ihre unkomplizierte und freundliche Art, verschönert wurde. Für die inhaltliche und sprachliche Kontrolle der vorliegenden Doktorarbeit möchte ich mich bei Teresa Lehnert und Johannes Pollmächer bedanken.

Weiterhin möchte ich mich für die ausgezeichnete kollegiale und kooperative Atmosphäre am Hans-Knöll Institut sowie innerhalb des CRC/Transregio 124 FungiNet bedanken. Mein besonderer Dank geht dabei an unsere Kooperationspartner Prof. Dr. Oliver Kurzai, Dr. Kerstin Hünniger und Dr. Ines Leonhardt, aus der Forschungsgruppe *Fungal Septomics*. Die Entwicklung der virtuellen Vollblut-Infektionsmodelle in dieser Arbeit basieren nicht nur auf Daten, die von ihnen experimentell ermittelt wurden, sondern beruhen auch auf zahlreichen Treffen und Gesprächen. Für wertvolle Gespräche, die zur Entwicklung der Infektionsmodelle von *A. fumigatus* Lungeninfektionen beigetragen haben, danke ich Prof. Dr. Peter Zipfel.

Außerdem möchte ich mich bei der Graduiertenschule Jena School for Microbial Communication (JSMC) bedanken, bei der ich assoziierte Doktorandin war, sowie bei der Jenaer Graduiertenakademie (JGA), die viele lehrreiche Kurse zur persönlichen und wissenschaftlichen Weiterentwicklung bereitgestellt hat.

Meinen engen Freunden Julia, Enrico, Franziska, Steffen, Sarah, René und Sebastian danke ich für ihren emotionalen Rückhalt, für die vielen lustigen Spiele- und Filmabende, für den gemeinsamen Sport und die vielen schöne Momente, die mich oft auf andere Gedanken brachten und diese anschließend wieder frisch für die Arbeit waren.

Ein großer Dank für den moralischen Rückhalt geht an mein familiäres Umfeld. Für unser gutes Verhältnis, unsere vielen gemeinsamen Interessen und dass wir über alles reden können, danke ich meiner Schwester Nicole.

Nicht zuletzt möchte ich mich bei meinen Eltern bedanken. Ihr habt mir diesen Weg nicht nur durch Eure finanzielle Unterstützung während des Studium, sondern auch durch Eure liebevolle Erziehung ermöglicht, mit der Ihr mir viel mehr als nur das Nötigste mit auf den Weg gegeben habt. Mit Liebe, stets offenen Ohren und guten Ratschlägen habt ihr mich in guten Phasen begleitet und in schwierigen Phasen aufgefangen. Ich danke Euch!

Ehrenwörtliche Erklärung

Hiermit erkläre ich, dass mir die geltende Promotionsordnung der Fakultät für Biowissenschaften bekannt ist und ich mich mit bestem Wissen an diese Ordnung gehalten habe.

Die vorliegende Dissertation habe ich selbständig und nur unter Verwendung der angegebenen Hilfsmittel, Daten und Quellen angefertigt. Unterstützung während meiner wissenschaftlichen Arbeit und zur Erstellung des vorliegenden Dissertationstextes habe ich nur von den genannten Co-Autoren und in der Danksagung genannten Personen erhalten. Ich habe keine Hilfe von externen Vermittlungs- oder Beratungsdiensten in Anspruch genommen. Niemand hat mittelbare oder unmittelbare geldwerte Leistungen erhalten, für Arbeiten die im Zusammenhang mit dem Inhalt der vorgelegten Dissertation stehen.

Die vorgelegte Dissertation wurde bisher nicht als Prüfungsarbeit für eine andere wissenschaftliche Prüfung eingereicht. Im Speziellen habe ich sie an keiner anderen Hochschule eingereicht, um einen akademischen Grad zu erhalten.

Jena, den 27. Juni 2018

Sandra Timme